UNIVERSITÉ DE STRASBOURG

ÉCOLE DOCTORALE MSII (ED N°269)

laboratoire des sciences de l'ingénieur, de l'informatique

et de l'imagerie (ICUBE)-UMR 7357

THÈSE présentée par :

Lei MA

soutenue le : **6 Dec 2022**

pour obtenir le grade de : **Docteur de l'université de Strasbourg**

Discipline/ Spécialité : Mécanique/ Génie Civil

Modélisation par éléments discrets du comportement en fatigue des bétons bitumineux par une méthode énergétique.

THÈSE dirigée par :	
M. CHAZALLON Cyrille	Professeur, INSA de Strasbourg
M. DESCANTES Yannick	Chargé de recherches (HDR), IFSTTAR
RAPPORTEURS :	
M. NICOT François	Professeur, Université Savoie Mont Blanc
M. CHEVOIR François	Directeur de recherches, IFSTTAR
AUTRES MEMBRES DU JURY :	
M. RAGUENEAU Frédéric	Professeur, ENS Cachan
M. KOVAL Georg	Maître de conférences, INSA de Strasbourg

UNIVERSITY OF STRASBOURG

Discrete element modeling of asphalt concrete fatigue behavior by an energetic method

by

Lei MA

A thesis submitted in partial fulfillment for the
degree of Doctor of Philosophy

in the
Doctoral School of MSII

Dec 2022

Acknowledgements

This PhD work is under the guidance of my supervisor Cyrille CHAZALLON, associate professor Georg KOVAL, and co-director Yannick DESCANTES. My deepest gratitude goes foremost to my advisers, Georg KOVAL, Cyrille CHAZALLON, and Yannick DESCANTES, who provided constructive advice, foresighted instruction and continuous encouragement and support. Georg KOVAL daily accompanies me during my study and enlighten me during creative discussions. Cyrille CHAZALLON is a very supportive and patient professor, who enable me to qualify as a Ph.D. student. Yannick DESCANTES impressed me by serious scientific attitude and deep insights.

I would like to thank my colleagues in the Group of Civil Engineering and Energy at INSA Strasbourg, Saïda MOUHOUBI, Hossein NOWAMOOZ, Juan Carlos QUEZADA GUAJARDO, for their hospitality during my time as a Ph.D. student. Special thanks to my fellow Ph.D. students, Guixian Liu, Fujiao TANG, Anicet DANSOU, Laura GAILLARD, Léo COULON, Haittao GE, Chong Wang, Xiang ZHANG, Oussama HAMMOUD, Victor DESLOGES and Marieh FATAHIZADEH for all the great moments we shared.

I am also grateful to the China Scholarship Council (CSC) who provided me with a full scholarship for three-and-a-half years that guaranteed the smooth completion of my thesis.

Finally, I give my thanks to my family and Miss ZHANG Qi for their endless and unconditional encouragement and support.

The difficulties we met, confused me; the inspirations we witnessed, thrilled me; the solutions we found, relieved me; the knowledge we learned, rose me; the unknowns we opened, modest me; the path we came, led me; the time we shared, memorized me. Thinking is invitation, chaos gladly accept. But, if I may, if possible, I would rather be humble my whole life to just pursue a glance for the light of the wisdom and beauty.

Résumé étendu

Contexte

Les questions environnementales poussent le secteur de la construction à rechercher des pratiques plus durables. En ce qui concerne l'industrie des chaussées routières, les efforts visant à allonger la durée de vie des structures de chaussée et à réduire la quantité de matériaux consommés sont des éléments clés pour la réduction des impacts environnementaux, notamment en ce qui concerne les émissions de dioxyde de carbone pendant la construction, la réparation et la reconstruction des chaussées.

Le phénomène de fatigue est l'une des principales causes de dégradation des chaussées, entraînant une réduction de leur durée de vie. L'analyse et la prédiction de ces effets sur les structures de chaussée font l'objet d'une attention croissante de la part des praticiens afin d'optimiser la conception et la gestion des routes.

Les sollicitations répétées (trafic et température), sont responsables d'une détérioration mécanique continue des matériaux de structure, qui conduit à l'initiation et à la propagation de fissures en fonction du nombre de cycles. Plusieurs processus physiques, tels que la non-linéarité du module complexe, l'auto-échauffement, la thixotropie et la coalescence des fissures sont impliqués dans les phénomènes de fatigue du béton bitumineux (matériau de chaussée le plus courant).

Aujourd'hui, les essais expérimentaux sont le principal outil pour déterminer la performance en fatigue du béton bitumineux, bien que tous les mécanismes de fatigue ne soient pas encore complètement connus. L'étude des mécanismes essentiels a été réalisée au cours des dernières décennies par le biais de simulations numériques.

Le béton bitumineux est un matériau composite composé de granulats, de liant bitumineux et éventuellement de matériaux de remplissage. Il présente naturellement une microstructure hétérogène qui affecte de nombreux aspects du comportement en fatigue. Dans la méthode des éléments discrets (DEM), le matériau est décrit au moyen d'un assemblage de particules interagissant par contact, ce qui se transforme en un outil numérique efficace pour imiter l'effet des hétérogénéités.

Plan du Mémoire

Objectif de la recherche

L'objectif global de cette thèse est de proposer des modèles de contact en DEM qui permettent de traiter l'ensemble du processus de fatigue lors d'essais de laboratoire à température et fréquence de chargement constantes. Afin d'atteindre cet objectif, les problématiques suivantes sont enoncées :

- Définir une formulation énergétique d'un modèle de contact pour la croissance des fissures en fatigue pour les fissures longues.
- Proposer une description physique et un modèle subséquent pour l'initiation des fissures.
- Combinez les deux aspects dans un seul modèle de contact.

Organisation de la thèse

Cette thèse est organisée en plusieurs parties :

Le chapitre 2 passe en revue les phénomènes de fatigue des matériaux, les essais de fatigue couramment réalisés, les processus physiques impliqués et les étapes correspondantes de l'évolution de la fatigue. Les connaissances de base de la mécanique de la rupture élastique linéaire et de la libération d'énergie pendant le processus de fissuration sont présentées. Les modèles existants sont évalués, y compris le modèle d'endommagement, le modèle de croissance des fissures et le modèle de zone cohésive. Les possibilités d'amélioration sont clarifiées.

Dans le chapitre 3, un modèle de contact, le modèle-p, pour la croissance des fissures en fatigue est proposé.

Dans le chapitre 4, le modèle-p est validé par des comparaisons respectivement avec les calculs théoriques et l'expérimentation.

Au chapitre 5, le modèle-p est simplifié en modèle-sp. De plus, ce modèle-sp est utilisé de manière créative comme un modèle d'endommagement qui peut saisir l'ensemble du processus d'évolution de la fatigue pour différents niveaux de déformation des essais de fatigue. Le modèle-sp est validé par des comparaisons avec l'expérimentation pour différents matériaux et méthodes d'essai.

Enfin, les conclusions de ce travail sont présentées et plusieurs perspectives d'études futures sont indiquées au chapitre 6.

Représentation d'une fissure en DEM

Un modèle de propagation de fissure et un modèle d'endommagement sont proposés dans ce travail, lesquels sont à l'origine des solutions permettant de représenter des fissures en DEM.

Afin de permettre de représenter une fissure en DEM de n'importe quelle longueur dans un échantillon, les corrélations formulées dans cette section donnent le moyen de relier précisément la propagation de la fissure a_c ($0 \leq a_c \leq d_c$, où d_c est la longueur du domaine de contact voir Figure 3.3, dans ce cas, d_c égal au diamètre de la particule, $d_c = d$) à la dégradation de la rigidité de contact ($0 \leq D \leq 1$). L'idée de base est d'établir une bijection, une correspondance biunivoque, entre ces deux quantités a_c et D.

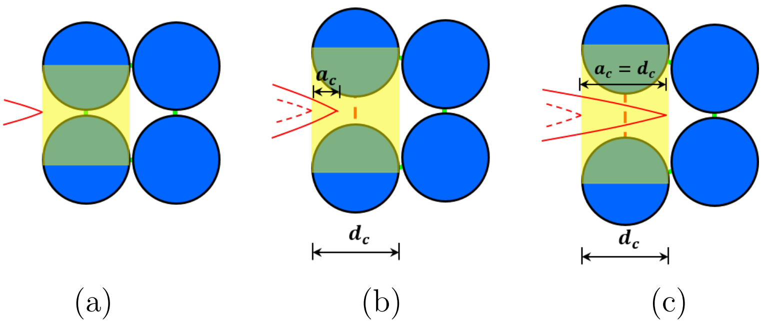

Figure 1: (a) Pointe de fissure au voisinage d'un contact et avec propagation de la fissure de (a) à (b) puis à (c), sa trajectoire pendant la rupture du contact est décrite par la variable a_c ($0 \leq a_c \leq d_c$).

Prenons un exemple pour illustrer la bijection. Dans la Figure 3.4a, une plaque longue et rectangulaire avec une pré-fissure initiale de longueur a_0 est soumise à une contrainte uniforme constante σ, qui conduit à un déplacement vertical élastique $\bar{\delta}_0$. La propagation Δa de la fissure conduit à une variation du déplacement vertical $\Delta\bar{\delta}$ (voir Figure 3.4b). L'augmentation progressive de la longueur de la fissure de a_0 à $a_0 + \Delta a$ est illustrée sur la Figure 3.4c. Pour simuler un tel processus, un assemblage composé de particules monodispersées de diamètre d organisées en un assemblage granulaire bidimensionnel régulier et carré (Figure 3.4d) est conceptuellement adopté pour modéliser la plaque élastique. Dans cet exemple, nous avons choisi $a_0 = 4d$, $\Delta a = d$. La fissure est simplement représentée par quatre contacts qui ont été coupés. La propagation de la fissure est représentée dans ce cas en coupant le cinquième contact (clairement représenté sur la Figure 3.4e). Cela peut faire avancer la

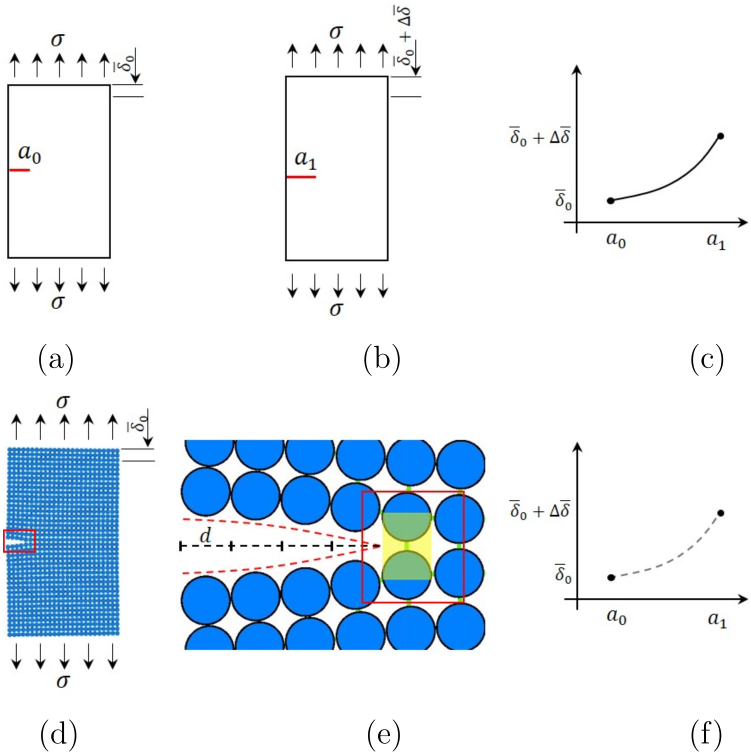
σ
$\overline{\delta}_0$
a_0
σ
$\overline{\delta}_0 + \Delta\overline{\delta}$
a_1
$\overline{\delta}_0 + \Delta\overline{\delta}$
$\overline{\delta}_0$
a_0
a_1
d

(a) (b) (c)

(d) (e) (f)

Figure 2: (a) Plaque élastique avec fissure initiale a_0 sous contrainte σ, déplacement résultant $\overline{\delta}_0$ (b) effet d'une croissance de fissure (de a_0 à a_1) sur les déplacements en fonction de la longueur de la fissure, (c) évolution du déplacement. (d) échantillon DEM correspondant, (e) zoom de la longueur propagée (d), et (f) évolution correspondante des déplacements en fonction de la longueur de la fissure.

fissure d'un 'saut'. Cependant, la continuité du processus de rupture reste dépendante de la rupture du contact (comme le suggère la Figure 3.4f).

Afin de caractériser spécifiquement le processus de rupture d'un contact, l'effet mécanique de la propagation virtuelle de la pointe de fissure sur une distance d_c, définie comme le domaine de contact, est analysé. La longueur d_c correspond au déplacement de la pointe de fissure si le contact est coupé. Progressivement, le déplacement de la pointe de la fissure, défini par la longueur a_c ($0 \leq a_c \leq d_c$ comme indiqué sur la Figure 3.3), induit une réduction de la rigidité du contact. On peut adopter une variable d'état D ($0 \leq D \leq 1$) pour décrire cette dégradation de la rigidité du contact concernée par le processus de propagation de la pointe de fissure. Aucun processus de propagation n'est observé pour $a_c = 0$, ce qui est automatiquement lié à un contact intact

($D = 0$). En revanche, si $a_c = d_c$, la pointe de fissure s'est propagée et a coupé le contact ($D = 1$).

Une relation cohérente entre la propagation de la pointe de fissure a_c et la dégradation de la rigidité D permet au modèle discret de définir un déplacement de fissure plus petit que la dimension des particules composant le matériau. Dans les sections suivantes, une relation $a_c - D$ basée sur le bilan énergétique d'un contact est proposée.

Définition du ratio de pente p

Le premier élément pour comprendre la relation entre la propagation de la fissure et le processus de dégradation du contact à la pointe de la fissure dans l'échantillon de DEM est l'évolution de la force et des déplacements. Si seul le contact à la pointe de la fissure est relâché ($0 \leq D \leq 1$), dans des conditions élastiques, le matériau entourant la pointe de la fissure se comporte comme un système élastique. Par simplicité, remplaçons le matériau environnant par un ressort élastique représentant l'élasticité du matériau k_p, comme proposé dans la Figure 3.5. Si l'on considère le processus de rupture de manière opposée, où la force de contact peut fermer la fissure, l'action individuelle de la force de contact associée à la pointe de la fissure peut réduire linéairement l'écart entre les deux particules. De manière naturelle, une valeur décroissante de $F = \delta(1-D)k_0$ peut simplement augmenter proportionnellement la distance entre les deux particules (décrite par δ), ce qui explique la trajectoire linéaire observée lors du processus de rupture ($0 \leq D \leq 1$), comme le montre la Figure 3.6.

Dans la Figure 3.6, un contact qui représente une partie du matériau d'une plaque est décrit par les deux systèmes de ressorts et l'évolution de la force de contact F et du déplacement δ dans le système de coordonnées. Quatre états sont choisis, à savoir, (o) une plaque pré-fissurée sans chargement, (A) une plaque soumise à une contrainte constante σ, (B) une fissure se propage jusqu'à la limite du domaine de contact, (C) une fissure traverse totalement le domaine de contact. Trivialement, la force élastique maximale, juste avant le processus de rupture du contact (processus de (B) à (C)) est égale à $F_{max} = k_0\delta_0$. Pour cette même force F_{max} agissant sur le ressort $2k_p$, le déplacement associé au matériau environnant est simplement $\delta_p = F_{max}/k_p$. Après le processus de rupture progressive, la force diminue de F_{max} à 0 suivant la pente de rupture k_p et le ressort du matériau environnant n'est plus en tension. L'augmentation totale du contact rompu est finalement de $\delta_{max} = \delta_0 + \delta_p = \delta_0(1 + k_0/k_p)$, lorsque $F = 0$.

Définissons le rapport de pente p comme le rapport entre la pente élastique k_0

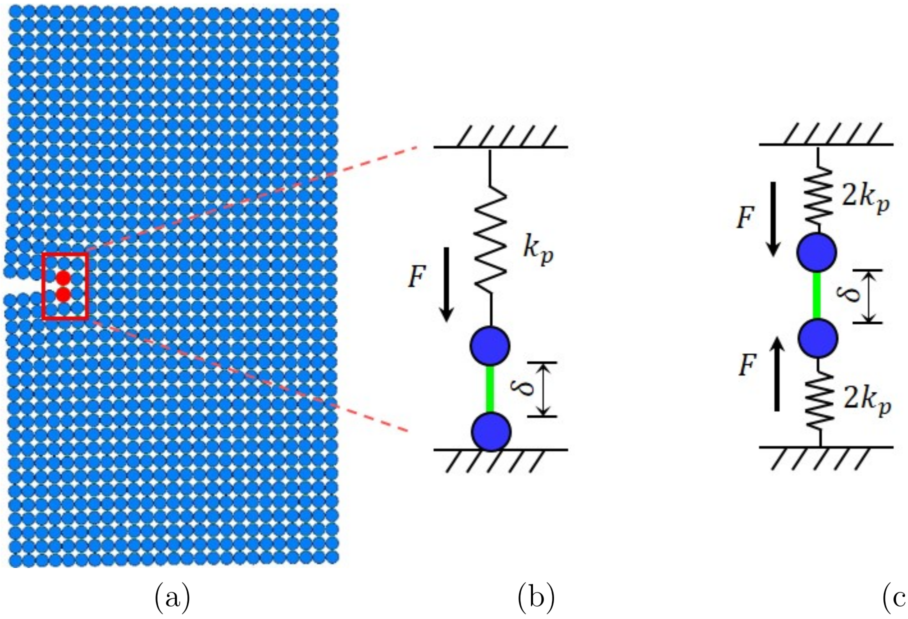

(a) (b) (c)

Figure 3: Description schématique de la relation mécanique entre le contact à la pointe de la fissure et les particules voisines. (a) Plaque pré-fissurée et (b) son comportement élastique simplifié près de la pointe de la fissure, où k_p représente la rigidité du matériau entourant la pointe de la fissure, F et δ sont la force et le déplacement de contact, (c) une description plus intuitive de (b).

et la valeur absolue de la pente de rupture k_p, soit $p = k_0/k_p$. Physiquement, le rapport de pente p est une quantité qui caractérise la relation entre la rigidité du contact et la rigidité de son voisinage. Cela signifie que le rapport de pente p tient compte de l'effet du matériau environnant sur la pointe de la fissure.

Pour décrire le changement de la position de la fissure et du déplacement du contact avec la propagation de la fissure, la figure 3.7 montre deux états de la position de la fissure et du déplacement du contact, se référant respectivement aux états (B) et (C) de la figure 3.6.

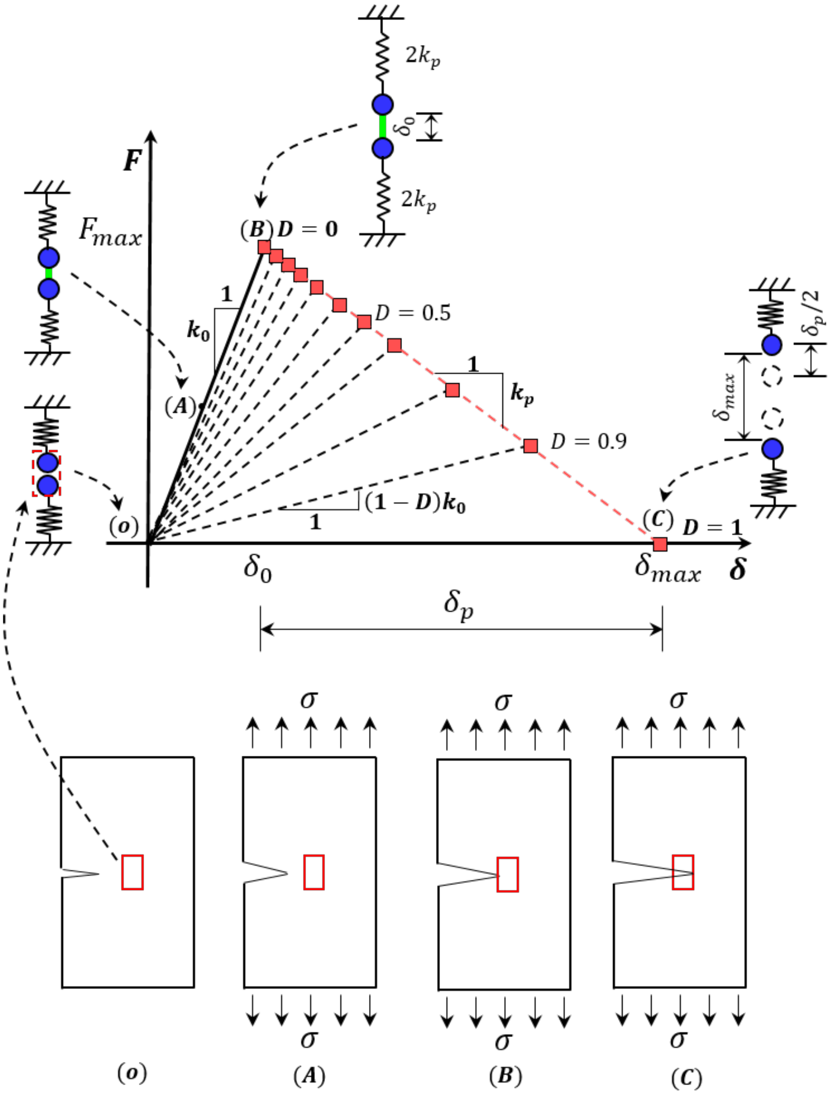
2k_p
δ_0
2k_p
F
F_{max}
(B) D = 0
1
k_0
D = 0.5
1
k_p
(A)
D = 0.9
(1 − D)k_0
1
(o)
(C) D = 1
$\delta_p/2$
δ_{max}
δ_0
δ_{max}
δ
δ_p
σ
σ
σ
σ
σ
σ
(o)
(A)
(B)
(C)

Figure 4: Description de l'évolution d'un contact pour l'ensemble du processus allant de la fissure proche à la fissure traversant ce contact. En bas de la figure, (o) une plaque pré-fissurée dans laquelle un rectangle rouge représente le contact dont le comportement est décrit par les deux systèmes de ressorts et l'évolution de la force de contact F et du déplacement δ dans le système de coordonnées, (A) plaque soumise à une contrainte constante σ, (B) fissure se propageant jusqu'à la limite du domaine de contact, (C) fissure traversant totalement le domaine de contact. De (B) à (C), la croissance de la fissure dans le domaine de contact est représentée par le processus de dégradation de la rigidité de contact, pour $(0 \leq D \leq 1)$, où k_0 est la rigidité de contact initiale, et $(1 - D)k_0$ est sa valeur dégradée.

En ce qui concerne la méthode proposée qui représente la propagation des fissures, lorsqu'elle est comparée au modèle de la zone cohésive (CZM), il convient de mentionner une similitude et une différence majeures entre eux. Tous deux utilisent un changement progressif de la propriété mécanique de l'élément situé à l'avant d'une pointe de fissure pour représenter la propagation de la fissure. Pour le CZM, la séparation est régie par la déformation δ qui suit une courbe de radoucissement définie artificiellement. Il est important de noter que pour la méthode discutée ci-dessus, comme le montre la Figure 3.6, la séparation est uniquement régie par la dégradation de la rigidité de contact, et la courbe de radoucissement n'est pas définie mais se forme naturellement et c'est ce qui différencie principalement les deux méthodes.

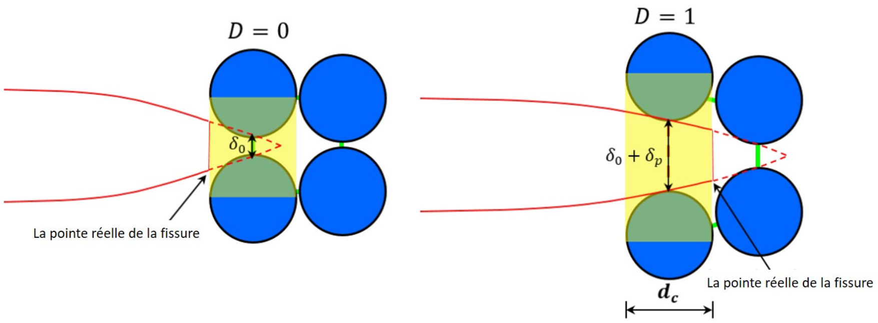
$D = 0$
δ_0
La pointe réelle de la fissure
$D = 1$
$\delta_0 + \delta_p$
La pointe réelle de la fissure
d_c

(a) (b)

Figure 5: Description schématique de la position de la fissure et du déplacement du contact. (a) Pointe de fissure à la limite du domaine de contact, où δ_0 est le déplacement de contact, et (b) fissure traversant totalement le domaine de contact.

Équivalence énergétique

Le principe d'équivalence énergétique se base sur le fait que l'énergie libérée dans les échantillons DEM doit être la même que dans le matériau réel pendant un certain incrément de fissure. Ainsi, l'équivalence de l'énergie libérée dans une fissure et dans un contact pour la même longueur propagée peut finalement conduire aux correspondances entre a_c et D

$$\frac{a_c}{d_c} = \frac{1-(1-D)}{1+p(1-D)}, \tag{1}$$

ou inversement

$$1-D = \frac{1-\dfrac{a_c}{d_c}}{1+p\dfrac{a_c}{d_c}}. \tag{2}$$

Les équations 3.16 et 3.17 fournissent une relation directe entre la propagation de la fissure et l'endommagement dans un contact ($0 \leq a_c/d_c \leq 1$ en conformité avec $0 \leq D \leq 1$). Toutes les informations sont entièrement définies au niveau du contact (propriétés k_0 et d_c) ou mesurées lors de la séparation du contact ($F \times \delta$) comme k_p (qui conduit à $p = k_0/k_p$). Cette approche locale explicite de la libération d'énergie permet l'application directe de modèles de mécanique de la rupture pour simuler la propagation des fissures.

Forme incrémentale de la relation fissure-dommage

La relation $a_c - D$ décrite dans les équations 3.16 et 3.17 suppose une pente de séparation constante (constante p), ce qui est raisonnable pour des structures élastiques avec des fissures qui n'interagissent pas, donc ne modifient pas la réponse mécanique près de la pointe de la fissure de l'une à l'autre. Tout comportement non linéaire du matériau qui réduit sa rigidité (comme un endommagement) ou la proximité de fissures qui modifie les conditions aux limites près d'une pointe de fissure peut affecter la valeur de p. La situation générale décrite dans la Figure 3.18 est considérée et une forme incrémentale de $a_c - D$ est proposée.

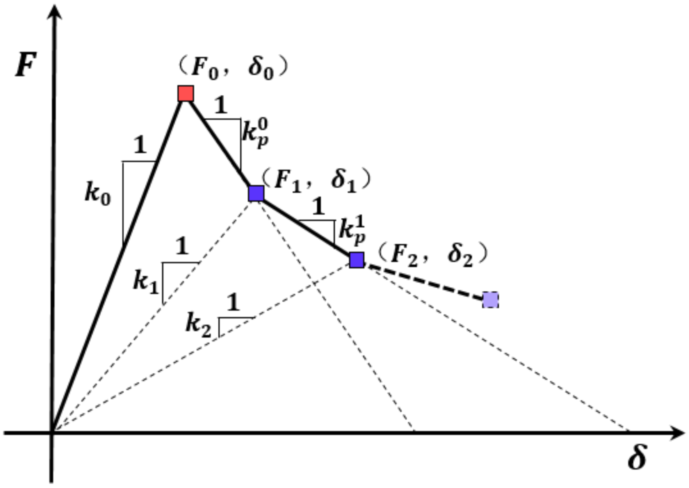

Figure 6: Description schématique de la séparation non-linéaire par traction de contact.

Dans une formulation incrémentale, les incréments de propagation de fissures da sont associés à des incréments de dommages dD. L'évolution des fissures et l'évolution des dommages peuvent s'écrire comme suit

$$\begin{cases} a_{ci+1} = a_{ci} + da \\ D_{i+1} = D_i + dD \end{cases} \tag{3}$$

où i décrit les événements de propagation. La Figure 3.19 montre schématiquement la relation entre les formulations directe et en taux.

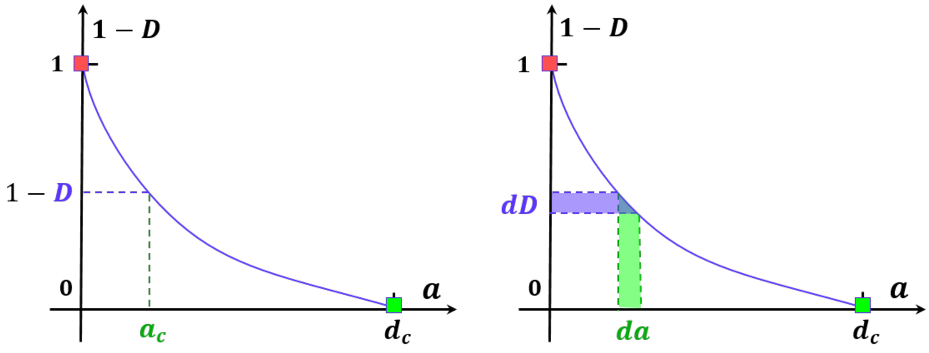

(a) (b)

Figure 7: Transformations (a) entre a_c et D, (b) entre da et dD.

En considérant le contact endommagé comme un nouveau contact mais avec un domaine de contact réduit, on peut finalement obtenir

$$da = \frac{(d_c - a_c)dD}{(1-D)[1+p(1-D-dD)]}, \tag{4}$$

ou inversement

$$dD = (1-D)\left(1 - \frac{\left(1 - \dfrac{da}{d_c - a_c}\right)}{1 + p(1-D)\left(\dfrac{da}{d_c - a_c}\right)}\right). \tag{5}$$

La relation des taux $da - dD$ permet d'écrire la relation directe entre un incrément de fissure da et un incrément de dégradation de la rigidité dD, pour un rapport de pente instantané p et une dégradation de la rigidité D donnés. L'équation 3.24 associée à l'équation 3.18, permet une description continue de la relation entre a_c et D.

La loi de Paris

La transformation $da - dD$ permet également d'écrire une représentation énergétiquement cohérente de la propagation d'une fissure causée par un dommage du contact sur une longueur inférieure à l'échelle de la particule. La loi de Paris est un critère de fatigue qui se base sur la libération d'énergie par cycle pour déterminer l'ampleur de la propagation d'une fissure.

La loi de Paris est un critère de croissance des fissures en fatigue dans lequel l'incrément de fissure pendant un cycle de chargement da est déterminé par une fonction puissance de la plage de facteurs d'intensité de contrainte correspondante $\Delta K = K_{max} - K_{min}$ dans le cycle de chargement. Le rapport de contrainte est défini comme le rapport entre la contrainte minimale et la contrainte maximale subies pendant un cycle de chargement $R = \sigma_{min}/\sigma_{max}$. Pour $R \leq 0$, $\Delta K = K_{max} - 0 = K_{max}$. Nous supposons que l'incrément de fissure da se produit au moment où $K = K_{max}$ pendant un cycle de chargement. Ainsi, en considérant la relation entre le taux de libération d'énergie G et le facteur d'intensité de la contrainte K (dans une contrainte plane, par exemple), $G = K_{max}^2/E$. La loi de Paris peut alors être réécrite comme suit

$$\frac{da}{dN} = C(GE)^{m/2}, \tag{6}$$

où da/dN est la vitesse de croissance de la fissure, a est la longueur de la fissure et N est le nombre de cycles de chargement, C et m sont des paramètres de fatigue et E est le module de Young du matériau. Le taux de libération d'énergie $G = dU/da$ peut être calculé localement, au niveau d'un contact, sur la base de la libération d'énergie correspondante associée à une propagation de fissure donnée da.

Comparaisons entre les résultats théoriques et le modèle-p

Compte tenu du rôle clé du rapport de pente p, le modèle de propagation des fissures proposé est appelé modèle-p. Les calculs théoriques et les résultats expérimentaux sont utilisés pour être comparés au modèle-p.

La Figure 4.2a montre l'évolution du rapport de rigidité en fonction du nombre de cycles de chargement N pour un échantillon compact carré sous chargement de fatigue contrôler en contrainte. Dans la Figure 4.2b, on peut voir l'augmentation correspondante des fissures. Dans la Figure 4.2c, la dégradation du contact peut être clairement associée à l'augmentation de la fissure à différents états des rapports de rigidité. Les résultats pour tous les diamètres de particules sont proches des résultats théoriques, bien que des résultats plus proches soient observés pour les particules plus petites.

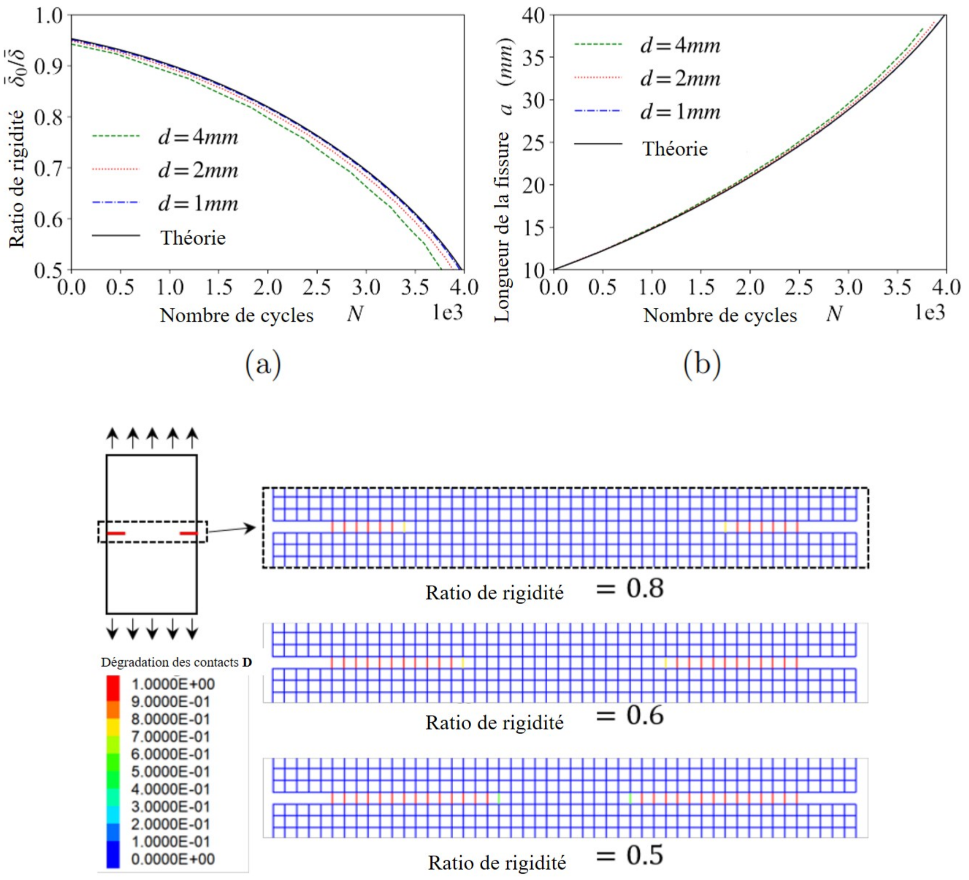

(a) (b)

(c)

Figure 8: Simulations d'une plaque symétrique fissurée sur les bords sous chargement de fatigue en contrainte avec des échantillons de forme carré pour différentes tailles de particules et comparaison avec les résultats théoriques de (a) la croissance de la fissure et (b) le rapport de rigidité en fonction du nombre de cycles N dans des conditions de contrainte contrôlées. (c) Carte de dégradation du contact pendant l'évolution de la fatigue pour $d = 2mm$.

Comparaisons entre les résultats expérimentaux et le modèle-p

Pour vérifier la validation du modèle-p, deux expériences sont comparées aux résultats de la simulation.

La première expérience a consisté à analyser des poutres en béton pré-fissurées soumises à des essais de fatigue en flexion trois points (voir Figure 4.12). Dans les simulations, on utilise trois échantillons DEM de forme carrée dont la taille des particules est respectivement de $d = 3$ mm, 2 mm et

$1\ mm$. Dans la Figure 4.12b, l'évolution du rapport de longueur de fissure a/H en fonction du nombre de cycle N est présentée. Un très bon accord entre l'expérience et les simulations est observé.

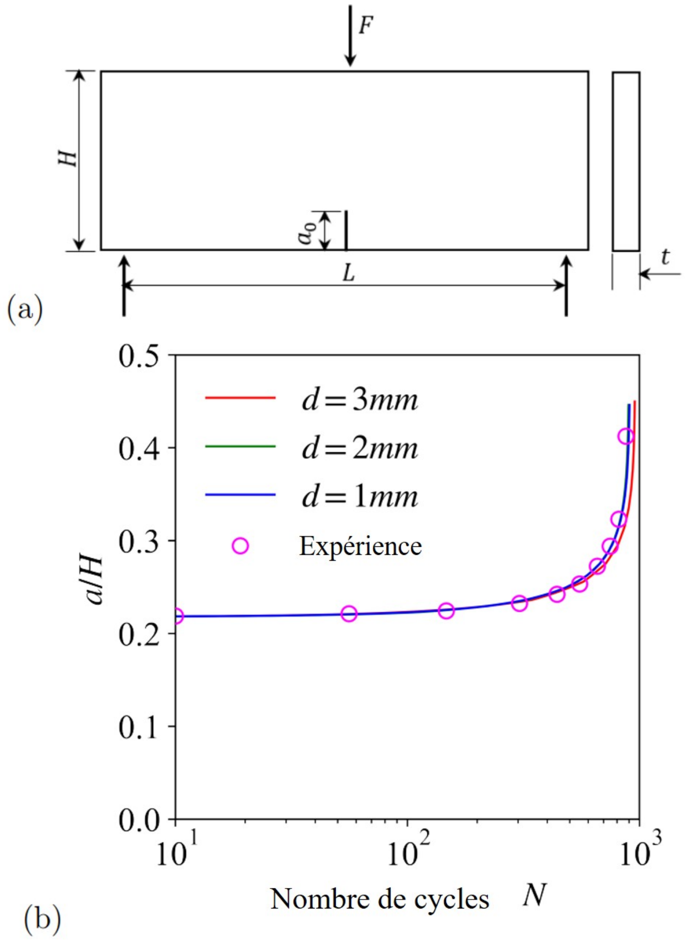

Figure 9: (a) Géométrie de la poutre en flexion trois points. (b) Evolution du rapport de longueur de fissure a/H en fonction du nombre de cycle N . Comparaison entre les résultats des essais et la simulation DEM.

La deuxième expérience est menée pour un essai de fatigue en traction avec entaille sur un seul bord de l'acier $S460$. Les dimensions de l'éprouvette sont indiquées sur la Figure 4.13a. L'éprouvette est soumise à une contrainte cyclique avec une amplitude maximale $\sigma_{max} = 29.63$; MPa et un rapport de contrainte $R = 0.5$.

En considérant le rapport de contrainte R, avec $\Delta K = K_{max}(1 - R)$, la loi de Paris (Equation 3.25) peut être réécrite comme suit

$$\frac{da}{dN} = C(1-R)^m (GE)^{m/2}. \tag{7}$$

Les simulations en DEM se basent sur des particules circulaires, avec les tailles $d = 3\ mm$, $2\ mm$ et $1\ mm$. Dans la Figure 4.13b, l'évolution de la longueur de la fissure a en fonction du nombre de cycle N est présentée.

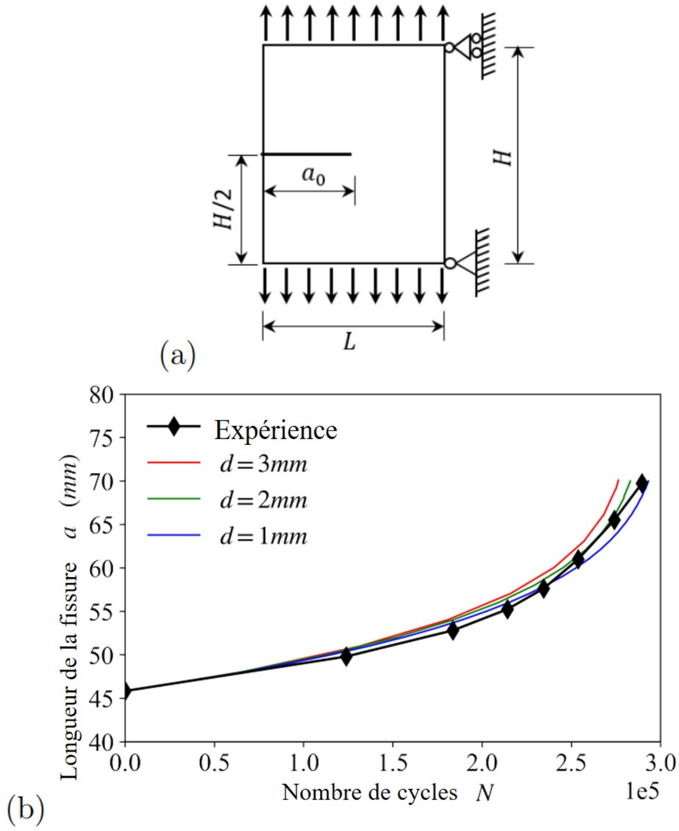

Figure 10: (a) Géométrie de l'essai de fatigue en traction avec entaille sur un seul bord. (b) Evolution de la longueur de la fissure a en fonction du nombre de cycle N . Comparaison entre les résultats de l'essai et la simulation DEM.

Les deux comparaisons avec les résultats théoriques et expérimentaux confirment la capacité de modélisation de la propagation des fissures en fatigue du modèle p proposé. En outre, deux avantages du modèle de contact proposé méritent d'être soulignés. Premièrement, une fois que les processus de dégradation du contact sont déclenchés par une dégradation initiale donnée D_{ini}, seules les forces de contact F et les déplacements de contact δ sont nécessaires pour continuer. Avec des informations aussi limitées, le modèle p peut toujours calculer le taux de libération d'énergie G et l'incrément de fissure da, puis représenter da par les dommages de contact dD. Cette caractéristique en fait un modèle local qui peut être facilement programmé dans un modèle numérique. Deuxièmement, le modèle p montre une grande précision par rapport à la loi de Paris, ce qui prouve une bonne incorporation de la loi de fatigue.

Modèle de dommages basé sur le modèle-p

La Figure 5.5 décrit essentiellement l'idée de représenter le processus d'endommagement par la dégradation de la rigidité de contact.

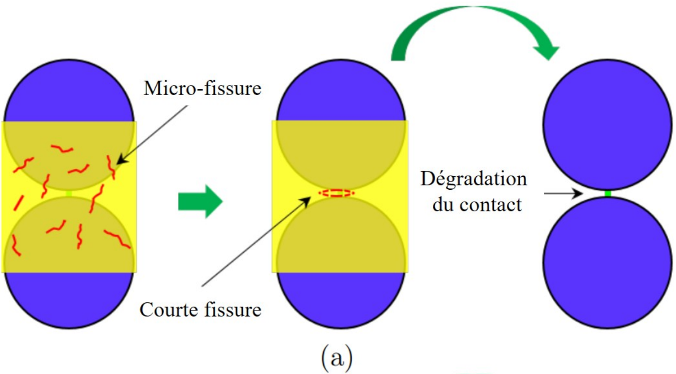
Micro-fissure
Dégradation du contact
Courte fissure

(a)

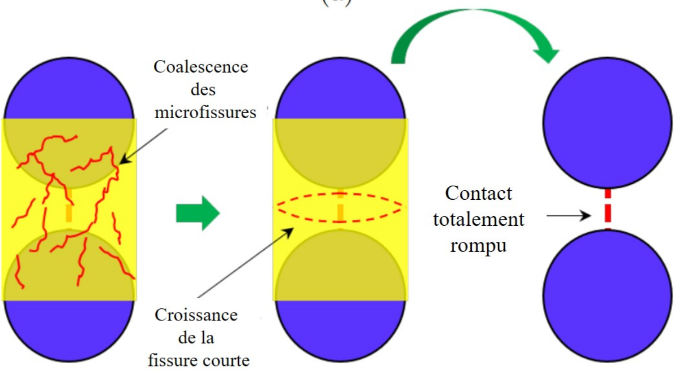
Coalescence des microfissures
Contact totalement rompu
Croissance de la fissure courte

(b)

Figure 11: Schéma de la modélisation du processus d'endommagement par le modèle *sp*, (a) état initial du matériau, avant le développement du réseau de microfissures, et (b) matériau continuellement endommagé, causé par le développement et la coalescence des microfissures.

Le développement des dommages peut être considéré comme le développement d'un réseau de microfissures. Au début, le matériau contient quelques microfissures ou défauts isolés. Avec la charge de fatigue, ces microfissures se développent lentement et finissent par fusionner les unes avec les autres (Figure 5.5). En considérant l'ensemble du réseau de microfissures dans le domaine de contact comme une fissure courte dont la croissance suit une variante de la loi de Paris.

Le modèle-p est simplifié en modèle-sp dans lequel un paramètre supplémentaire p est introduit. Le paramètre p utilisé dans la transformation $da - dD$ (Equations 3.23 et 3.24) devient un paramètre imposé ; une propriété intrinsèque de la rupture de contact, au lieu d'une quantité mesurée (rapport de pente, sa signification physique originale).

Comme le montrent les exemples de la Figure 5.3, dans le modèle-sp, lorsque $p = 5$ est égal au rapport de séparation du contact, le taux de libération d'énergie G calculé reste constant pendant la pénétration de la fissure dans le contact, c'est comme ce qui se passe dans le modèle-p, tandis que si p est supérieur au rapport de séparation du contact, l'évolution du taux de libération d'énergie G résultant est une courbe décroissante, et au contraire si p est inférieur au rapport de séparation du contact, l'évolution du taux de libération d'énergie G résultant est une courbe croissante.

La différence entre la valeur imposée de p et la valeur mesurée (la signification physique originale) de p permet une variation de la valeur calculée du taux de libération d'énergie G. Un tel effet de variation du paramètre p sur G résulte finalement en une évolution de la dégradation de la rigidité de contact qui capture l'ensemble du processus d'évolution de la fatigue, y compris l'initiation et la propagation des fissures.

Comparaisons entre les résultats expérimentaux et le modèle-sp

La Figure 5.12 montre la simulation et l'expérimentation des essais de fatigue en Traction-Compression avec des niveaux d'essai respectifs, 79 $\mu\varepsilon$, 92 $\mu\varepsilon$ et 108 $\mu\varepsilon$.

Les bons accords entre la simulation et l'expérimentation dans la Figure 5.12 soutiennent fortement la validation du modèle-sp dans la modélisation de l'évolution de la fatigue des matériaux.

La Figure 5.16 montre la simulation et l'expérimentation d'essais de fatigue en flexion 4 points avec des niveaux d'essai respectifs, 150 $\mu\varepsilon$, 135 $\mu\varepsilon$ et 115 $\mu\varepsilon$.

La Figure 5.17 présente la distribution des dommages et les trajectoires des fissures dans les échantillons des simulations d'essais de fatigue en flexion 4

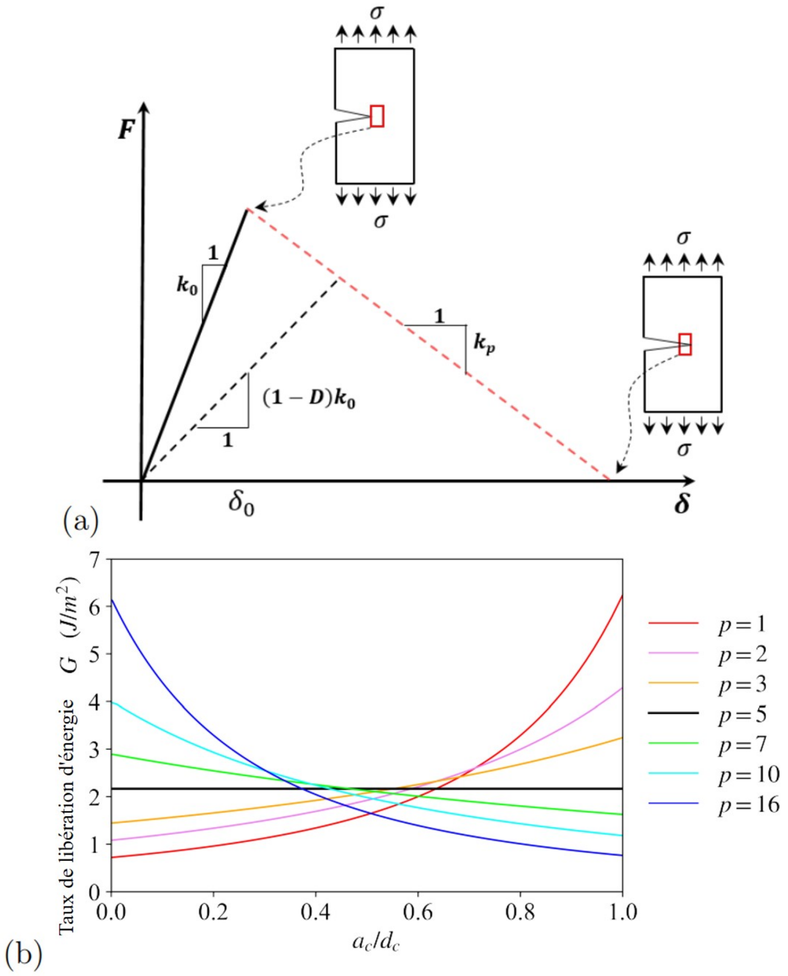

Figure 12: (a) Exemple d'un contact en rupture avec une rigidité initiale k_0, lorsque la fissure atteint sa limite, le déplacement du contact est δ_0. Au cours du processus de rupture, il s'avère que le rapport de pente est $p = k_0/k_p = 5$. (b) Valeurs correspondantes du taux de libération d'énergie G pour différentes valeurs du paramètre p introduit dans l'équation 3.17.

points, on peut remarquer que ces échantillons ont en commun le fait que les dommages et les petites fissures sont distribués principalement près du haut et du bas de l'échantillon avec une ou deux fissures principales indiquant la défaillance finale de l'échantillon.

La figure 5.21 montre la simulation et l'expérimentation d'essais de fatigue par flexion à 2 points avec des niveaux d'essai, respectivement, de 160 $\mu\varepsilon$, 130 $\mu\varepsilon$ et 100 $\mu\varepsilon$.

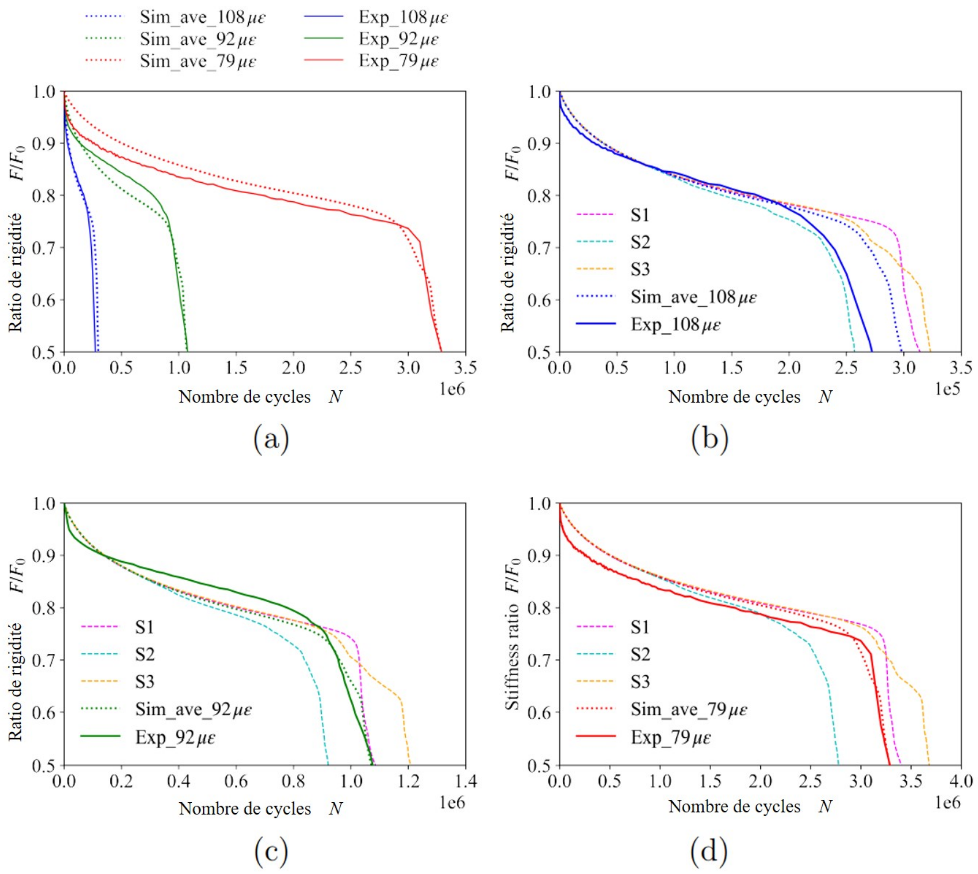

(a) (b) (c) (d)

Figure 13: Résultats de la simulation des essais T-C, (a) comparaison des résultats moyens de la simulation et de l'expérimentation [1] avec différents niveaux de déformation, et évolution de la fatigue des trois échantillons avec des niveaux de déformation respectifs de (b) 108 $\mu\varepsilon$, (c)92 $\mu\varepsilon$ et (d) 79 $\mu\varepsilon$.

La distribution des dommages et les trajectoires des fissures dans les trois échantillons des simulations d'essais de fatigue en flexion 2 points sont présentées dans la Figure 5.22.

De bons accords sont observés dans la comparaison de la simulation et de l'expérience pour les essais 2PB et 4PB. L'utilisation du modèle-*sp* en DEM permet de capturer avec succès l'évolution de la fatigue et la défaillance localisée dans les essais de fatigue. Il fonctionne également correctement pour différents niveaux de déformation.

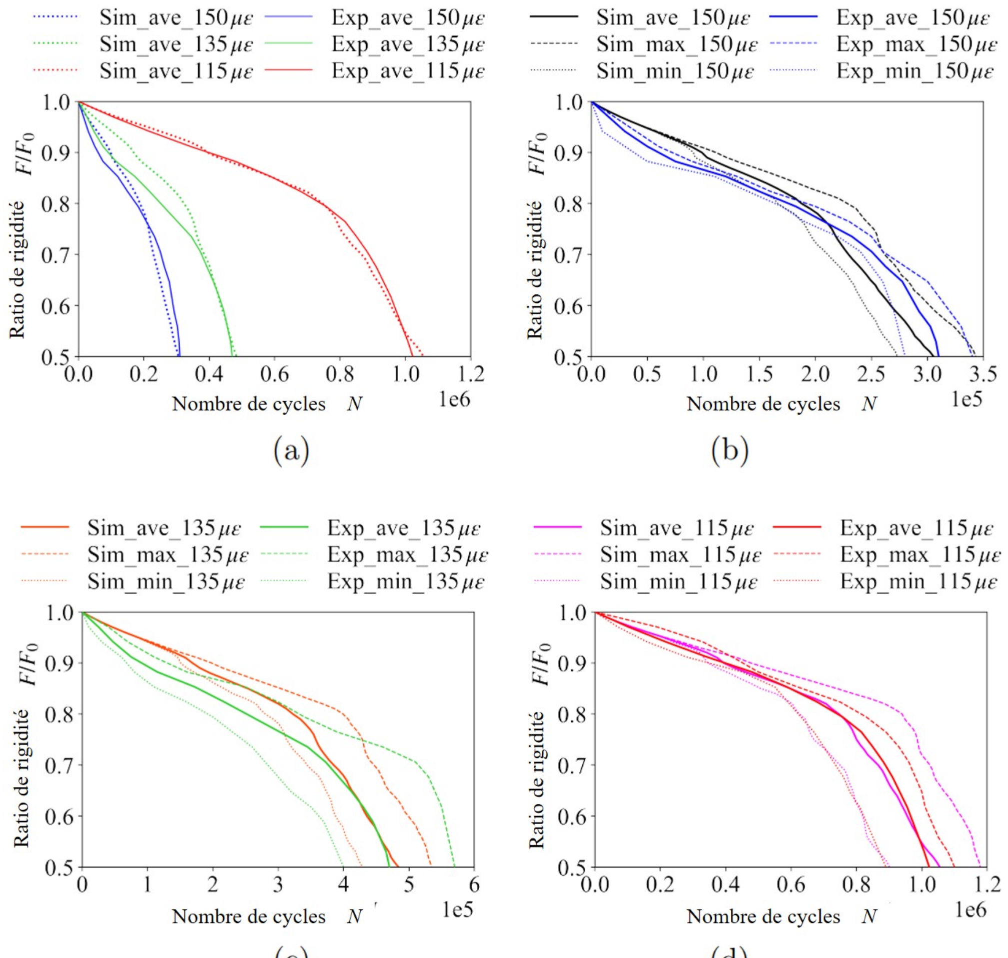

(a) (b)

(c) (d)

Figure 14: Comparaison entre la simulation et l'expérimentation [150] des tests 4PB, (a) courbes moyennes pour différents niveaux de déformation, (b) courbes moyennes et enveloppes pour le niveau de déformation 150 $\mu\varepsilon$, (c) 135 $\mu\varepsilon$ et (d) 115 $\mu\varepsilon$.

Conclusions et perspectives

Conclusions

Dans cette thèse, le comportement en fatigue du béton bitumineux est modélisé par la méthode des éléments discrets. La propagation des fissures et le processus d'endommagement sont analysés.

La méthode des éléments discrets présente l'avantage de modéliser l'hétérogénéité du matériau et la défaillance localisée dans le développement

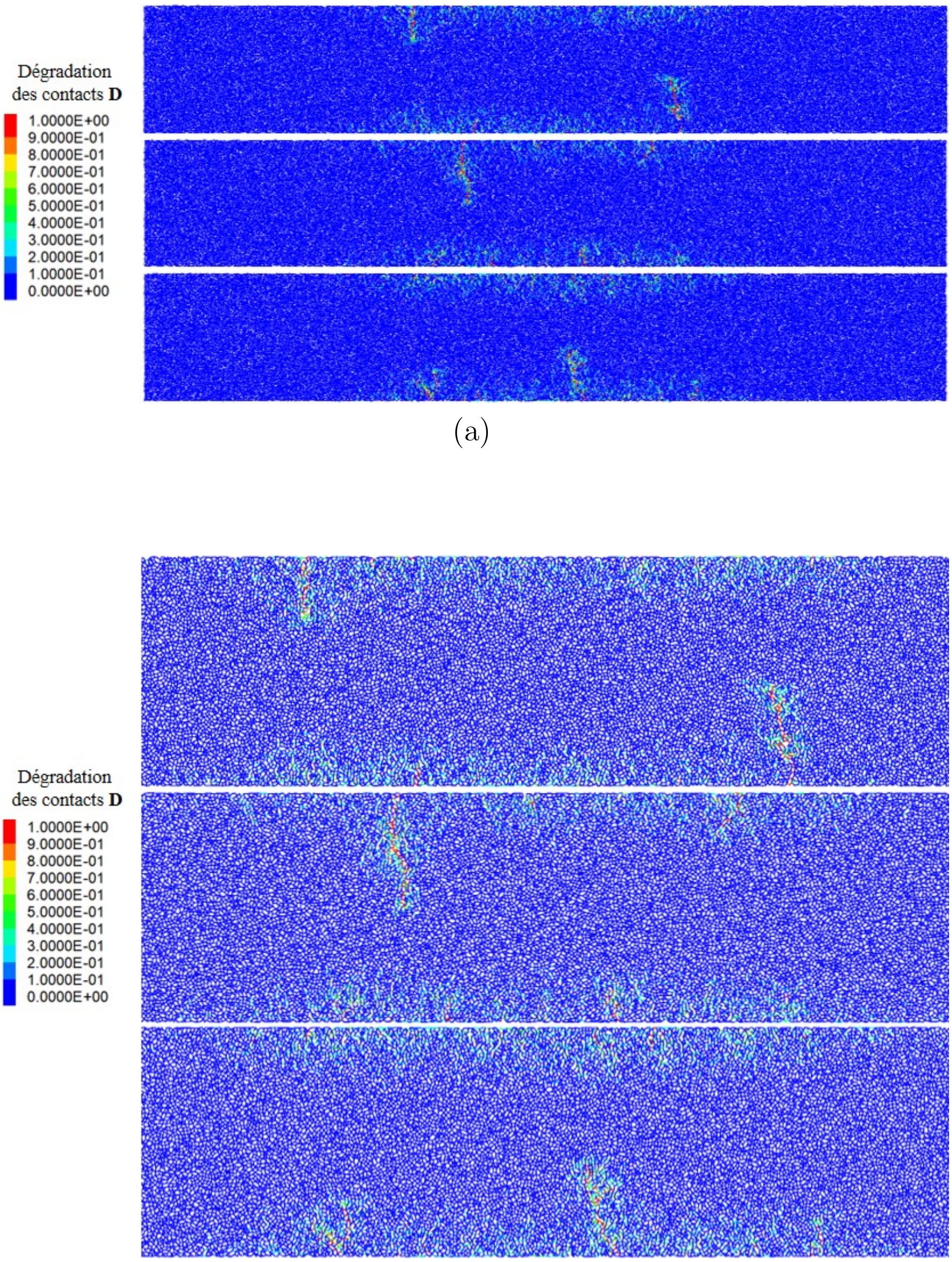

(a)

(b)

Figure 15: (a) Cartes de distribution des dommages pour les trois échantillons au rapport de rigidité $F/F_0 = 0,5$, pour un niveau de déformation d'essai $150\,\mu\varepsilon$, (b) zoom correspondant de (a).

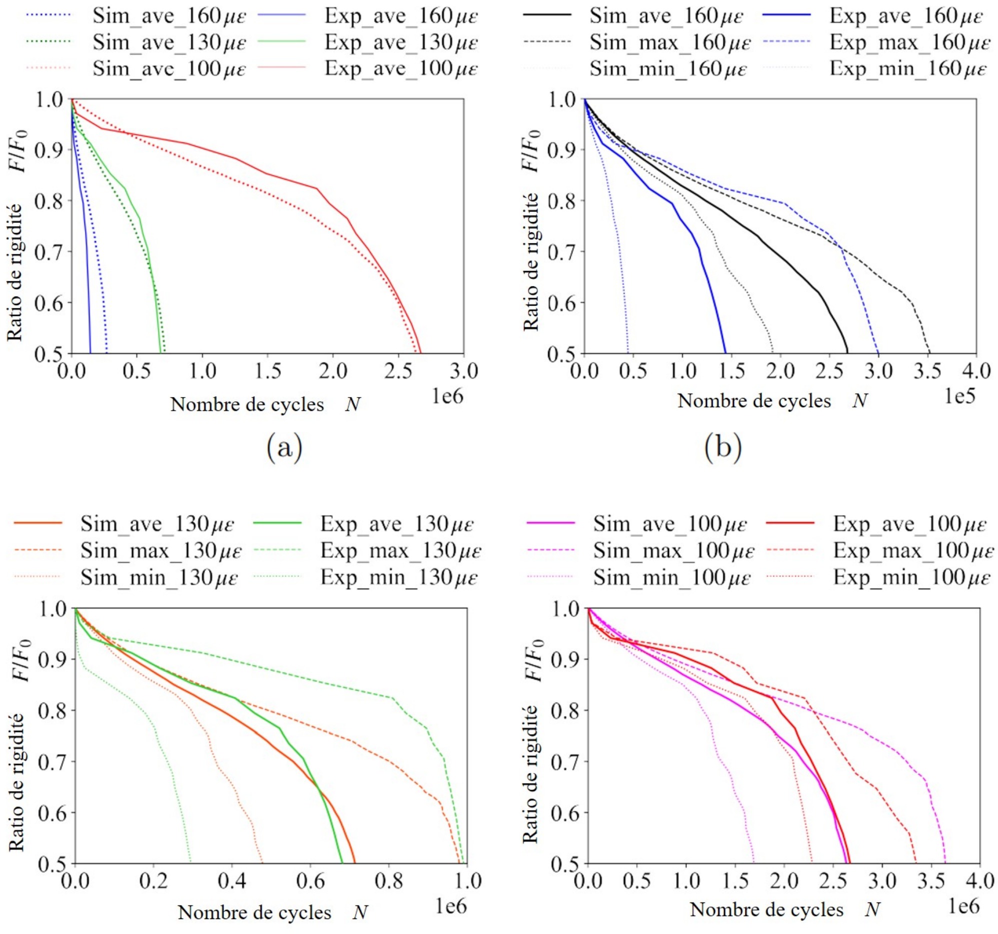

(a) (b)

(c) (d)

Figure 16: Comparaison entre la simulation et l'expérimentation [150] des essais 2PB, (a) courbes moyennes pour différents niveaux de déformation d'essai, (b) courbes moyennes et enveloppes pour le niveau de déformation d'essai 160 $\mu\varepsilon$, (c) 130 $\mu\varepsilon$ et (d) 100 $\mu\varepsilon$.

de la fatigue. Cependant, il est encore difficile de modéliser l'ensemble du processus d'évolution de la fatigue, notamment en tenant compte des essais de fatigue à différents niveaux. Pour modéliser correctement la propagation des fissures en fatigue, deux capacités sont nécessaires, premièrement, la capacité de représenter une quantité d'incrément de fissure, deuxièmement, la capacité de calculer la variable principale de la loi de fatigue choisie, par exemple, pour la loi de Paris, la variable principale est la gamme du facteur d'intensité de contrainte pendant un cycle de chargement. En outre, pour modéliser l'ensemble du processus d'évolution de la fatigue, y compris

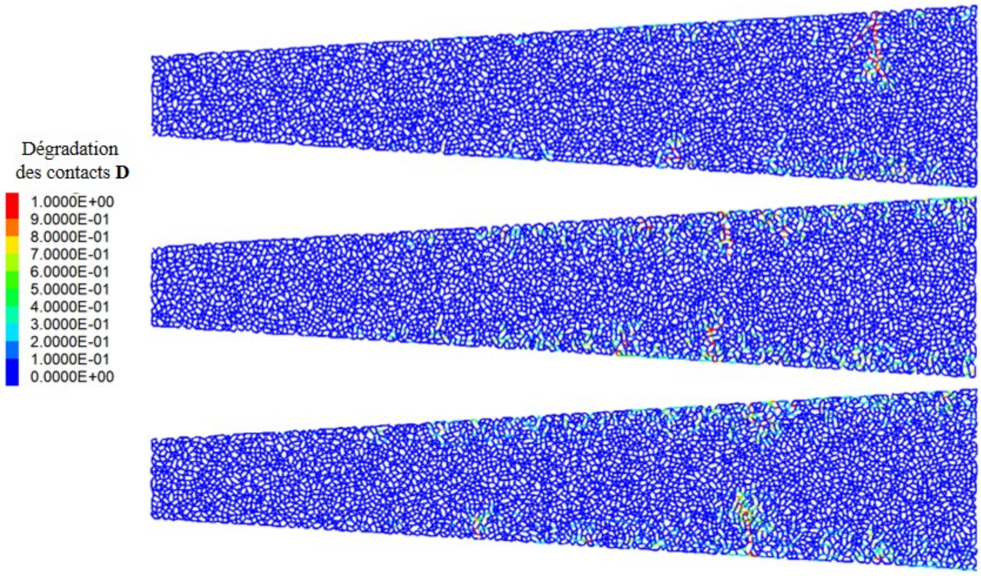

Figure 17: Cartes de distribution des dommages pour les trois échantillons (rotation de 90°) au rapport de rigidité $F/F_0 = 0.5$, pour un niveau de déformation d'essai $160\,\mu\varepsilon$.

l'initiation et la propagation des fissures, un modèle d'endommagement plus général est nécessaire.

Les deux problèmes principaux pour la modélisation de la propagation des fissures, à savoir comment représenter une minuscule croissance de fissure da causée par un cycle de chargement et comment déterminer la quantité de croissance de fissure da, sont résolus. Le premier problème est résolu avec succès par les transformations $a_c - D$ proposées qui sont basées sur l'équivalence énergétique entre l'énergie dissipée due à la dégradation de la rigidité de contact et l'énergie libérée pendant la propagation de la fissure. Ces transformations permettent de transformer librement l'incrément de fissure da en incrément de dégradation de la rigidité de contact dD ou de manière réversible de dD à da. En profitant des transformations $a_c - D$, la loi de Paris est facilement incorporée sous la forme d'une relation entre le taux de croissance de fissure da/dN et le taux de libération d'énergie G. Après avoir résolu les deux problèmes principaux grâce notre modèle de contact adapté la croissance des fissures de fatigue, le modèle-p est proposé et confirmé à la fois par la comparaison avec le calcul théorique et la comparaison avec l'expérience.

Les avantages du modèle-p résident dans sa caractéristique locale et sa précision. Premièrement, une fois que les processus de dégradation du contact sont déclenchés par une dégradation initiale donnée D_{ini}, seules les forces de contact F et les déplacements de contact δ sont nécessaires pour continuer. Avec des informations aussi limitées, le modèle p peut toujours calculer le taux de libération d'énergie G et l'incrément de fissure da, puis représenter da par le dommage de contact dD. Cette caractéristique locale fait qu'il peut être naturellement adopté dans la simulation DEM. Deuxièmement, sa précision indique un grand potentiel pour une large gamme de tests de fatigue.

Un modèle d'endommagement est proposé dans lequel le développement de l'endommagement du matériau est causé par le développement d'un réseau de microfissures qui peut être représenté comme une seule croissance de fissure courte régie par une variante de la loi de Paris. Pour capturer le processus d'endommagement à l'échelle du contact, un paramètre supplémentaire p est introduit. En fixant une valeur constante du paramètre p dans les transformations $a_c - D$, le modèle-p est simplifié en modèle-sp qui permet une variation de la valeur calculée du taux de libération d'énergie G. Un tel effet de variation du paramètre p sur G résulte finalement en une évolution de la dégradation de la rigidité du contact qui capture l'ensemble du processus d'évolution de la fatigue, y compris l'initiation et la propagation des fissures. Le modèle d'endommagement proposé (modèle-sp) est comparé à l'expérimentation des essais de T-C, de flexion à 2 points et de flexion à 4 points. Il montre une forte capacité à ajuster les courbes d'évolution de la fatigue pour différents types d'essais, différents matériaux d'essai et avec différents niveaux d'essai.

Perspectives

A partir des méthodes et modèles discutés dans cette thèse, pour améliorer continuellement la modélisation du comportement de la propagation de fissures en fatigue, plusieurs extensions de l'étude méritent d'être approfondies dans le futur. En particulier :

- Le modèle d'endommagement proposé peut saisir globalement l'ensemble du processus d'évolution de la fatigue, tandis que les phénomènes physiques liés à la non-linéarité, à l'auto-échauffement et à la thixotropie, doivent également être directement pris en compte.
- L'utilisation des modèles proposés dans des échantillons tridimensionnels peut couvrir davantage de processus physiques dans le matériau réel, comme une initiation de fissure plus détaillée et une coalescence de fissure plus complexe.
- Pour reproduire de manière plus réaliste l'hétérogénéité du matériau, on peut accorder plus d'attention à la granularité du matériau.

- Les simulations sont comparées à des calculs théoriques ou à des expériences en laboratoire. Une comparaison avec les observations in situ sur le terrain doit également être effectuée.

Contents

Acknowledgments i

Résumé étendu iii

1 Introduction 1
- 1.1 General background . . . 1
- 1.2 Objectives . . . 2
- 1.3 Organization of the thesis . . . 2

2 Literature review 5
- 2.1 Introduction . . . 6
- 2.2 Asphalt concrete . . . 6
- 2.3 Material fatigue behavior . . . 8
  - 2.3.1 Overview about fatigue behavior . . . 8
  - 2.3.2 Fatigue behavior for asphalt concrete . . . 8
- 2.4 Modeling of fatigue damage . . . 16
  - 2.4.1 Numerical methods . . . 17
  - 2.4.2 Damage model . . . 17
- 2.5 Relevant knowledge of fracture mechanics . . . 22
  - 2.5.1 Crack modes . . . 22
  - 2.5.2 The elastic stress field near a crack tip . . . 22
  - 2.5.3 Energy release rate . . . 24
  - 2.5.4 Energy release rate in cracked plate . . . 25
  - 2.5.5 The relation between G and K in Mode I . . . 28
  - 2.5.6 Fatigue crack growth-Paris' law . . . 31
  - 2.5.7 Fracture process zone (FPZ) . . . 32
- 2.6 Numerical modeling of fatigue crack growth . . . 33
  - 2.6.1 Crack growth model . . . 33
  - 2.6.2 Transition from damage model to crack propagation . . . 39
  - 2.6.3 Conclusion . . . 40
- 2.7 Summary of the chapter . . . 41

3 Contact model for fatigue crack growth 43
- 3.1 Introduction . . . 44
- 3.2 Discrete element method . . . 44
  - 3.2.1 Contact behavior . . . 44
  - 3.2.2 Work at contact level . . . 46

3.2.3 Isotropic Elasticity 46
3.3 Contact behavior at the crack tip 47
3.4 Contact separation - elastic case 49
3.4.1 Definition of the slope ratio p 49
3.4.2 Study of the slope ratio p 52
3.4.3 Energetic analysis of the contact separation 59
3.5 Verification of $a_c - D$ transformations 61
3.6 Contact separation - non elastic case 63
3.6.1 Incremental form of the crack-damage relation 64
3.6.2 Contact evolution scheme 64
3.7 Implementation of fatigue crack growth 67
3.7.1 Paris' law 67
3.7.2 A quasi-static approach to simulate fatigue cycles . . . 67
3.7.3 Numerical procedures for the fatigue crack growth calculation in DEM 69
3.8 Summary of the chapter 3 70

4 Modeling cracked samples under fatigue loading 71
4.1 Introduction 72
4.2 DEM simulation procedures 72
4.2.1 Particle sample arrangements and crack description . . 72
4.2.2 Non local crack tip identification and numerical procedure 74
4.3 Comparison of the model with theoretical results 74
4.3.1 Sample dimensions and material properties 74
4.3.2 Cyclic loading 75
4.3.3 Numerical results 75
4.4 Identification of the dimension d_c 79
4.5 Parametric study 84
4.5.1 Effect of parameter C 84
4.5.2 Effect of parameter m 84
4.6 Comparison of the proposed contact model with experimental results 86
4.7 Summary of the chapter 88

5 A damage model for crack initiation and multi-cracking 91
5.1 Introduction 91
5.1.1 Physical interpretation of the parameter p 93
5.1.2 A variant Paris' law 96
5.1.3 Contact endurance limit 97
5.2 Complete damage model (sp-model) 98

5.3 Simulation approach for fatigue tests in DEM 99
5.4 Modeling of Tension-Compression fatigue test 102
    5.4.1 Effect of the parameter p 103
    5.4.2 Effect of the contact endurance limit 104
    5.4.3 Simulation versus experimental results of T-C fatigue tests 106
5.5 4PB fatigue tests 110
    5.5.1 Simulation results of 4PB tests 110
5.6 2PB fatigue tests 116
    5.6.1 Simulation results of 2PB tests 117
5.7 Summary of the chapter 122

6 Conclusions and perspectives **123**
6.1 Conclusions 123
6.2 Perspectives 124

A Discrete element method **125**
    A.0.1 Algorithm of DEM calculation [101] 125
    A.0.2 Stabilisation [4] 126
    A.0.3 Viscous damping 126
    A.0.4 Other 127

B Samples generation [4] **129**
B.1 Particle generation and internal stress control 129
B.2 Floater elimination procedure 130
B.3 Interactive procedure and adopted parameters 130
B.4 Generator random seed 131

C Theoretical calculation of cracked plate **133**
C.1 The stiffness of cracked finite plate 133
C.2 Verification of formulas describing the stiffness of cracked finite plate 137

D Theoretical calculation of fatigue evolution **141**
D.1 Calculation of theoretical results 141

E Stability and robustness analysis **145**
E.1 Effect of parameter D_{ini} 145
E.2 Robustness analysis 151

F Morphology method **157**
F.1 Using p-model in randomly packed samples 157

F.1.1 Simulation procedures 158
F.1.2 Sample preparation 158
F.1.3 Simulation results in randomly packed samples 159

G Technique to save simulation time **163**

H Reaction force evolution **165**

List of Figures

1 (a) Pointe de fissure au voisinage d'un contact et avec propagation de la fissure de (a) à (b) puis à (c), sa trajectoire pendant la rupture du contact est décrite par la variable a_c ($0 \leq a_c \leq d_c$). v

2 (a) Plaque élastique avec fissure initiale a_0 sous contrainte σ, déplacement résultant $\bar{\delta}_0$ (b) effet d'une croissance de fissure (de a_0 à a_1) sur les déplacements en fonction de la longueur de la fissure, (c) évolution du déplacement. (d) échantillon DEM correspondant, (e) zoom de la longueur propagée (d), et (f) évolution correspondante des déplacements en fonction de la longueur de la fissure. vi

3 Description schématique de la relation mécanique entre le contact à la pointe de la fissure et les particules voisines. (a) Plaque pré-fissurée et (b) son comportement élastique simplifié près de la pointe de la fissure, où k_p représente la rigidité du matériau entourant la pointe de la fissure, F et δ sont la force et le déplacement de contact, (c) une description plus intuitive de (b). viii

4 Description de l'évolution d'un contact pour l'ensemble du processus allant de la fissure proche à la fissure traversant ce contact. En bas de la figure, (o) une plaque pré-fissurée dans laquelle un rectangle rouge représente le contact dont le comportement est décrit par les deux systèmes de ressorts et l'évolution de la force de contact F et du déplacement δ dans le système de coordonnées, (A) plaque soumise à une contrainte constante σ, (B) fissure se propageant jusqu'à la limite du domaine de contact, (C) fissure traversant totalement le domaine de contact. De (B) à (C), la croissance de la fissure dans le domaine de contact est représentée par le processus de dégradation de la rigidité de contact, pour ($0 \leq D \leq 1$), où k_0 est la rigidité de contact initiale, et $(1 - D)k_0$ est sa valeur dégradée. ix

5 Description schématique de la position de la fissure et du déplacement du contact. (a) Pointe de fissure à la limite du domaine de contact, où δ_0 est le déplacement de contact, et (b) fissure traversant totalement le domaine de contact. x

6 Description schématique de la séparation non-linéaire par traction de contact. xi
7 Transformations (a) entre a_c et D, (b) entre da et dD. xii
8 Simulations d'une plaque symétrique fissurée sur les bords sous chargement de fatigue en contrainte avec des échantillons de forme carré pour différentes tailles de particules et comparaison avec les résultats théoriques de (a) la croissance de la fissure et (b) le rapport de rigidité en fonction du nombre de cycles N dans des conditions de contrainte contrôlées. (c) Carte de dégradation du contact pendant l'évolution de la fatigue pour $d = 2mm$. xiv
9 (a) Géométrie de la poutre en flexion trois points. (b) Evolution du rapport de longueur de fissure a/H en fonction du nombre de cycle N . Comparaison entre les résultats des essais et la simulation DEM. xv
10 (a) Géométrie de l'essai de fatigue en traction avec entaille sur un seul bord. (b) Evolution de la longueur de la fissure a en fonction du nombre de cycle N . Comparaison entre les résultats de l'essai et la simulation DEM. xvi
11 Schéma de la modélisation du processus d'endommagement par le modèle sp, (a) état initial du matériau, avant le développement du réseau de microfissures, et (b) matériau continuellement endommagé, causé par le développement et la coalescence des microfissures. xvii
12 (a) Exemple d'un contact en rupture avec une rigidité initiale k_0, lorsque la fissure atteint sa limite, le déplacement du contact est δ_0. Au cours du processus de rupture, il s'avère que le rapport de pente est $p = k_0/k_p = 5$. (b) Valeurs correspondantes du taux de libération d'énergie G pour différentes valeurs du paramètre p introduit dans l'équation 3.17. xix
13 Résultats de la simulation des essais T-C, (a) comparaison des résultats moyens de la simulation et de l'expérimentation [1] avec différents niveaux de déformation, et évolution de la fatigue des trois échantillons avec des niveaux de déformation respectifs de (b) 108 $\mu\varepsilon$, (c)92 $\mu\varepsilon$ et (d) 79 $\mu\varepsilon$. xx
14 Comparaison entre la simulation et l'expérimentation [150] des tests 4PB, (a) courbes moyennes pour différents niveaux de déformation, (b) courbes moyennes et enveloppes pour le niveau de déformation 150 $\mu\varepsilon$, (c) 135 $\mu\varepsilon$ et (d) 115 $\mu\varepsilon$. xxi

15 (a) Cartes de distribution des dommages pour les trois échantillons au rapport de rigidité $F/F_0 = 0,5$, pour un niveau de déformation d'essai 150 $\mu\varepsilon$, (b) zoom correspondant de (a). xxii
16 Comparaison entre la simulation et l'expérimentation [150] des essais 2PB, (a) courbes moyennes pour différents niveaux de déformation d'essai, (b) courbes moyennes et enveloppes pour le niveau de déformation d'essai 160 $\mu\varepsilon$, (c) 130 $\mu\varepsilon$ et (d) 100 $\mu\varepsilon$. xxiii
17 Cartes de distribution des dommages pour les trois échantillons (rotation de 90°) au rapport de rigidité $F/F_0 = 0.5$, pour un niveau de déformation d'essai 160 $\mu\varepsilon$. xxiv

2.1 Scheme of volumetric properties of a bituminous mixtures, where V_{tot} is a unit volume of mixture, VMA (Voids in Mineral) and VFA (Voids Filled with Asphalt) [8]. 6
2.2 Schemes of vehicle loading and pavement layer response [1]. . . 8
2.3 Example of fatigue cracks on pavement [21]. 9
2.4 Typical fatigue tests: Tension-Compression (T/C), Two Point Bending (2PB), Three Point Bending (3PB), Indirect Tensile (IDT) and Four Point Bending Test (4PB), (Modified from [2]). 10
2.5 Configuration of 4-point bending test. 11
2.6 (a) 4-point bending test samples and (b) test equipment [3]. . 11
2.7 Schematic description of loading and response in: (a, b) strain controlled mode, and (c, d) stress controlled mode [7]. 12
2.8 A typical fatigue evolution curve during fatigue test. 13
2.9 Schema of damage development in bituminous mixtures under traffic load (Modified from [52]). 14
2.10 Typical mechanical behavior domains of bituminous mixtures depending on strain amplitude ε and number of cycles N, for a given temperature [55]. 15
2.11 Example of Wohler curve and endurance limit [8]. 15
2.12 An example of concentrated damage (crack) in asphalt concrete (Modified from [52]). 16
2.13 4PB test experimental results and simulations in FEM by Arsenie [3], (Modified from [4]). 17
2.14 Damage maps (blue to red means $D = 0$ to $D = 1$) displaying different localization levels of 4-point bending fatigue test simulations by using damage model: (a) finite element method conducted by Arsenie [3], (Modified from [101]), (b) regular packing discrete element method conducted by Gao [101], (Modified from [101]), (c) randomly packing discrete element method conducted by Liu [4], (Modified from [4]). 18

2.15 4PB test simulation in DEM by Liu [4], experimental results by Arsenie [3]. 19
2.16 (a) Finite element mesh and (b) discrete element mesh, (Modified from [83]). 19
2.17 (a) Finite element mesh refinement for crack propagation, (Modified from [84])and (b) discrete element particles detachment for crack propagation, (Modified from [78]). 20
2.18 Example of mesh assignment based on material image, (Modified from [99]). 20
2.19 4PB test simulation in DEM by Gao [101], experimental results and simulations in FEM by Arsenie [3, 102, 103]. 21
2.20 Schematic of the basic fracture modes: (a) Mode I (opening), (b) Mode II (sliding) and (c) Mode III (tearing) [104]. 22
2.21 A center cracked infinite plate subjected to uniform remote tension [101]. 23
2.22 The rectangular and polar coordinate components of stress field around the crack tip. 24
2.23 Scheme of the stress distribution near a crack tip as a function of the stress intensity factor K [105]. 25
2.24 Case 1: plate subjected to a constant force, (a) original state, (b) loading state, (c) crack growth. 26
2.25 Case 2: after tension, plate displacement δ is fixed, (a) original state, (b) loading state, (c) crack growth. 26
2.26 Case 3: after tension, plate top is restrained by elastic constraint with stiffness k, (a) original state, (b) loading state, (c) crack growth. 27
2.27 Case 4: after tension, plate top is restrained by elastic constraint with varying stiffness k and position, (a) original state, (b) loading state, (c) crack growth, (d) after elastic constraint stiffness and position change, crack continually grows. 27
2.28 Released energy during crack extension: (a) constant force, (b) fixed displacement, (c) elastic constraint and (d) varying elastic constraint. 29
2.29 Stress distribution before extension and surface opening after extension [101]. 30
2.30 Scheme of the stress intensity factor range ΔK. 31
2.31 Schematic of the fatigue crack growth behavior for long crack and short crack (Modified from [114]). 32
2.32 The schematic map of fracture process zone by Otsuka (Modified from [125]). 33

2.33 Multiphases and corresponding separation model, (Modified from [131]). . . . 34
2.34 Schematic of crack propagation modeling: (a) nodes and crack in FEM with cohesive zone elements (a) and (b) enriched nodes and crack in XFEM, (Modified from [136]). . . . 34
2.35 Example of crack propagation in XFEM, (Modified from [136]). 35
2.36 Schematic of transformation between crack and damage by Nguyen, (Modified from [78]). . . . 36
2.37 The cohesive zone in front of a crack tip. . . . 37
2.38 An example of the traction separation law for CZM, (Modified from [4]). . . . 37
2.39 DEM sample in hexagonal packing, (Modified from [140]). . . 37
2.40 Crack trajectory resulting from CZM, (Modified from [140]). . 38
2.41 Fatigue curve for tensile simulation by Gao, (Modified from [101]). . . . 38
2.42 Contact stress-displacement behavior in pure cyclic tension test by Nguyen, (Modified from [78]). . . . 39
2.43 Three examples of damage zones in TLS, the black line is the front of damage zone and white zone is the fully damaged material area, (Modified from [143]). . . . 40

3.1 (a) Material description in DEM, where the black lines represent the contacts, and (b) their rheological representation. (c) Contact relative displacement, and (d) corresponding normal and shear forces. (e) Representation of the contact domain. (Modified from [4]). . . . 45
3.2 Particle arrangements and corresponding contact maps: (a) square-packed, (b) hexagonal packed, and (c) randomly packed. 47
3.3 (a) Crack tip at vicinity of a contact and with crack propagation from (a) to (b) then to (c),its trajectory during the rupture of the contact described by the variable a_c ($0 \leq a_c \leq d_c$). . . . 48
3.4 (a) Elastic plate with initial crack a_0 under stress σ, resulting displacement $\bar{\delta}_0$ (b) effect of a crack growth (from a_0 to a_1) over the displacements versus crack length, (c) evolution of the displacement. (d) DEM corresponding sample, (e) zoom of the propagated length (d), and (f) the corresponding evolution of the displacements versus crack length. . . . 48

3.5 Schematic description of the mechanical relation between the contact at the crack tip and the neighboring particles. (a) Pre-cracked plate and (b) its simplified elastic behavior near the crack tip, where k_p represents the stiffness of material surrounding the crack tip, F and δ are contact force and displacement, (c) a more intuitive description of (b). 50

3.6 Description of the evolution of a contact for the whole process from crack near to crack through this contact. At the bottom of figure, (o) a pre-cracked plate in which a red rectangular represents the contact whose behavior is described by both spring systems and the evolution of contact force F and displacement δ in the coordinate system, (A) plate subjected to a constant stress σ, (B) crack propagates till the boundary of the contact domain, (C) crack totally through the contact domain. From (B) to (C), crack growth within the contact domain is represented by the process of the contact stiffness degradation, for $(0 \leq D \leq 1)$, where k_0 is the initial contact stiffness, and $(1 - D)k_0$ is its degraded value. 51

3.7 Schematic description of the position of crack and contact displacement. (a) Crack tip at the boundary of the contact domain, where δ_0 is the contact displacement, and (b) crack totally through the contact domain. 52

3.8 (a) Geometry of the plate, crack propagation modeling in (b) square and (c) hexagonal packed samples. 53

3.9 (a) Value of the slope ratio p as a function of the length to plate width ratio a/b for different particle diameters $(0.5\,mm \leq d \leq 2\,mm)$ of a plate with symmetric edge cracks, simulated by square packed samples and (b) a zoom of the values of p as a function of the crack to diameter ratio a/d during crack initiation $a/d \leq 5$. 54

3.10 (a) Value of the slope ratio p as a function of the crack length to plate width ratio a/b for different particle diameters $(0.5\,mm \leq d \leq 2\,mm)$ of a plate with center crack, simulated by square packed samples and (b) a zoom of the values of p as a function of the crack to diameter ratio a/d during crack initiation $a/d \leq 5$. 55

3.11 Comparison of p as a function of the crack length to plate width ratio a/b, for center crack and symmetric edge cracks propagation, result from respectively square and hexagonal packed samples, with diameter $d = 1mm$. 56

3.12 Value of the slope ratio p for crack at different vertical positions (y/d, where y is the distance from loading boundary and $d = 2\,mm$ is particle diameter) and with different crack length (a/b), (a) with imposed stress and (b) with imposed strain ($\varepsilon = 100\,\mu\varepsilon$). The black dashed line represents $p = 2.8$ in both (a) and (b). 57

3.13 Comparison of the slope ratio p as a function of the crack length to plate width ratio a/b, for center crack, (a) with imposed stress and (b) with imposed strain ($\varepsilon = 100\,\mu\varepsilon$). The black dashed line represents $p = 2.8$. 58

3.14 Schematic description of the limitation of the slope ratio p, for $p = 0$ corresponding to the homogeneous state and $p = \infty$ corresponding to the ultimate state. 58

3.15 (a) Released energy during contact degradation. (b) Cracked plate, and (c) zoom of the crack propagation at the scale of one contact. 60

3.16 Plate under uniform stress and the associated boundary displacement for (a) intact and (b) cracked cases. 62

3.17 (a) Comparison of the ratio of displacement $\bar{\delta}/\bar{\delta}_0$ between theoretical results and simulation results and (b) a zoom for $0.2 \leq a/2b \leq 0.22$. 63

3.18 Schematic description of nonlinear contact traction separation. 64

3.19 Transformations (a) between a_c and D, (b) between da and dD. 65

3.20 (a) Description of the contact and force-displacement evolution during a propagation event, (b) a certain state in (a). . . 66

3.21 Quasi-static loading and extraction of the values of stress intensity range ΔK at crack tips. 68

3.22 Schematic description of the procedures of fatigue crack growth calculation. 70

4.1 Definition of a crack for (a) square, (b) hexagonal and (c) randomly packed samples. Identification of the crack domain d_c for square and hexagonal packed samples. 73

4.2 Simulations of a symmetric edge cracked plate under stress fatigue loading with square packed samples for different particle sizes and comparison with theoretical results of (a) crack growth and (b) the stiffness ratio as functions of the number of cycles N in controlled stress conditions. (c) Contact degradation map during fatigue evolution for $d = 2mm$. . . . 76

4.3 Simulations of a symmetric edge cracked plate under stress controlled fatigue loading with hexagonal packed samples and comparison with theoretical results of the stiffness ratio as a function of the number of loading cycles N for (a) different particle size (Poisson's ratio $\nu = 0$) and (b) different Poisson's ratios (and $d = 2mm$) in controlled stress conditions. 77

4.4 Simulations of a symmetric edge cracked plate under strain fatigue loading with square packed samples for different particle sizes and comparison with theoretical results of (a) crack growth and (b) the stiffness ratio as functions of the number of cycles N in controlled strain conditions. 77

4.5 Simulations of a symmetric edge cracked plate with square packed samples and comparison with theoretical results of the energy release rate G under stress controlled fatigue loading for particle size (a) $d = 2\ mm$ and (b) $d = 1\ mm$, and under strain controlled fatigue loading for particle size (c) $d = 2\ mm$ and (d) $d = 1\ mm$. 78

4.6 Stiffness ratio of a double edge cracked plate under stress fatigue: for a square packed sample (a) as a function of the number of cycles N and (b) as a function of $[d'_c/(1.0d)]^{1+m/2}N$; for a hexagonal packed sample (c) as a function of the number of cycles N and (d) as a function of $[d'_c/(0.5d)]^{1+m/2}N$. 80

4.7 Stiffness ratio of a single edge cracked plate under stress fatigue for a random packed sample (a) as a function of the number of cycles N and (b) as a function of $[d'_c/(0.875d)]^{1+m/2}N$, for Paris's law parameters: $C = 1.0 \times 10^{-12}\,(\mathrm{m/cycle}/(\mathrm{Pa}\sqrt{\mathrm{m}})^m)$ and $m = 1.25$, and that of (c) and (d) for $C = 2.0 \times 10^{-22}\,(\mathrm{m/cycle}/(\mathrm{Pa}\sqrt{\mathrm{m}})^m)$ and $m = 3$. . . . 81

4.8 (a)Stiffness ratio of a double edge cracked plate under stress fatigue for random packed sample $s1$ to $s6$, as a function of the number of cycles N. And each calibrated value of d_c, based on Equation 4.3 and theoretical results for Paris's law parameters: $C = 1.0 \times 10^{-12}\,(\mathrm{m/cycle}/(\mathrm{Pa}\sqrt{\mathrm{m}})^m)$ and $m = 1.25$. (b) Comparison of simulations with $d_c = 0.958d$ and the theoretical results. 83

4.9 Crack trajectories for all six randomly packed samples. 83

4.10 Fatigue evolution (a) versus number of cycles N and (b) versus $C \times N$ for different values of parameter C. 85

4.11 Fatigue evolution (a) versus number of cycles N and (b) versus number of cycles N_{norm} for different values of parameter m. . . 86

4.12 (a) Geometry of the three-point bending beam. (b) Evolution of the crack length ratio a/H as a function of the number of cycle N . Comparison between test results and DEM simulation. 87
4.13 (a) Geometry of the single edge notch tension fatigue test. (b) Evolution of the crack length a as a function of the number of cycle N . Comparison between test results and DEM simulation. 88

5.1 (a) Scheme of the three fatigue stages and (b) its effect on the propagation of cracks per cycle da/dN as a function of crack length a or stress intensity range ΔK, solid line for long crack (except a is too small or too large, crack propagation complies with Paris' law), and dotted lines indicate tow possibilities of the unknown law for short crack (modified from [114]). 92
5.2 Curves relating stiffness reduction $1 - D$ and relative propagated length a_c/d_c for different values of p, based on Equation 3.16. 94
5.3 (a) Example of a contact in rupture with initial stiffness k_0, when crack reaches its boundary, contact displacement is δ_0. During the rupture process, the measured slope ratio $k_0/k_p = 5$. (b) Corresponding values of energy release rate G for different values of parameter p adopted in Equations 3.23 and 3.24. 95
5.4 Simulations of a symmetric edge cracked plate with square packed samples and comparison with theoretical results of the energy release rate G under stress controlled fatigue loading for particle size $d = 2\ mm$ (a) p is measured cycle by cycle, generally $p \approx 2.85$ and (b) p is imposed as a parameter, $p = 2.6$. 96
5.5 Scheme of the equivalent propagated length for an initially micro-cracked contact: (a) initial state of material, and (b) progressive coalescence of cracks. 98
5.6 Flowchart of the damage model (*sp*-model) applicable to any couple of interacting particles. 99
5.7 (a) Geometry of 4PB tests, (b) samples in DEM, and (c) simulation implementation. 100
5.8 (a) Configuration of T-C test, and (b) details of test equipment. (Modified from [8]) 102
5.9 (a) Fatigue evolution expressed by the stiffness ratio (represented as the ratio of the reaction force to the initial reaction force, F/F_0) as a function of the number of cycle N for different values of parameter p, and (b) stiffness ratio versus the normalized number of cycle. 103

5.10 Effect of parameter p on fatigue damage distribution at stiffness ratio $F/F_0 = 0.5$, where red means totally broken and blue means intact. 104

5.11 Comparison of results for different levels of contact endurance limit ε_{lim}, for test strain levels respectively (a) 108 $\mu\varepsilon$, (b) 92 $\mu\varepsilon$ and (c) 79 $\mu\varepsilon$. 105

5.12 T-C fatigue tests simulation results, (a) comparison of average simulation results (three samples) and experimentation [1] with different test strain levels, and fatigue evolution of all three samples (S1, S2 and S3) with strain levels respectively (b) 108 $\mu\varepsilon$, (c) 92 $\mu\varepsilon$ and (d) 79 $\mu\varepsilon$. 107

5.13 Crack distribution maps of all three samples, (a) contact degradation map (where red is totally broken and blue is intact), and (b) contact opening map representing by the ratio of the contact displacement δ at stiffness ratio $F/F_0 = 0.5$ to the contact displacement at test beginning ($F/F_0 = 1$) δ_0 (where red means $\delta/\delta_0 \geq 10$ and blue means $\delta/\delta_0 = 0$), for simulation with strain level 108 $\mu\varepsilon$. 108

5.14 Fatigue lines of experiments and simulation for T-C fatigue tests. The slopes of fatigue lines in log-log scale coordinates and the coefficient of determination R^2 are presented. 109

5.15 Comparison between envelop curves and average curves of 4PB fatigue test simulations and that of experiments [150], for different test strain levels. For example, Sim_ave_ 115 $\mu\varepsilon$ is the average curve of simulation of all three samples at test stain level 115 $\mu\varepsilon$, Sim_max_ 115 $\mu\varepsilon$ is the maximum boundary of the envelop of all simulations at test stain level 115 $\mu\varepsilon$, and sign of min for the minimum boundary of the envelop of all simulations. So that for experimental results with sign Exp. . 111

5.16 Comparison between 4PB fatigue test simulations and experiments [150], (a) average curves for different test strain levels, (b) average and envelop curves for test strain level 150 $\mu\varepsilon$, (c) 135 $\mu\varepsilon$ and (d) 115 $\mu\varepsilon$. For example, Sim_ave_ 115 $\mu\varepsilon$ is the average curve of simulation of all three samples at test stain level 115 $\mu\varepsilon$, Sim_max_ 115 $\mu\varepsilon$ is the maximum boundary of the envelop of all simulations at test stain level 115 $\mu\varepsilon$, and sign of min for the minimum boundary of the envelop of all simulations. So that for experimental results with sign Exp. . 112

5.17 (a) Damage distribution maps (where red is totally broken and blue is intact) for all three samples at stiffness ratio $F/F_0 = 0.5$, for test strain level $150\,\mu\varepsilon$, (b) corresponding zoom of (a). Main cracks are marked by red rectangular. 114
5.18 Fatigue lines of experiments and simulation for 4PB fatigue tests. The slopes of fatigue lines in log-log scale coordinates and the coefficient of determination R^2 are presented. 115
5.19 (a) Configuration of 2PB fatigue test, (b) details of test sample, and (c) sample dimension and test scheme. (Modified from [8, 151]) 116
5.20 Comparison between envelop curves and average curves of 2PB fatigue tests simulation and that of experimentation [150], for different test strain levels. For example, Sim_ave_ $160\,\mu\varepsilon$ is the average curve of simulation of all three samples at test stain level $160\,\mu\varepsilon$, Sim_max_ $160\,\mu\varepsilon$ is the maximum boundary of the envelop of all simulations at test stain level $160\,\mu\varepsilon$, and sign of min for the minimum boundary of the envelop of all simulations. So that for experimental results with sign Exp. . 118
5.21 Comparison between 2PB fatigue tests simulation and experimentation [150], (a) average curves for different test strain levels, (b) average and envelop curves for test strain level $160\,\mu\varepsilon$, (c) $130\,\mu\varepsilon$ and (d) $100\,\mu\varepsilon$. For example, Sim_ave_ $160\,\mu\varepsilon$ is the average curve of simulation of all three samples at test stain level $160\,\mu\varepsilon$, Sim_max_ $160\,\mu\varepsilon$ is the maximum boundary of the envelop of all simulations at test stain level $160\,\mu\varepsilon$, and sign of min for the minimum boundary of the envelop of all simulations. So that for experimental results with sign Exp. . 119
5.22 Damage distribution maps (where red is totally broken and blue is intact) for all three samples (90° rotated) at stiffness ratio $F/F_0 = 0.5$, for test strain level $160\,\mu\varepsilon$. Main cracks are marked by red rectangular. 120
5.23 Fatigue lines of experiments and simulation for 2PB fatigue tests. The slopes of fatigue lines in log-log scale coordinates and the coefficient of determination R^2 are presented. 121

A.1 Operations executed during each calculation cycle. 125

B.1 Square sample generation. (a) Initial particle distribution ($h_r \approx 1.37\times10^{-2}$. and 2 floater particles are indicated in black. (b) At the end of the generation process ($h_r \approx 1.04\times10^{-9}$, no floater is observed), (Modified from [4]). 131

C.1 (a) Plate deformation without crack, (b) plate deformation with crack, (c) the average relative displacement at plate ends versus crack length in the plate, (d) the external force versus the average relative displacement, describing the released energy during plate cracking. 134
C.2 (a) Finite plate with symmetric edge cracks, (b) finite plate with center crack. 136
C.3 Comparison of the average relative displacement $\bar{\delta}$ between analytic results and simulation results, for (a) plate with edge crack, (b) plate with symmetric edge cracks, (c) plate with center crack. 139

D.1 Quasi-static process for stress controlled fatigue test. 141
D.2 Quasi-static process for strain controlled fatigue test. 142

E.1 Fatigue evolution from simulation results with different parameter D_{ini}. 146
E.2 Energy release rate from simulation results with parameter $D_{ini} = 1.0 \times 10^{-2}$. 146
E.3 The contact separation ratio p evolution from simulation results with parameter $D_{ini} = 1.0 \times 10^{-2}$. 147
E.4 Energy release rate from simulation results with parameter $D_{ini} = 1.0 \times 10^{-3}$. 147
E.5 The contact separation ratio p evolution from simulation results with parameter $D_{ini} = 1.0 \times 10^{-3}$. 148
E.6 Energy release rate from simulation results with parameter $D_{ini} = 1.0 \times 10^{-4}$. 148
E.7 The contact separation ratio p evolution from simulation results with parameter $D_{ini} = 1.0 \times 10^{-4}$. 149
E.8 Energy release rate from simulation results with parameter $D_{ini} = 1.0 \times 10^{-5}$. 149
E.9 The contact separation ratio p evolution from simulation results with parameter $D_{ini} = 1.0 \times 10^{-5}$. 150
E.10 Schematic description of the error for contact traction separation slope calculation. 151
E.11 Energy release rate from simulation results with balance level 1.0×10^{-5}. 152
E.12 The contact separation ratio p evolution from simulation results with balance level 1.0×10^{-5}. 152
E.13 Energy release rate from simulation results with balance level 1.0×10^{-6}. 153

E.14 The contact separation ratio p evolution from simulation results with balance level 1.0×10^{-6}. 153
E.15 Energy release rate from simulation results with balance level 1.0×10^{-7}. 154
E.16 The contact separation ratio p evolution from simulation results with balance level 1.0×10^{-7}. 154
E.17 Fatigue evolution from simulation results with different balance level. 155

F.1 Examples for triangle and polygon contact structure in randomly packed sample. 157
F.2 (a) Initial crack tip identification, yellow contacts shows crack surface near crack tip, and (b) schematic for the effective width of contact domain d_c detection. 158
F.3 (a) Crack path in contact degradation map, red to green corresponds to $D = 1$ to $D = 0$, and (b) d_c of contacts on crack path, red contact means its $d_c = d_{min}$ and green means $d_c = \frac{1}{2}d_{min}$. 159
F.4 Comparison of simulations results with theoretical results, in samples with average particle diameter $\overline{d} = 2mm$. 160
F.5 Crack paths in contact degradation map, red to green corresponds to $D = 1$ to $D = 0$, in samples with average particle diameter $\overline{d} = 2mm$, s1-s6 represent sample 1-sample 6. 161
F.6 Comparison of simulations results with theoretical results, in samples with average particle diameter $\overline{d} = 1mm$. 162
F.7 Crack paths in contact degradation map, red to green corresponds to $D = 1$ to $D = 0$, in samples with average particle diameter $\overline{d} = 1mm$, s1-s6 represent sample 1-sample 6. 162

G.1 Illustration of scales in simulation. 164
G.2 Examples for different scale times and corresponding consumed time. 164

H.1 T-C fatigue tests simulation results, (a) comparison of average simulation results and experimentation [1] with different test strain levels, and reaction force evolution of all three samples with strain levels respectively (b) $108\,\mu\varepsilon$, (c) $92\,\mu\varepsilon$ and (d) $79\,\mu\varepsilon$. 165

H.2 Comparison of reaction force evolution between 4PB fatigue tests simulation and that of experimentation [150], (a) average curves for different test strain levels, (b) average and all curves for test strain level 150 $\mu\varepsilon$, (c) 135 $\mu\varepsilon$ and (d) 115 $\mu\varepsilon$. 166
H.3 Comparison of reaction force evolution between 2PB fatigue tests simulation and experimentation [150], (a) average curves for different test strain levels, (b) average and all curves for test strain level 160 $\mu\varepsilon$, (c) 130 $\mu\varepsilon$ and (d) 100 $\mu\varepsilon$. 167

List of Tables

4.1 Set of parameters for the analysis of parameter C in fatigue simulations. 84
4.2 Set of parameters for the analysis of parameter m in fatigue simulations. 85

5.1 Set of parameters for simulations testing the effect of p. 103
5.2 Model parameters for T-C fatigue tests simulations (without scaling). 104
5.3 Parameter setting for 4PB fatigue tests simulations. 111
5.4 Parameter setting for 2PB fatigue tests simulations. 117

E.1 Parameters set for simulations to research the effect of parameter D_{ini}. 145

Chapter 1

Introduction

Contents

1.1 General background 1
1.2 Objectives 2
1.3 Organization of the thesis 2

The work of this thesis was undertaken at the National Institute of Applied Science of Strasbourg (INSA de Strasbourg), in the Laboratory ICUBE (UMR7357), and was funded by the China Scholarship Council (CSC). The work is related to the project *SolDuGri* funded by the French National Research Agency (ANR).

1.1 General background

Environmental issues push the construction industry to search for more sustainable practices. Concerning the road pavement industry, efforts to lengthen the service life of pavement structures and reduce the quantity of consumed materials are key elements for the reduction of environmental impacts, specially related to carbon dioxide emission during pavement construction, reparation and reconstruction.

Fatigue phenomenon is one of the main cause of pavement distresses, causing the reduction of service life. The analysis and prediction of its effects over the pavement structures acquire increasing attention of practitioners in order to optimize the design and management of roads.

Repeated loadings (traffic and temperature), are responsible for a continuous mechanical deterioration of the structural materials, which leads to the initiation and propagation of cracks depending on the number of cycles. Several physical processes, such as the non-linearity of the complex modulus, selfheating, thixotropy and crack coalescence are involved in the fatigue phenomena of asphalt concrete (most common pavement material).

Nowadays, experimental tests are the main tool to determine the fatigue performance of asphalt concrete, although all fatigue mechanisms are still not completely understood. Investigation of essential mechanisms has been performed in the last decades through numerical simulations.

Asphalt concrete is a composite material composed by aggregates, bituminous binder and eventually filler materials. It naturally presents an heterogenous microstructure which affects many aspects of the fatigue behavior. In the discrete element method (DEM), the material is described by means of an assembly of particles interacting through contact, which turns into an effective numerical tool to mimic the effect of heterogeneities.

1.2 Objectives

The global aim of this thesis is to propose DEM contact models which can deal with the whole fatigue process during laboratory tests under constant temperature and loading frequency. In order to fulfill this global purpose, the following objectives are stated:

- Define an energetic formulation of a contact model for fatigue crack growth for long cracks.
- Propose a physical description and subsequent model for crack initiation.
- Combine both aspects in a single contact model.

1.3 Organization of the thesis

This dissertation is organized in the following parts:

In Chapter 2 a review of the fatigue phenomena, usual fatigue tests, and physical processes involved. Basic knowledge of linear elastic fracture mechanics and energy release during cracking process are introduced. Existing models are discussed, including damage, crack growth and cohesive zone approaches. Advantages and disadvantages of each point of view are commented.

In Chapter 3, the energy release of a contact at a crack tip is analysed. A relation between the crack propagation length and the contact stiffness reduction is proposed leading to a fatigue crack growth model, p-model.

In Chapter 4, the p-model is applied to theoretical calculation of simple structures. The physical effects of the parameters of the contact model associated to particle micro-structure are explored. Simulations are then compared to a experimental test of crack propagation.

In Chapter 5, a generalization of the p-model is proposed. A damage model able to describe the whole fatigue process, from crack initiation to crack propagation is presented, the sp-model. Simulations are then compared to different fatigue experiments: tension-compression, four-point and two-point bending fatigue tests.

Finally, the conclusions of the work are presented and several perspectives for future studies are pointed out in Chapter 6.

Chapter 2

Literature review

Contents

2.1 Introduction 6

2.2 Asphalt concrete 6

2.3 Material fatigue behavior 8

  2.3.1 Overview about fatigue behavior 8

  2.3.2 Fatigue behavior for asphalt concrete 8

    2.3.2.1 Fatigue tests 9

    2.3.2.2 Physical processes involved in a fatigue test . . 12

    2.3.2.3 Fatigue endurance limit 14

2.4 Modeling of fatigue damage 16

  2.4.1 Numerical methods 17

  2.4.2 Damage model 17

2.5 Relevant knowledge of fracture mechanics 22

  2.5.1 Crack modes 22

  2.5.2 The elastic stress field near a crack tip 22

  2.5.3 Energy release rate 24

  2.5.4 Energy release rate in cracked plate 25

  2.5.5 The relation between G and K in Mode I 28

  2.5.6 Fatigue crack growth-Paris' law 31

  2.5.7 Fracture process zone (FPZ) 32

2.6 Numerical modeling of fatigue crack growth 33

  2.6.1 Crack growth model 33

    2.6.1.1 Stress intensity factor calculation 35

    2.6.1.2 Representation of crack growth 36

  2.6.2 Transition from damage model to crack propagation . . 39

  2.6.3 Conclusion 40

2.7 Summary of the chapter 41

2.1 Introduction

Fatigue phenomenon is characterized as material mechanical weakening caused by cyclic loading whose magnitude does not exceed material elastic domain. Fatigue damage is the phenomenon due to repeated traffic or climatic loadings is the main source of distresses attributed to the reduction of service life of civil engineering infrastructures such as road and airport pavements. Research efforts have been done in the last decades to improve experimental characterization of such phenomena [1–3]. More recently, the contribution of computer modeling has allowed a better interpretation of fatigue tests, which has helped researchers to identify the main physical mechanisms related to the degradation of properties of the materials [4–6].

2.2 Asphalt concrete

Asphalt concrete (AC) is a composite material, composed by a mixture of mineral aggregates and bitumen [7], see in Figure 2.1. The AC material has been widely used in pavement construction due to its good performance in terms of toughness, resistance, durability, installation and maintainability. Mainly, the collective effect of aggregates and bitumen forms the performance of asphalt concrete [4].

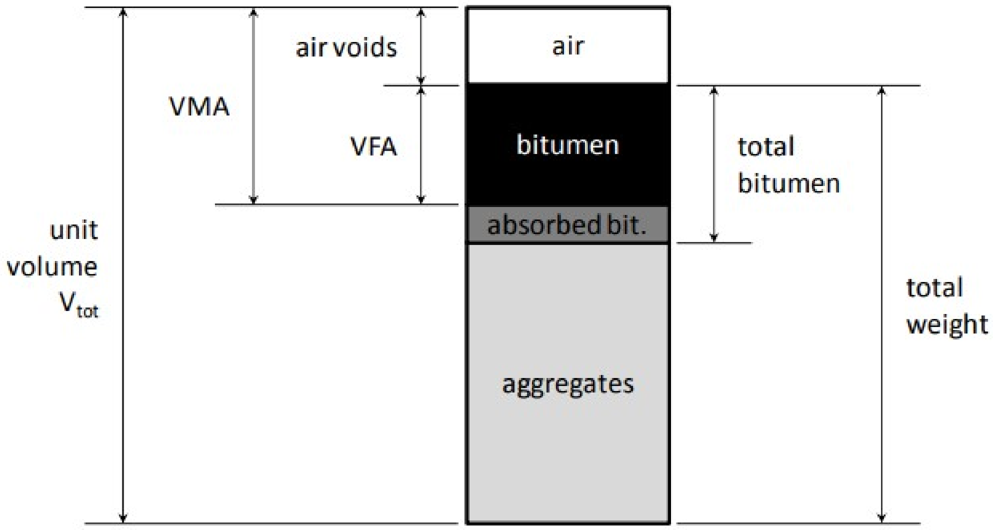

Figure 2.1: Scheme of volumetric properties of a bituminous mixtures, where V_{tot} is a unit volume of mixture, VMA (Voids in Mineral) and VFA (Voids Filled with Asphalt) [8].

Aggregates are considered as the skeleton of the AC material which principally provides the load-bearing capacity through their high strength and interlocking ability. Such a role requires the aggregates to fulfill several requirements including angularity, polish resistance, shock resistance, freeze/thaw resistance and binder/aggregate compatibility [8].

The gradation of aggregates describes the particle size distribution of aggregates of the AC material based on sieve analysis. A good gradation of aggregates tends to an optimal density of the mixtures both for the cement concrete [9] and asphalt concrete [10, 11]. There is also the gradation optimization aiming to the minimum air void [12], for a better rutting resistance. When the sample is loaded, among all aggregates, some aggregates belong to the load chains by their inter particle contacts [13, 14]. The shape and surface texture of aggregates have an influence on the fatigue resistance of the mixtures [15].

The cohesion of the AC material is provided by the bituminous binder which includes the bitumen and the mineral powder. The bituminous binder also contributes to the elasticity, plasticity and viscosity of asphalt concrete. Generally, the hydrocarbon bitumen mainly contains two important elements, carbon $(82 - 88\%)$ and hydrogen $(8 - 11\%)$. Also some other elements exist in bitumen at relatively low proportion, such as sulfur $(0 - 6\%)$, oxygen $(0 - 1.5\%)$, nitrogen $(0 - 1\%)$ and traces of heavy metals, iron, vanadium, aluminum, nickel, etc... [16]. Bitumen is composed of high molecular weight species which are formed by molecules connected through $\pi - \pi$ bonds, and this feature is helpful to explain the AC material sensitivity to changes in shear conditions and temperature [17].

Different additives may be added into bitumen and resulting modified bitumen improve the performance of material in service period or in production procedures. Common additives are adhesion agents, polymers, sulfur, waxes and crumb rubber [18].

Air void has also some influence on the performances of AC materials, when air void content decreases the stiffness of asphalt mixtures increases [8,19,20]. The void content has different effects on the fatigue resistance depending on the loading conditions: in strain controlled fatigue test, with the void content decreasing, the fatigue life decreases; however, in stress controlled fatigue test, with the void content decreasing, the fatigue life increases [8].

2.3 Material fatigue behavior

2.3.1 Overview about fatigue behavior

In the 19_{th} century, with the development of the industrial revolution, standard production and transportation designedly or undesignedly exert repetitive loading on structures that finally leads to fatigue failures of materials. Fatigue failures were related to accidents of steam engines, pumps,locomotives and axles, like the Versailles train crash of 1842. Fatigue phenomenon was recognized as a kind of fracture process occurring after materials were exposed to a large number of repetitive loading cycles with the magnitude of repetitive load remaining below the material strength. In 1837, Wilhelm Albert published the first laboratory study on fatigue. Jean-Victor Poncelet for the first time use the word 'fatigue' to describe the phenomenon, in 1839.

2.3.2 Fatigue behavior for asphalt concrete

Asphalt concrete is an important component of multi-layer road pavements, and during service time, it suffers repetitive traffic loads. Bending caused by traffic loads leads to both compression stress in the bulk section and tension stress at the bottom of the layer as shown in Figure 2.2. For a long service time, the repetitive stresses and strains in asphalt concrete lead to fatigue cracks, for example, as shown in Figure 2.3.

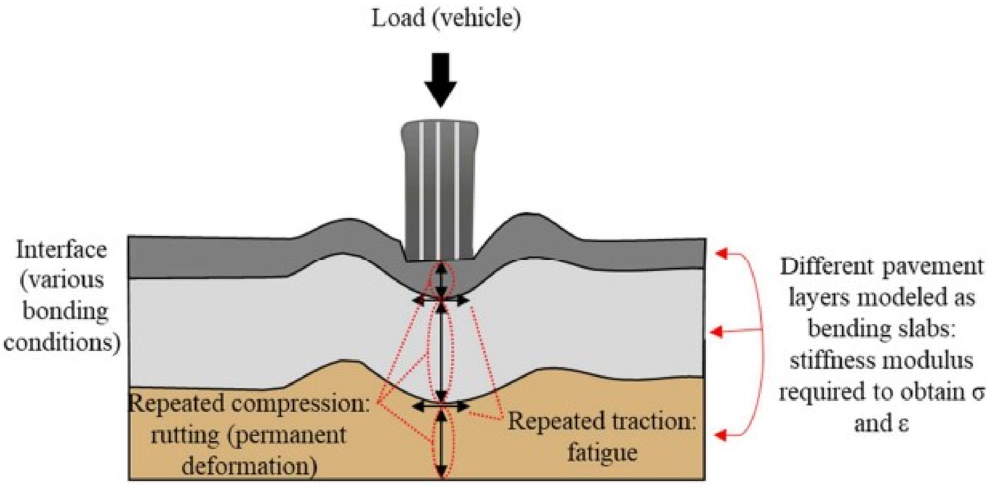
Load (vehicle)
Interface (various bonding conditions)
Repeated compression: rutting (permanent deformation)
Repeated traction: fatigue
Different pavement layers modeled as bending slabs: stiffness modulus required to obtain σ and ε

Figure 2.2: Schemes of vehicle loading and pavement layer response [1].

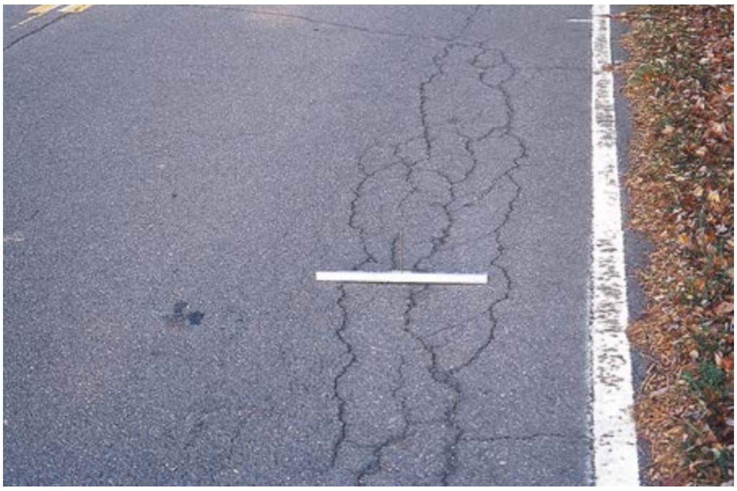

Figure 2.3: Example of fatigue cracks on pavement [21].

2.3.2.1 Fatigue tests

In order to investigate fatigue phenomenon in asphalt concrete, laboratory tests were designed to observe the evolution of the mechanical properties under cyclic loading, in specific controlled conditions. Typical fatigue tests include bending tests, two point bending, three point bending and four point bending, tension-compression test and indirect tensile test (Figure 2.4 and 2.5). Different types of fatigue tests show a significant influence on the test results for the same material [2]. Figure 2.5 shows an example of the configuration of a 4-point bending test, also test samples and test equipment are shown in Figure 2.6.

Generally, in laboratory, two main types of cyclic loading, i.e. stress controlled and strain controlled, are applied for fatigue tests [22–24]. Figure 2.7 typically shows loadings and responses in different loading modes. In stress controlled mode, a constant stress is imposed and the corresponding strain level of the specimen is monitored, then one of the fatigue failure criteria is based on the moment when the specimen finally reaches excessive tensile strains [25–27]. In strain controlled mode, the most widely used fatigue failure criterion is the 50% reduction of specimen stiffness compared with initial stiffness [28], as shown in Figure 2.8. We can mention that some other failure criteria have been suggested by different researchers [29, 30]. The most commonly used loading signal shape is sinusoidal, as shown in Figure 2.5, but there are also square or haversine forms [31, 32].

For strain controlled 4-point bending (4PB) test, as an example, a sinusoidal

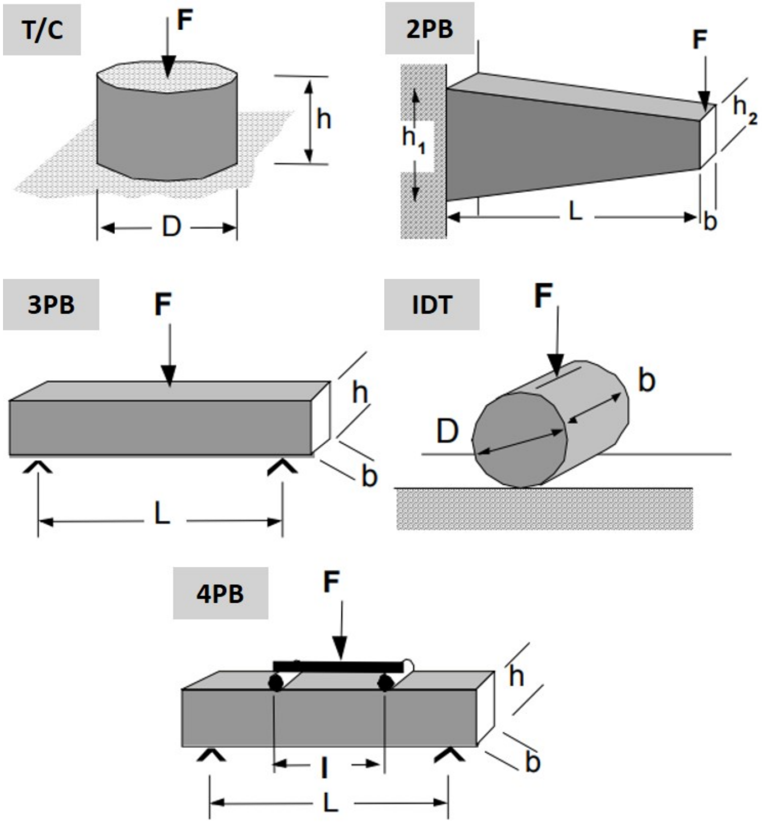

Figure 2.4: Typical fatigue tests: Tension-Compression (T/C), Two Point Bending (2PB), Three Point Bending (3PB), Indirect Tensile (IDT) and Four Point Bending Test (4PB), (Modified from [2]).

displacement signal $\delta_v(t)$ with constant amplitude $\delta_{v,max}$ is imposed at two middle points of the specimen (see Figure 2.5). Consequently the bottom and top of the central cross-section are subjected to a sinusoidal strain wave $\varepsilon(t)$, whose amplitude ε_{max} is identified as the test strain level, for instance 150 $\mu\varepsilon$, 135 $\mu\varepsilon$ and 115 $\mu\varepsilon$. The relation between $\delta_{v,max}$ and ε_{max} can be described by the expression [4]:

$$\delta_{v,max} = \frac{5}{3}\frac{A^2}{h}\varepsilon_{max} \tag{2.1}$$

And the reaction force F_v can be obtained by the equation [4,33]:

$$F_v = \frac{6}{5}\frac{EI}{A^3}\delta_{v,max} \tag{2.2}$$

where A is the distance between the two loading points, E is the elastic

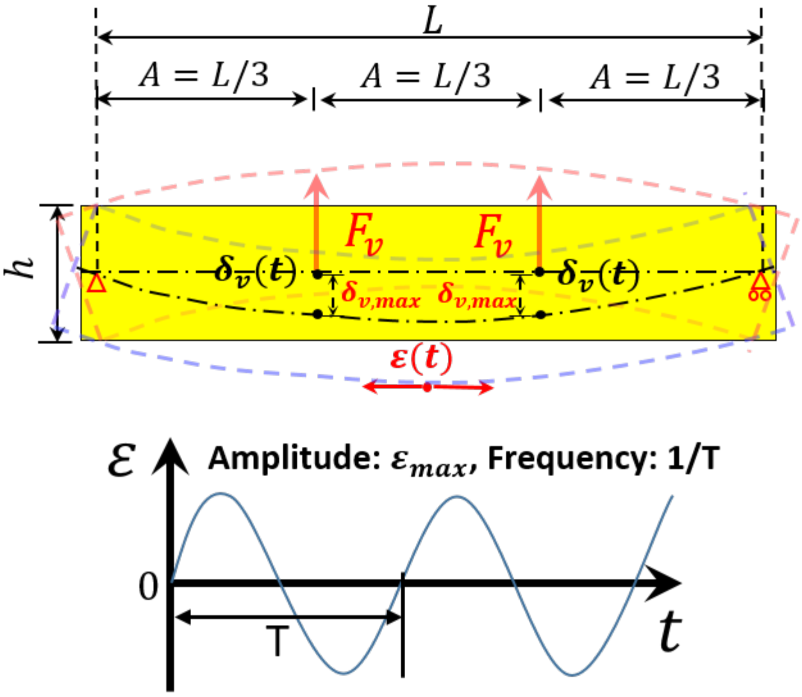
L
A = L/3
A = L/3
A = L/3
h
F_v
F_v
$\delta_v(t)$
$\delta_v(t)$
$\delta_{v,max}$
$\delta_{v,max}$
$\varepsilon(t)$
ε
Amplitude: ε_{max}, Frequency: 1/T
0
T
t

Figure 2.5: Configuration of 4-point bending test.

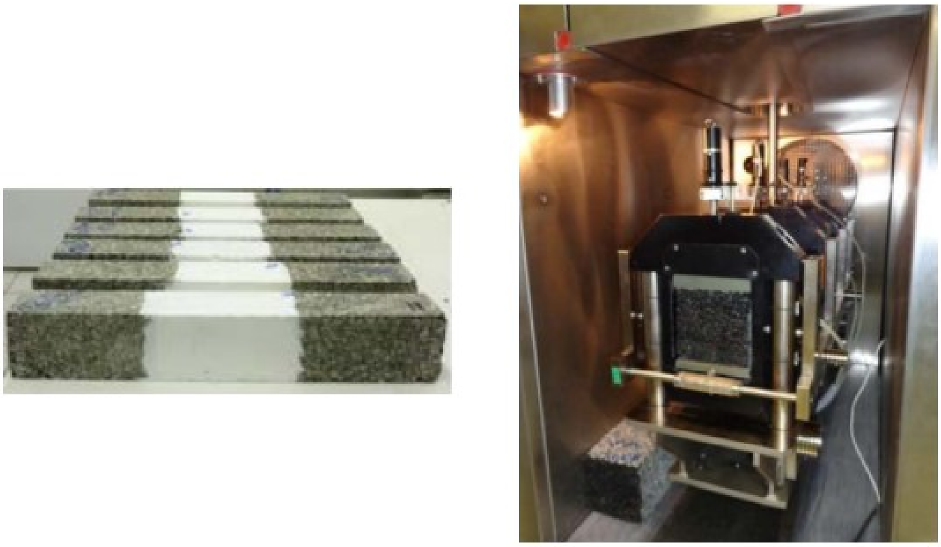

(a) (b)

Figure 2.6: (a) 4-point bending test samples and (b) test equipment [3].

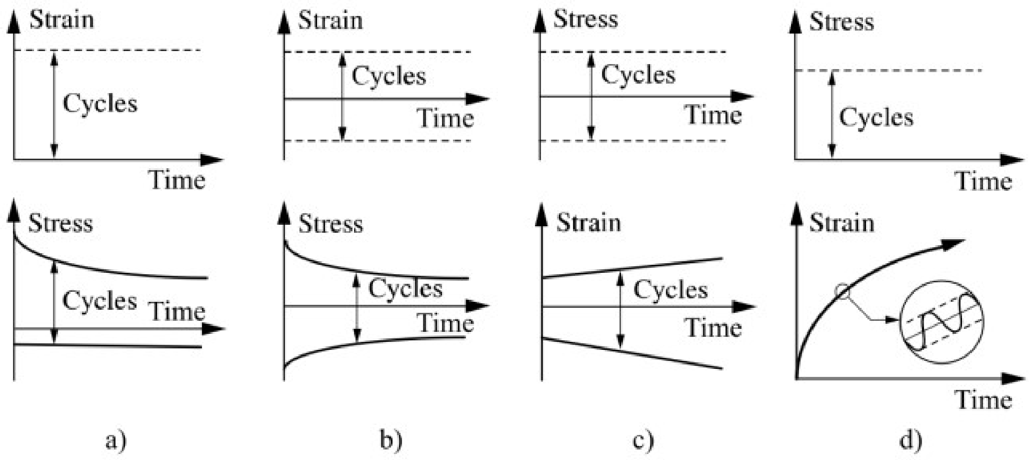

Figure 2.7: Schematic description of loading and response in: (a, b) strain controlled mode, and (c, d) stress controlled mode [7].

modulus, I is the moment of inertia of the cross-section and h is the test specimen height.

2.3.2.2 Physical processes involved in a fatigue test

During a fatigue test, the global stiffness of specimen progressively degrades with increasing number of loading cycles. The fatigue evolution consists of three distinct phases [34, 35] (see Figure 2.8). During phase I, the stiffness initially decreases sharply. However, several physical phenomena including non-linearity, self-heating and thixotropy play a more crucial role to the decrease than fatigue. Phase II is characterized by a quasi-linear development trend, during which, the gradient of stiffness change stabilizes and micro-cracks network progresses. Finally, in phase III, micro-cracks coalesce into macro cracks whose propagation leads to the fracture of material.

One important difference between the laboratory fatigue test and the pavement in real traffic condition is that cyclic loading is generally applied continuously during tests and on the contrary for real pavement the pause between two vehicles passing may last relatively longer than the period of the loading wave in laboratory tests. Fatigue life obtained from laboratory tests may hence deviate from the fatigue distress in real pavement [36]. For continuously performed fatigue tests without the pause between loads the transient reversible variations, mentioned as non-linearity, self-heating and thixotropy, are incorporated in stiffness evolution during tests, especially in phase I.

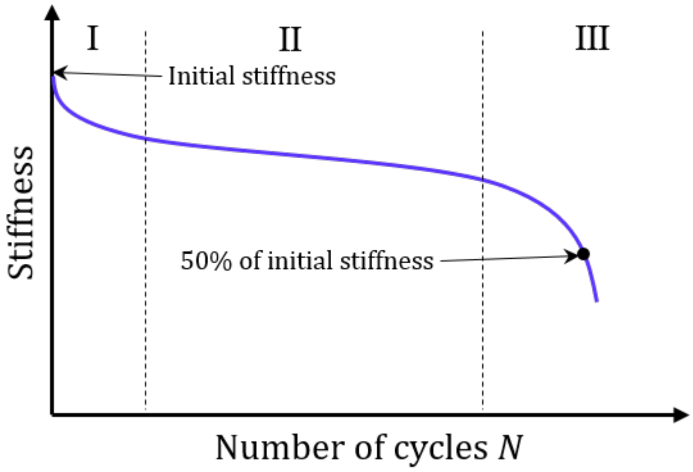

Figure 2.8: A typical fatigue evolution curve during fatigue test.

Non-linearity refers to the disproportion between strain amplitude and stress amplitude, when the applied strain level is higher than the linear viscoelastic limit of material [37, 38]. Considering the micro structure inside the material, the binder within the aggregate surrounding space can concentrate a significantly higher strain level than the overall strain [39].

Under repetitive loadings, viscoelastic materials exhibit a temperature increase (self-heating), due to the energy dissipation [40,41]. Such phenomenon also has been observed during fatigue tests on bituminous mixtures [42, 43]. Since the mechanical behavior of bituminous mixture is typically temperature dependent, self-heating plays an important role in the evolution of material properties during fatigue test [44].

Thixotropy is defined as the viscosity decrease of the sample, previously at rest when a flow is suddenly applied, and the subsequent viscosity recovery after the flow is stopped [45]. Phenomena of thixotropy occurrence have been observed in bituminous mixtures [46–50]. Thixotropy may have a stronger influence than self-heating on the variation of material mechanical properties during fatigue tests of mastics [51].

Besides these reversible phenomena, Moreno-Navarro [52] suggested that the steep decrease of modulus in phase I may be related to both the reversible phenomena and the accumulated permanent deformation which can influence the viscoelastic properties of material (i.e. strain hardening [53, 54], material tend to more stiffness and elasticity), and finally results in breakage of molecular chain bonds and the forming of stress concentration and cracks (see Figure 2.9).

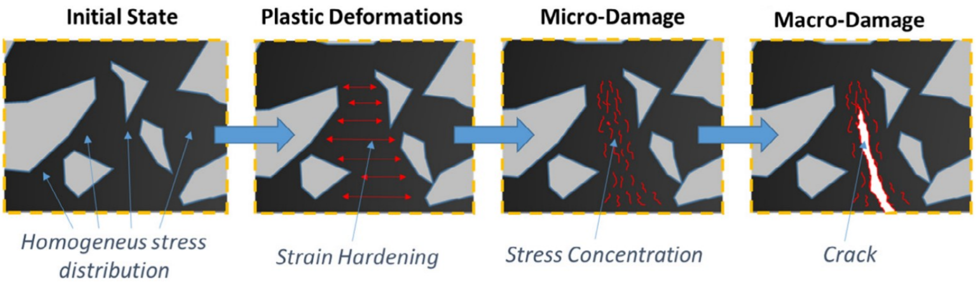

Figure 2.9: Schema of damage development in bituminous mixtures under traffic load (Modified from [52]).

Generally, the mechanical behavior of bituminous mixtures may be influenced by several factors, temperature, applied strain amplitude and number of loading cycles. Referring to small strain amplitude and relatively low number of loading cycles, bituminous mixtures behave as a linear viscoelastic material, and the effect caused by the viscosity of material has very limited influence, it can be considered as a kind of linear elastic material, at a very low temperature. Whereas referring to large strain amplitude, it becomes a nonlinear mechanical behavior. However, even under relatively small strain amplitude, with a relatively large number of loading cycles, it may lead to failure caused by fatigue. Temperature also has a strong influence on the behavior of bituminous mixtures [55]. Temperature affects the phenomena including non-linearity, viscoelasticity and fatigue, as shown in Figure 2.10.

2.3.2.3 Fatigue endurance limit

Wöhler introduced the Wöhler curve (S-N curve) that relates the magnitude of the applied repetitive stress and the number of cycles to failure (known as 'fatigue life') [56, 57]. In semi-logarithmic scale, the S-N curve shows a straight line as shown in Figure 2.11.

An obvious tendency in S-N curves is that with loading amplitude decreasing the fatigue life increases, till a certain value of loading amplitude, the straight line in S-N curve becomes flat, meaning an infinite fatigue life. The 'endurance limit' was introduced by Wöhler [56], defined as a certain stress level below which the fatigue damage is not accumulative, an infinite or a very huge number of loading cycles could be applied without leading to material failure [58], for instance, for portland cement concrete the stress level for a fatigue life equal to 2 million cycles is the endurance limit (EL) [59].

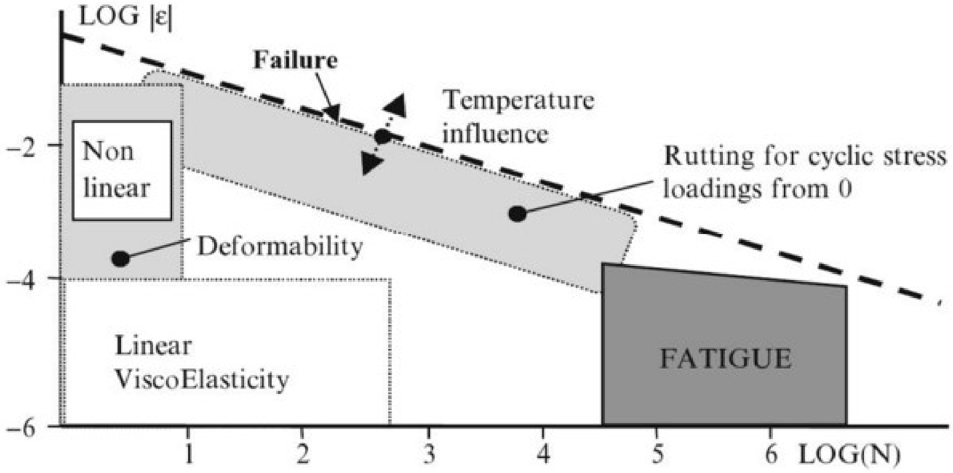
LOG |ε|
Failure
Temperature influence
Rutting for cyclic stress loadings from 0
Non linear
Deformability
Linear ViscoElasticity
FATIGUE
−2
−4
−6
1
2
3
4
5
6
LOG(N)

Figure 2.10: Typical mechanical behavior domains of bituminous mixtures depending on strain amplitude ε and number of cycles N, for a given temperature [55].

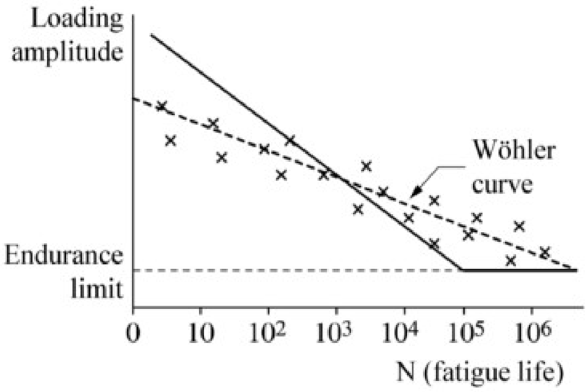

Figure 2.11: Example of Wohler curve and endurance limit [8].

Lower strain level at the bottom of the asphalt pavement leads to less probability of cracking [60–62], and below a given strain level the structural damage becomes not accumulative [63], this kind of pavement is called as 'perpetual' pavement [64]. Such conception is the basis for the fatigue endurance limit of asphalt concrete [65]. First research in asphalt concrete, Monismith and McLean [66] proposed an endurance limit of 70 microstrain. Some different values of asphalt concrete fatigue endurance limit are reported in [67–70].

2.4 Modeling of fatigue damage

Existing modeling methods of fatigue evolution can be categorized into two main directions, based on damage mechanics or fracture mechanics. The damage models intend to establish the evolution law of damage variable which represents the loss of material mechanical capacity, with respect to an increasing number of loading cycles [71–74]. On the other hand, crack growth models relate the crack growth increment per loading cycle to fracture mechanics features for cracking state, such as stress intensity factor, energy release rate and crack tip opening [75–78].

A favorable fatigue model is supposed to capture both the fatigue evolution, like global stiffness change (see Figure 2.8), and localized failure, like crack distribution and propagation (see Figure 2.12). For instance, in Arsenie's study [3], the fatigue evolution is in good agreement with experimental data (Figure 2.13), however, fatigue damage did not localize (Figure 2.14a). In another example, Liu [4] observed localized failure in simulations (Figure 2.14c) and modeled 4PB test at relatively high strain level, 150 $\mu\varepsilon$ and 135 $\mu\varepsilon$, but simulation results for strain level 115 $\mu\varepsilon$ did not agree with experimental result so well (Figure 2.15).

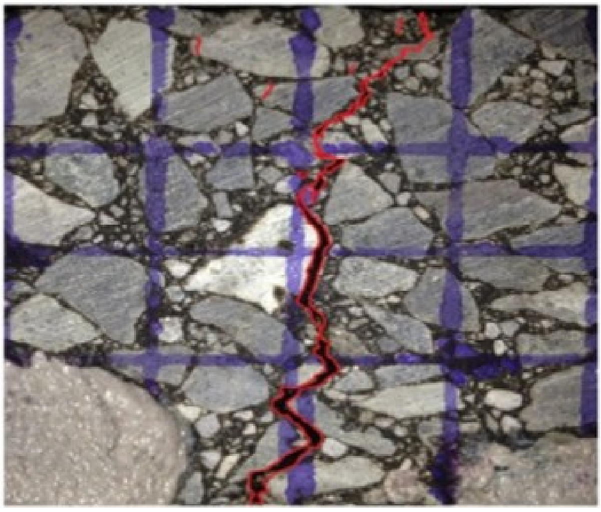

Figure 2.12: An example of concentrated damage (crack) in asphalt concrete (Modified from [52]).

Generally, local damage models use information from local mechanical response of the material (material in one element domain), such as strain, stress or energy, to determine the damage evolution of material within this corresponding element domain. However, due to mesh-dependency, it is dif-

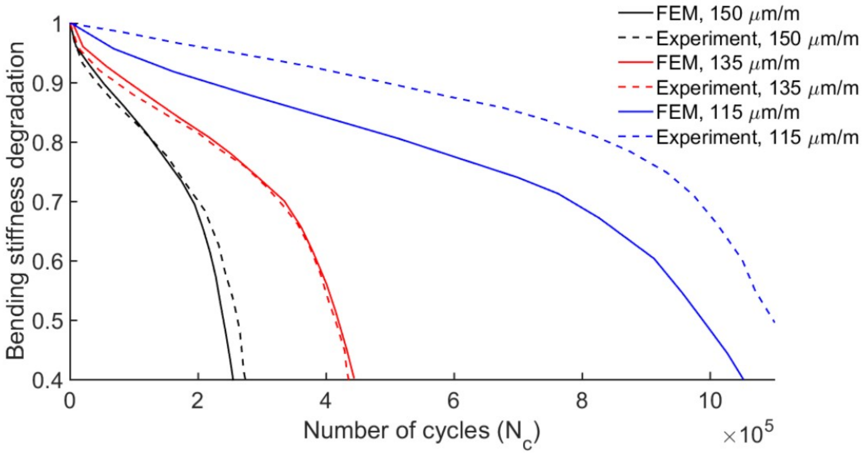

Figure 2.13: 4PB test experimental results and simulations in FEM by Arsenie [3], (Modified from [4]).

ficult to deal with high stress gradient, like stress near crack tip. Furthermore, the strain singularity in an element near the crack tip may lead to an unrealistically huge damage rate which may present a spurious localization [79, 80]. Non-local damage models need more information beyond the mechanical response of only one element, consequently more programming and computation efforts are required to implement non-local models than corresponding local models [81, 82].

2.4.1 Numerical methods

Both the continuous method (finite element method (FEM) [85] and extended element method (XFEM) [86]) and the discrete element method (DEM) [87] can be used for fatigue behavior modeling. Compared with continuous method, its discrete nature enables DEM to easily reproduce the heterogeneous micro-structure of granular materials (Figure 2.16) and deal with large deformation, which is a strong advantage for crack propagation modeling [88]. Furthermore, mesh refinement may be needed to simulate crack propagation in FEM (Figure 2.17).

2.4.2 Damage model

Usually a damage variable D is used to describe the deterioration of material load-bearing capacity, for virgin material $D = 0$ and $D = 1$ for totally broken with no stiffness. For isotropic damage case, the effective modulus E can be expressed as

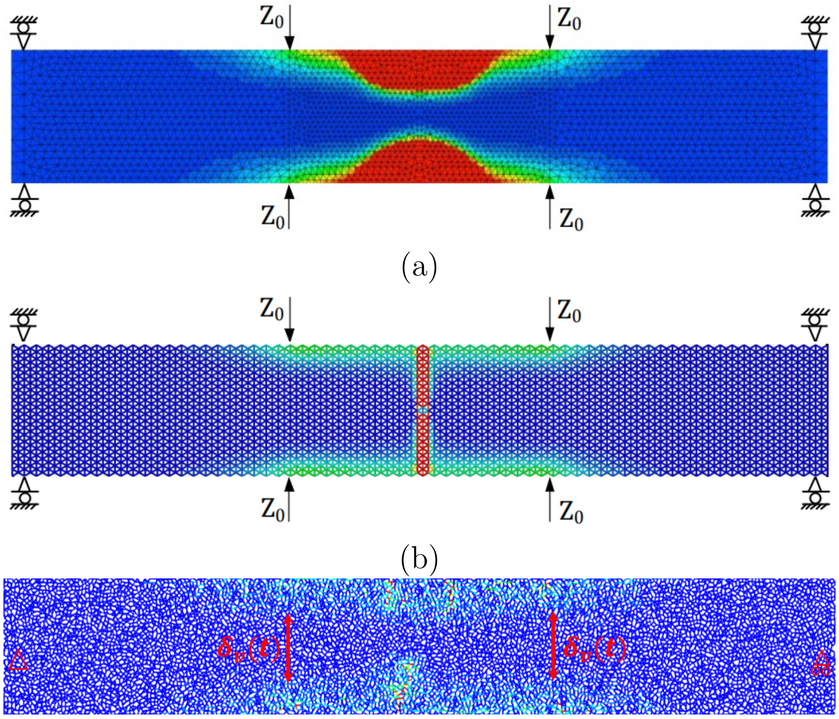

(a)

(b)

(c)

Figure 2.14: Damage maps (blue to red means $D = 0$ to $D = 1$) displaying different localization levels of 4-point bending fatigue test simulations by using damage model: (a) finite element method conducted by Arsenie [3], (Modified from [101]), (b) regular packing discrete element method conducted by Gao [101], (Modified from [101]), (c) randomly packing discrete element method conducted by Liu [4], (Modified from [4]).

$$E = (1 - D)E_0 \tag{2.3}$$

where E_0 is the modulus of virgin material.

Various damage models have been developed based on different theories and assumptions. The viscoelastic continuum damage (VECD) model is based on the Schapery's work potential theory [89] and the elastic–viscoelastic correspondence principle [90], by which the time dependency of material are transformed in the change of mechanical properties, like the reduction of pseudo stiffness. Studies [91–95] use the VECD model to generally model the mechanical behavior change of viscoelastic materials. Generally, these models show good agreement with experimentation in the first two phases of fatigue evolution. The disturbed state concept (DSC) model [96] considers

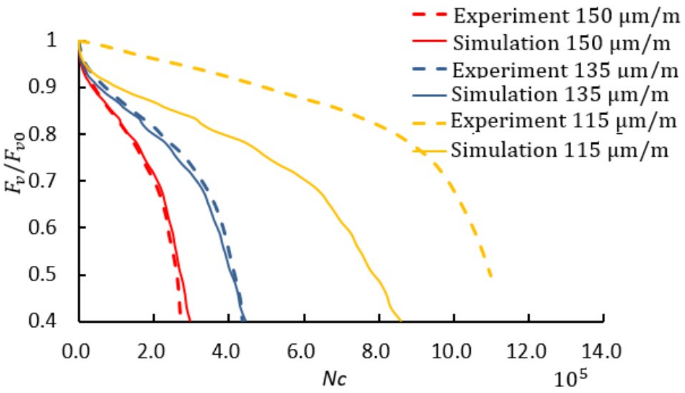

Figure 2.15: 4PB test simulation in DEM by Liu [4], experimental results by Arsenie [3].

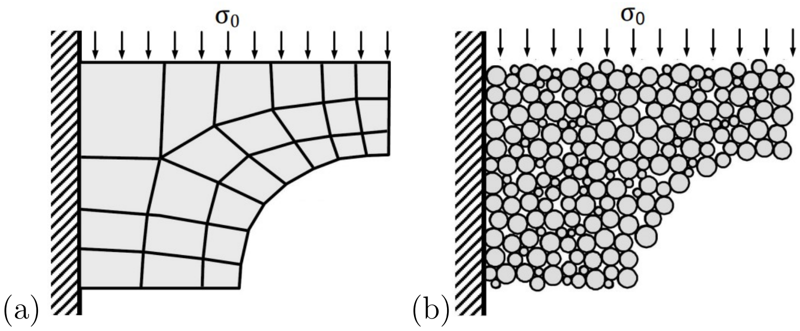

Figure 2.16: (a) Finite element mesh and (b) discrete element mesh, (Modified from [83]).

the behavior of a deforming material as the collective responses of two components, relatively intact (RI) and fully adjusted (FA). This model is used to characterize asphalt concrete behaviors, such as elastic, plastic, creep, rutting, fracture and reflection cracking [97, 98]. One of the machine learning methods, the recurrent neural network (RNN) is trained by experimental results to predict the fatigue behavior of asphalt [5].

The randomness of asphalt concrete structures can be represented by the mesh distribution according to material image [99] (Figure 2.18) or Monte Carlo Simulation method [100].

Attempts to use only a damage model [73] to simulate the entire process of asphalt concrete 4PB fatigue test [3] were made respectively by Arsenie [3], Gao [101] and Liu [4]. Their work may be evaluated from two aspects, localized failure and fatigue evolution.

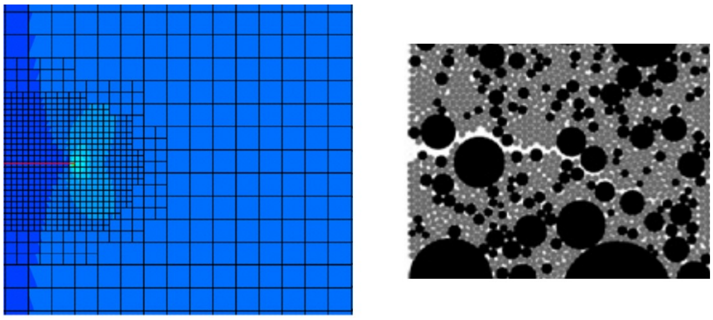

(a) (b)

Figure 2.17: (a) Finite element mesh refinement for crack propagation, (Modified from [84])and (b) discrete element particles detachment for crack propagation, (Modified from [78]).

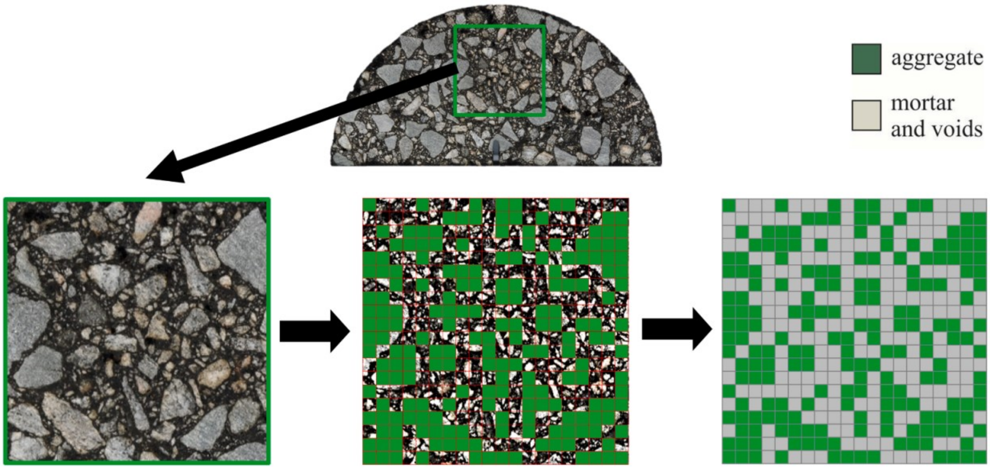

Figure 2.18: Example of mesh assignment based on material image, (Modified from [99]).

A strong tendency of increasing damage localization is shown following the order Arsenie [3], Gao [101] and Liu [4], see Figure 2.14, due to both the different numerical methods they used and the adaption they made to incorporate the damage model. Arsenie used FEM and originally non-local definition of strain to determine the damage rate, whereas the strain is obtained by an average with weight function based on a characteristic length [3, 73]. Such a non-local continuous method may to a certain extent yield unrealistic damage distribution, in fact, no localization (Figure 2.14a). Gao used regular packing DEM and a relatively local definition of strain related to surrounding contact pairs. This approach resulted in an improvement on damage localization(Figure 2.14b), but a sudden and unrealistic crack propagation was observed(Figure 2.19).

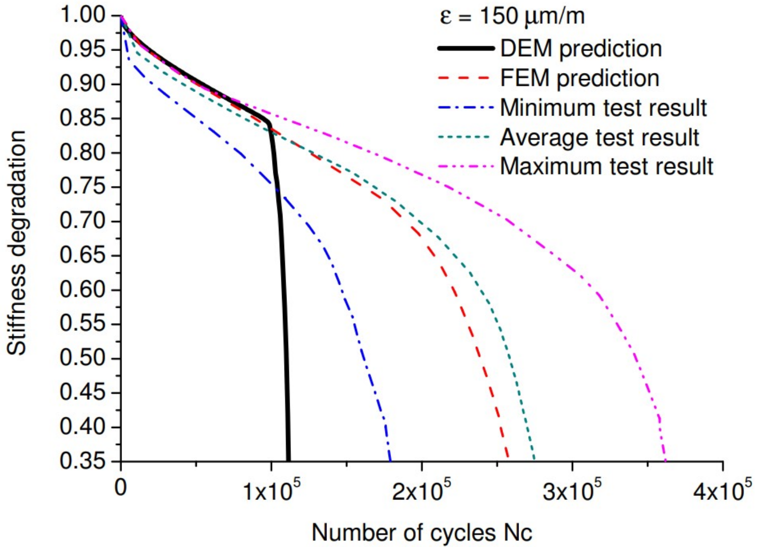

Figure 2.19: 4PB test simulation in DEM by Gao [101], experimental results and simulations in FEM by Arsenie [3, 102, 103].

Liu finally realized good damage localization (Figure 2.14c) by applying DEM to randomly packed materials and a totally local definition of strain determined only by the contact length and its displacement. It should be mentioned that the damage distribution in phases I and II (distributed green or some red contact near top and bottom in Figure 2.14c) is reasonable and is caused by the heterogeneous structure and local damage model, while the 'fracture' like damage distribution (connected red contacts from edge to inside in Figure 2.14c) may result from strain singularity of local damage model. Anyway, it is a promising method to achieve damage distribution and localization by DEM with local model.

However, as shown in Figure 2.15, globally, one may notice that it is still a challenge to use only damage model to catch all three phases of fatigue evolution in fatigue test, as we can see on the deviation of numerical damage curve from experimental one for strain level 115 $\mu\varepsilon$. Focusing on the beginning of simulation curves and experimental curves, where a large damage rate dominates specimen degradation, obvious deviation occurs for tests with strain level 115 $\mu\varepsilon$. Even for experimental curves, strain effect strongly changes shapes of fatigue curves and final fatigue lives. Thus, a new damage model which can capture material fatigue responses for different strain level tests would be welcome.

2.5 Relevant knowledge of fracture mechanics

2.5.1 Crack modes

A crack in a solid consists of disjoined upper and lower faces. The junction segment of the two crack faces forms the crack tip [104]. The movement of two crack faces with respect to each other depends on external forces exerted on the cracked body. Corresponding to three direction relative moments, three fundamental fracture modes are categorized by Irwin [105]. Mode I (opening), the two crack surfaces move apart from each other in y direction (see Figure 2.20), their movements being symmetric with respect to the crack plane. Mode II (sliding), the two crack faces slide against each other in x direction, perpendicularly to the crack tip and within the same plane . Mode III (tearing), the two crack faces tear over each other in z direction, parallel to the crack tip and within the same plane. Any crack mode in a cracked body can be described as one of these three modes, or combinations of them.

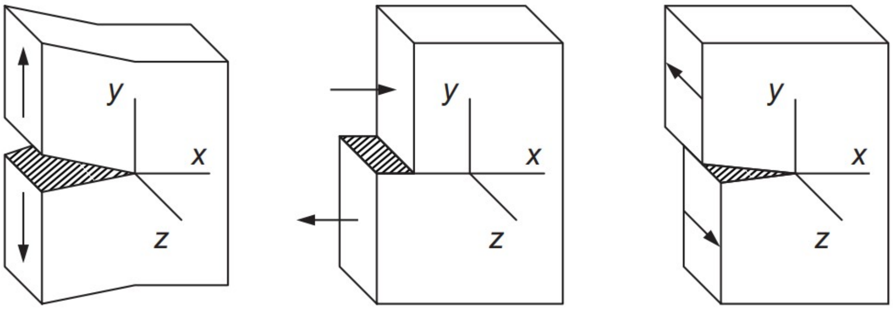

(a) (b) (c)

Figure 2.20: Schematic of the basic fracture modes: (a) Mode I (opening), (b) Mode II (sliding) and (c) Mode III (tearing) [104].

2.5.2 The elastic stress field near a crack tip

The Westergaard function method [104,106] yields the $2D$ elasticity solution of stress field near a crack tip within an infinite plane under uniform remote tension stress (see Figure 2.21). The Westergaard solutions are given below in the coordinate system shown in Figure 2.22. The origins of the polar coordinate system (r,θ) and rectangular coordinate system (X,Y) are located at the crack tip.

The stress and displacement fields given by Westergaard Function Method

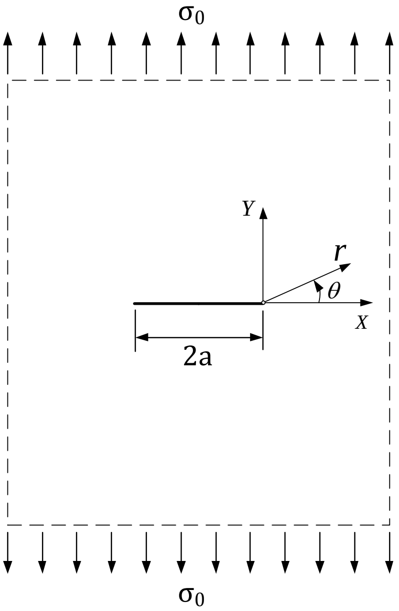

Figure 2.21: A center cracked infinite plate subjected to uniform remote tension [101].

in the polar coordinate system in Mode I are given by:

$$\sigma_{rr} = \frac{K}{\sqrt{2\pi r}} \cos\frac{\theta}{2}\left(1 + \sin^2\frac{\theta}{2}\right) \tag{2.4}$$

$$\sigma_{\theta\theta} = \frac{K}{\sqrt{2\pi r}} \cos^3\frac{\theta}{2} \tag{2.5}$$

$$\sigma_{r\theta} = \frac{K}{\sqrt{2\pi r}} \sin\frac{\theta}{2}\cos^2\frac{\theta}{2} \tag{2.6}$$

$$u_r = \frac{K}{8\mu\pi}\sqrt{2\pi r}\left[(2\kappa - 1)\cos\frac{\theta}{2} - \cos\frac{3\theta}{2}\right] \tag{2.7}$$

$$u_\theta = \frac{K}{8\mu\pi}\sqrt{2\pi r}\left[(2\kappa + 1)\sin\frac{\theta}{2} - \sin\frac{3\theta}{2}\right] \tag{2.8}$$

where K is the stress intensity factor (SIF) [105], as shown in Figure 2.23, E is the Young's modulus, ν is Poisson ratio, shear modulus $\mu = E/[2(1+\nu)]$, $\kappa = 3 - 4\nu$ for plane strain and $\kappa = (3-\nu)/(1+\nu)$ for plane stress.

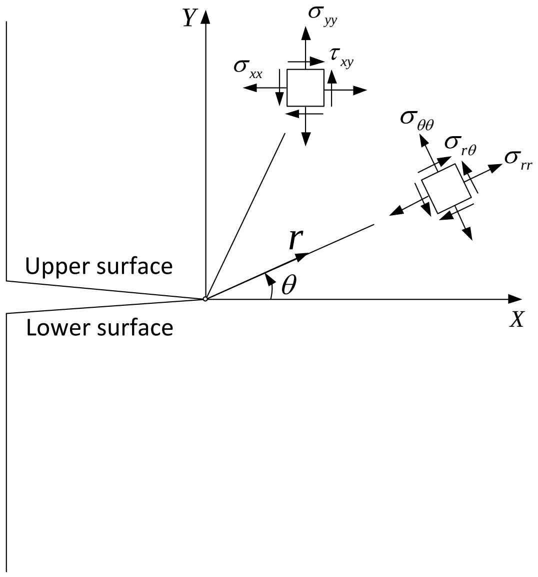
Y
σ_{yy}
τ_{xy}
σ_{xx}
$\sigma_{\theta\theta}$
$\sigma_{r\theta}$
σ_{rr}
r
θ
Upper surface
Lower surface
X

Figure 2.22: The rectangular and polar coordinate components of stress field around the crack tip (Modified from [107]).

When $\theta = 0$ and $r = x$, the stress in y direction can be obtained from Equation 2.5, as:

$$\sigma_{yy} = \frac{K(a)}{\sqrt{2\pi x}} \tag{2.9}$$

For infinite plate with center crack subjected to remote uniform tension stress, the stress intensity factor can be written as:

$$K = \sigma_0 \sqrt{\pi a} \tag{2.10}$$

where σ_0 is the remote stress, and a is crack length.

Furthermore, the stress intensity factor K for a finite plate with different crack distributions (edge crack, center crack, symmetric edge cracks) has been approximately described [108].

2.5.3 Energy release rate

Griffith [109] first proposed the energetic method to characterize material fracture behavior. The condition for crack propagation is that the energy

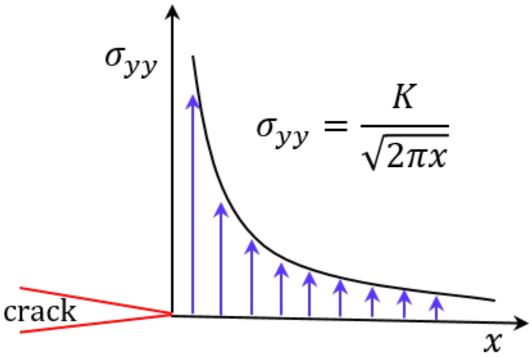

Figure 2.23: Scheme of the stress distribution near a crack tip as a function of the stress intensity factor K [105].

released during crack extension is equal or more than the needed surface energy to generate the newly extended crack surface. Thus, the energy release rate G is the energy dissipated during fracture per unit of newly created fracture surface area, and can it be calculated by Equation 2.11:

$$G = -\frac{\partial(V - W)}{\partial Q} \tag{2.11}$$

where V is the potential energy available for crack growth, W is the work associated with any external forces acting, and Q is the extended crack area.

2.5.4 Energy release rate in cracked plate

The Griffith theory of fracture is based on the principle of energy conservation, during crack extension for the system (cracked body) the released energy must be equal to the added energy. A single-edge-cracked elastic plate with unitary thickness t can be used to easily describe the energy release process [104], and four cases of loadings are schematically illustrated in Figures 2.24 to 2.27.

- Case 1: Plate subjected to a constant force F.
- Case 2: After tension, plate displacement δ is fixed.
- Case 3: After tension, plate top is restrained by elastic constraint with stiffness k.
- Case 4: After tension, plate top is restrained by elastic constraint with varying stiffness k and position.

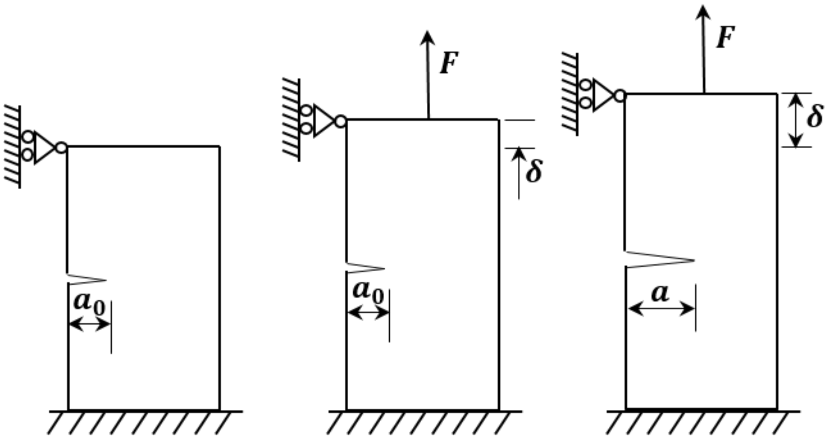

(a) (b) (c)

Figure 2.24: Case 1: plate subjected to a constant force, (a) original state, (b) loading state, (c) crack growth.

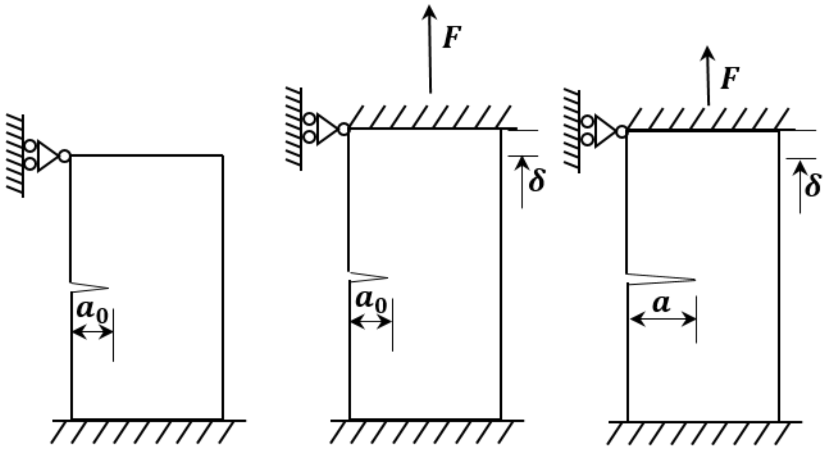

(a) (b) (c)

Figure 2.25: Case 2: after tension, plate displacement δ is fixed, (a) original state, (b) loading state, (c) crack growth.

For all four cases, Equation 2.11 can be rewritten as

$$G = \frac{dU}{dA} = \frac{dW - dV}{tda} \tag{2.12}$$

where

- dA is the crack surface increment, $dA = t \times da$, where da is the crack

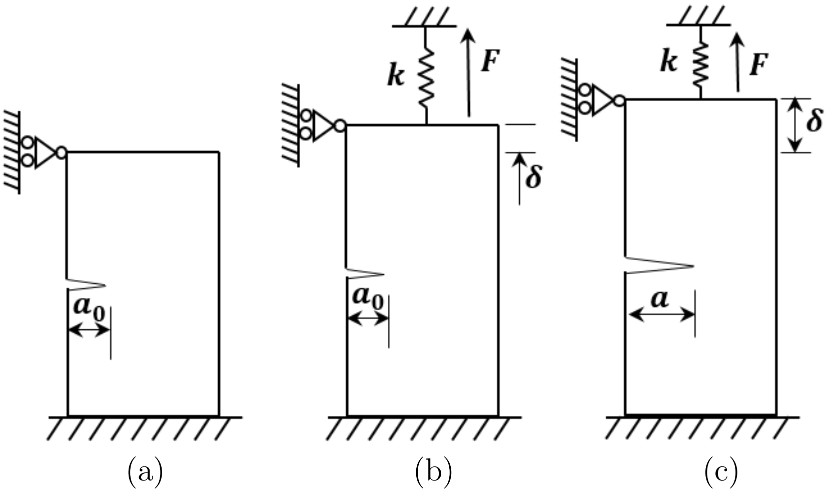

(a) (b) (c)

Figure 2.26: Case 3: after tension, plate top is restrained by elastic constraint with stiffness k, (a) original state, (b) loading state, (c) crack growth.

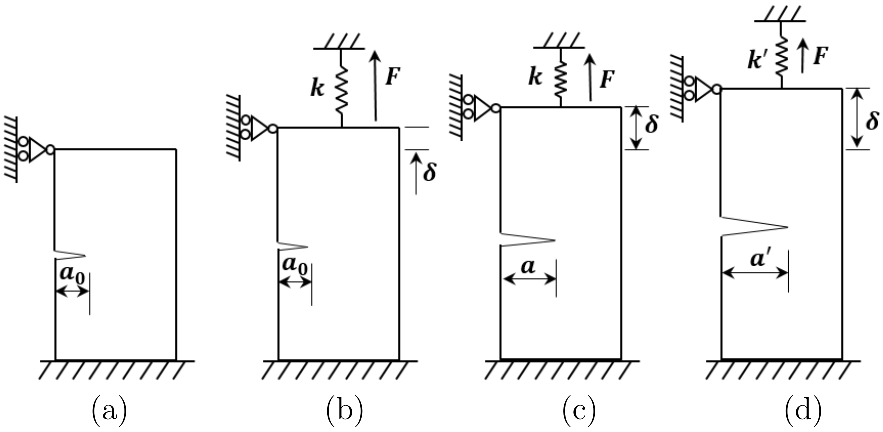

(a) (b) (c) (d)

Figure 2.27: Case 4: after tension, plate top is restrained by elastic constraint with varying stiffness k and position, (a) original state, (b) loading state, (c) crack growth, (d) after elastic constraint stiffness and position change, crack continually grows.

length increment and t is the thickness of the plate.

- dU is the released energy during crack extension dA.
- dW is the work done by external force during crack extension.
- dV is the strain energy increment during crack extension.

As shown in Figure 2.28, dW can be geometrically expressed as the area of quadrangle formed by (A,B,C,D), $S_{\square ABCD}$, and dV is equal to the difference between the area of triangles, $S_{\Delta ODC}$ the strain energy after crack extension, and the area of triangles, $S_{\Delta OAB}$ the strain energy before crack extension. Thus the released energy dU during crack extension, according to Equation 2.12, can be expressed as

$$\begin{aligned} dU_R &= S_{\square ABCD} - (S_{\Delta ODC} - S_{\Delta OAB}) \\ &= S_{\Delta OAD} \end{aligned} \tag{2.13}$$

Upon setting $O(0,0)$, and other two vertices $A(\delta_1, F_1)$, $D(\delta_2, F_2)$, the triangle surface $S_{\Delta OAD}$ can be easily calculated by the Gauss area formula as

$$S_{\Delta OAD} = \frac{1}{2} |\delta_2 F_1 - \delta_1 F_2| \tag{2.14}$$

It should be noted that restrained by an elastic constraint (Case 3), the curve formed by the reaction force F and plate displacement δ descends following a slope $-k$ which relate to the stiffness of corresponding elastic constraint, and if the elastic constraint varies during crack propagation, consequently the curve slope changes accordingly (see Figure 2.28d). Imagining that within the region of a cracked plate like in Figure 2.24, a small region which contains the crack tip can be considered as a secondary micro 'cracked plate', and the material surrounding this micro 'cracked plate' can be considered as an elastic constraint. By thinking this way, one may notice that the varying elastic constraint represents meaningful physical processes, such as micro crack network development surrounding the macro crack tip, damage zone or multi cracks propagation.

2.5.5 The relation between G and K in Mode I

The released energy during crack growth can be calculated by the the crack closure method (CCM). The stress distribution before extension and crack surface opening after propagation are shown in Figure 2.29.

The work done to close the crack new increment da is exactly the released energy during crack extension da from its origin position. To calculate the work, the stress field before extension can be described by Equation 2.9, and the displacement of the newly opened surface can be calculated in x'-y' coordinates by Equation 2.8, with $\theta = \pi$, as

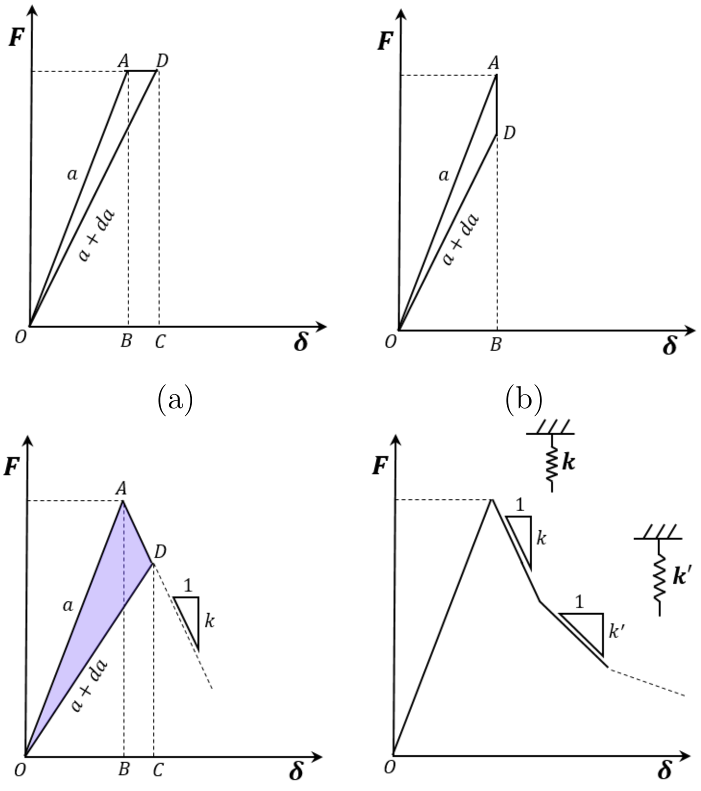

(a) (b)

(c) (d)

Figure 2.28: Released energy during crack extension: (a) constant force, (b) fixed displacement, (c) elastic constraint and (d) varying elastic constraint.

$$u_y = \frac{\kappa + 1}{4\mu\pi} K \sqrt{2\pi(-x')} \tag{2.15}$$

Noting that $x' = x - da$, we rewrite this expression as

$$u_y = \frac{\kappa + 1}{4\mu\pi} K \sqrt{2\pi(da - x)} \tag{2.16}$$

where $K = K(a + da)$. Because da is vanishingly small, K in Eq. 2.16 can be taken to be equal to $K(a)$.

Then the equivalence between the work done to close the crack surface (upper and lower) and the released energy during crack extension can be written as

$$Gda = 2 \int_0^{da} \frac{1}{2} \sigma_{yy} u_y dx \tag{2.17}$$

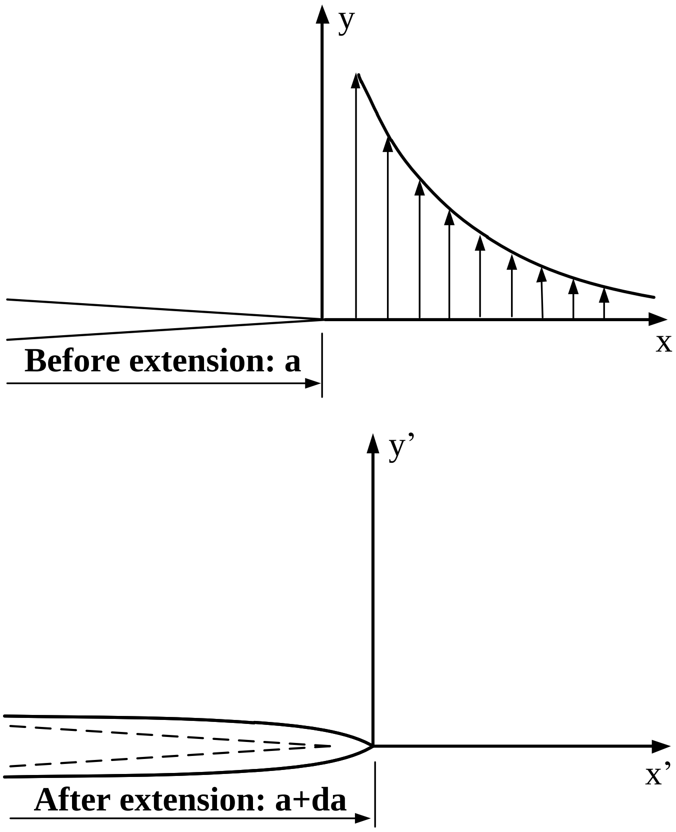
y
x
Before extension: a
y'
x'
After extension: a+da

Figure 2.29: Stress distribution before extension and surface opening after extension [101].

Substituting Equation 2.9 and 2.16 into Equation 2.17, we have the relation between G and K, as

$$G = \frac{\kappa + 1}{8\mu} K^2 \tag{2.18}$$

For plain strain, $\kappa = 3 - 4\nu$, we have

$$G = \frac{1-\nu}{2\mu} K^2 = \frac{1-\nu^2}{E} K^2 \tag{2.19}$$

For plain stress, $\kappa = (3-\nu)/(1+\nu)$, we have

$$G = \frac{K^2}{2\mu(1+\nu)} = \frac{K^2}{E} \tag{2.20}$$

2.5.6 Fatigue crack growth-Paris' law

For a wide variety of materials, fatigue crack growth may be well described by the well-known Paris' law [110], in which the crack increment during one loading cycle da is determined by a power function of the corresponding stress intensity factor increment ΔK (Figure 2.30) during one loading cycle.

$$\frac{da}{dN} = C(\Delta K)^m \tag{2.21}$$

$$\Delta K = K_{max} - K_{min} \tag{2.22}$$

where da/dN is the crack growth rate, a is the crack length and N is the number of loading cycles, C and m are material parameters.

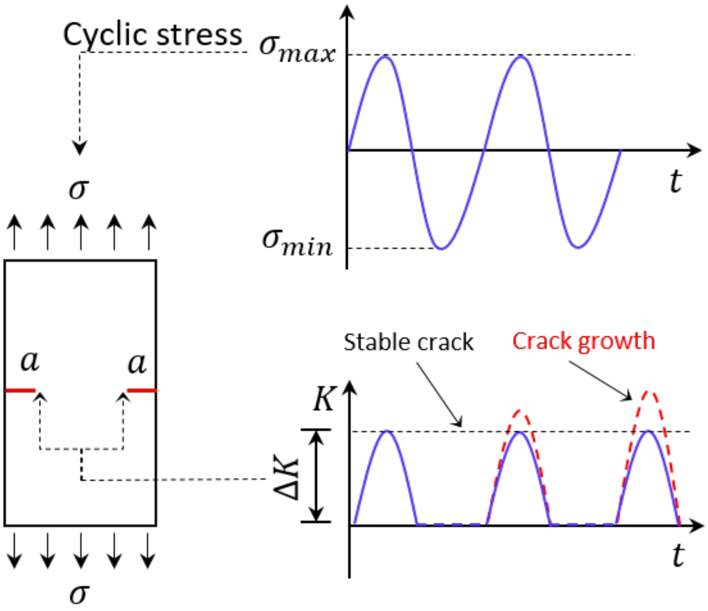

Figure 2.30: Scheme of the stress intensity factor range ΔK.

The parameter m in Paris' law mathematically relates to the slope of the curve relating the crack growth rate da/dN and ΔK in logarithmic scale, though such meaning of m is only validated for long crack (see Figure 2.31). Equation 2.21 may not be suitable for short cracks. The deviation from Paris' law for short crack fatigue propagation has been widely noticed and discussed [111–114]. Thus, to model different stages of cracking, crack initiation and propagation, different theories may be adopted.

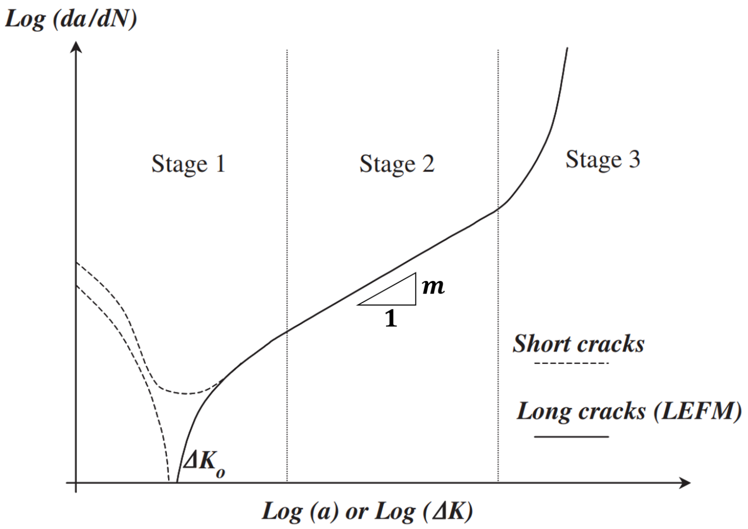

Figure 2.31: Schematic of the fatigue crack growth behavior for long crack and short crack (Modified from [114]).

2.5.7 Fracture process zone (FPZ)

Studying concrete fracture behavior, Glucklich [115] reported that during crack propagation, the strain energy was mainly converted into surface energy and the surface area absorbing this energy was larger than the effective crack surface. Also it was noticed that ahead of the macro crack exists a damage zone with variable size [116], such a zone is named the fracture process zone (FPZ).

Micro cracks in FPZ absorb energy by opening surface with increasing deformation, during the macro crack propagation, and the size and shape of the FPZ have been investigated by different techniques, including high-speed photography [117], ultrasonic measurement [118], optical microscopy [119], laser speckle interferometry [120], scanning electron microscopy [121, 122], compliance and multicutting techniques [123], and acoustic emission (AE) technique [124].

By using X-rays and three-dimensional Acoustic Emission (AE) techniques to monitor micro-cracks behavior during splitting test on concrete, Otsuka [125] defined the micro-cracks zone as two overlapping zones, fracture core zone (FCZ) and fracture process zone (FPZ), corresponding to 70% and 95% of the total energy of all AE events as shown in schematic map of Figure 2.32. In FCZ, it is observed that AE events are more densely distributed than the FPZ, which implies that a more densely distributed micro-cracks network exists in this area.

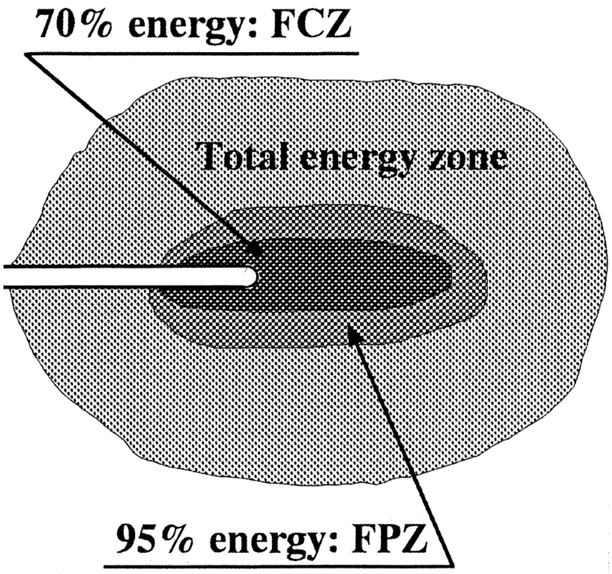

Figure 2.32: The schematic map of fracture process zone by Otsuka (Modified from [125]).

2.6 Numerical modeling of fatigue crack growth

2.6.1 Crack growth model

In FEM, meshes need to coincide with crack trajectory [126]. By using zero thickness interface elements, FEM can incorporate the cohesive zone method (CZM) [127, 128], and cracks propagate along the boundary of finite element meshes [129]. A crack can penetrate through a finite element, with the element erosion in FEM [130]. To adapt the heterogeneity of asphalt concrete, contact phases are defined, aggregate phase, mastic phase and interface between the aggregate and mastic [131], as shown in Figure 2.33. In addition, the non-ordinary state-based peridynamics (NOSB-PD) can be employed by the FEM to model crack branching in asphalt mixtures [6]. Study [132] uses the Gibbs potential-based multinetwork formulation of viscoelasticity to model the crack initiation and propagation.

In XFEM, crack propagation path may be arbitrary and no element remeshing is needed [133, 134]. Through the use of the partition of unity [135], XFEM can model crack location and growth which is independent of meshes.

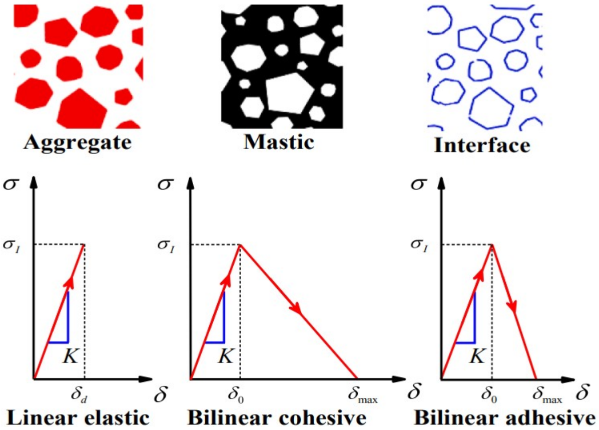
Aggregate
Mastic
Interface
σ
σ_I
K
δ_d
δ
δ_0
δ_{max}
Linear elastic
Bilinear cohesive
Bilinear adhesive

Figure 2.33: Multiphases and corresponding separation model, (Modified from [131]).

The element nodes within the domain close to the crack are enriched with additional degrees of freedom and shape functions which allows the state of discontinuity caused by the crack to be modeled [136] (Figure 2.34). An example of crack propagation in XFEM is shown in Figure 2.35. Even though, XFEM deals a crack deed no element remeshing, it still need to add more enriched nodes, which increases complexity of program and calculation. Furthermore, modeling a relatively large number distributed micro-cracks in which some finally develops to macro or short cracks, and crack bifurcation are still challenges for XFEM. But the discrete nature of DEM allows to model these phenomena simply and naturally.

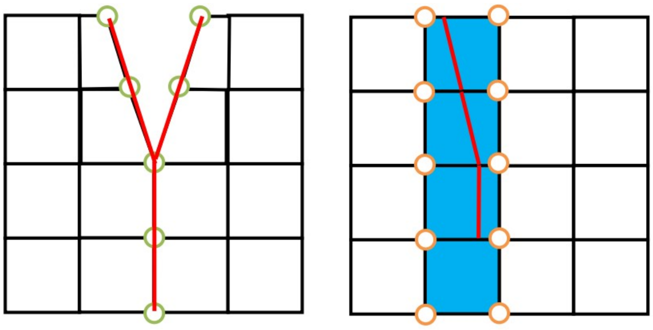

(a) (b)

Figure 2.34: Schematic of crack propagation modeling: (a) nodes and crack in FEM with cohesive zone elements (a) and (b) enriched nodes and crack in XFEM, (Modified from [136]).

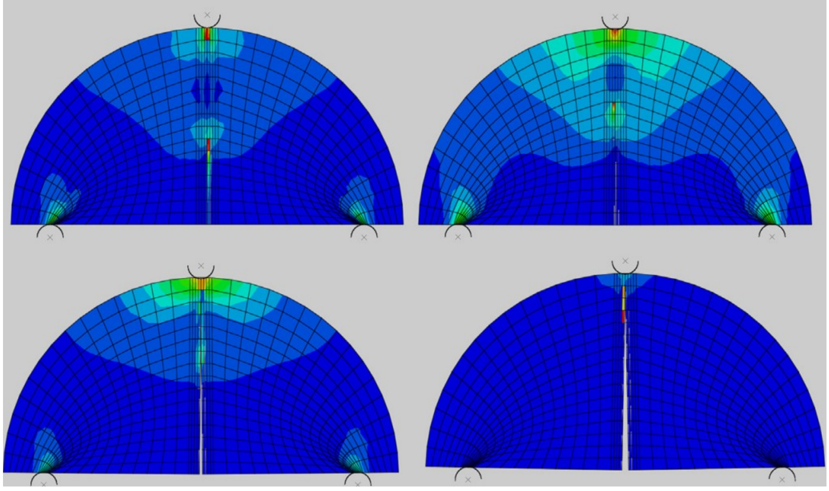

Figure 2.35: Example of crack propagation in XFEM, (Modified from [136]).

Noting the successful realization of damage distribution and localization in simulations by DEM, we now review two fatigue crack growth models for DEM, respectively proposed by Gao [101] and Nguyen [78]. Two issues will be investigated, firstly, how the model incorporates fatigue crack growth law (in these two cases, Paris' law), or how the model calculates the key fracture features (stress intensity factor K), secondly, how the model represents the change of material properties caused by crack growth.

2.6.1.1 Stress intensity factor calculation

Gao's model [101] uses the relation between stress intensity factor K and energy released rate G (Equation 2.20) to replace the ΔK in Paris' law by ΔG. The advantage of this approach is the avoidance of global variables needed in conventional formulas [108] to calculate K, such as remote stress σ, crack length a and specimen dimensions. The disadvantage is that the energy release rate G is based on the degradation process of the former contact, therefore, since this approach is non-local and crack path dependent, it is complex to implement and can not be used for distributed cracks in heterogeneous materials.

On the contrary, Nguyen [78] uses conventional formula to calculate stress intensity factor K, while the global variables in formula are replaced by a group of corresponding local variables. The idea is assuming the contact domain as a 'small plate' (Figure 2.36), thus, in the formulas for K, the remote stress is replaced by contact stress, crack length is replaced by a presumed crack length within contact domain, and contact domain dimension is also used. Such replacement allows the local model to calculate K, however, using such a ‘small plate’ to model real specimen with a macro crack has not been validated. Anyway, this model is local and can lead to a value of K only based on one contact state.

Seemingly, a local model can easily and precisely calculate the stress intensity factor, to be incorporated in Paris’ law.

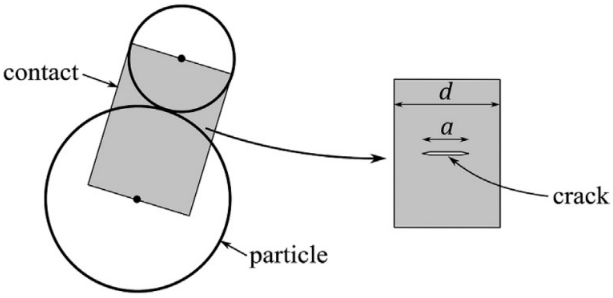

Figure 2.36: Schematic of transformation between crack and damage by Nguyen, (Modified from [78]).

2.6.1.2 Representation of crack growth

The cohesive zone model (CZM) [137] assumes that the stress distribution ahead of the crack tip is gradually increasing due to the fracture process zone (FPZ), as shown in Figure 2.37, unlike the singularity near the crack tip resulting from the linear elastic fracture mechanics (LEFM).

In the CZM, the cohesive zone consists of two cohesive surfaces ahead of the nominal crack tip, where the cohesive traction between the two cohesive surfaces is based on the distance between the two cohesive surfaces, according to the cohesive law [138] described in Figure 2.38.

The CZM is implemented into the DEM, to investigate the fracture behavior of asphalt concrete [139–141], as shown in Figure 2.39 and 2.40.

Naturally, the CZM relates the crack surface opening to the traction force. In DEM, the traction separation law can be seen as a special constitutive contact model describing the relation between contact force and contact displacement. But if we want to represent a certain crack length a or crack length increment da in DEM samples, the correspondence between the crack length a or the crack length increment da and specific mechanical properties, such as contact stiffness, contact force, contact displacement or dissipated energy, has to be established.

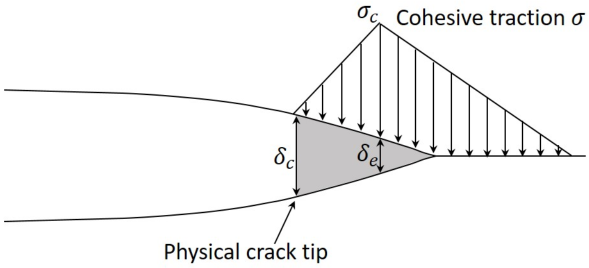
σ_c
Cohesive traction σ
δ_c
δ_e
Physical crack tip

Figure 2.37: The cohesive zone in front of a crack tip.

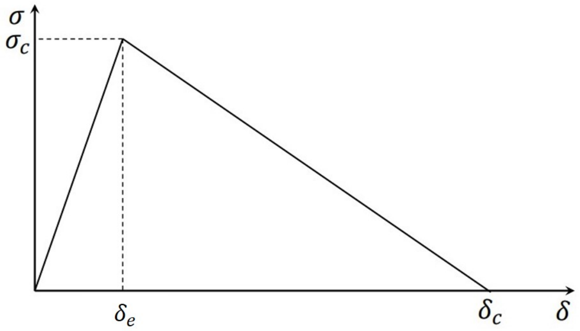

Figure 2.38: An example of the traction separation law for CZM, (Modified from [4]).

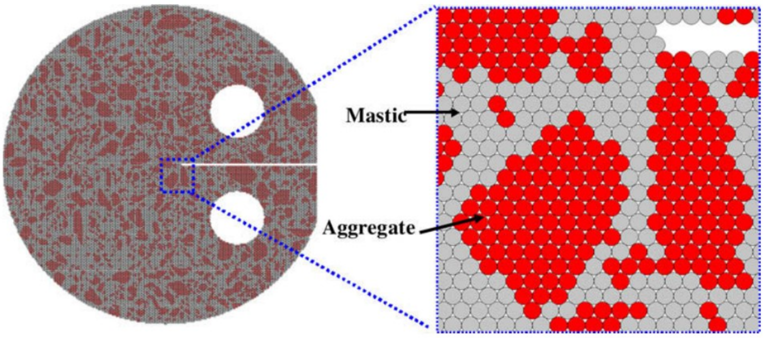
Mastic
Aggregate

Figure 2.39: DEM sample in hexagonal packing, (Modified from [140]).

Given a certain crack length increment da after a loading cycle based on fatigue law, a corresponding degradation of contact dD should happen to express such a small change on material mechanical properties due to crack growth. Gao's model does not explain such a transformation, but counts the number of loading cycles and keeps undamaged $D = 0$, then suddenly rupture (from $D = 0$ to $D = 1$) till a certain value which is determined by

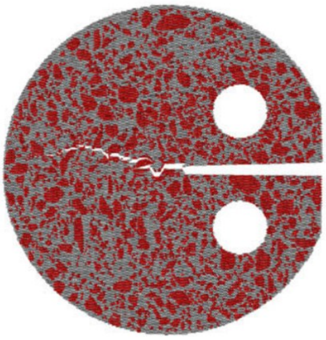

Figure 2.40: Crack trajectory resulting from CZM, (Modified from [140]).

Paris' law using energy release rate and particle size. Some simulation results are shown in Figure 2.41.

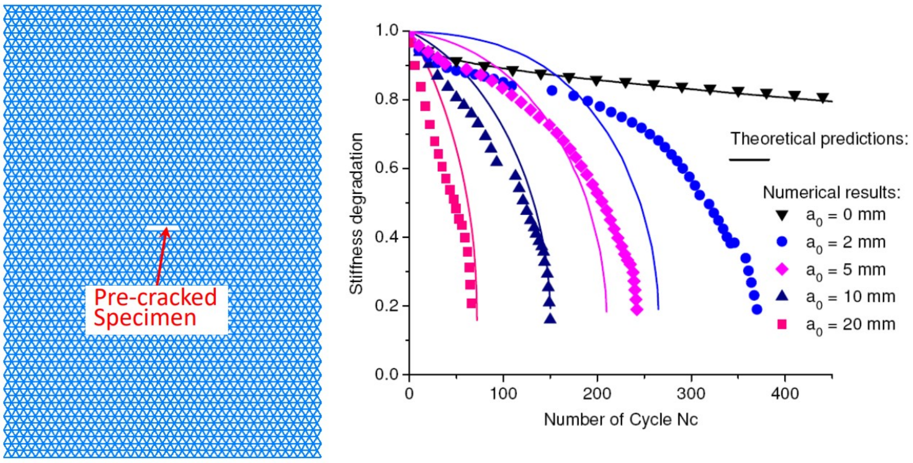

Figure 2.41: Fatigue curve for tensile simulation by Gao, (Modified from [101]).

In Nguyen's model, the contact damage level D is assumed to have a linear relationship with the presumed 'crack' length within contact domain (Figure 2.36), thus,

$$D = \frac{a}{d} \tag{2.23}$$

$$\Delta D = \frac{\Delta a}{d} \tag{2.24}$$

where the denominator d is the width of contact domain.

As shown in Figure 2.42, after every loading cycle the contact stiffness slightly decreases, consistently with the stress-displacement slope decrease. However, contact stiffness decrease and fatigue-crack-growth behavior ceases when a yield criterion is fulfilled, then the stress-displacement relation starts to follow a soften curve based on fracture behavior. When crack propagates in real materials, the crack tips may totally go through a region of material and the stress in this region may drop to zero. During such process, the stress in this region decreases, the stress intensity factor K at crack tip increases. But in Nguyen's model, when a crack almost thoroughly through a contact domain, the contact stress would close to zero, the K calculated by variables including contact stress would drop to almost zero too, which is the opposite to what happened in real crack propagation.

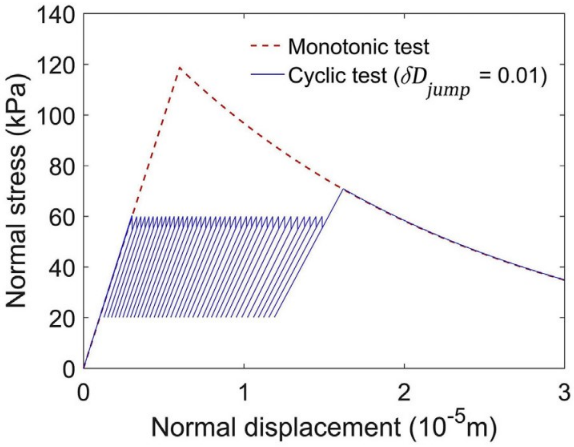

Figure 2.42: Contact stress-displacement behavior in pure cyclic tension test by Nguyen, (Modified from [78]).

The linear transformation from da to dD is pretty inspiring, nevertheless without theoretical justification. A new transformation from da to dD which can be based on a rigorous derivation and can fulfill the transformation during the whole process of crack propagating through the contact domain would be greatly helpful for fatigue simulation.

2.6.2 Transition from damage model to crack propagation

It may be difficult to use only damage model or crack growth model to describe the three phases of fatigue evolution during tests, since different physical processes dominate at different stage of fatigue, crack initiation and crack propagation. Material can not be considered as homogeneous after macro crack appearance and propagation. A transition between phase II and III has been noticed in fatigue test, and a global damage variable of specimen D_{III} was proposed to distinguish the transition [2, 142]. This variable describes the transition based on the modulus change of specimen during fatigue tests, it points out at which moment the material of the specimen becomes heterogeneous, however, a local transition method is still needed to determine when and where the macro crack occurs in the specimen domain.

A thick level set (TLS) [143] is proposed and used in XFEM, by which damaged zone and totally damaged zone (like crack) are separated by a level set, material at a distance from the front of damage zone being considered completely damaged. Such method can be considered as performing the transition from damage to fracture [79]. While the damage zone in TLS method is always a level surrounding the 'crack path' (totally damaged zone), as shown in Figure 2.43, however, due to heterogeneity of real material, damage and micro cracks may be distributed diffusely within a relatively wide region in material domain. DEM has some advantages for modeling heterogeneous micro structure of material and can easily realize distributed damage in simulation, see Figure 2.14c as an example. Nevertheless, to the author's knowledge, a transition method for DEM able to reasonably model the transition from damage model to fracture model, when and where macro cracks occur, has not been proposed.

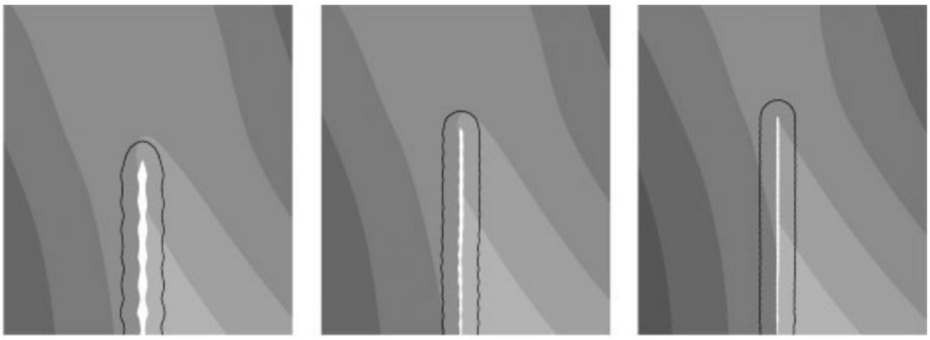

Figure 2.43: Three examples of damage zones in TLS, the black line is the front of damage zone and white zone is the fully damaged material area, (Modified from [143]).

2.6.3 Conclusion

In the above sections, damage model, cohesive zone model, crack growth model and transition method are reviewed. Common numerical methods, FEM, XFEM and DEM are compared. FEM and XFEM can to a certain extent reproduce heterogeneity and randomness of materials, but need additional operation and more complex than that in DEM. For single or a few number of cracks, FEM and XFEM can also model crack propagation with element mesh refinement or enriched nodes, but in real materials, a relatively large number of cracks occur during fatigue process. In these aspects, DEM shows great potential. Randomly packed DEM with local damage model leads to good damage distribution and initiation of localization, after that, spurious localization occurs like fracture behavior due to strain singularity near crack tip. Great efforts and advances have been made by previous researchers in fatigue crack growth model for DEM, while two issues remain to be addressed, effective approach to calculate stress intensity factor K and good transformation from computational crack increment da to contact stiffness degradation increment dD. Transition method from damage to crack propagation for DEM has still not been developed.

2.7 Summary of the chapter

Material fatigue phenomena, especially asphalt concrete, are firstly presented, and physical processes involved and corresponding fatigue evolution stages are explained using an example of 4-point bending fatigue test. Then basic fracture mechanics relevant about fatigue crack growth is mentioned as it is helpful to understand crack propagation in material. Discussion of both existing damage models and crack growth models highlights the advantage of DEM over FEM and XFEM in modeling damage distribution and localization, whilst necessitates the following three improvements in fatigue behavior simulation:

- A crack growth model which can easily and precisely incorporate fatigue evolution law, and rigorous transformation from crack increment da to stiffness loss dD to effectively represent crack growth effect on material. Such a transformation is one of the core ideas and first novelty in this research work.
- A new damage model capable of modeling the whole process of fatigue evolution including crack initiation and crack propagation.

CHAPTER 3

Contact model for fatigue crack growth

Contents

3.1 Introduction 44

3.2 Discrete element method 44

- 3.2.1 Contact behavior 44
- 3.2.2 Work at contact level 46
- 3.2.3 Isotropic Elasticity 46

3.3 Contact behavior at the crack tip 47

3.4 Contact separation - elastic case 49

- 3.4.1 Definition of the slope ratio p 49
- 3.4.2 Study of the slope ratio p 52
  - 3.4.2.1 Crack propagation strategy 53
  - 3.4.2.2 Analysis of the p ratio variations 53
- 3.4.3 Energetic analysis of the contact separation 59
  - 3.4.3.1 Energy release of a contact 59
  - 3.4.3.2 Energy release in a crack 59
  - 3.4.3.3 Energy equivalence 61

3.5 Verification of $a_c - D$ transformations 61

3.6 Contact separation - non elastic case 63

- 3.6.1 Incremental form of the crack-damage relation 64
- 3.6.2 Contact evolution scheme 64

3.7 Implementation of fatigue crack growth 67

- 3.7.1 Paris' law 67
- 3.7.2 A quasi-static approach to simulate fatigue cycles 67
- 3.7.3 Numerical procedures for the fatigue crack growth calculation in DEM 69

3.8 Summary of the chapter 3 70

3.1 Introduction

In polycyclic fatigue processes, crack increments are relatively small, much smaller than the particle scale used in simulations. In DEM for crack propagation in real conditions, the contact model should precisely quantify the effect (energetically consistent) of very small crack increment. In this chapter, the energy release of one contact is analyzed with the aim of expressing its stiffness reduction as a function of a virtual crack propagation.

3.2 Discrete element method

3.2.1 Contact behavior

A typical elastic bonded contact model is presented in Figure 3.1. The normal and tangential components of the contact force are governed by Equations 3.1, where δ_n and δ_s are respectively the normal and tangential relative displacements (with time derivatives $\dot{\delta}_n$ and $\dot{\delta}_s$), k_n and k_s are the normal and tangential stiffnesses of contact, c_n and c_s are the normal and tangential viscous damping coefficients.

$$\begin{cases} F_n = k_n\delta_n - c_n\dot{\delta}_n \\ \\ F_s = k_s\delta_s - c_s\dot{\delta}_s \end{cases} \tag{3.1}$$

To avoid disturbing viscoelastic effect, the damping parameters are smaller than values of the critical damping constant c_i (see in Appendix A) to improve the convergence in quasi static conditions without any disturbing viscous effect. In Appendix A , more details about the algorithm and numerical strategies are discussed.

The resultant contact force can be expressed as:

$$F = \sqrt{{F_n}^2 + {F_s}^2}, \tag{3.2}$$

based on normal and shear components, F_n and F_s respectively. Its orientation can be described by the angle θ defined as [4]

$$\theta = \arctan\frac{F_n}{F_s}, \tag{3.3}$$

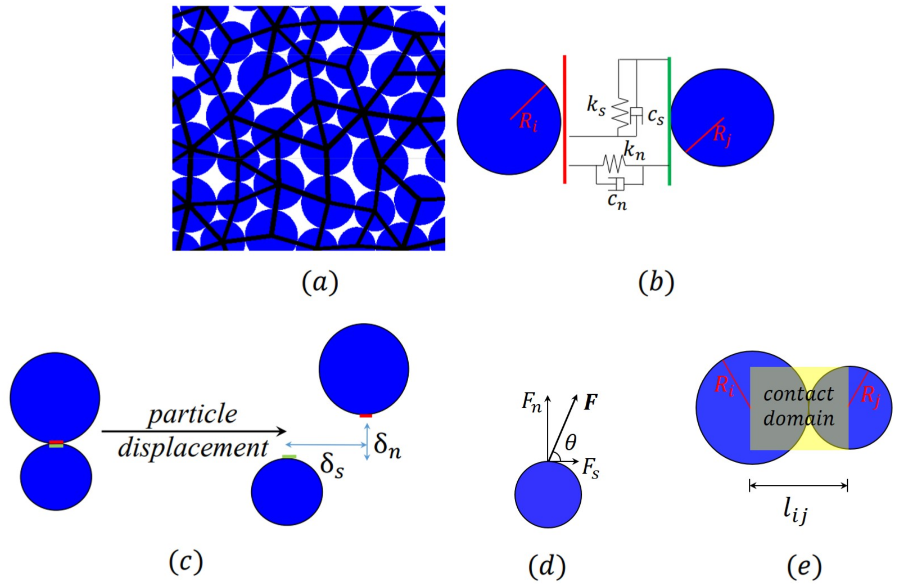

Figure 3.1: (a) Material description in DEM, where the black lines represent the contacts, and (b) their rheological representation. (c) Contact relative displacement, and (d) corresponding normal and shear forces. (e) Representation of the contact domain. (Modified from [4]).

as shown in Figure 3.1d.

The projection of the contact displacement on the direction of the resultant force F is defined by δ

$$\delta = \delta_n \sin\theta + \delta_s \cos\theta \tag{3.4}$$

The corresponding strain level of contact can be defined as

$$\varepsilon = \frac{\delta}{(R_i + R_j)}, \tag{3.5}$$

where δ is defined by Equation 3.4, R_i and R_j are the radii of two connecting particles (Figure 3.1e).

Contact stiffness degradation can be expressed by the following equations:

$$\begin{cases} k_n = k_{n0}(1-D)\delta_n \\ \\ k_s = k_{s0}(1-D)\delta_s \end{cases} \tag{3.6}$$

where D is a damage variable representing the loss of contact stiffness, k_{n0} and k_{s0} are the initial values of the normal and tangential stiffnesses.

3.2.2 Work at contact level

The work done by external force W_F can be calculated as

$$
\begin{aligned}
W_F &= \frac{1}{2}\left(F_n\delta_n + F_s\delta_s\right) \\
&= \frac{1}{2}\left(F\delta_n \sin\theta + F\delta_s \cos\theta\right) \\
&= \frac{1}{2}F\delta
\end{aligned}
\tag{3.7}
$$

where F is the resultant force defined in Equation 3.2 and δ is defined in Equation 3.4.

3.2.3 Isotropic Elasticity

To make the particle assembly (including randomly packed assembly, as shown in Figure 3.1) generally and evenly exhibit a uniformed modulus, the contact stiffness can be directly related to the contact elastic modulus E_{cmod} and the parameter k_{ratio} (ratio of the normal to shear stiffness) by the expressions [144]:

$$
\begin{cases}
k_n = \dfrac{E_{cmod}A_c}{l_{ij}} = \dfrac{E_{cmod} \times t \times 2min(R_i, R_j)}{(R_i + R_j)} \\[2ex]
k_s = \dfrac{k_n}{k_{ratio}}
\end{cases}
\tag{3.8}
$$

where the contact is supposed to behave as a prismatic bar with a cross section $A_c = 2 \times min(R_i, R_j) \times t$, length $l_{ij} = R_i + R_j$, R_i and R_j are the radii of the particles and t is the thickness of the specimen in experimentation. Calibration tests can be used to reach the elastic parameters of the material (for the isotropic case: Young's modulus E and Poisson ratio ν) [145], which may be dependent on particles granular assembly (as shown in Figure 3.2), granulometry, etc.

Analytical equations exist for ordered packing. For the square-packed sample $A_c = t \times d$, $l_{ij} = d$, d is the diameter of the particles, and $E_{cmod} = E$ which leads to

$$
k_n = k_s = Et, \tag{3.9}
$$

for $k_{ratio} = 1$.

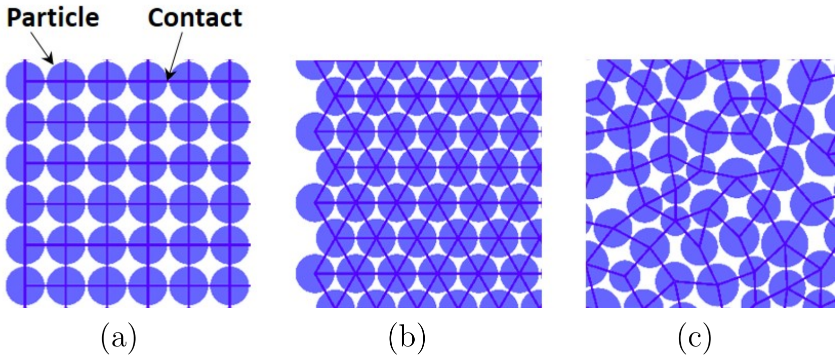

(a) (b) (c)

Figure 3.2: Particle arrangements and corresponding contact maps: (a) square-packed, (b) hexagonal packed, and (c) randomly packed.

For hexagonal packed sample, Tavarez [146, 147] established the relation between contact stiffness and material elastic parameters (Young's modulus E and Poisson ratio ν). In plane stress it corresponds to:

$$\begin{cases} k_n = \dfrac{Et}{\sqrt{3}\,(1-\nu)}, \\[2ex] k_s = \dfrac{1-3\nu}{1+\nu} k_n = \dfrac{1-3\nu}{\sqrt{3}\,(1-\nu^2)} Et. \end{cases} \tag{3.10}$$

3.3 Contact behavior at the crack tip

In order to enable the DEM to represent a crack of any length in a sample, the correlations formulated in this section work as a bridge to precisely connect the crack propagation a_c ($0 \leq a_c \leq d_c$, where d_c is the contact domain length see Figure 3.3, in this case, d_c equal to particle diameter, $d_c = d$) to the contact stiffness degradation ($0 \leq D \leq 1$). The basic idea is to establish a bijection, one-to-one correspondence, between these two quantities a_c and D.

Let us consider an example to illustrate the bijection. In Figure 3.4a, a long and rectangular plate with an initial pre-crack of length a_0 is subjected to a constant uniform stress σ, which leads to an elastic vertical displacement $\bar{\delta}_0$. The propagation Δa of the crack leads to a variation of the vertical displacement $\Delta\bar{\delta}$ (see Figure 3.4b). The progressive increase of the crack length from a_0 to $a_0+\Delta a$ is shown in Figure 3.4c. To simulate such a process, an assembly composed of monodisperse particles of diameter d organized in a bi-dimensional regular square-packed granular assembly(Figure 3.4d) is

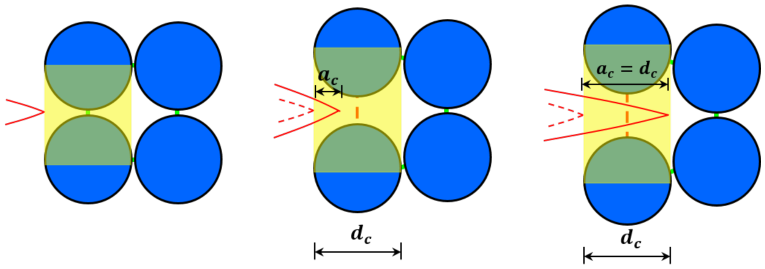
a_c
d_c
$a_c = d_c$
d_c

(a) (b) (c)

Figure 3.3: (a) Crack tip at vicinity of a contact and with crack propagation from (a) to (b) then to (c),its trajectory during the rupture of the contact described by the variable a_c ($0 \leq a_c \leq d_c$).

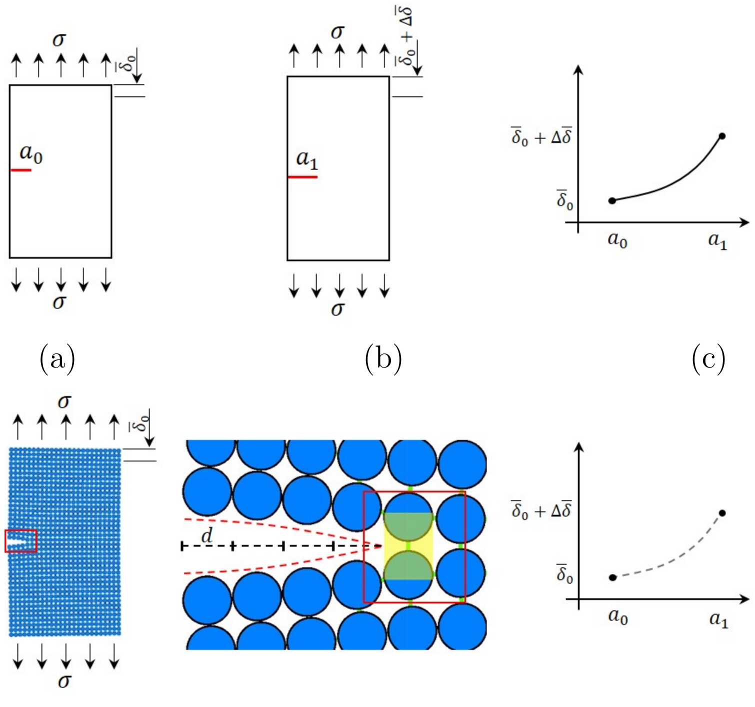
σ
$\bar{\delta}_0$
a_0
σ
σ
$\bar{\delta}_0 + \Delta\bar{\delta}$
a_1
σ
$\bar{\delta}_0 + \Delta\bar{\delta}$
$\bar{\delta}_0$
a_0
a_1
σ
$\bar{\delta}_0$
σ
d
$\bar{\delta}_0 + \Delta\bar{\delta}$
$\bar{\delta}_0$
a_0
a_1

(a) (b) (c)

(d) (e) (f)

Figure 3.4: (a) Elastic plate with initial crack a_0 under stress σ, resulting displacement $\bar{\delta}_0$ (b) effect of a crack growth (from a_0 to a_1) over the displacements versus crack length, (c) evolution of the displacement. (d) DEM corresponding sample, (e) zoom of the propagated length (d), and (f) the corresponding evolution of the displacements versus crack length.

conceptually adopted to model the elastic plate. In this example, $a_0 = 4d$, $\Delta a = d$. The crack is simply represented by four contacts which were cut off. The propagation of the crack is represented in this case by cutting the fifth contact (clearly represented in Figure 3.4e). It can make the crack a "jump" forward. However the continuity of the process of rupture remain dependent on the contact rupture (as suggested in Figure 3.4f).

In order to specifically characterize the rupture process of one contact, the mechanical effect of the virtual propagation of the crack tip through a distance d_c, defined as the contact domain, is analyzed. The length d_c corresponds to the crack tip displacement if the contact is cut off. Gradually, the displacement of the crack tip, defined by the length a_c ($0 \leq a_c \leq d_c$ as shown in Figure 3.3), induces a reduction of the stiffness of the contact. One may adopt a state variable D ($0 \leq D \leq 1$) to describe this degradation of stiffness of the contact concerned by the crack tip propagation process. No propagation process is observed for $a_c = 0$, which is automatically related to an intact contact ($D = 0$). On the other hand, if $a_c = d_c$, the crack tip has propagated and cut the contact off ($D = 1$).

A consistent relation between the crack tip propagation a_c and the stiffness degradation D allows the discrete model to define crack displacement smaller than the dimension of the particles composing the material. In the following sections, a relation $a_c - D$ based on the energy balance of a contact is proposed.

3.4 Contact separation - elastic case

3.4.1 Definition of the slope ratio p

The first element to understand the relation between the crack propagation and the degradation process of the contact at the crack tip in DEM sample is the evolution of the force and the displacements. If only the contact at the crack tip is released ($0 \leq D \leq 1$), in elastic conditions, the material surrounding the crack tip behaves as an elastic system. By simplicity, let us replace the surrounding material by an elastic spring representing the material elasticity k_p, as proposed in Figure 3.5. If one considers the rupture process in the opposite way, where the contact force may close the crack, the individual action of the contact force associated to crack tip may reduce the gap between the two particles linearly. In the natural way, a decreasing value of $F = \delta(1 - D)k_0$ may simply increase proportionally the distance between the two particles (described by δ), which explains the observed linear path during the rupture process ($0 \leq D \leq 1$), as shown in Figure 3.6.

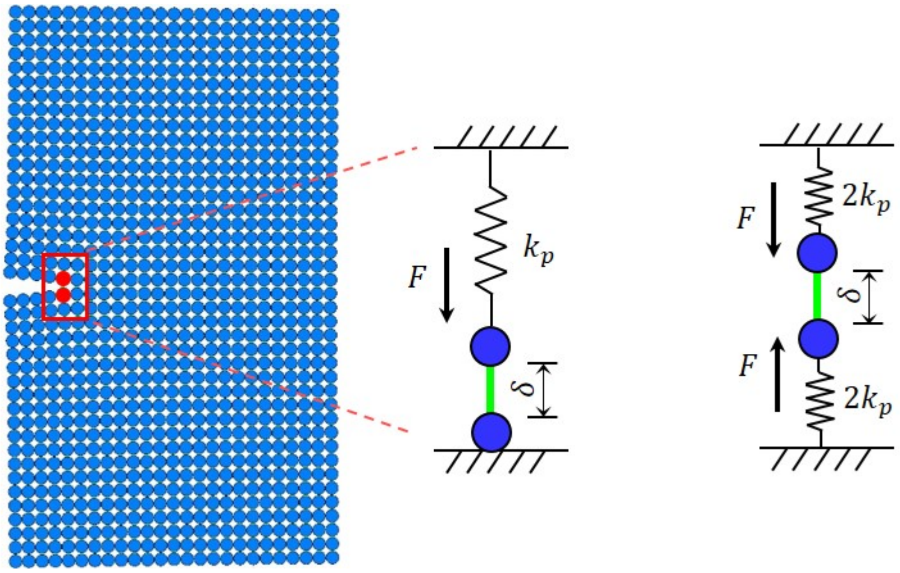

(a) (b) (c)

Figure 3.5: Schematic description of the mechanical relation between the contact at the crack tip and the neighboring particles. (a) Pre-cracked plate and (b) its simplified elastic behavior near the crack tip, where k_p represents the stiffness of material surrounding the crack tip, F and δ are contact force and displacement, (c) a more intuitive description of (b).

In Figure 3.6, a contact which represents a part of material of a plate is described by both spring systems and the evolution of contact force F and displacement δ in the coordinate system. And four states are chosen, specifically, (o) a pre-cracked plate without loading, (A) plate subjected to a constant stress σ, (B) crack propagates till the boundary of the contact domain, (C) crack totally through the contact domain. Obviously, the maximum elastic force, right before the rupture process of the contact (process from (B) to (C)) is equal to $F_{max} = k_0 \delta_0$. For this same force F_{max} acting over the spring $2k_p$, the displacement associated to the material surrounding material is simply $\delta_p = F_{max}/k_p$. After the progressive rupture process, the force decrease from F_{max} to 0 following the rupture slope k_p and the surrounding material spring is no longer in tension. The total increase of the broken contact is finally $\delta_{max} = \delta_0 + \delta_p = \delta_0(1 + k_0/k_p)$, when $F = 0$.

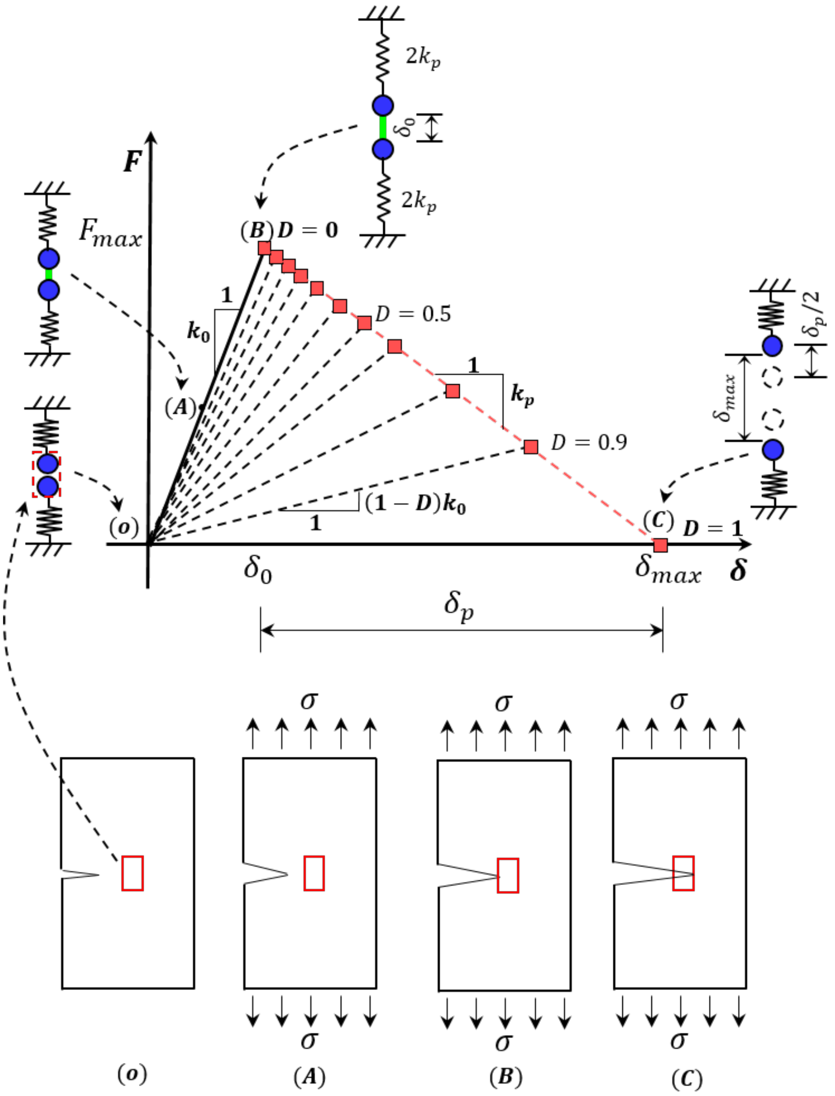

Figure 3.6: Description of the evolution of a contact for the whole process from crack near to crack through this contact. At the bottom of figure, (o) a pre-cracked plate in which a red rectangular represents the contact whose behavior is described by both spring systems and the evolution of contact force F and displacement δ in the coordinate system, (A) plate subjected to a constant stress σ, (B) crack propagates till the boundary of the contact domain, (C) crack totally through the contact domain. From (B) to (C), crack growth within the contact domain is represented by the process of the contact stiffness degradation, for $(0 \leq D \leq 1)$, where k_0 is the initial contact stiffness, and $(1 - D)k_0$ is its degraded value.

Let us define the slope ratio p as the ratio between the elastic slope k_0 and k_p the absolute value of the rupture slope, that is $p = k_0/k_p$. Physically, the slope ratio p is a quantity which characterizes the relation between the stiffness of the contact and the stiffness of its vicinity. It means that the slope ratio p account for the effect of the surrounding material on the crack tip.

To describe the change of crack position and contact displacement with crack propagation, Figure 3.7 shows two states of crack position and contact displacement, respectively referring to the states (B) and (C) in Figure 3.6.

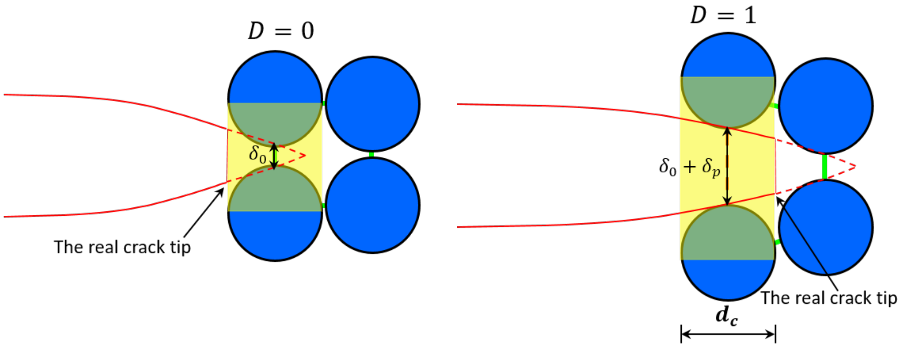

(a) (b)

Figure 3.7: Schematic description of the position of crack and contact displacement. (a) Crack tip at the boundary of the contact domain, where δ_0 is the contact displacement, and (b) crack totally through the contact domain.

For the proposed method which represents crack propagation, when compared with CZM, a major similarity and a major difference between them should be mentioned. Both of them using gradual change of mechanical property of element ahead a crack tip to represent crack propagation. For CZM, the separation is governed by the deformation δ which follows an artificially defined softening curve (Figure 2.38). Importantly, for the method discussed above, as shown in Figure 3.6, the separation is only governed by the contact stiffness degradation, and the softening curve is not defined but forming naturally. That is the biggest difference between them two.

3.4.2 Study of the slope ratio p

In the following analysis, one may observe the effect of the crack length, crack distribution, loading condition and particle size on the slope ratio p.

3.4.2.1 Crack propagation strategy

To continually observe the rupture process at the crack tip, the crack propagation is performed by orderly releasing contacts (for each contact, $0 \leq D \leq 1$) in the crack growing direction, in samples, as shown in Figure 3.8. For symmetric edge cracks (Figure 3.9) and center crack (Figure 3.10), contact degradation is symmetrically and synchronously operated.

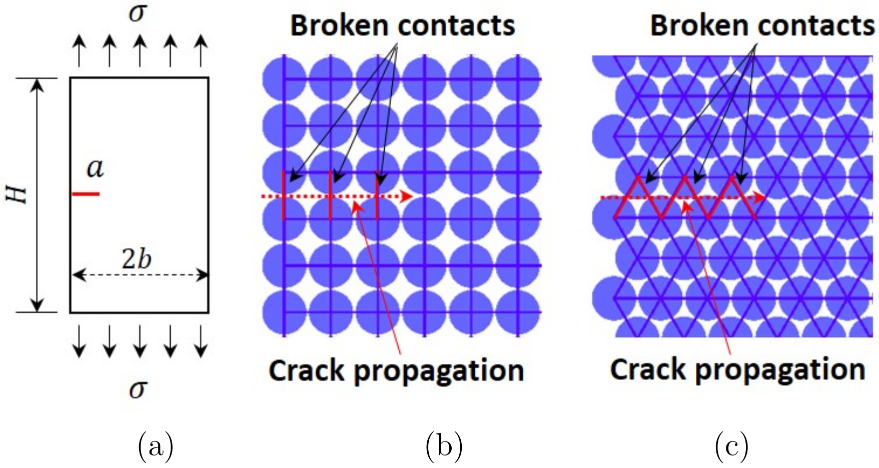

(a) (b) (c)

Figure 3.8: (a) Geometry of the plate, crack propagation modeling in (b) square and (c) hexagonal packed samples.

Crack propagation is performed on plates with height $H = 160\ mm$, width $2b = 100\ mm$ and unitary thickness ($t = 1\ m$). The material Young's modulus $E = 10$ GPa, subjected to constant vertical stress $\sigma = 0.625$ MPa, Figure 3.8a. In plane stress the Poisson ratio ν is not relevant (Section 2.5.5).The crack grows from $a = 0$ to $a/2b = 0.8$. Three different particle diameters are tested 0.5 mm, 1 mm and 2 mm.

For square packed samples, the elastic stiffness is $k_n = 1 \times 10^{10}\ N/m$ as defined in Equation 3.9. Then, for simplicity and without effects on the results, $k_s = k_n$.

For hexagonal packed samples, the elastic stiffness is $k_n = 5.77 \times 10^{9}\ N/m$ as defined in Equation 3.10. A value of $k_s = k_n$ is also chosen, associated to a Poisson ratio $\nu = 0$.

3.4.2.2 Analysis of the p ratio variations

In Figures 3.9 and 3.10, the variations of the slope ratio p as a function of the crack length to plate width ratio a/b during crack initiation and subsequent

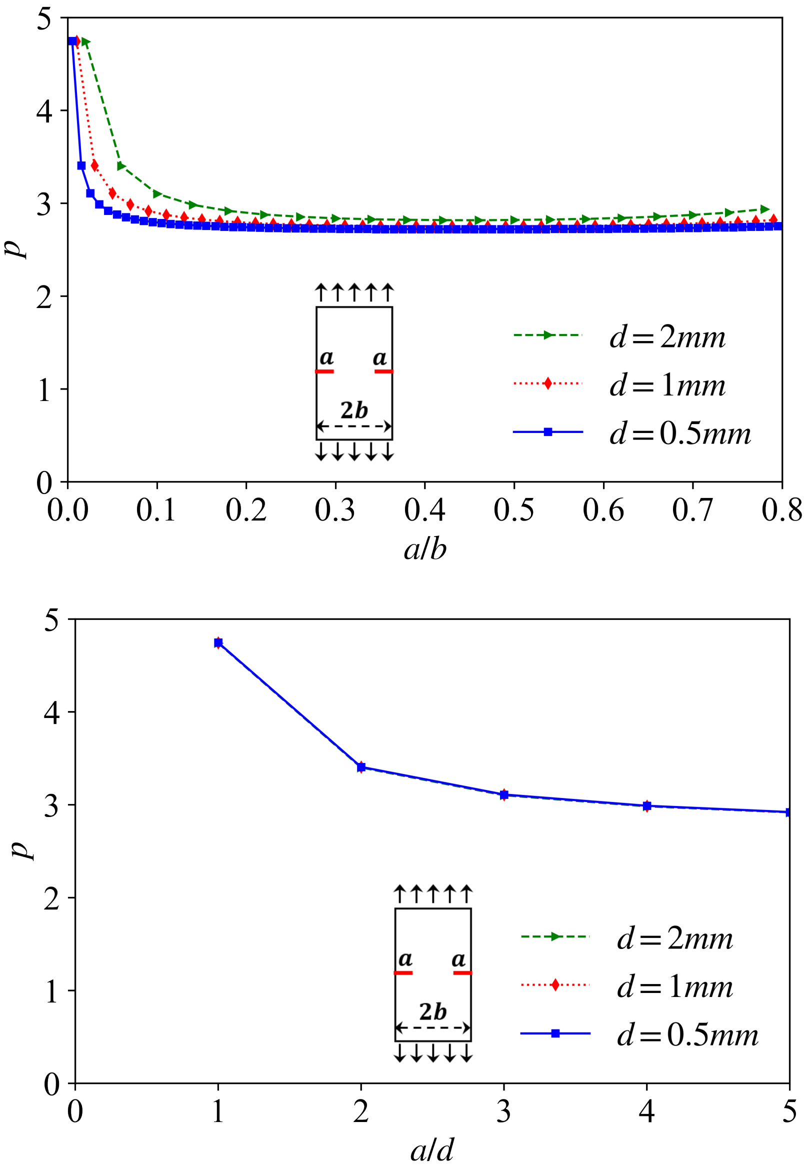

(a)

(b)

Figure 3.9: (a) Value of the slope ratio p as a function of the length to plate width ratio a/b for different particle diameters ($0.5\,mm \leq d \leq 2\,mm$) of a plate with symmetric edge cracks, simulated by square packed samples and (b) a zoom of the values of p as a function of the crack to diameter ratio a/d during crack initiation $a/d \leq 5$.

propagation are presented. For well developed cracks ($a/b \geq 0.1$), a stable p value can be observed. The effect of the diameter of the particles is mostly

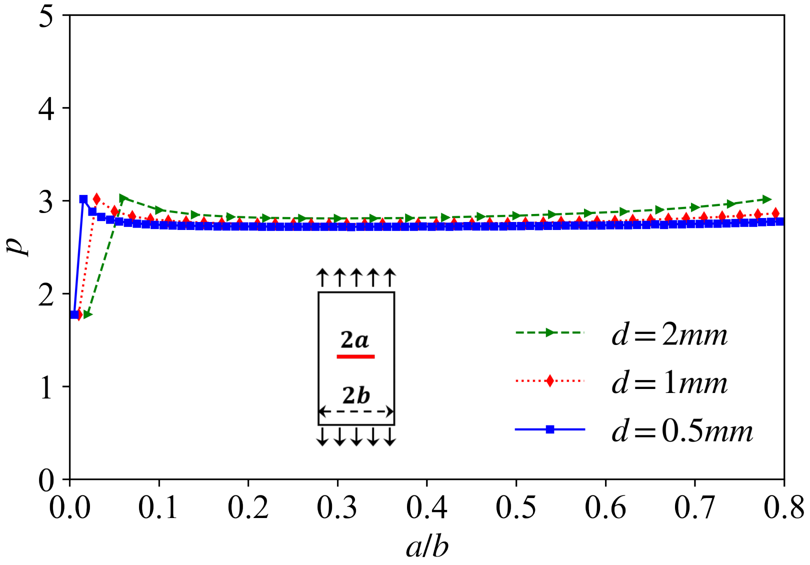

(a)

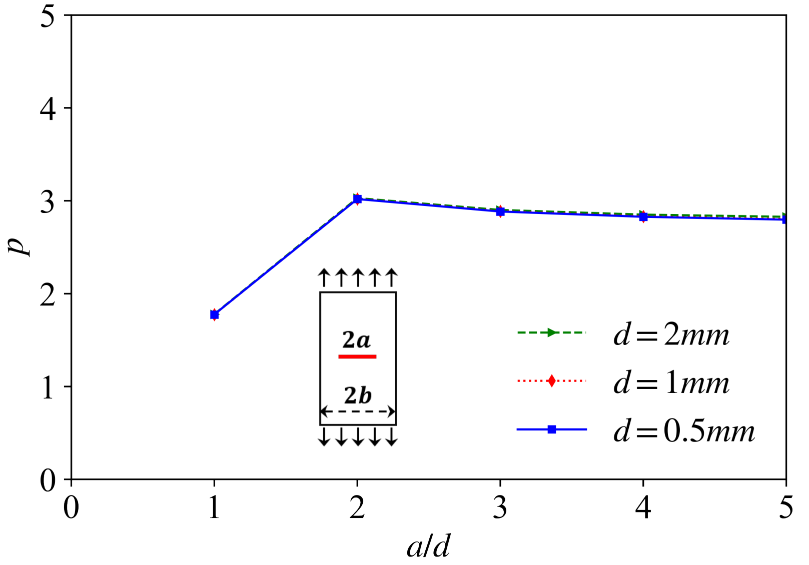

(b)

Figure 3.10: (a) Value of the slope ratio p as a function of the crack length to plate width ratio a/b for different particle diameters $(0.5\,mm \leq d \leq 2\,mm)$ of a plate with center crack, simulated by square packed samples and (b) a zoom of the values of p as a function of the crack to diameter ratio a/d during crack initiation $a/d \leq 5$.

due to a more precise definition of the crack tip for smaller particles, where the value of p get stable earlier for smaller particle. The value of p is specially affected during crack initiation where the stress conditions passes from homogeneous (no crack) to singular state (with crack) at the crack tip. This evolution seems more dependent on the number of particles which represents the relative crack length than absolute length as suggested by the results of p as a function of the crack length to diameter ratio a/d (see Figures 3.9b and 3.10b).

The comparison between the values of p for the plates with central and symmetric edge cracks (Figure 3.11) confirms that for fully developed cracks a stable value of p is observed, which only depends on particle packed structures.

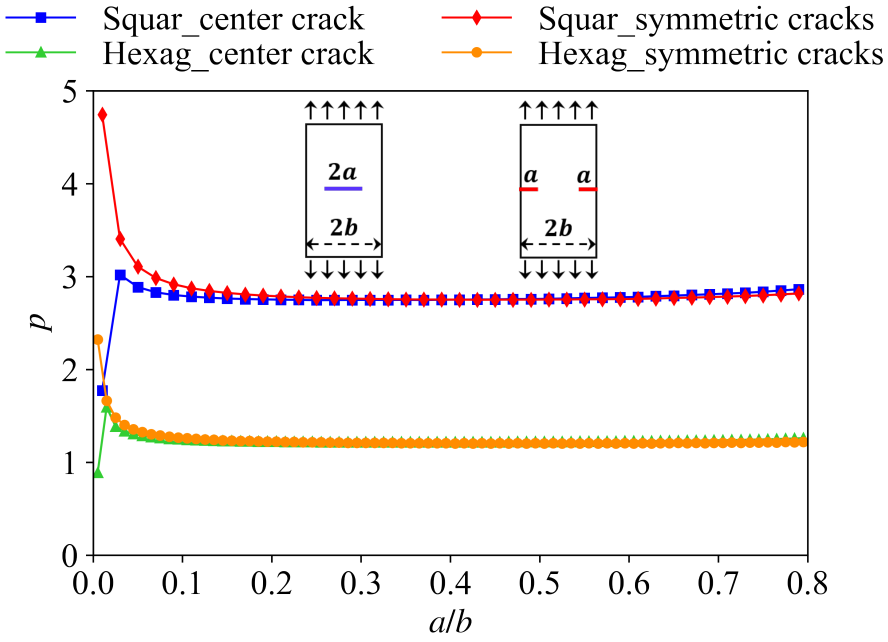

Figure 3.11: Comparison of p as a function of the crack length to plate width ratio a/b, for center crack and symmetric edge cracks propagation, result from respectively square and hexagonal packed samples, with diameter $d = 1mm$.

Figures 3.12 shows the effect of loading condition on the value of p for different crack lengths and at different vertical positions. For well developed cracks, when the crack positions are far from the loading boundary, the loading conditions have only slight effect on the value of p, which is described more clearly in Figure 3.13.

Based on the definition of the slope ratio p, geometrically, the limitation of p is $0 \leq p \leq \infty$. Physically, $p = 0$ and $p = \infty$ respectively correspond to

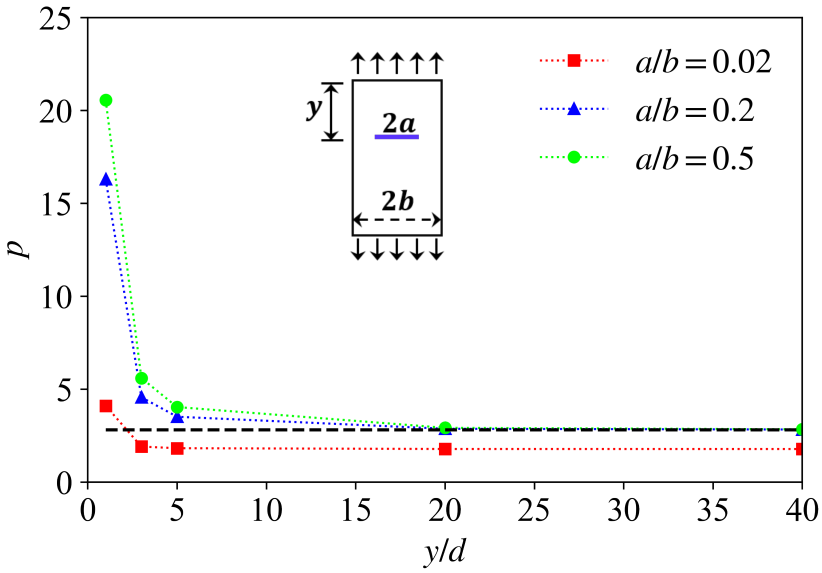

(a)

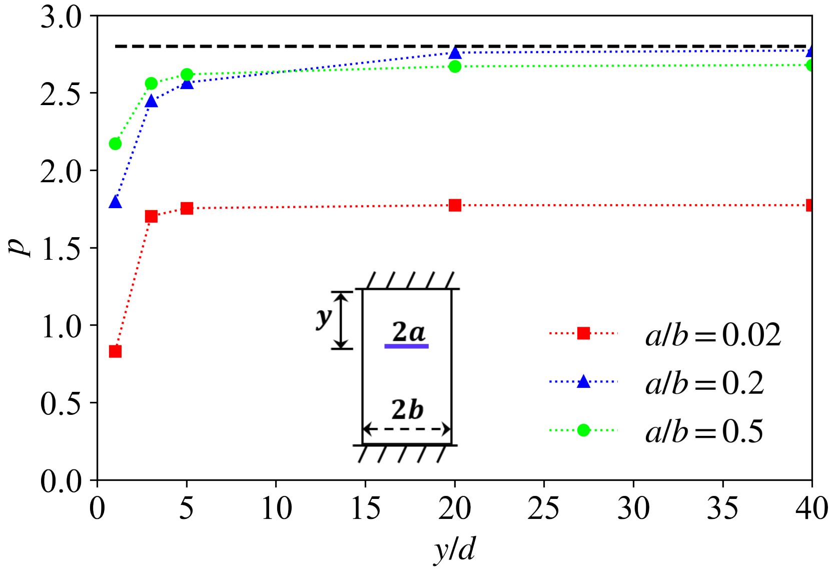

(b)

Figure 3.12: Value of the slope ratio p for crack at different vertical positions (y/d, where y is the distance from loading boundary and $d = 2\,mm$ is particle diameter) and with different crack length (a/b), (a) with imposed stress and (b) with imposed strain ($\varepsilon = 100\,\mu\varepsilon$). The black dashed line represents $p = 2.8$ in both (a) and (b).

the homogeneous and ultimate states of materials, as shown in Figure 3.14. As an example, one may notice that in Figure 3.13 when the crack is small,

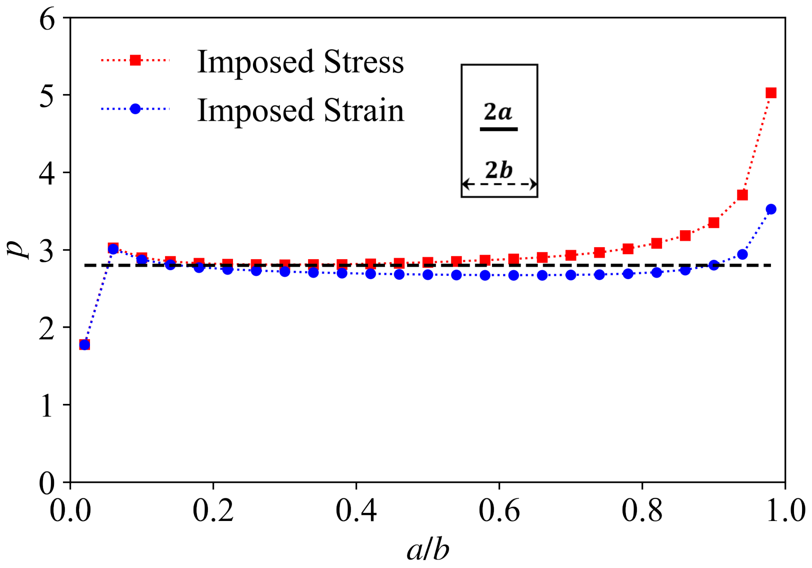

Figure 3.13: Comparison of the slope ratio p as a function of the crack length to plate width ratio a/b, for center crack, (a) with imposed stress and (b) with imposed strain ($\varepsilon = 100\,\mu\varepsilon$). The black dashed line represents $p = 2.8$.

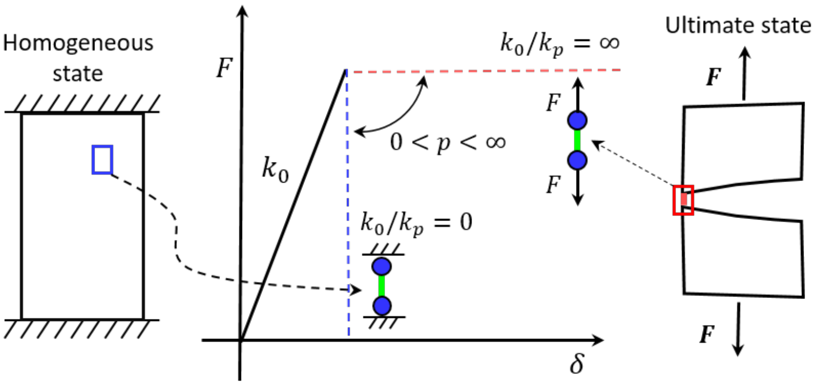
Homogeneous state
F
k_0
$k_0/k_p = \infty$
$0 < p < \infty$
$k_0/k_p = 0$
F
F
Ultimate state
F
F
δ

Figure 3.14: Schematic description of the limitation of the slope ratio p, for $p = 0$ corresponding to the homogeneous state and $p = \infty$ corresponding to the ultimate state.

the value of p tends to be lower than its stable value for well developed crack, and when the crack is almost cutting off the plates, p tends to increase dramatically.

3.4.3 Energetic analysis of the contact separation

In this section, the relation between the propagated crack length and stiffness reduction $a_c - D$ is formulated with the energy equivalence between the released energy during DEM contact degradation (damage) and cracking of physical material.

3.4.3.1 Energy release of a contact

The partial energy released during the contact separation process U_B can be calculated (as already discussed in Section 2.5.4) as the surface area of the triangle formed by the origin point $O\,(0,0)$, point $A\,(\delta_0, F_0)$ representing coordinated by the contact force and contact displacement before degradation, and point $B\,(\delta_i, F_i)$ representing coordinated by the contact force and contact displacement after degradation of the stiffness, as shown in Figure 3.15a. That is to say $U_B = S_{\Delta OAB}$. The total energy released by the contact corresponds to $U_C = S_{\Delta OAC}$.

The ratio U_B/U_C can be calculated by

$$\frac{U_B}{U_C} = \frac{S_{\Delta OAB}}{S_{\Delta OAC}} = \frac{S_{\Delta OAC} - S_{\Delta OBC}}{S_{\Delta OAC}} = 1 - \frac{F_i}{F_0} = 1 - (1-D)\frac{\delta_i}{\delta_0}, \tag{3.11}$$

where $F_0 = k_0\delta_0$ and $F_i = (1-D)k_0\delta_i$.

The length of the bottom line $\overline{OC}$, can be geometrically obtained based on δ_0 or δ_i by the relation $\overline{OC} = \delta_0(1+p) = \delta_i(1+p(1-D))$ (where $p = k_0/k_p$). Introducing the consequent ratio δ_i/δ_0 into Equation 3.11, one gets the ratio U_B/U_C

$$\frac{U_B}{U_C} = 1 - (1-D)\frac{1+p}{1+p(1-D)} = \frac{1-(1-D)}{1+p(1-D)}. \tag{3.12}$$

3.4.3.2 Energy release in a crack

The released energy in cracking process can be described by the energy release rate $G = dU/dA$ (see Section 2.5.4) defined as the released energy dU per unit of crack area increment dA (in 2D, $dA = t \times da$, where t is the thickness of the geometry, see Figure 3.15b). Integrating Equation 2.12, the released energy during crack growth U_{ac}, can be calculated as

$$U_{ac} = t\int_0^{a_c} G\,da \approx tGa_c. \tag{3.13}$$

It should be noted that the energy release rate G is supposed to remain constant during crack growth at the scale of a contact ($0 \leq a_c \leq d_c$). This

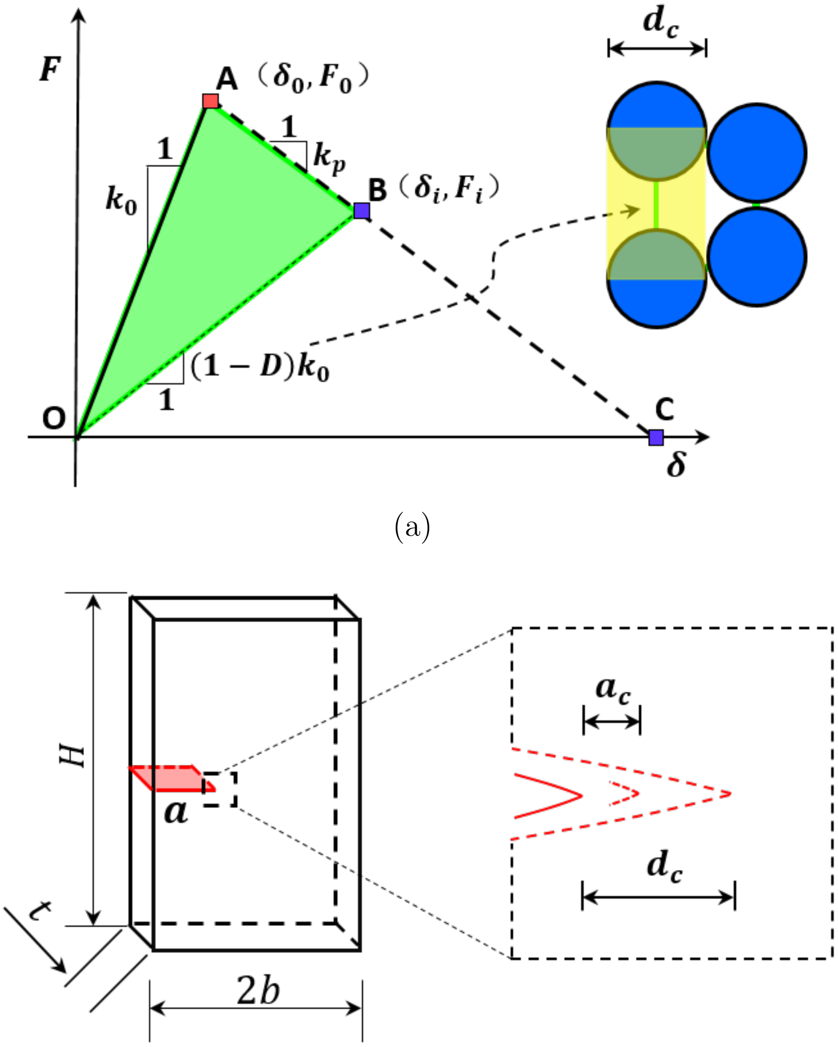

(a)

(b) (c)

Figure 3.15: (a) Released energy during contact degradation. (b) Cracked plate, and (c) zoom of the crack propagation at the scale of one contact.

hypothesis is a simplification of the real process, where some variation may exist, specially during crack initiation. Consequently, the total released energy (for a crack growth $a_c = d_c$) is simply equal to

$$U_{dc} = tGd_c. \tag{3.14}$$

Combining Equations 3.13 and 3.14, yields the energy ratio U_{ac}/U_{dc}

$$\frac{U_{ac}}{U_{dc}} = \frac{a_c}{d_c}. \tag{3.15}$$

3.4.3.3 Energy equivalence

The equivalence of the energy released in a crack and in a contact for the same propagated length can be obtained by combination of Equations 3.12 and 3.14, where one may get by definition $U_B/U_C = U_{ac}/U_{dc}$. It finally leads to the correspondences between a_c and D

$$\frac{a_c}{d_c} = \frac{1-(1-D)}{1+p(1-D)}, \tag{3.16}$$

or conversely

$$1-D = \frac{1-\dfrac{a_c}{d_c}}{1+p\dfrac{a_c}{d_c}}. \tag{3.17}$$

Equations 3.16 and 3.17 provide a direct relation between the crack propagation and damage in a contact ($0 \leq a_c/d_c \leq 1$ in compliance with $0 \leq D \leq 1$). All information is entirely defined at contact level (properties k_0 and d_c) or measured during contact separation ($F \times \delta$) like k_p (which leads to $p = k_0/k_p$). This explicit local approach of the energy release allows the direct application of fracture mechanics models to simulate the crack propagation as it will be seen in the next sections.

3.5 Verification of $a_c - D$ transformations

The energy released by cracks in simple structures is precisely related to boundary behavior, which can be adopted to verify the $a_c - D$ transformations (in Equations 3.16 and 3.17).

A simple rectangular plate with dimensions (height $H = 160$ mm, width $2b = 100$ mm and unitary thickness t) under uniform stress $\sigma = 0.625$ MPa is considered as shown in Figure 3.16a. The material Young's modulus $E =$ 10 GPa. Before cracking, it simply presents an elastic boundary displacement $\bar{\delta}_0$. The boundary displacement for $\bar{\delta}$ (see Figure 3.16b can be theoretically calculated for any crack dimension based on existing solutions for the stress intensity factor (as shown in Appendix C).

In Figure 3.17a, the theoretical results of the ratio between the boundary displacements $\bar{\delta}/\bar{\delta}_0$ is presented as a function of the crack length $0 \leq a/2b \leq 0.5$. For comparison purpose, contacts are progressively released ($0 \leq D \leq 1$) in three simulations with a square packed sample with $d = 0.5$ mm, 1 mm and 2 mm, corresponding to $0.2 \leq a/2b \leq 0.22$. The proximity of the scale of

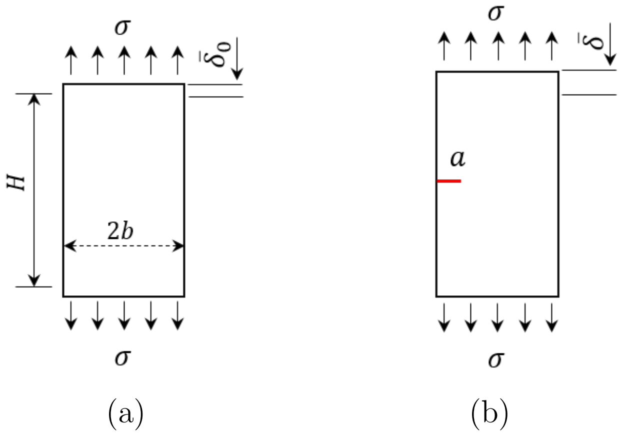

Figure 3.16: Plate under uniform stress and the associated boundary displacement for (a) intact and (b) cracked cases.

the simulated displacements with respect to theory (in Figure 3.17a) confirms the ability of the discrete model to describe the mechanical behavior of the system.

The effect of the $a_c - D$ transformations can be clearly observed in Figure 3.17b. For $d = 2\ mm$, the trend for the displacement ratio $\bar{\delta}/\bar{\delta}_0$ of the simulation is parallel and follows closely the theoretical results, for a single contact release. The offset between simulations and theory decreases with particle diameter d, which is consistent with the mechanical hypothesis considered (energy release rate G is assumed constant during crack crossing one contact). Thus, particle diameter decrease naturally results higher precision of G with respect to theoretical calculation. For $d = 1\ mm$ and $d = 0.5\ mm$, 2 and 4 contacts are released respectively. A clear continuity of $\bar{\delta}/\bar{\delta}_0$ is observed, which indicates that cracks can be described bellow a particle scale with the proposed formulation (in Equation 3.17).

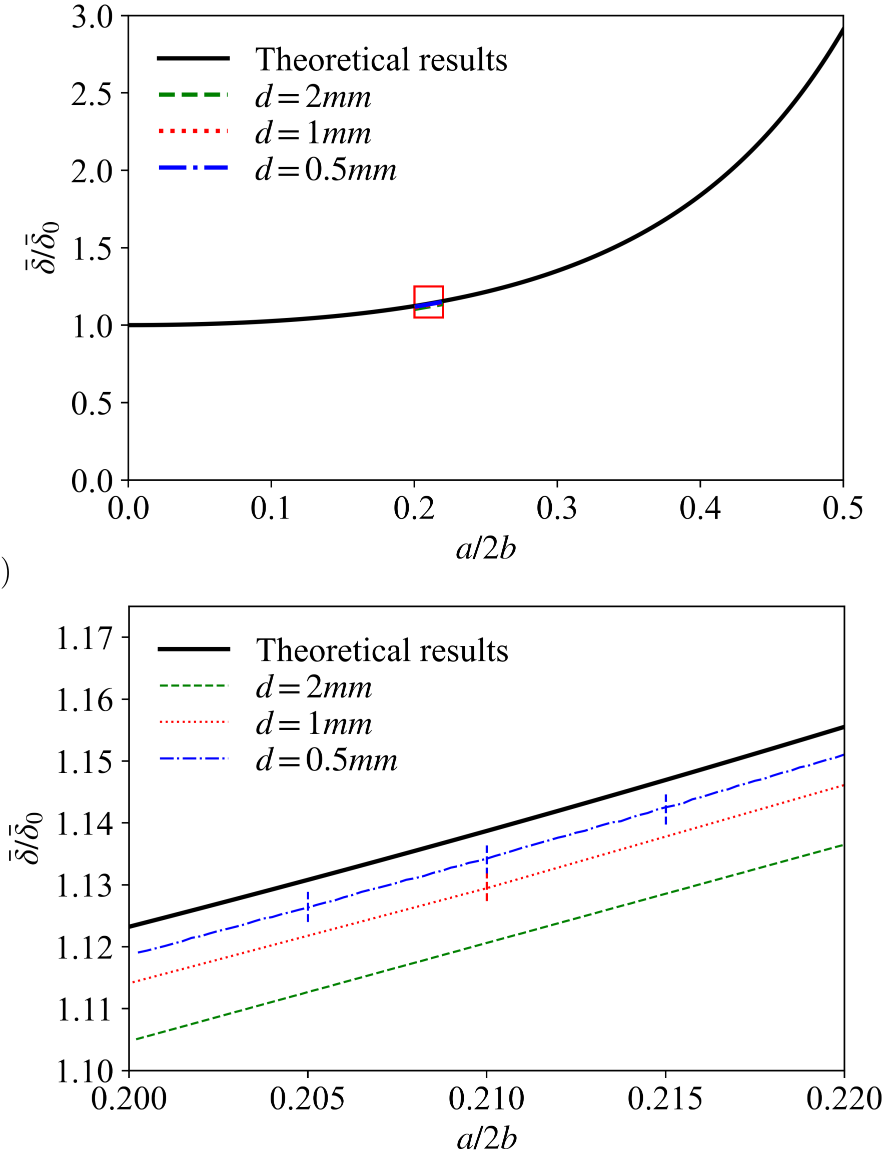

(a)

(b)

Figure 3.17: (a) Comparison of the ratio of displacement $\bar{\delta}/\bar{\delta}_0$ between theoretical results and simulation results and (b) a zoom for $0.2 \leq a/2b \leq 0.22$.

3.6 Contact separation - non elastic case

The $a_c - D$ relation described in Equations 3.16 and 3.17 supposes a constant separation slope (constant p), which is reasonable for elastic structures with cracks that do not interact, hence do not modify the mechanical response close to the crack tip from one to another. Any non linear behavior of the material which reduces its stiffness (like damage) or the proximity of cracks which modifies the boundary conditions near a crack tip may affect the value of p (see discussion in Section 3.4.1). The general situation described in Figure 3.18 is considered in this section, where an incremental form of $a_c - D$ is proposed.

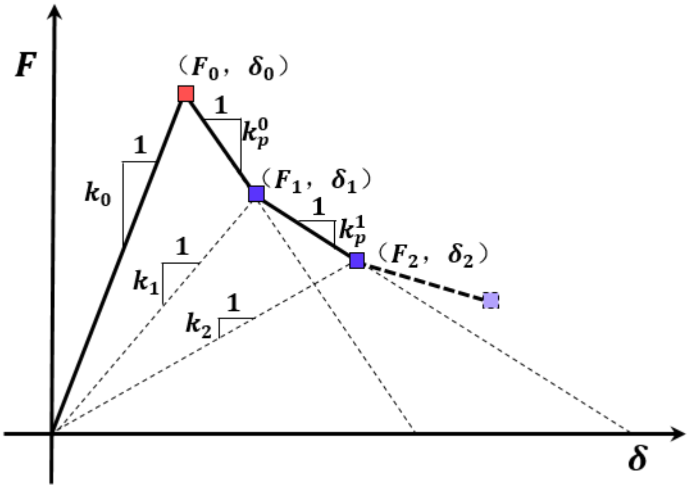

Figure 3.18: Schematic description of nonlinear contact traction separation.

3.6.1 Incremental form of the crack-damage relation

In an incremental formulation, increments of crack propagation da are associated to increments of damage dD. The crack evolution and the damage evolution may be written as

$$\begin{cases} a_{ci+1} = a_{ci} + da \\ D_{i+1} = D_i + dD \end{cases} \tag{3.18}$$

where i describes the propagation events. Figure 3.19 schematically shows the relation between the direct and the rate formulations.

3.6.2 Contact evolution scheme

The deduction of the relation $da - dD$ is based on the scheme shown in Figure 3.20a, where the incremental propagation of the crack is described by events where p remains constant piece by piece. The stiffness reduction of

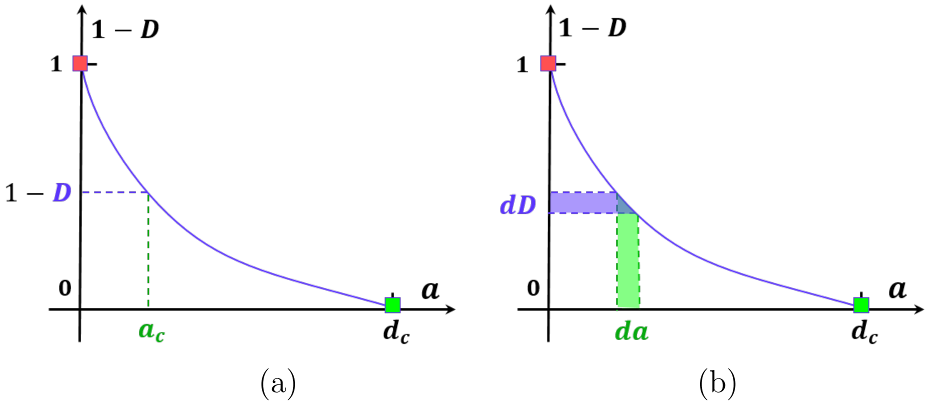

Figure 3.19: Transformations (a) between a_c and D, (b) between da and dD.

the contact induced by the crack propagation can be seen after each event as a new contact. As represented in Figure 3.20b at the beginning of each propagation event, one may suppose an initial contact stiffness k_i for a contact with a reduced domain $d_c - a_{ci}$. After a propagation da an apparent stiffness reduction dD' is observed, with the new contact stiffness $k_{i+1} = (1 - dD')k_i$ and an apparent slope ratio $p' = k_i/k_{pi}$. These elements can be automatically introduced in Equation 3.16, which takes the following shape

$$\frac{da}{d_c - a_c} = \frac{1 - (1 - dD')}{1 + p'(1 - dD')}. \tag{3.19}$$

The final step is to adapt the apparent parameters (dD' and p', defined with respect to the stiffness k_i) to the parameters defined with respect to the initial contact stiffness k_0 (dD and p).

The apparent stiffness reduction is defined by

$$1 - dD' = \frac{k_{i+1}}{k_i} = \frac{(1 - D_{i+1})k_0}{(1 - D_i)k_0} = \frac{(1 - D_{i+1})}{(1 - D_i)}, \tag{3.20}$$

where $k_i = (1 - D_i)k_0$ and $k_{i+1} = (1 - D_{i+1})k_0$. The evolution of the stiffness reduction given in Equation 3.18 can be introduced in Equation 3.20. After some algebraic work isolating dD', one may have

$$dD' = \frac{dD}{1 - D_i}. \tag{3.21}$$

The apparent slope ratio p' is defined as

$$p' = \frac{k_i}{k_{pi}} = \frac{(1 - D_i)k_0}{k_{pi}} = (1 - D_i)p_i. \tag{3.22}$$

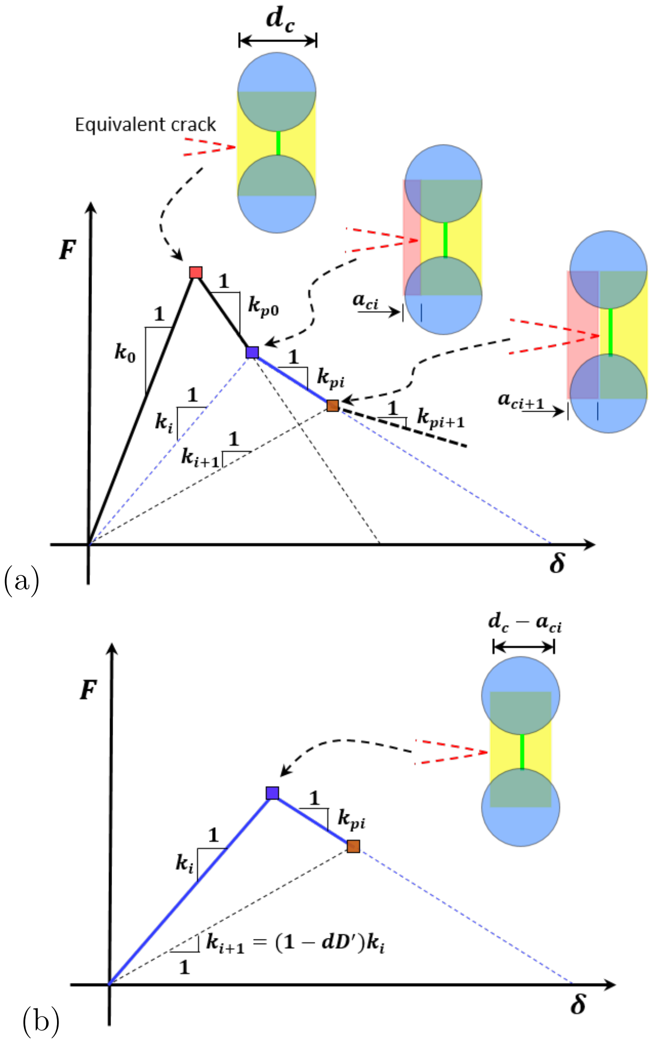
d_c
Equivalent crack
F
1
k_{p0}
1
k_0
a_{ci}
1
k_{pi}
1
k_i
1
k_{i+1}
a_{ci+1}
1
k_{pi+1}
δ
(a)
$d_c - a_{ci}$
F
1
k_{pi}
1
k_i
$k_{i+1} = (1 - dD')k_i$
1
δ
(b)

Figure 3.20: (a) Description of the contact and force-displacement evolution during a propagation event, (b) a certain state in (a).

Replacing Equations 3.21 and 3.22 into Equation 3.19, one may finally get

$$da = \frac{(d_c - a_c)dD}{(1 - D)[1 + p(1 - D - dD)]}, \tag{3.23}$$

or conversely

$$dD = (1 - D)\left(1 - \frac{\left(1 - \dfrac{da}{d_c - a_c}\right)}{1 + p(1 - D)\left(\dfrac{da}{d_c - a_c}\right)}\right), \tag{3.24}$$

where the index i was dropped.

The rate relation $da - dD$ allows the direct relation between a crack increment da and stiffness degradation increment dD, for a given instantaneous slope ratio p and stiffness degradation D. Equation 3.24 associated to Equation 3.18, allows a continuous description of the relation between a_c and D.

3.7 Implementation of fatigue crack growth

The transformation $da-dD$ allows an energetically consistent representation of a crack propagation caused by contact damage over a length smaller than the particle scale. Paris' law is a fatigue criterion which relies on the energy release per cycle to determine how much a crack propagates.

3.7.1 Paris' law

As introduced in Section 2.5.6, Paris' law is a fatigue crack growth criterion in which the crack increment during one loading cycle da is determined by a power function of the corresponding stress intensity factor range $\Delta K = K_{max} - K_{min}$ in the loading cycle, (Equation 2.21). Stress ratio is defined as the ratio of the minimum stress to the maximum stress experienced during one loading cycle $R = \sigma_{min}/\sigma_{max}$. For $R \leq 0$, $\Delta K = K_{max} - 0 = K_{max}$. We assume that the crack increment da happens at the moment where $K = K_{max}$ during one loading cycle. Thus, considering the relation between the energy release rate G and the stress intensity factor K (in plane stress, for example), in Equation 2.20, $G = K_{max}^2/E$. Then the Paris' law can be rewritten as

$$\frac{da}{dN} = C(GE)^{m/2}, \tag{3.25}$$

where da/dN is the crack growth rate, a is the crack length and N is the number of loading cycles, C and m are fatigue parameters and E is the Young's modulus of the material. The energy release rate $G = dU/da$ can be calculated locally, at a contact, as discussed in Section 3.4.3.1, based on the corresponding energy release associated to a given crack propagation da. The explicit numerical approach is discussed in the following sections.

3.7.2 A quasi-static approach to simulate fatigue cycles

In controlled conditions, if we neglect any dynamic effect, the loading cycles imposed at the boundaries are in phase with the mechanical efforts inside the structure. For centered loading cycles, the whole structure (in homogeneous conditions) or part of it (in all other cases) are periodically submitted to tension and compression efforts. If one supposes a slow evolution of the material during one cycle, it is reasonable to admit that tension and compression efforts present the same magnitude (but different signs). In this case, for Paris' law, tension ranges can be simply obtained with a static loading representing the amplitude of the loading cycle. For the zones in compression, the absolute value of the mechanical efforts correspond to the same values when in tension.

As shown in Figure 3.21 the range of the stress intensity factor ΔK (or any other mechanical quantity like stress and strain) is obtained in quasi-static conditions.

As shown in Figure 3.21, considering a fatigue test under stress control, the plate subjected to sinusoidal cyclic stress (illustrated by the dotted sinusoidal curve in the top right coordinate system of Figure 3.21), the resultant stress intensity range ΔK at crack tips is a semi sinusoidal curve during tension half cycle and keep 0 in compression half cycle (illustrated by the dotted semi sinusoidal curve in the bottom right coordinate system of Figure 3.21), during every loading cycle crack grows and consequently cause the stress concentration intensity increase at crack tips.

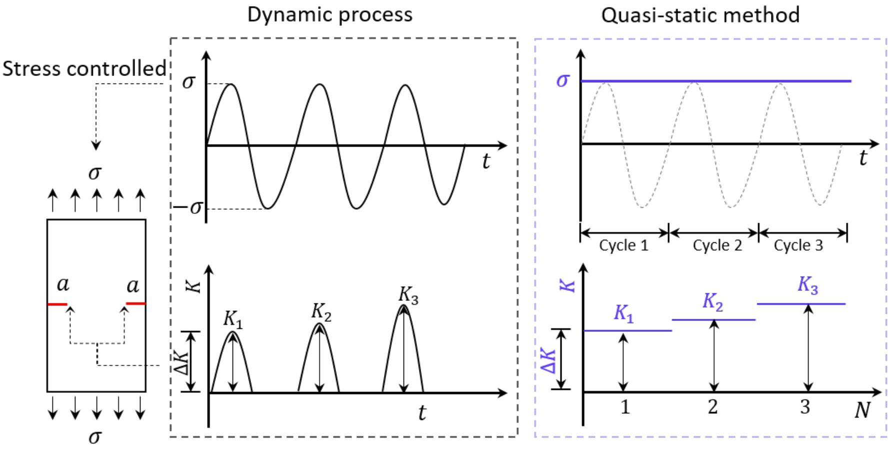

Figure 3.21: Quasi-static loading and extraction of the values of stress intensity range ΔK at crack tips.

3.7.3 Numerical procedures for the fatigue crack growth calculation in DEM

The local calculation of the rupture process depends on the progressive release of energy to be defined. As shown in Figure 3.22 (to be simple, elastic separation case is used), an initial (numerical) damage D_{ini} is introduced to give rise to a first release of energy dU and the identification of the value of p. The application of Equation 3.23 allows the identification of da corresponding to $dD = D_{ini} - 0$. The energy release rate can be calculated and the analysis of the crack growth process can start.

The explicit numerical procedure can be presented as follows :

1) Definition and application of the initial degradation value D_{ini}, for example $D_{ini} = 1 \times 10^{-4}$;

2) Measurement of dU and p;

3) Put the initial values of $D = 0$, $a_c = 0$ and $dD = D_{ini}$ and p into Equation 3.23 and calculate corresponding da;

4) Update $D = D + dD$ and $a_c = a_c + da$ (until $D = 1$, complete rupture);

5) Calculation of $G = dU/(tda)$;

6) Paris' law, Equation 3.25, and calculation of the new crack increment da;

7) The new da, present D, a_c and p, into Equation 3.24, calculation of the corresponding new degradation increment dD;

8) Measurement of new dU and p and cycle back to step 4.

Considering the key role of the slope ratio p, this model scheme is called p-model in the following. In Chapter 4 applications of p-model are presented where its capabilities and limitations are discussed.

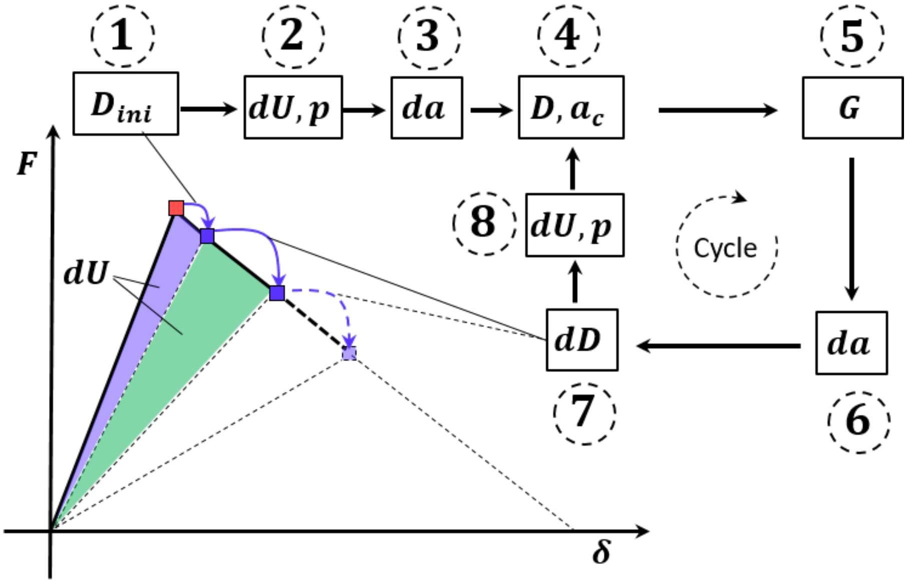

Figure 3.22: Schematic description of the procedures of fatigue crack growth calculation.

3.8 Summary of the chapter 3

In Chapter 3, the basic equations characterizing the elasticity and rupture of the contacts in discrete element method is presented. The crack tip behavior is analyzed in detail for an elastic medium and the effect of a discrete description of the material is identified on the diagram force×displacements. Consequently, a damage like model is adopted to describe the loss of stiffness of each contact during crack propagation.

An energetic consistent approach is proposed where each damage increment dD is associated to a crack increment da. Crack increments with dimensions much below particle scale become clearly described. Finally, it allowed Paris' law to be adapted to relate the energy release rate G to the crack increment da in fatigue tests.

Chapter 4

Modeling cracked samples under fatigue loading

Contents

4.1 Introduction 72

4.2 DEM simulation procedures 72

  4.2.1 Particle sample arrangements and crack description . . 72

  4.2.2 Non local crack tip identification and numerical procedure 74

4.3 Comparison of the model with theoretical results . . . 74

  4.3.1 Sample dimensions and material properties 74

  4.3.2 Cyclic loading 75

  4.3.3 Numerical results 75

    4.3.3.1 Crack length and stiffness evolution 75

    4.3.3.2 Evolution of the energy release rate 76

4.4 Identification of the dimension d_c 79

4.5 Parametric study 84

  4.5.1 Effect of parameter C 84

  4.5.2 Effect of parameter m 84

4.6 Comparison of the proposed contact model with experimental results 86

4.7 Summary of the chapter 88

4.1 Introduction

Chapter 3 presents the fatigue rupture of a contact localized at the crack tip consistently with Paris' law. Based on the analysis of pre-cracked samples, where crack tips are clearly identified (similarly to most of the methods in continuum mechanics) practical elements are discussed in this chapter. First, the DEM simulation procedures are presented, then simulation results for regularly packed samples are compared with theoretical calculation. The the width of the contact domain d_c for different contact structures is discussed followed by parametric studies of parameters C and m. Finally, comparison of the proposed model with experiments are shown.

4.2 DEM simulation procedures

4.2.1 Particle sample arrangements and crack description

Particle regular structures like square and hexagonal packed samples (see Figure 4.1) are adopted here to verify theoretical results considering the more intuitive description of cracks and their evolution. As can be seen in Figure 4.1a, the width of the contact domain d_c for a square packed samples is identical to the particle diameter d. In hexagonal packed samples, during one contact total degradation, crack propagates for a distance of $d_c = d/2$, as shown in Figure 4.1b.

However, regular packings are often less realistic to describe geomaterials since their behavior is associated with those of ideal materials, completely homogeneous. The value of d_c for randomly packed samples is not directly identified, but it depends on the granulometry, void ratio, etc (as discussed further in Section 4.4).

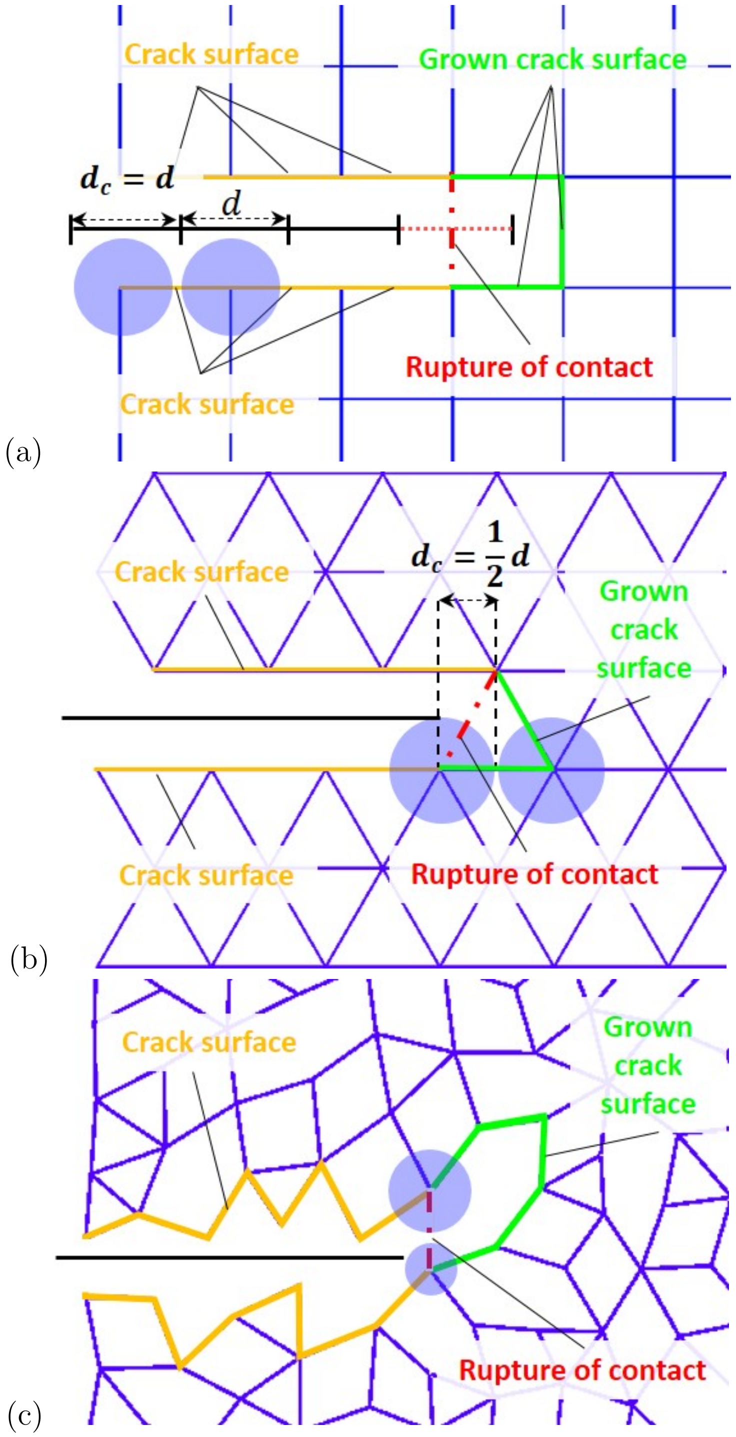
(a)
Crack surface
Grown crack surface
$d_c = d$
d
Rupture of contact
Crack surface
(b)
Crack surface
$d_c = \frac{1}{2}d$
Grown crack surface
Crack surface
Rupture of contact
(c)
Crack surface
Grown crack surface
Rupture of contact

Figure 4.1: Definition of a crack for (a) square, (b) hexagonal and (c) randomly packed samples. Identification of the crack domain d_c for square and hexagonal packed samples.

4.2.2 Non local crack tip identification and numerical procedure

As shown in Figure 4.1, as soon as a contact is in rupture due to crack propagation, crack surfaces continually grow and crack tip continually advances. The new crack tip is identified as the contact where the strain level ε (Equation 3.5) is maximum in the newly grown crack surface. Thus, the rupture of this contact begins, following the Paris' law formulation discussed in Chapter 3.

Hence, multicracked systems in fatigue may be simulated with the following steps:

1) Sample preparation.

2) Initialization of cracks.

3) Load application.

4) Attribute rupture model to contacts at the crack tips.

5) Start fatigue crack propagation.

6) After each total contact rupture, identification of the new crack tips and return to step 4. Repeat the procedure until the end of the fatigue test.

4.3 Comparison of the model with theoretical results

The relevance of the formulation and the physical effects of model parameters are examined in this section through the comparison between numerical and theoretical results (see Appendix D). Two different cyclic boundary conditions are adopted: stress and strain control.

4.3.1 Sample dimensions and material properties

A theoretical fatigue test of a rectangular plate with symmetric edge cracks is used as a reference for comparison. The plate dimensions are: height $H = 160\ mm$, width $2b = 100\ mm$ and thickness $t = 1\ m$, with initial crack lengths $a_0 = 10\ mm$

A material with Young's modulus $E = 10$ GPa and Poisson's ratio $\nu = 0$ is adopted. Parameters used in the fatigue model are $D_{ini} = 1.0 \times 10^{-3}$,

$C = 1.0 \times 10^{-12}$ (m/cycle/(Pa$\sqrt{\text{m}}$)^m) and $m = 1.25$. For these simulations, samples with square and hexagonal packed are employed with 3 different particle diameters: $d = 4\ mm$, $d = 2\ mm$ and $d = 1\ mm$, contact stiffnesses setting based on Equations 3.9 and 3.10.

4.3.2 Cyclic loading

For stress controlled tests, sinusoidal stress with amplitude $\sigma_{max} = 1.0$ MPa is applied. The crack propagation induces a reduction of the global stiffness of the plate. For a constant stress amplitude, it yields an increase on the displacements amplitude. Fatigue evolution is monitored by the sample stiffness ratio (see Appendix C) expressed as $\bar{\delta}_0/\bar{\delta}$ which is the ratio of the average displacements at the extremities of a plate without a crack ($\bar{\delta}_0$) compared to the ones of a cracked plate ($\bar{\delta}$).

For strain controlled tests, sinusoidal strain with amplitude $\varepsilon_{max} = 100\ \mu\varepsilon$ is applied. The crack propagation induces a reduction of the global stiffness of the plate. For a constant strain amplitude, it corresponds to a decrease of the amplitude of the measured forces. Fatigue evolution is monitored by the sample stiffness ratio expressed as F/F_0 which is the ratio of the resultant forces at the extremities of a plate without a crack (F_0) compared to the one of a cracked plate (F).

4.3.3 Numerical results

4.3.3.1 Crack length and stiffness evolution

Figure 4.2a shows the evolution of the stiffness ratio as a function of the number of loading cycles N for a square packed sample under stress control fatigue loading. In Figure 4.2b one can see the corresponding crack increase. In Figure 4.2c the contact degradation can be clearly associated to the crack increase at different states of stiffness ratios. The results for all particle diameters are close to the theoretical results, although closer results are observed for smaller particles.

The same trends with respect of the stiffness ratio are observed for hexagonal packed (as visible in Figure 4.3a). Furthermore, hexagonal structure allows the control of the Poisson's ratio ν (as described in Equation 3.10). In Figure 4.3b the complete absence of effect of ν is consistent with the linear elastic fracture mechanics theory.

The results for strain controlled tests (Figure 4.4) follow exactly the same

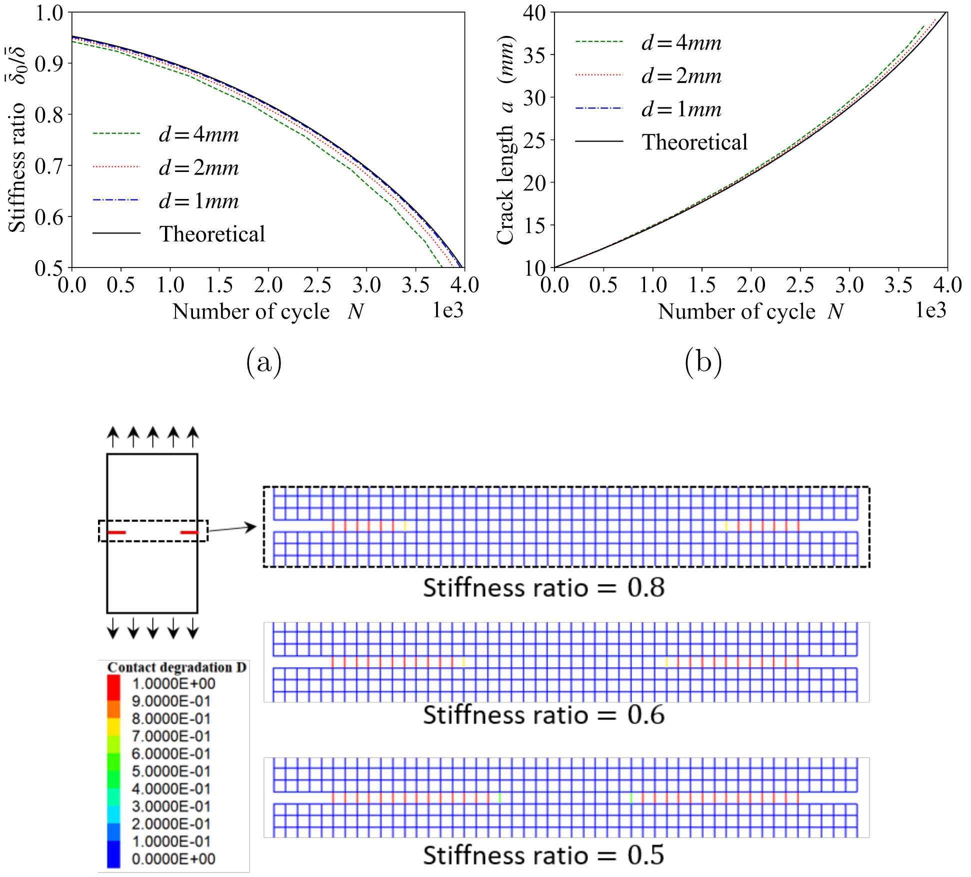

(a) (b)

(c)

Figure 4.2: Simulations of a symmetric edge cracked plate under stress fatigue loading with square packed samples for different particle sizes and comparison with theoretical results of (a) crack growth and (b) the stiffness ratio as functions of the number of cycles N in controlled stress conditions. (c) Contact degradation map during fatigue evolution for $d = 2mm$.

trends as those observed for stress controlled tests in comparison to theoretical predictions.

4.3.3.2 Evolution of the energy release rate

The best fit of theoretical result by the simulation results obtained for smaller particles can be explained by the analysis of the trends of the energy release rate G shown in Figure 4.5. In the formulation presented in Chapter 3, the value of G is supposed to be constant during crack propagates through

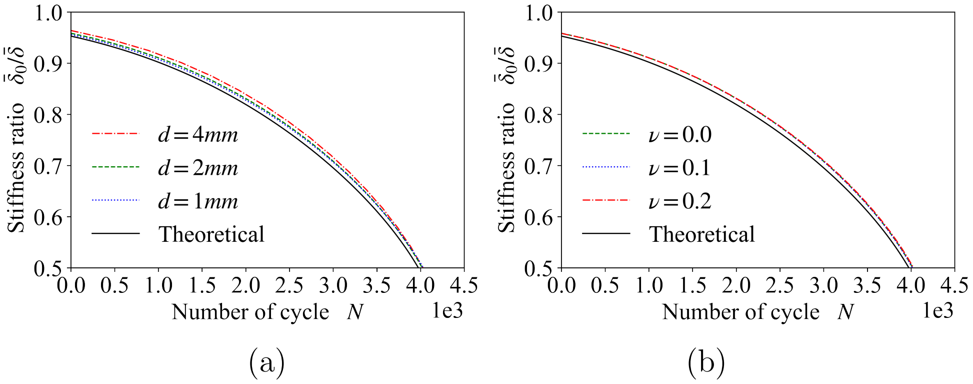

Figure 4.3: Simulations of a symmetric edge cracked plate under stress controlled fatigue loading with hexagonal packed samples and comparison with theoretical results of the stiffness ratio as a function of the number of loading cycles N for (a) different particle size (Poisson's ratio $\nu = 0$) and (b) different Poisson's ratios (and $d = 2mm$) in controlled stress conditions.

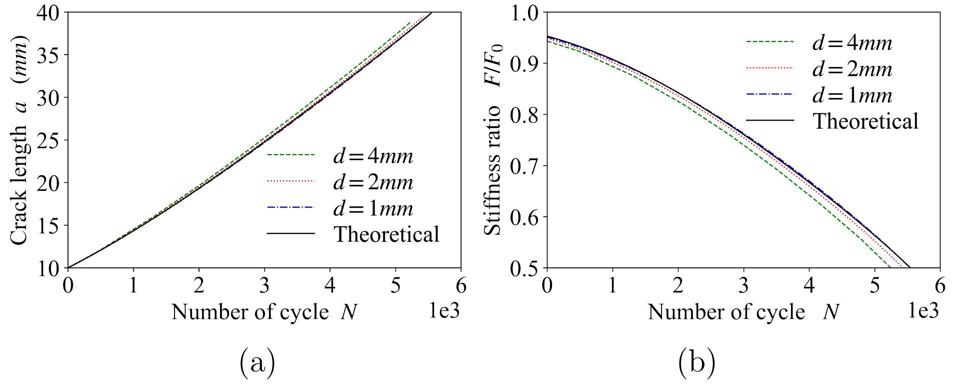

Figure 4.4: Simulations of a symmetric edge cracked plate under strain fatigue loading with square packed samples for different particle sizes and comparison with theoretical results of (a) crack growth and (b) the stiffness ratio as functions of the number of cycles N in controlled strain conditions.

a contact. This assumption is well verified by the shape of the simulations curves of G, composed by uniform segments. Each of these uniform segments corresponds to the process of the crack propagates through a contact. The evolution of G depends on the boundary conditions (Figures 4.5a and b were obtained for stress controlled, whilst Figures 4.5c and d for strain controlled). However, the decrease of particle size from $d = 2$ mm (Figures 4.5a and c) to $d = 1$ mm (Figures 4.5b and d) allows a better approximation of the theoretical trends in both cases.

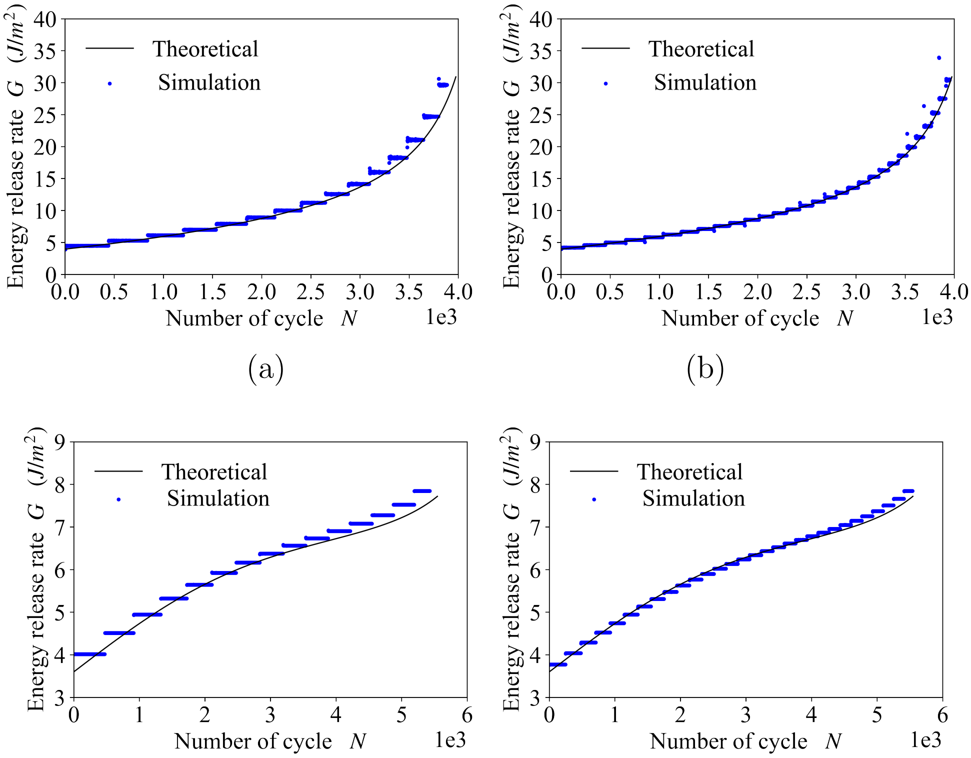

(a) (b)

(c) (d)

Figure 4.5: Simulations of a symmetric edge cracked plate with square packed samples and comparison with theoretical results of the energy release rate G under stress controlled fatigue loading for particle size (a) $d = 2$ mm and (b) $d = 1$ mm, and under strain controlled fatigue loading for particle size (c) $d = 2$ mm and (d) $d = 1$ mm.

The values of G are usually constant per segment, but some rare deviations can be observed, specially for imposed stress cases. This phenomenon is due to the sensitivity of the value of the slope ratio p in the first rupture cycle associated to the value of the parameter D_{ini}. More details of this point are discussed in Appendix E.

4.4 Identification of the dimension d_c

The contact domain length d_c is a parameter of the propagation model which depends directly on the particle diameter d, but also on particle arrangement. As discussed in Section 4.2.1, d_c is equal to d for a square arrangement, and it becomes $d/2$ for a hexagonal arrangement. In these examples, it can be visually identified. However, a more general interpretation of this intrinsic scale of the granular arrangement can be obtained.

The propagated crack length inside the contact domain can be written as $a_c = \alpha d_c$ for $0 \leq \alpha \leq 1$. Replacing this expression for a_c in Equation 3.23, one may get

$$\frac{d\alpha}{1-\alpha} = \frac{dD}{(1-D)[1+p(1-D-dD)]}, \tag{4.1}$$

which means that a relative variation of the propagated length $d\alpha$ is directly associated to a stiffness reduction dD independently of d_c. A stiffness reduction dD induces a release of energy dU, consequently, it is also independent of d_c.

The energy release rate (see Section 2.5.4) can be defined as $G = dU/(t \times da)$. Introducing in Equation 3.25 of the Paris' law: $a_c = \alpha d_c$, $da = d\alpha d_c$ and the previous definition of G, one may get after some algebraic work

$$(d\alpha d_c)^{1+m/2} = C \left(\frac{dU}{t} E \right)^{m/2} dN. \tag{4.2}$$

For a different value of contact domain d'_c, the only difference in Equation 4.2 would be in the number of cycles dN', since the rest of the parameters ($d\alpha$, m, C, dU, t and E) is completely independent of d_c. It means that dividing Equation 4.2 by itself with another value of contact domain d'_c (and consequently another number of cycles dN'), one may simply get

$$dN' = \left(\frac{d'_c}{d_c} \right)^{1+m/2} dN. \tag{4.3}$$

Equation 4.3 predicts that the effect of a different contact domain value d'_c with respect to a reference one d_c would be only in the scale of the number of cycles. This result is presented in Figure 4.6a for a fatigue test similar to the previous section for imposed stress with square packed samples and three different values of d_c': $0.5d$, $1.0d$ and $1.5d$. In Figure 4.6b, all curves collapse when the number of cycles is divided by $(d_c'/d_c)^{1+m/2}$ with $d_c = 1.0d$. Similarly, Figure 4.6c shows the results for hexagonal packed samples with three different values of d_c': $0.25d$, $0.5d$ and $0.75d$. In Figure 4.6d, all curves collapse with $d_c = 0.5d$.

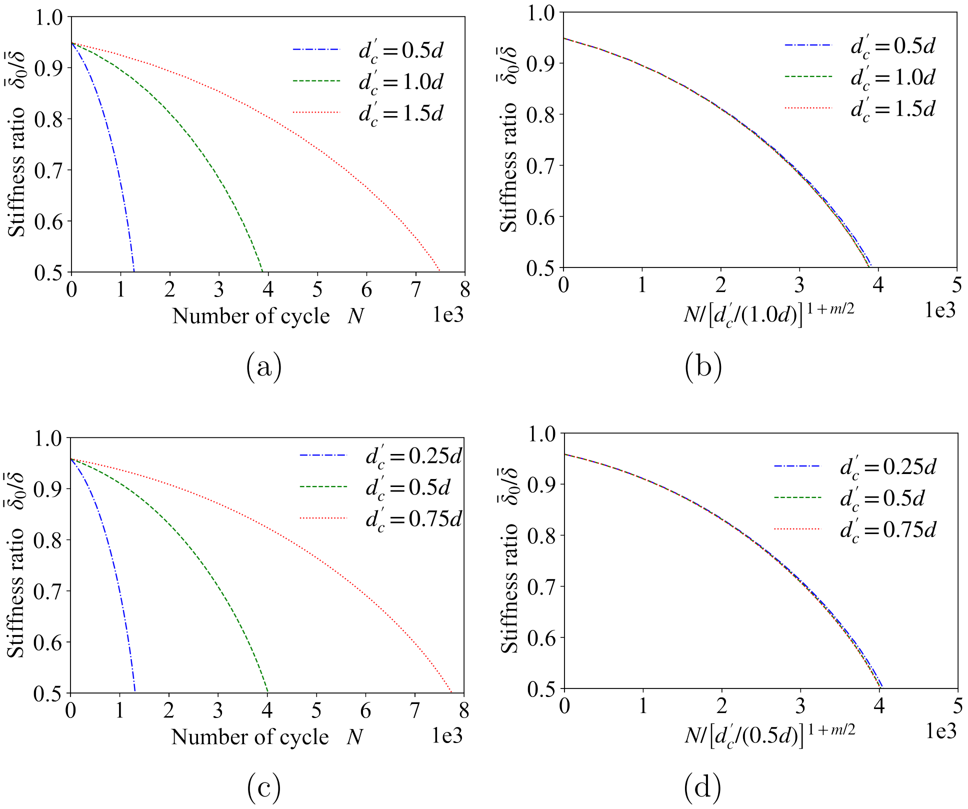

(a) (b)

(c) (d)

Figure 4.6: Stiffness ratio of a double edge cracked plate under stress fatigue: for a square packed sample (a) as a function of the number of cycles N and (b) as a function of $[d_c'/(1.0d)]^{1+m/2}N$; for a hexagonal packed sample (c) as a function of the number of cycles N and (d) as a function of $[d_c'/(0.5d)]^{1+m/2}N$.

The effect described in Equation 4.3 allows the determination of d_c based on the comparison of a simulation with any value of d_c' and theoretical results.

For randomly packed structures the parameter d_c is not trivial, depending on the texture of the arrangement. Six samples with an average diameter $d = 2\ mm$, minimum diameter $d_{min} = 1.54\ mm$ and maximum diameter $d_{max} = 2.46\ mm$ where generated as detailed in Appendix B. Due to the heterogeneity and randomness of randomly packed samples, to perform the same modulus as the target material, the contact stiffness can not be set directly as $E_{cmod} = E$ which is good for square packed samples (Section 3.2.3). And an appropriate value of E_{cmod} need to be determined by simulation tests [4]. In this case, based on tension test simulation, the contact stiffness setting are calibrated as $E_{cmod} = 1.21 \times E$ and $k_{ratio} = 1.0$, where E is material Young's modulus.

To reduce the effect of cracks interaction, reference fatigue test is set as single edge cracked plate, with initial crack lengths $a_0 = 10\ mm$, sinusoidal stress with amplitude $\sigma_{max} = 1.0$ MPa, plate dimensions and material properties are taken similar to those used in previous fatigue tests (Section 4.3.1).

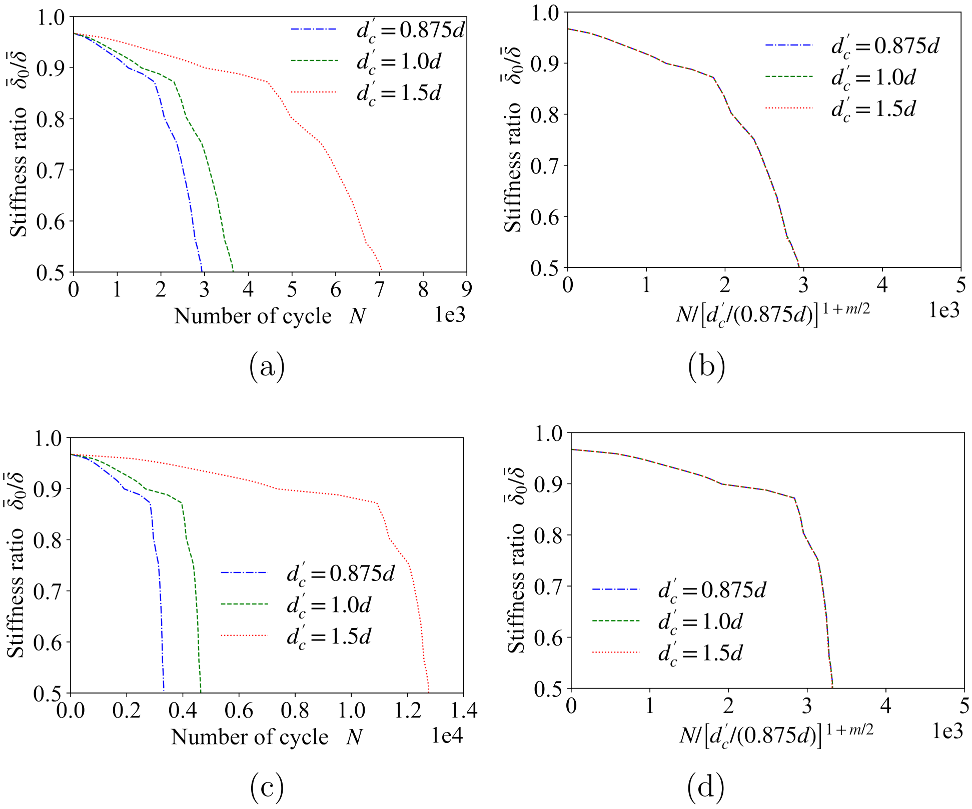

(a) (b)

(c) (d)

Figure 4.7: Stiffness ratio of a single edge cracked plate under stress fatigue for a random packed sample (a) as a function of the number of cycles N and (b) as a function of $[d_c'/(0.875d)]^{1+m/2}N$, for Paris's law parameters: $C = 1.0 \times 10^{-12}$ (m/cycle/(Pa$\sqrt{\text{m}}$)^m) and $m = 1.25$, and that of (c) and (d) for $C = 2.0 \times 10^{-22}$ (m/cycle/(Pa$\sqrt{\text{m}}$)^m) and $m = 3$.

The fatigue behavior of one of the randomly packed samples is shown in Figure 4.7a for three different values of d'_c: $0.875d$, $1.0d$ and $1.5d$, where for randomly packed samples, the mentioned diameter d is the minimum diameter of the two particles sharing a contact, $d = d_{min}$. All curves collapse to $d_c = 0.875d$ as shown in Figure 4.7b.

In Figures 4.6 and 4.7a and b the parameters of Paris's law are $C = 1.0 \times 10^{-12}\,(\mathrm{m/cycle}/(\mathrm{Pa}\sqrt{\mathrm{m}})^m)$ and $m = 1.25$. In Figure 4.7c and d another set of parameters ($C = 2.0 \times 10^{-22}\,(\mathrm{m/cycle}/(\mathrm{Pa}\sqrt{\mathrm{m}})^m)$ and $m = 3$) is adopted. The same effect is observed, since it depends on the crack trajectory and this is not affected by C and m.

To identify the value of d_c that yields the best fit of the stiffness ratio as a function of the number of cycles for theoretical calculation in the case of randomly packed samples, $d'_c = 0.875d$ is set for all six samples, then based on Equation 4.3 and theoretical results, the fatigue behavior and corresponding calibrated d_c value of each of them are shown in Figure 4.8a. An average value of contact domain $d_c = 0.958$ is obtained as the identified contact domain d_c for samples with the same granulometry as these six samples. Finally simulations with $d_c = 0.958d$ confirms the results, and good agreement between the average curve and the theoretical results is observed (Figure 4.8b). Crack trajectories of all six samples are shown in Figure 4.9.

The contact domain length d_c is a parameter with an average value for a given particle arrangement, but it presents a natural variation since it depends on crack path during rupture. In Appendix F, a more detailed explanation of the variation of d_c is proposed based on the analysis of the morphology of the particle arrangement.

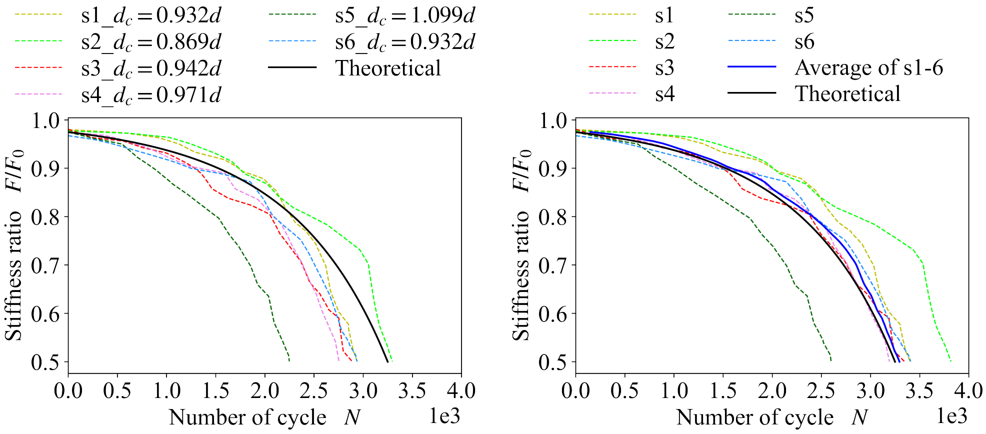

(a) (b)

Figure 4.8: (a)Stiffness ratio of a double edge cracked plate under stress fatigue for random packed sample $s1$ to $s6$, as a function of the number of cycles N. And each calibrated value of d_c, based on Equation 4.3 and theoretical results for Paris's law parameters: $C = 1.0 \times 10^{-12}\ (\text{m/cycle}/(\text{Pa}\sqrt{\text{m}})^m)$ and $m = 1.25$. (b) Comparison of simulations with $d_c = 0.958d$ and the theoretical results.

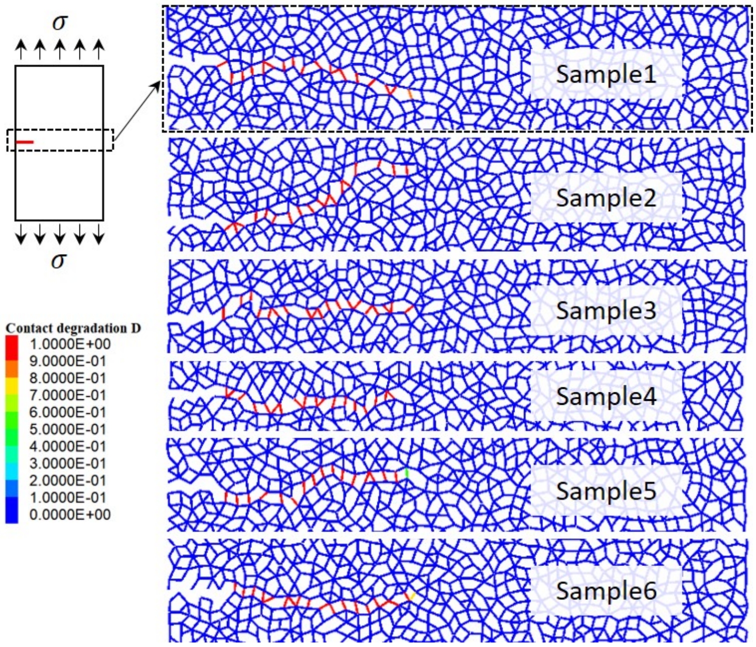
σ
σ
Contact degradation D
1.0000E+00
9.0000E-01
8.0000E-01
7.0000E-01
6.0000E-01
5.0000E-01
4.0000E-01
3.0000E-01
2.0000E-01
1.0000E-01
0.0000E+00
Sample1
Sample2
Sample3
Sample4
Sample5
Sample6

Figure 4.9: Crack trajectories for all six randomly packed samples.

4.5 Parametric study

The effect of parameters C and m over the fatigue behaviour is analysed in the following section. Stress controlled tests are performed on the same plate with double edge cracks and the same material parameters as in Section 4.3.3 unless told otherwise.

4.5.1 Effect of parameter C

The effect of parameter C is examined by comparing three fatigue simulations. In all simulations, the particle size $d = 2\ mm$ is adopted as well as the parameters in Table 4.1.

Table 4.1: Set of parameters for the analysis of parameter C in fatigue simulations.

D_{ini}	C (m/cycle/(Pa$\sqrt{\text{m}}$)^m)	m
1.0×10^{-3}	1.0×10^{-12}	1.25
1.0×10^{-3}	2.0×10^{-13}	1.25
1.0×10^{-3}	1.0×10^{-13}	1.25

As shown in Figure 4.10a, with parameters D_{ini} and m unchanged, parameter C has a multiplying effect on the fatigue life, the number of cycles till a certain failure limit. This effect is clearly visible, by displaying the fatigue evolution as a function of $C \times N$ (see Figure 4.10b). With this scaling, the three curves with different C are perfectly superposed. Such property of C can be used to save calculation time for long life materials in fatigue simulations by setting a relatively bigger parameter C and then scaling the results.

4.5.2 Effect of parameter m

The effect of parameter m is examined by comparing three fatigue simulations. In all simulations, the particle size $d = 2\ mm$ is adopted as well as parameters in Table 4.2.

Since parameter m is an exponent in Equation 3.25 which determines the crack increment da, a larger value of m indicates that crack propagation in the material is more sensitive to the value of the energy release rate G. As shown in Figure 4.11a, with larger values of m, the fatigue process is dramatically accelerated.

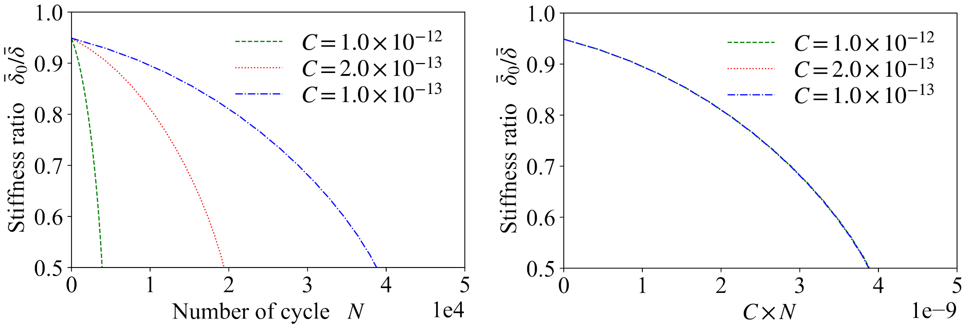

(a) (b)

Figure 4.10: Fatigue evolution (a) versus number of cycles N and (b) versus $C \times N$ for different values of parameter C.

Table 4.2: Set of parameters for the analysis of parameter m in fatigue simulations.

D_{ini}	C (m/cycle/(Pa$\sqrt{\text{m}}$)^m)	m
1.0×10^{-3}	3.0×10^{-22}	1.25
1.0×10^{-3}	3.0×10^{-22}	2.0
1.0×10^{-3}	3.0×10^{-22}	3.0

The effect of m on fatigue evolution shape can be more visible if the results are shown as a function of a normalized number of cycle N_{norm} (as shown in Figure 4.11b). One may propose a normalization by the number of cycles associated to a similar stiffness ratio:

$$N_{norm} = \frac{N}{N_{0.5}} \tag{4.4}$$

where $N_{0.5}$ is the number of cycles corresponding to $\bar{\delta}_0/\bar{\delta} = 0.5$.

Generally, parameter C globally effects on fatigue life, which possibly relates to material strength or toughness. Parameter m effects on fatigue rate with respect to crack propagation, which possibly relates to material brittleness. Higher value of parameter m indicates higher brittleness and more concentration of energy release at crack tip, more obvious acceleration in the last phase of fatigue evolution.

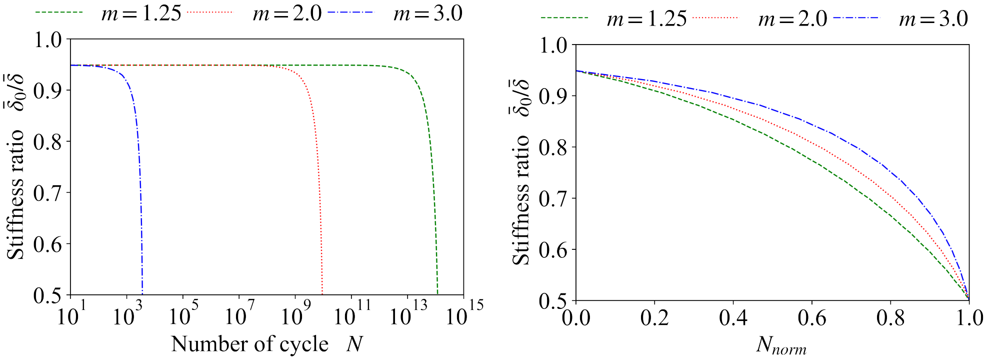

(a) (b)

Figure 4.11: Fatigue evolution (a) versus number of cycles N and (b) versus number of cycles N_{norm} for different values of parameter m.

4.6 Comparison of the proposed contact model with experimental results

Bažant and Xu [148] analyzed pre-cracked concrete beams subjected to three point bending fatigue tests (see Figure 4.12). A cyclic force is applied with a maximum amplitude $F = 4147.4$ N. Experimental results obtained with the largest sample in this study (height $H = 152.4\ mm$, span $L = 381\ mm$ and thickness $t = 38.1\ mm$) are compared to those from DEM simulations. The material presents a Young's modulus $E = 27120$ MPa. For initial crack length, a value of $a_0 = 33.3\ mm$ is considered ($a/H = 0.219$), which corresponds to the result at $N = 10$ cycles in experimentation.

Three square packed DEM samples respectively with particle size $d = 3\ mm$, $2\ mm$ and $1\ mm$, are used in simulations, with parameter set $D_{ini} = 1.0 \times 10^{-3}$, $C = 1.06 \times 10^{-60}$ $(\mathrm{m/cycle/(Pa\sqrt{m})}^m)$ and $m = 9.27$. In Figure 4.12b, the evolution of the crack length ratio a/H as a function of the number of cycle N is presented. A very good agreement between the experiment and the simulations is observed.

Ma et al. [149] conducted a single edge notch tension fatigue test of steel $S460$ with Young's modulus $E = 200$ GPa. The specimen dimensions are height $H = 108\ mm$, total length $L = 90\ mm$ and thickness $t = 6\ mm$, with initial crack $a_0 = 45.8\ mm$ (Figure 4.13a). The specimen subjected to a cyclic stress with a maximum amplitude $\sigma_{max} = 29.63$ MPa and stress ratio $R = 0.5$.

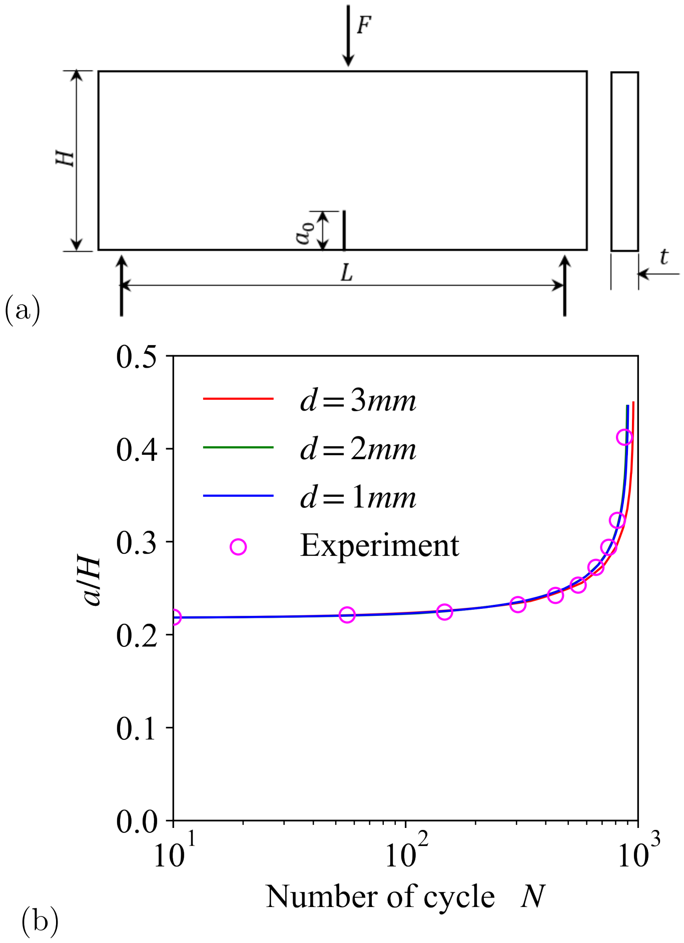

Figure 4.12: (a) Geometry of the three-point bending beam. (b) Evolution of the crack length ratio a/H as a function of the number of cycle N. Comparison between test results and DEM simulation.

Considering the stress ratio R, with $\Delta K = K_{max}(1-R)$ and Equation 2.20, the Paris' law (Equation 3.25) can be rewritten as

$$\frac{da}{dN} = C(1-R)^m (GE)^{m/2}. \tag{4.5}$$

Three square packed DEM samples respectively by particle size $d = 3\ mm$, $2\ mm$ and $1\ mm$, are used in simulations, with parameter set $D_{ini} = 1.0 \times 10^{-3}$, $C = 1.98 \times 10^{-23}$ $(\mathrm{m/cycle}/(\mathrm{Pa}\sqrt{\mathrm{m}})^m)$ and $m = 2.1$. To save simulation time, scaling effect of parameter C is used, in programming parameter C is set 100 times bigger than 1.98×10^{-23}, after program running the results are correspondingly scaled 100 times. In Figure 4.13b, the evolution of the crack length a as a function of the number of cycle N is presented.

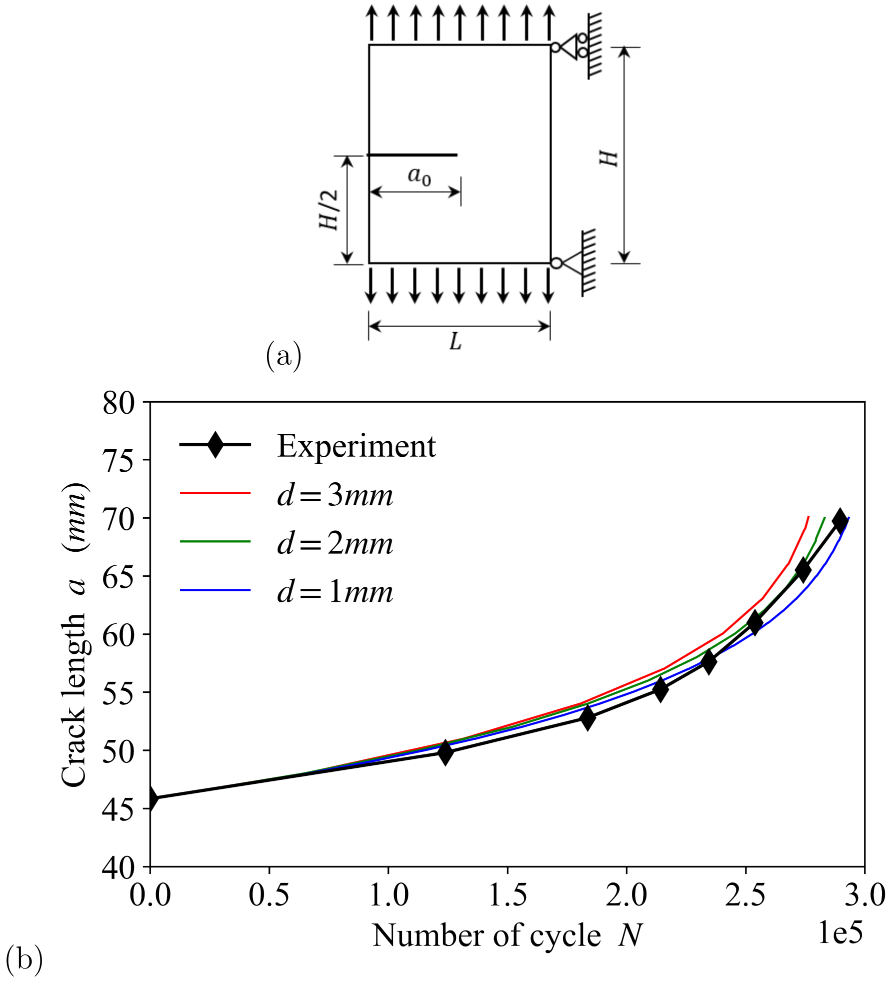

Figure 4.13: (a) Geometry of the single edge notch tension fatigue test. (b) Evolution of the crack length a as a function of the number of cycle N . Comparison between test results and DEM simulation.

4.7 Summary of the chapter

Chapter 4 deal with the application of the formulation (p-model) of Chapter 3 to multi-particle crack propagation.

Comparisons of the simulations with theoretical results show the relevance of the proposed formulations. The energy release rate is well identified numerically and the assumption of a constant energy release rate per contact appears reasonable.

The contact domain length d_c, a particular parameter of the discrete approach, is shown to be a characteristic length of the sample arrangement. Its effect on the numerical results is shown and a systematic procedure for its identification is proposed.

After a parametric study presenting the effect of the parameters of the Paris' law (C and m), a comparison with experimental results confirms the good trends observed with the theoretical analysis.

Both comparisons with theoretical and experimental results support the fatigue crack propagation modeling ability of the proposed p-model. Besides, two advantages shown in the proposed contact model are worthy to be noticed. First, once after the contact degradation processes are triggered by a given initial degradation D_{ini}, only contact forces F and contact displacements δ are needed to continue. With such a limited information, p-model still can calculate energy release rate G and crack increment da, then represents da by contact damage dD. This feature make it a local model and can be easily programmed into DEM. Second, p-model shows high precision with respect to Paris' law, which evidences a good incorporation of fatigue law.

Chapter 5

A damage model for crack initiation and multi-cracking

Contents

5.1 Introduction **91**
  5.1.1 Physical interpretation of the parameter p 93
  5.1.2 A variant Paris' law 96
  5.1.3 Contact endurance limit 97
5.2 Complete damage model (*sp*-model) **98**
5.3 Simulation approach for fatigue tests in DEM **99**
5.4 Modeling of Tension-Compression fatigue test **102**
  5.4.1 Effect of the parameter p 103
  5.4.2 Effect of the contact endurance limit 104
  5.4.3 Simulation versus experimental results of T-C fatigue tests 106
    5.4.3.1 Scaling technique 106
5.5 4PB fatigue tests **110**
  5.5.1 Simulation results of 4PB tests 110
5.6 2PB fatigue tests **116**
  5.6.1 Simulation results of 2PB tests 117
5.7 Summary of the chapter **122**

5.1 Introduction

Fatigue process can be divided in three stages with respect to the propagation of cracks (see Figure 5.1) as discussed by [114]. The first stage is characterized by the propagation of distributed inner micro-cracks and defects. The propagation and coalescence of the major ones lead to a regime dominated by relatively big cracks (stage 2), where their propagation per cycle da/dN

as a function of the stress intensity factor range ΔK follows approximately a power law (see Paris' law, Chapter 2). When some cracks are big enough to mobilize the toughness of the material, the propagation per cycle da/dN accelerates corresponding to the final stage.

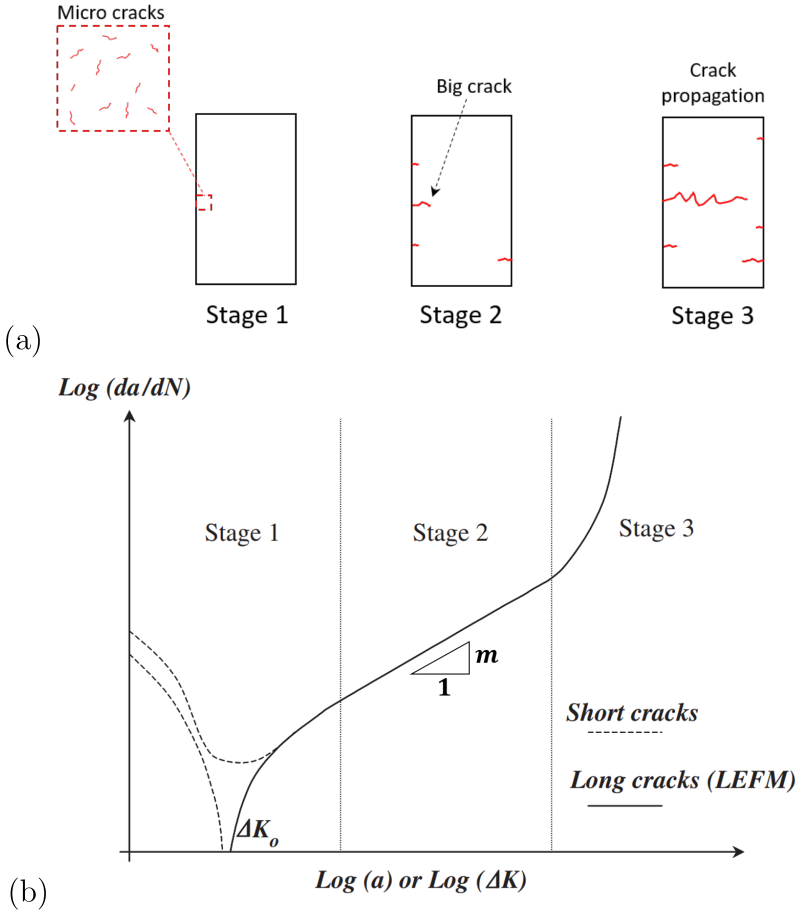
Micro cracks
Big crack
Crack propagation
Stage 1
Stage 2
Stage 3
(a)
Log (da/dN)
Stage 1
Stage 2
Stage 3
m
1
Short cracks
Long cracks (LEFM)
ΔK_o
Log (a) or Log (ΔK)
(b)

Figure 5.1: (a) Scheme of the three fatigue stages and (b) its effect on the propagation of cracks per cycle da/dN as a function of crack length a or stress intensity range ΔK, solid line for long crack (except a is too small or too large, crack propagation complies with Paris' law), and dotted lines indicate tow possibilities of the unknown law for short crack (modified from [114]).

The previous chapters present the main elements of an energetical contact model dealing with crack propagations in the framework of linear elastic fracture mechanics (LEFM). That is to say, the energy release is strictly governed by the behavior of crack tips. This approach corresponds to the description of stage 2.

In this chapter, a generalization of the proposed concepts leads to the construction of a damage model able to deal with rupture behavior from initiation to propagation of multiple cracks (stages 1 and 2). Basically, the energy release during material rupture is potentially distributed over all contacts instead of only at previously identified crack tips.

Based on an analysis of the physical effects of the slope ratio p, an implicit variant Paris' law is proposed. After the introduction of the concept of contact endurance limit, the complete damage model is presented.

The proposed damage model is used to simulate the whole process of fatigue tests (T-C, 4PB and 2PB, see Section 2.3.2.1), and comparisons between simulation and experimentation are analyzed.

5.1.1 Physical interpretation of the parameter p

As discussed in Chapter 3, $p = k_0/k_p$ represents the ratio between the elastic slope k_0 and k_p the absolute value of the rupture slope of a contact during the propagation of a crack (see Figures 3.6).

The values of p are shown to be measurable following the scheme presented in Figure 3.6. Considering the energy equivalence between crack propagation and energy release in a contact (see Chapter 3), the p variable (mainly governing the $a_c - D$ and $da - dD$ relations, Equations 3.16 and 3.23) conceptually characterizes the relation between the propagated length a_c and the stiffness reduction of the contact D.

Observing Equations 3.16 and 3.17, without consideration about the physical meaning of p, mere mathematically, the value of p obviously can effect the $a_c - D$ relation. In Figure 5.2, different values of p are adopted in Equation 3.17, and resultant curves of corresponding relation between $1 - D$ and a_c/d_c show the influence of value of p on $a_c - D$ relation.

In p-model (Section 3.7.3), the energy release rate G is calculated as $G = dU/(tda)$, which is related to $da - dD$ relation (Equations 3.23 and 3.24). And we already know that when value of p in Equations 3.23 and 3.24 is adopted as the measured slope ratio $p = k_0/k_p$, the resultant G values are constant during each contacts and are close to theory result (see Figure 4.5 in Section 4.3.3.2). Thus, it would be interesting to see what will result if an imposed value of p which is not equal to the measured slope ratio $p = k_0/k_p$ is adopted in Equations 3.23 and 3.24.

To present effect of p on the calculated G in p-model, different values of p are respectively adopted in the same example. Figure 5.3a shows the rupture

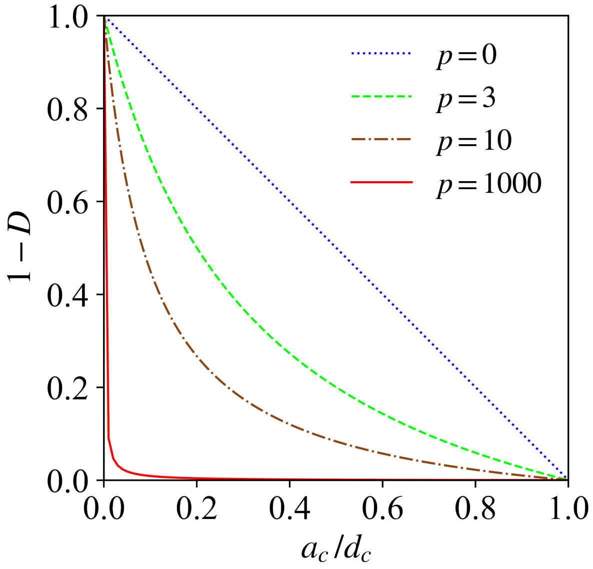

Figure 5.2: Curves relating stiffness reduction $1-D$ and relative propagated length a_c/d_c for different values of p, based on Equation 3.16.

process of a contact with initial stiffness $k_0 = 1.61 \times 10^9\ N/m$. When crack reaches contact domain ($d_c = 2\ mm$) boundary, contact displacement is $\delta_0 = 3\times 10^{-7}\ m$. During rupture process, the measured slope ratio $k_0/k_p = 5$. Plate thickness $t = 1\ m$, and crack growth is governed by p-model with parameters $D_{ini} = 1.0 \times 10^{-5}$, $C = 1.0 \times 10^{-27}\,(\mathrm{m/cycle}/(\mathrm{Pa}\sqrt{\mathrm{m}})^m)$ and $m = 4$.

Figure 5.3b shows G as a function of the ratio of a_c/d_c, with different imposed values of p. For $p = 5$, since it is equal to the measured slope ratio $k_0/k_p = 5$, one gets naturally a constant G, similar to Figure 4.5 in Section 4.3.3.2. For other values, a clear variant effect is observed. For p value is bigger than the measured slope ratio $k_0/k_p = 5$, resultant G evolution is a decreasing curve, and in contrast when p value is smaller than the measured slope ratio $k_0/k_p = 5$, resultant G evolution is a increasing curve.

Furthermore, the resultant values of G for different p in p-model are compared with theoretical result of G. In Figure 5.4, the same test which is performed for Figure 4.5a is presented for different values of p. The average measured slope ratio is $k_0/k_p \approx 2.85$ which induces constant values of G per contact. Figure 5.4a is exactly Figure 4.5a, As shown in Figure 5.4b smaller values of $p = 2.6$, induce increasing G during crack through each contact domain, and the collective results of G are still close to theoretical results.

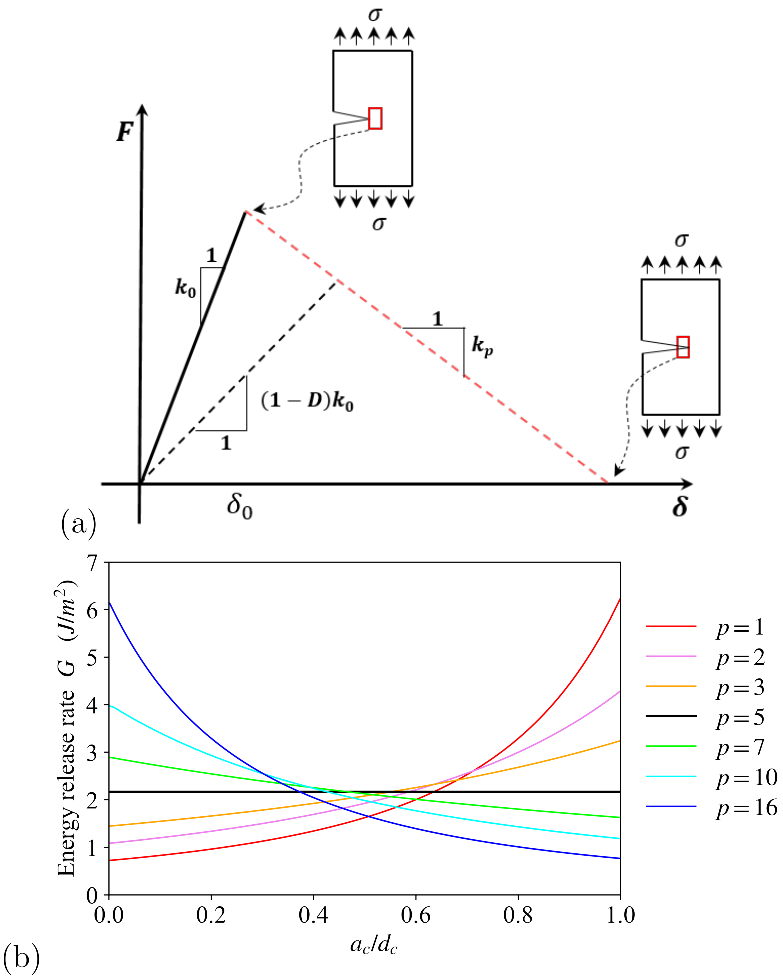

Figure 5.3: (a) Example of a contact in rupture with initial stiffness k_0, when crack reaches its boundary, contact displacement is δ_0. During the rupture process, the measured slope ratio $k_0/k_p = 5$. (b) Corresponding values of energy release rate G for different values of parameter p adopted in Equations 3.23 and 3.24.

One can conclude that when an imposed value of p is adopted in p-model, the calculated value of energy release rate G' in p-model can be expressed as $G' = f(p)G$, where $f(p)$ is an implicit function of p (no expression), and G is the calculated value of energy release rate that of the measured slope ratio k_0/k_p is adopted as the value of p in p-model.

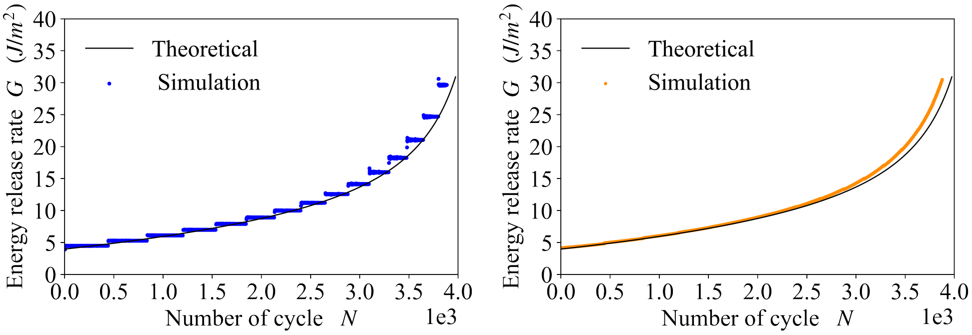

(a) (b)

Figure 5.4: Simulations of a symmetric edge cracked plate with square packed samples and comparison with theoretical results of the energy release rate G under stress controlled fatigue loading for particle size $d = 2\ mm$ (a) p is measured cycle by cycle, generally $p \approx 2.85$ and (b) p is imposed as a parameter, $p = 2.6$.

5.1.2 A variant Paris' law

Paris' law, Equation 2.21, is a power function, the constant power index m is related to the slope of the curve to crack growth rate da/dN and ΔK in logarithmic scale, as shown in Figure 5.1.

For long crack, there exist a clear linear straight stage 2 in Figure 5.1, where Paris' law is suitable. For short crack, Paris' law is not suitable and there does not exist a widely accepted fatigue law [114]. However, there must exist a function can express the relation of short crack growth rate da/dN and ΔK. Instead of a constant power index m and constant parameter C, varying m and C are surely able to display the relation between crack growth rate da/dN and ΔK. For example, C and m are respectively of two unknown function of number of loading cycle N, $C = f(N)$ and $m = g(N)$, then the crack growth rate for short crack can be described as:

$$\frac{da}{dN} = f(N)(\Delta K)^{g(N)} \tag{5.1}$$

Alternatively, one may use another one unknown function $q(N)$ to replace the two unknown function $f(N)$ and $g(N)$ by modifying the base of power function ΔK, Equation 5.1 can be rewritten as:

$$\frac{da}{dN} = C(q(N)\Delta K)^m = C(q(N)GE)^{m/2} \tag{5.2}$$

Theoretically, if the function $q(N)$ is complex enough, the Equation 5.2 can successfully describe the crack growth rate for short crack.

By assuming that G' has the same effect as $q(N)G$, the implicit variant Paris' law 5.2 can be easily realized in p-model, with a proper imposed value of p. It means that the effect of p may enable p-model the ability of modeling short crack propagation.

Continually, assuming the damage development of material is caused by micro-cracks network development which can be represented as a single short crack growth governed by a variant Paris' law (see Figure 5.5). As discussed above (Figure 5.3), the difference between the imposed value of p and the measured slope ratio k_0/k_p leads to variant effect of G which is used in Equation 3.25, and finally results a variant effect of Paris' law.

5.1.3 Contact endurance limit

During fatigue tests, fatigue damage distributes unevenly. For some parts of material subjected to relatively low strain level, fatigue damage is avoided. To take this phenomenon into consideration, a threshold is needed to determine whether a contact is suffering fatigue damage. Thus, a contact endurance limit ε_{lim} is introduced in simulations, based on the concept of fatigue endurance limit, in Section 2.3.2.3. For contacts where the strain level is below the endurance limit $\varepsilon < \varepsilon_{lim}$ no stiffness reductions are developed. In practice, D is not affected by the loading cycles for these contacts.

This parameter, which has a direct physical meaning, adds robustness to the model avoiding unrealistic rupture processes in contacts where the strain is too low or fluctuating around zero.

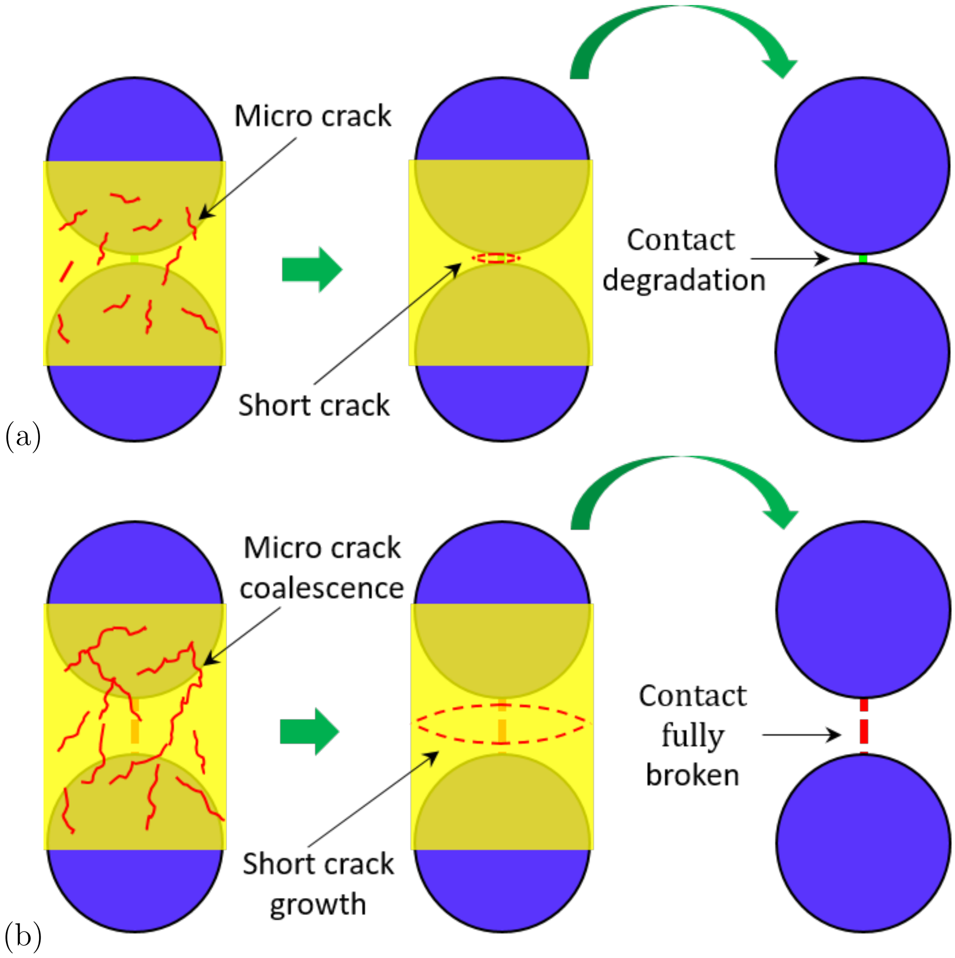
Micro crack
Short crack
Contact degradation
(a)
Micro crack coalescence
Short crack growth
Contact fully broken
(b)

Figure 5.5: Scheme of the equivalent propagated length for an initially micro-cracked contact: (a) initial state of material, and (b) progressive coalescence of cracks.

5.2 Complete damage model (*sp*-model)

Considering the developpements of chapters 3 and 4, and the discussion of the previous section, a damage model to be applied in all contacts identically, where the detection of crack tips is no longer necessary is introduced here.

A simplified p-model, the sp-model is proposed. Two main simplifications related to the parameters d_c (contact domain) and p (slope ratio), specially useful for randomly packed samples, are presented as follows:

- The effective width of the contact domain $d_c = d_{min}$, where d_{min} is the smallest diameter of the two particles composing this contact.

- the parameter p becomes an imposed parameter; an intrinsic property of the contact rupture, instead of a measured quantity.

The damage model contains four parameters: D_{ini}, C, m and p. A constant p enhances the stability and robustness of calculation and enables the model to deal with more complex situations, like multi cracks or crack propagation in softening material caused by damage. It avoids the effects of the fluctuations of the slope ratio expected in these cases. The complete flowchart of the damage model implementation is shown in Figure 5.6.

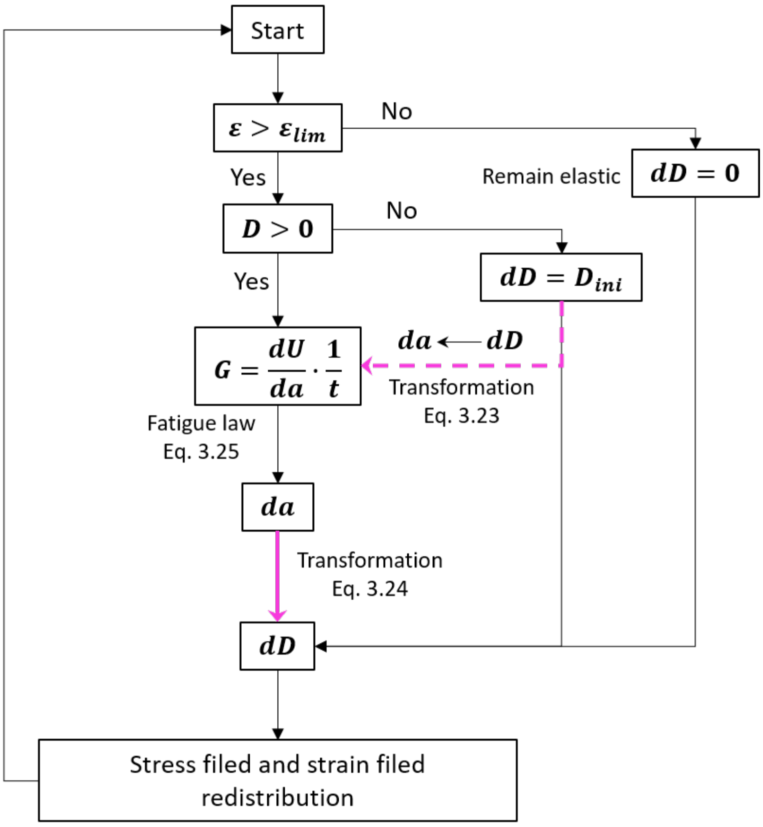
Start
$\varepsilon > \varepsilon_{lim}$
No
Yes
Remain elastic
$dD = 0$
$D > 0$
No
Yes
$dD = D_{ini}$
$G = \frac{dU}{da} \cdot \frac{1}{t}$
$da \leftarrow dD$
Transformation
Eq. 3.23
Fatigue law
Eq. 3.25
da
Transformation
Eq. 3.24
dD
Stress filed and strain filed redistribution

Figure 5.6: Flowchart of the damage model (sp-model) applicable to any couple of interacting particles.

5.3 Simulation approach for fatigue tests in DEM

The quasi-static method (Section 3.7.2) is used to conduct fatigue test simulation. Take 4PB fatigue test simulation as an example, the detailed procedures and principles are depicted in Figure 5.7, moreover, these procedures and principles are also practicable for T-C and 2PB fatigue tests simulation.

Strain loading is applied by four supports located on the neutral axis of the sample (Figure 5.7b), the two end supports are vertically fixed, and the two middle supports move downward till the displacement amplitude $\delta_{v,max}$ is reached. $\delta_{v,max} = 76.7\,\mu m$, $90\,\mu m$ and $100\,\mu m$ correspond respectively to test strain amplitudes $\varepsilon_{max} = 115\,\mu\varepsilon$, $135\,\mu\varepsilon$ and $150\,\mu\varepsilon$.

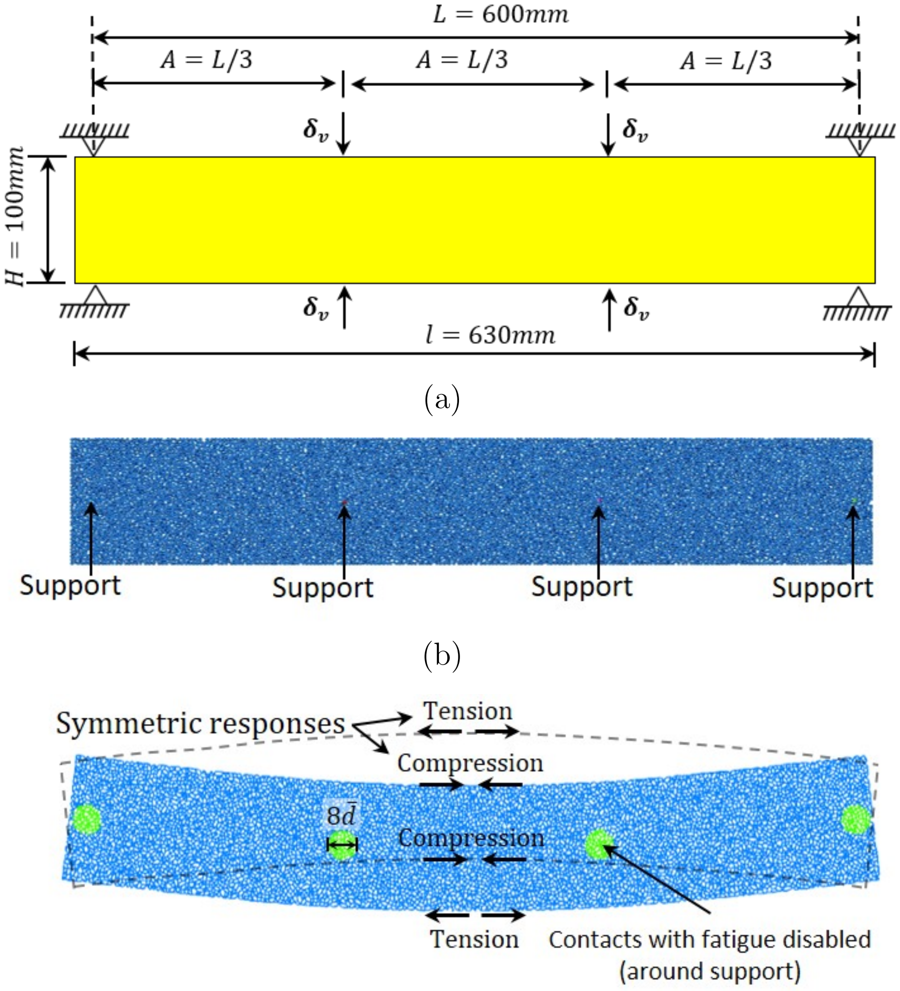
$L = 600mm$
$A = L/3$
$A = L/3$
$A = L/3$
δ_v
δ_v
$H = 100mm$
δ_v
δ_v
$l = 630mm$
Support
Support
Support
Support
Symmetric responses
Tension
Compression
$8\bar{d}$
Compression
Tension
Contacts with fatigue disabled (around support)

(a)

(b)

(c)

Figure 5.7: (a) Geometry of 4PB tests, (b) samples in DEM, and (c) simulation implementation.

Once the two middle supports have been moved downward to achieve the test strain amplitudes ε_{max} (Figure 5.7c), they are vertically fixed to keep the sample in the state of maximum strain level corresponding to the loading peak in experiments. Such a state corresponds to the beam bending downward, with bottom layers under tension and upper layers under compression. Thus only bottom layers are involved in the fatigue process, since material under compression does not experience fatigue. In experiment, beam bends alternately downward and upward, therefore, both upper and bottom layers are subjected to fatigue damage alternately. Of course, alternately moving down and up the two middle supports can be numerically achieved, but such a dynamic movement requires huge computational capacity and is time consuming.

As shown in Figure 5.7c, if material at a position (for example,top at middle span) is under compression when beam bends downward (during the fist half of loading cycle), then it will be under tension when beam bends upward (during the second half of loading cycle), and vice versa. The reacted compression force (during the fist half of loading cycle) and tension force (during the second half of loading cycle) at this position are theoretically equal but with inverse sign.

Given such symmetry, it is easy to represent both states of bending upward and downward by only the state of bending upward or downward. To capture fatigue development of the whole loading cycle, in simulation, keep the sample bending downward and make contacts both under tension and compression to be involved into fatigue process, since the contacts under tension represent material undergoing fatigue process in experiment when beam bends downward (during the fist half of loading cycle) and the contacts under compression represent material undergoing fatigue process when beam bends upward (during the second half of loading cycle). This symmetric responses assumption has been proved in previous studies by Liu [4].

By vertically fixing four supports, the sample keeps in the state of bending downward. Then the *sp*-model is applied to all contacts except for contacts in four circled regions surrounding supports (Figure 5.7c). These four fatigue free regions are set to avoid unrealistic fatigue development caused by stress concentration near supports.

With *sp*-model, fatigue development is represented by contact degradation increment dD. After each ‘loading cycle’, contact stiffness is updated, and stress and strain fields in sample are redistributed. Contact dissipated energy is used to calculate the energy release rate G by which contact degradation increment dD for next ‘loading cycle’ is determined. These steps are repeated to continue fatigue evolution till final failure. Globally, during the whole simulation, the sample keeps bending downward, it is like static, however, locally, its stress and strain fields slowly change for every ‘loading cycle’. That is the quasi-static method to model fatigue test. It is also adopted in T-C and 2PB fatigue tests simulation.

5.4 Modeling of Tension-Compression fatigue test

Simulation results are compared with experimental results [1] of Tension-Compression fatigue tests (see Section 2.3.2.1). Configuration setup and equipment are shown in Figure 5.8. Cylindrical specimens with dimensions of height 140 mm and diameter 75 mm are tested respectively for strain amplitudes 79 $\mu\varepsilon$, 92 $\mu\varepsilon$ and 108 $\mu\varepsilon$, at temperature 10°C with frequency $f = 10\ Hz$.

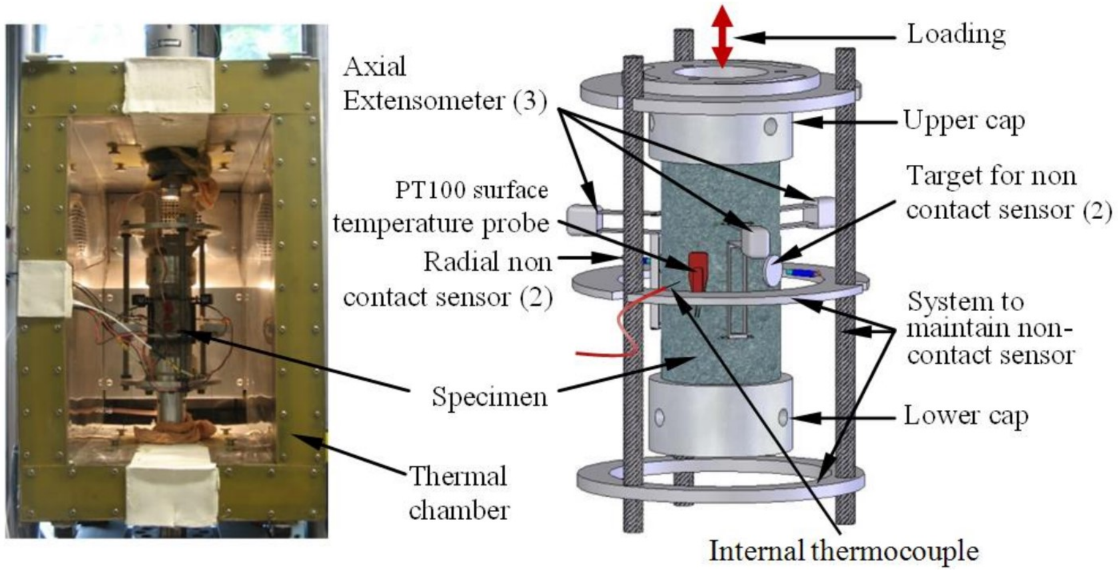
Axial
Extensometer (3)
PT100 surface
temperature probe
Radial non
contact sensor (2)
Specimen
Thermal
chamber
Loading
Upper cap
Target for non
contact sensor (2)
System to
maintain non-
contact sensor
Lower cap
Internal thermocouple

(a) (b)

Figure 5.8: (a) Configuration of T-C test, and (b) details of test equipment. (Modified from [8])

Three randomly packed samples with average particle diameter $\overline{d} = 1mm$, $d_{min} = 0.78mm$ and $d_{max} = 1.23mm$, are generated for simulations (sample generation procedures are detailed in Appendix B). Material Young’s modulus is considered as $E = 16489$ MPa, the average value of initial modulus of specimens in experimentation, and the contact stiffness setting are calibrated as $E_{cmod} = 1.21 \times E$ and $k_{ratio} = 1.0$, based on tension tests. Since simulations are in two dimensions $2D$ method, the cylinder is considered as an isopachous plate with width equal to cylinder diameter $75\,mm$ and thickness $t = 75\pi/4\,mm$ by which the intersection area is same as the cylinder.

5.4.1 Effect of the parameter p

In this section, the effect of p is analysed. Adopted sp-model parameters are gathered in Table 5.1. In Figure 5.9, simulations of tension-compression fatigue tests with different values of $p = 1, 3, 5, 7, 10$ are shown.

Table 5.1: Set of parameters for simulations testing the effect of p.

ε_{lim}	D_{ini}	C (m/cycle/(Pa$\sqrt{\text{m}}$)^m)	m
$70\,\mu\varepsilon$	1×10^{-4}	2.03×10^{-48}	8

The parameter p has a strong influence on both fatigue life and the shape of fatigue evolution curve, as shown in Figure 5.9. When p decreases, the fatigue life dramatically increases (see Figure 5.9a), the turn point of fatigue evolution curves occur at higher level of stiffness ratio (expressed as the ratio of the reaction force to the initial reaction force, F/F_0) and the accelerated part of fatigue evolution curves become steeper (see Figure 5.9b), which means the final failure caused by macro crack propagation occurs earlier and more sudden.

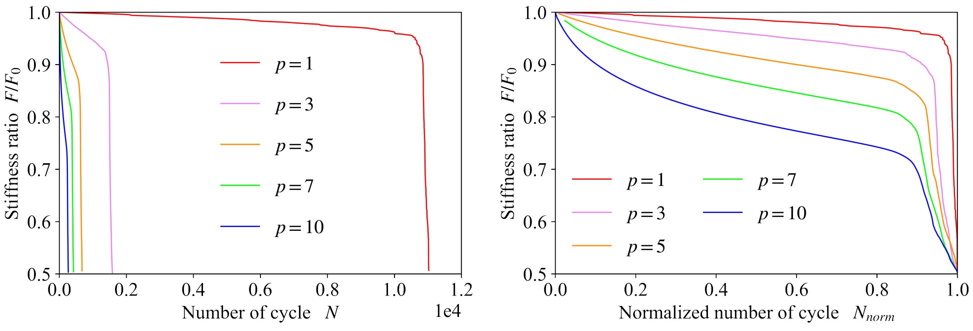

(a) (b)

Figure 5.9: (a) Fatigue evolution expressed by the stiffness ratio (represented as the ratio of the reaction force to the initial reaction force, F/F_0) as a function of the number of cycle N for different values of parameter p, and (b) stiffness ratio versus the normalized number of cycle.

Generally, a lower p indicates a more concentrated fatigue damage distribution. On the contrary, a higher p leads to more distributed fatigue damage, as shown in Figure 5.10.

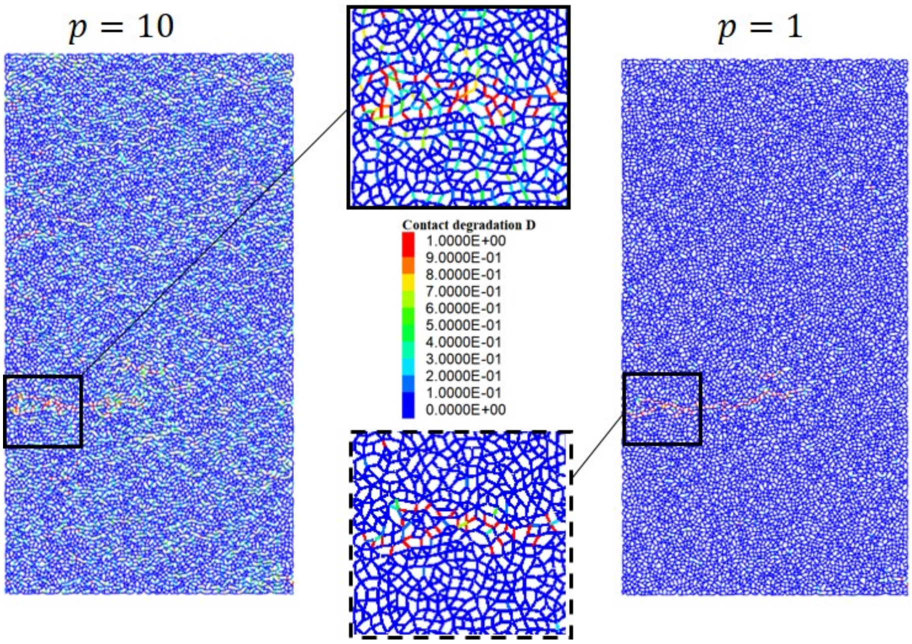

Figure 5.10: Effect of parameter p on fatigue damage distribution at stiffness ratio $F/F_0 = 0.5$, where red means totally broken and blue means intact.

5.4.2 Effect of the contact endurance limit

The effect of the contact endurance limit is investigated here. Adopted *sp*-model parameters are gathered in Table 5.2 with two aditional values of contact endurance limit $\varepsilon_{lim} = 50\,\mu\varepsilon$ and $80\,\mu\varepsilon$. Figure 5.11 shows results for three different imposed strain levels $79\,\mu\varepsilon$, $92\,\mu\varepsilon$ and $108\,\mu\varepsilon$.

Table 5.2: Model parameters for T-C fatigue tests simulations (without scaling).

ε_{lim}	D_{ini}	p	$C\,(\mathrm{m/cycle/(Pa\sqrt{m})^m})$	m
$70\,\mu\varepsilon$	1×10^{-4}	10	1.41×10^{-51}	8

As shown in Figure 5.11, despite a slight decrease of the stiffness reduction before fatigue evolution curve turning acceleration, a larger contact endurance limit ε_{lim} tends to decrease the fatigue life by hastening the strain localization leading to a global rupture. Larger cracks dominate the fatigue process causing a more brittle behaviour of the sample. This effect is more visible for lower strain limits because larger zones of the sample become simply elastic, inducing an even bigger localization of strain at crack tips.

In Figure 5.11c, the fatigue process is observed even for a strain level below the contact endurance limit. It is simply explained by the heterogeneity of the random pack structure of the sample, where strain can be locally larger than the average imposed on the sample.

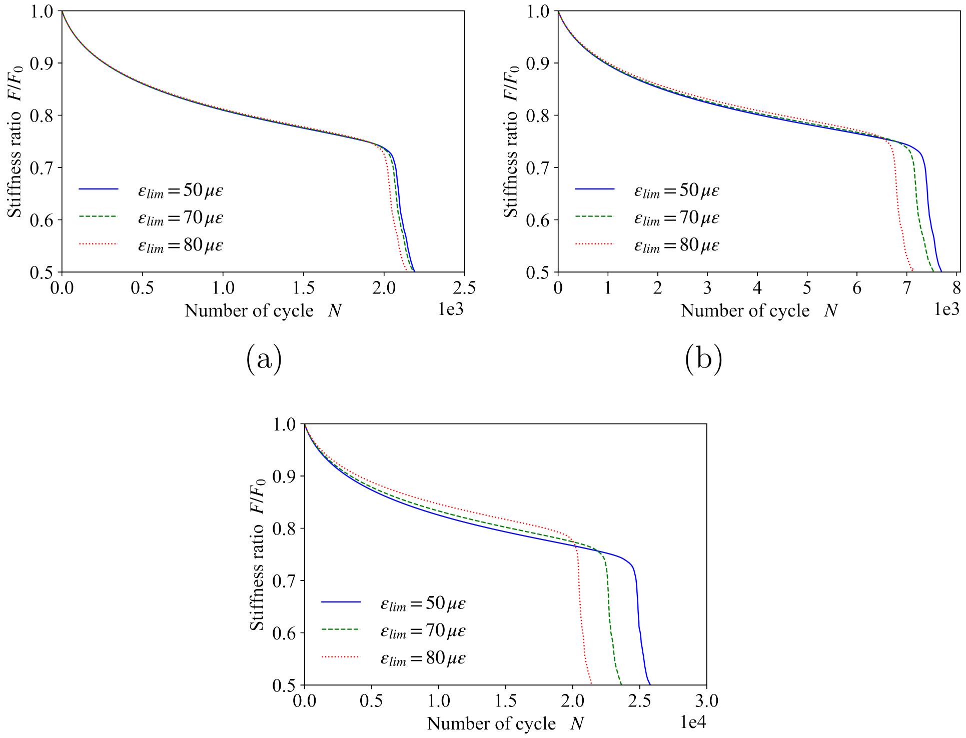

(a)

(b)

(c)

Figure 5.11: Comparison of results for different levels of contact endurance limit ε_{lim}, for test strain levels respectively (a) 108 $\mu\varepsilon$, (b) 92 $\mu\varepsilon$ and (c) 79 $\mu\varepsilon$.

The original purpose to introduce the contact endurance limit ε_{lim} is to control the range of contact involved in the damage process. From this point of view, expressing the material endurance limit as a contact endurance limit is reasonable, in a certain extent. When material subjected to a loading condition below its endurance limit, even though its mechanical properties still slowly change with number of loading cycles increase, these change are reversible due to non-linearity, self-healing and thixotropy. Thus, we can consider contact is undamaged under loading condition below the contact endurance limit.

5.4.3 Simulation versus experimental results of T-C fatigue tests

Simulations results are compared to experimental results of [1] in Figure 5.12. The model parameters are indicated in Table 5.2.

5.4.3.1 Scaling technique

To save simulation time, the scale effect of parameter C is used (discussed in Appendix G). For example, setting parameter C value 100 times larger than its nominal value in Table 5.2, will accelerate simulation 100 times. Thus, after simulation, the fatigue evolution curve should be scaled by a factor of 100 times. For T-C fatigue test simulation results are shown in Figure 5.12, a scaling factor of 144 was chosen.

Good agreement are obtained between simulations and experimental results of T-C fatigue tests. In Figure 5.13, the crack distribution of the three samples after a fatigue test with strain level of 108 $\mu\varepsilon$ is presented. In Figure 5.13a a distributed damage coexists with main crack, which shows the model capability of dealing with complex fatigue processes. More details about fatigue evolution expressed by the reaction force F are disclosed in Appendix H.

Fatigue lines of experiments and simulations are shown in Figure 5.14. The slopes of fatigue lines in log-log scale coordinates for experimental results is -7.9873 and -7.6732 for simulation, which is close to the value of parameter $m = 8$. The linearity of fatigue lines are expressed by the coefficient of determination $R^2 = 0.9981$ for experimental results and $R^2 = 0.9868$ for simulation, these values are close to 1 which means totally straight line. The test strain level ε_6 corresponding to fatigue life equal $N = 1.0 \times 10^6$, for experiments $\varepsilon_6 = 92.11\,\mu\varepsilon$, and $\varepsilon_6 = 92.37\,\mu\varepsilon$ for simulation.

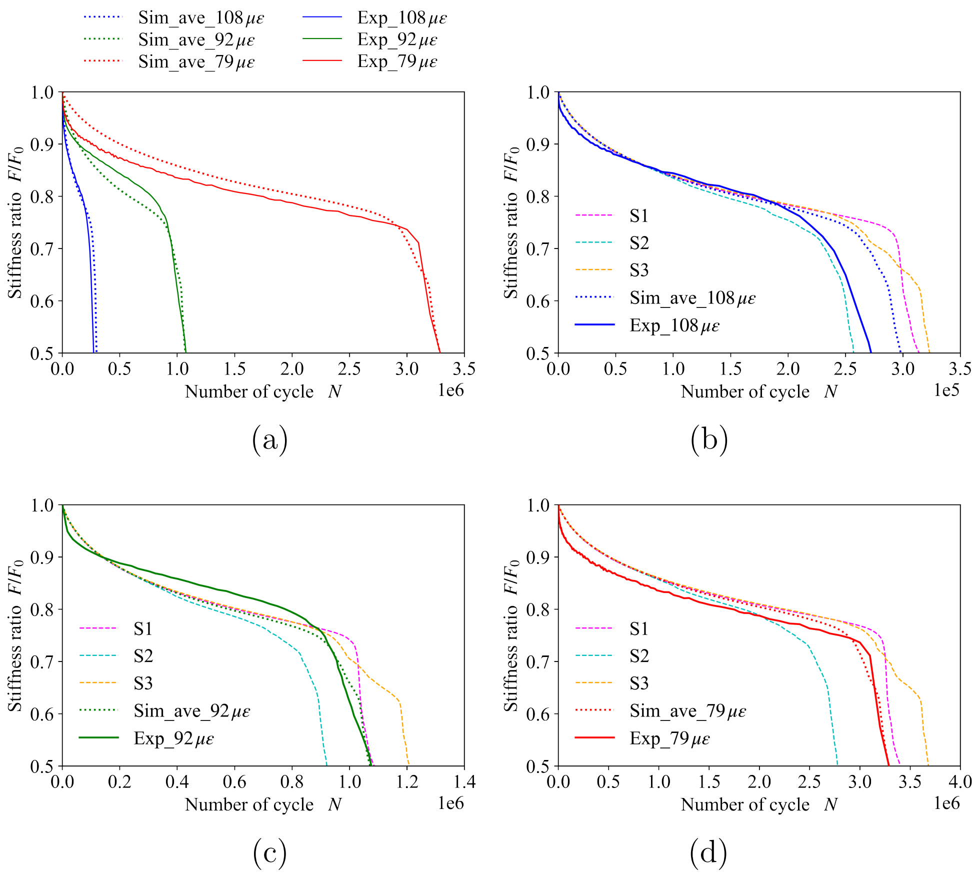

(a) (b)

(c) (d)

Figure 5.12: T-C fatigue tests simulation results, (a) comparison of average simulation results (three samples) and experimentation [1] with different test strain levels, and fatigue evolution of all three samples (S1, S2 and S3) with strain levels respectively (b) 108 $\mu\varepsilon$, (c) 92 $\mu\varepsilon$ and (d) 79 $\mu\varepsilon$.

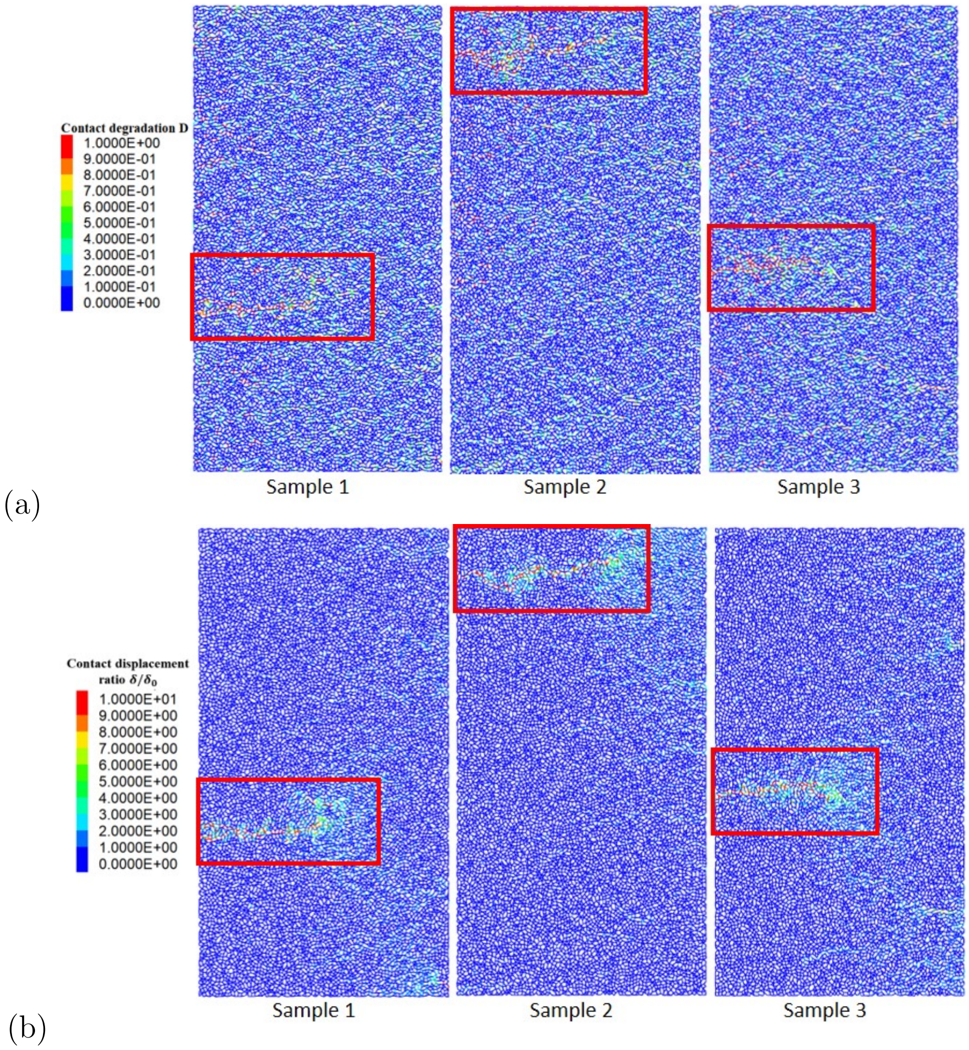

Figure 5.13: Crack distribution maps of all three samples, (a) contact degradation map (where red is totally broken and blue is intact), and (b) contact opening map representing by the ratio of the contact displacement δ at stiffness ratio $F/F_0 = 0.5$ to the contact displacement at test beginning $(F/F_0 = 1)$ δ_0 (where red means $\delta/\delta_0 \geq 10$ and blue means $\delta/\delta_0 = 0$), for simulation with strain level $108\,\mu\varepsilon$.

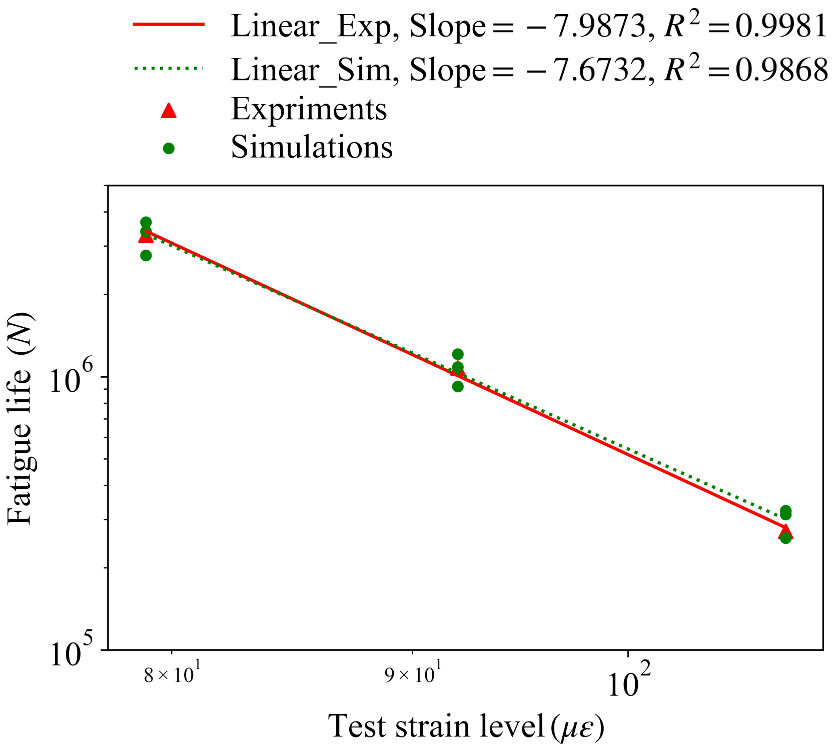

Figure 5.14: Fatigue lines of experiments and simulation for T-C fatigue tests. The slopes of fatigue lines in log-log scale coordinates and the coefficient of determination R^2 are presented.

5.5 4PB fatigue tests

The 4PB fatigue test experiments performed by Nguyen [150] are parts of the project *SolDuGri* funded by the French National Research Agency (ANR).

The dimensions of test specimens are presented in Figure 5.7a, the test beam has a total length $l = 630\,mm$, with height $H = 100\,mm$ and thickness $t = 100\,mm$. Three strain amplitudes are applied in strain controlled tests, $150\,\mu\varepsilon$, $135\,\mu\varepsilon$ and $115\,\mu\varepsilon$, at temperature $10°C$ with frequency $f = 25\ Hz$.

As mentioned in Chapter 2, in test, the relation between the displacement amplitude on the middle two points $\delta_{v,max}$ and the resultant strain amplitude in upper and bottom layers of beam at middle span ε_{max} can be described by (Equation 2.1):

$$\delta_{v,max} = \frac{5}{3}\frac{A^2}{H}\varepsilon_{max}. \tag{5.3}$$

And the corresponding reaction force F_v can be obtained by (Equation 2.2):

$$F_v = \frac{6}{5}\frac{EI}{A^3}\delta_{v,max}, \tag{5.4}$$

where A is distance between two loading points (Figure 5.7a), E is Young's modulus, I is moment inertia and H is the height of beam intersection.

Three randomly packed samples with average particle diameter $\overline{d} = 1.5mm$, $d_{min} = 1.15mm$ and $d_{max} = 1.85mm$, are generated for simulations. Material Young's modulus is taken as $E = 13894$ MPa (average value of initial modulus in experiments) and the contact stiffness settings are calibrated as $E_{cmod} = 1.43 \times E$ and $k_{ratio} = 1.0$, based on the reaction force and corresponding displacement of supports in bending tests (Equation 5.4).

5.5.1 Simulation results of 4PB tests

Simulation parameters are gathered in Table 5.3, and 875 times scaling is chosen (see Section 5.4.3.1). Comparison between simulation and experimentation is shown in Figures 5.15 and 5.16. More details about fatigue evolution expressed by the reaction force F are shown in Appendix H.

Figures 5.15 globally shows the good agreement between simulations and experiments for different test strain levels, which evidences the validation of *sp*-model. In Figure 5.16, the envelop curves of the experimental results and simulations are superposed well, which indicates the simulations for different

Table 5.3: Parameter setting for 4PB fatigue tests simulations.

ε_{lim}	D_{ini}	p	C (m/cycle/(Pa$\sqrt{\text{m}}$)^m)	m
70 $\mu\varepsilon$	1×10^{-4}	4.5	5.71×10^{-38}	5.5

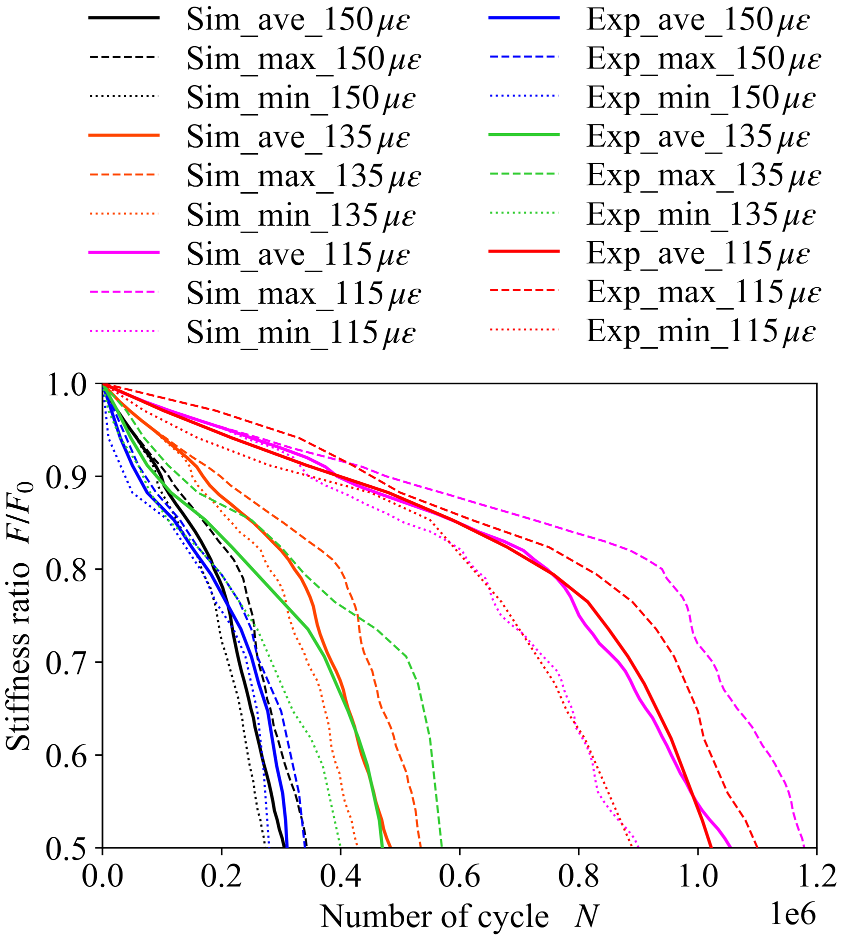

Figure 5.15: Comparison between envelop curves and average curves of 4PB fatigue test simulations and that of experiments [150], for different test strain levels. For example, Sim_ave_ 115 $\mu\varepsilon$ is the average curve of simulation of all three samples at test stain level 115 $\mu\varepsilon$, Sim_max_ 115 $\mu\varepsilon$ is the maximum boundary of the envelop of all simulations at test stain level 115 $\mu\varepsilon$, and sign of min for the minimum boundary of the envelop of all simulations. So that for experimental results with sign Exp.

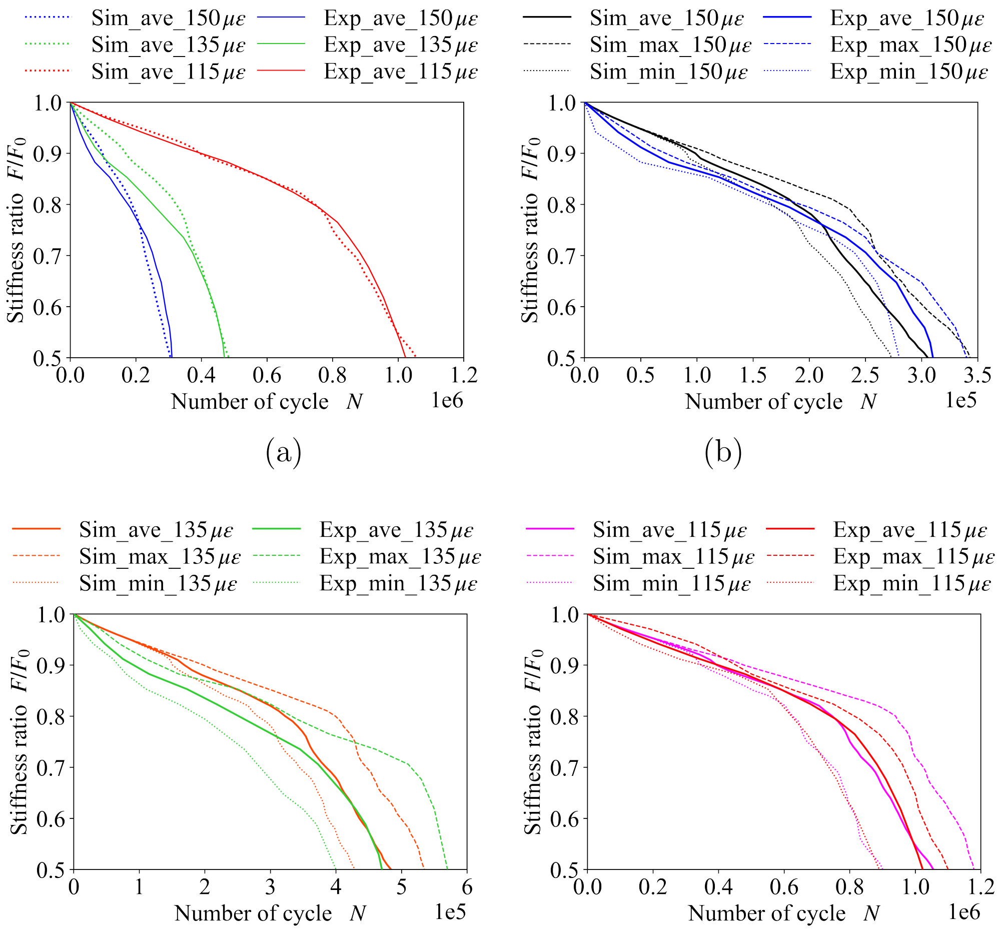

(a) (b)

(c) (d)

Figure 5.16: Comparison between 4PB fatigue test simulations and experiments [150], (a) average curves for different test strain levels, (b) average and envelop curves for test strain level 150 $\mu\varepsilon$, (c) 135 $\mu\varepsilon$ and (d) 115 $\mu\varepsilon$. For example, Sim_ave_ 115 $\mu\varepsilon$ is the average curve of simulation of all three samples at test stain level 115 $\mu\varepsilon$, Sim_max_ 115 $\mu\varepsilon$ is the maximum boundary of the envelop of all simulations at test stain level 115 $\mu\varepsilon$, and sign of min for the minimum boundary of the envelop of all simulations. So that for experimental results with sign Exp.

samples have the same disparity of the experiments for different specimen. It not just confirms the ability of *sp*-model for modeling fatigue tests but also supports the advantage of DEM in reproducing material heterogeneity and micro structures.

Figure 5.17 presents the damage distribution and crack trajectories in samples, one may notice the similarity among these samples that damage and small crack are distributed mainly near the top and bottom of sample with one or two main cracks indicating the final failure of sample.

Fatigue lines of experiments and simulations are shown in Figure 5.18. The slopes of fatigue lines in log-log scale coordinates for experimental results is -4.5100 and -4.6744 for simulation, which is close to the value of parameter $m = 5.5$. The linearity of fatigue lines are expressed by the coefficient of determination $R^2 = 0.9533$ for experimental results and $R^2 = 0.9627$ for simulation, these values are close to 1 which means totally straight line. The test strain level ε_6 corresponding to fatigue life equal $N = 1.0 \times 10^6$, for experiments $\varepsilon_6 = 115.09\,\mu\varepsilon$, and $\varepsilon_6 = 115.97\,\mu\varepsilon$ for simulation.

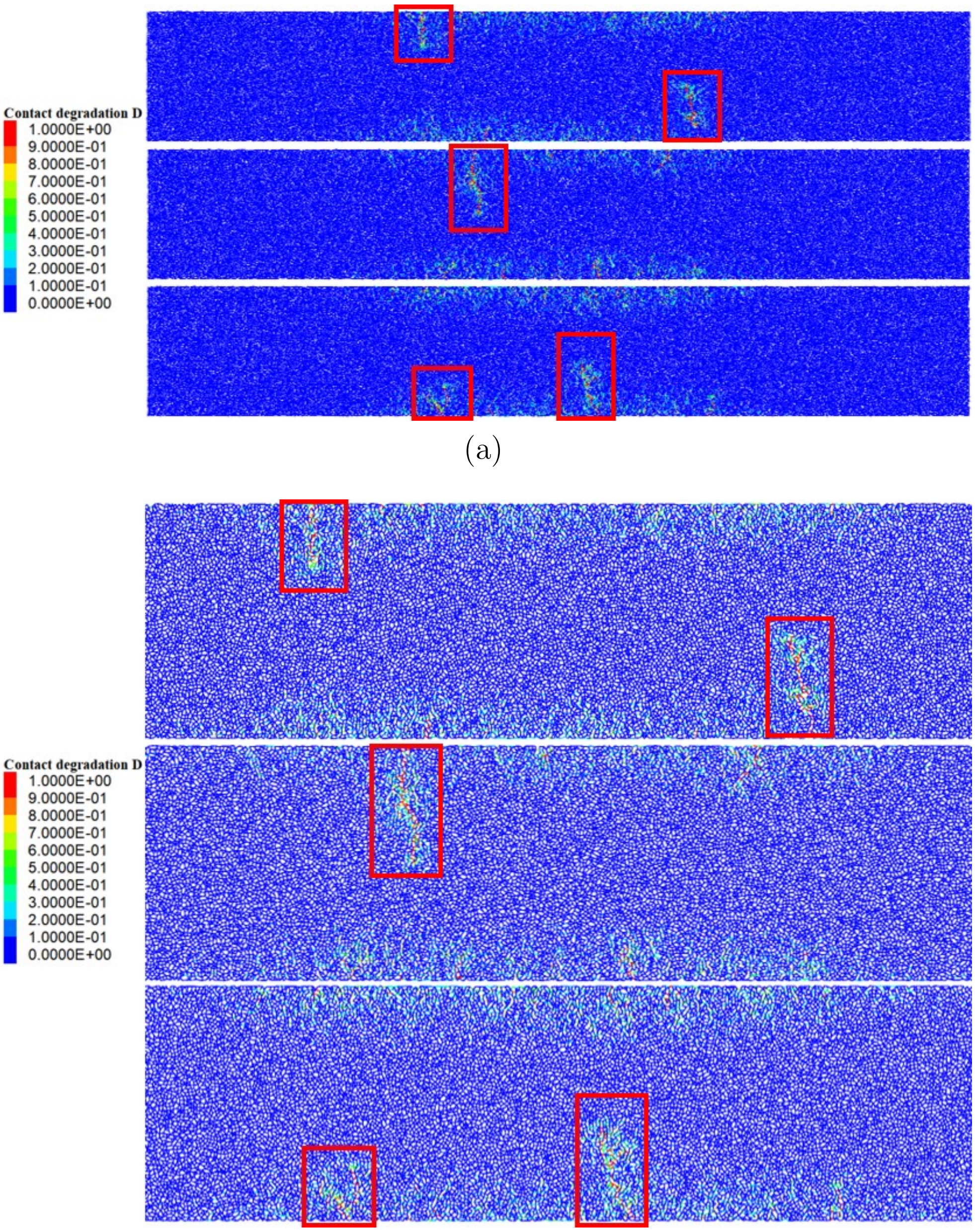

(a)

(b)

Figure 5.17: (a) Damage distribution maps (where red is totally broken and blue is intact) for all three samples at stiffness ratio $F/F_0 = 0.5$, for test strain level $150\,\mu\varepsilon$, (b) corresponding zoom of (a). Main cracks are marked by red rectangular.

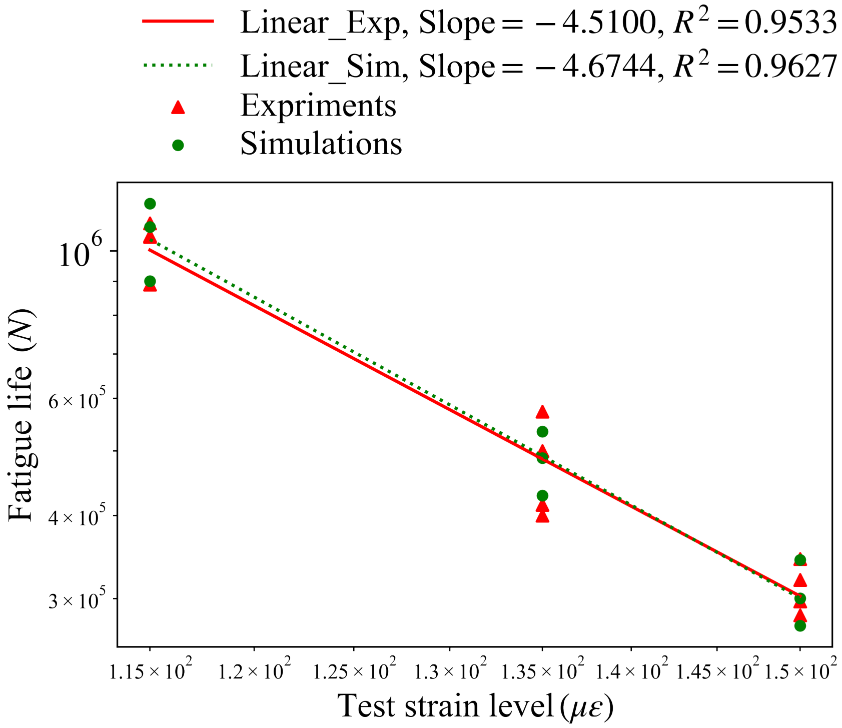

Figure 5.18: Fatigue lines of experiments and simulation for 4PB fatigue tests. The slopes of fatigue lines in log-log scale coordinates and the coefficient of determination R^2 are presented.

5.6 2PB fatigue tests

The 2PB fatigue tests experiments performed by Nguyen [150] are parts of the project *SolDuGri* funded by the French National Research Agency (ANR).

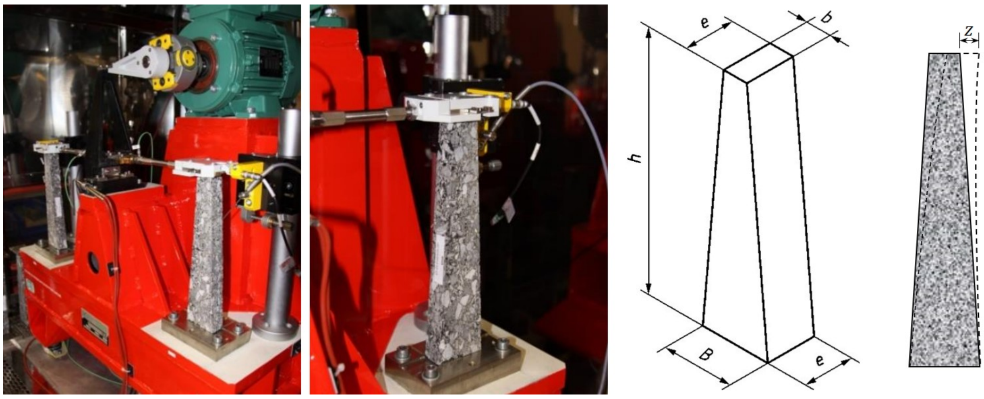

(a) (b) (c)

Figure 5.19: (a) Configuration of 2PB fatigue test, (b) details of test sample, and (c) sample dimension and test scheme. (Modified from [8, 151])

The 2PB test configuration and equipment are shown in Figure 5.19. The dimensions of test specimens as shown in Figure 5.19c are a wide base $B = 56\,mm$, with narrow base $e = 25\,mm$, width on top $b = 25\,mm$ and a total height $h = 250\,mm$. Three strain amplitudes are applied in strain controlled tests, $160\,\mu\varepsilon$, $130\,\mu\varepsilon$ and $100\,\mu\varepsilon$, at temperature $10°C$ with frequency $f = 25\ Hz$.

The relation between the displacement amplitude on the top of sample z (Figure 5.19c) and the corresponding strain amplitude ε_{max} can be described by [151]

$$\varepsilon_{max} = \frac{z\,(B-b)^2}{8bh^2\left[\frac{(b-B)(3B-b)}{2B^2} + \ln\frac{B}{b}\right]}, \tag{5.5}$$

and the corresponding reaction force F can be obtained by [152]:

$$F = \frac{zEe(B-b)^3}{12h^3\left[\left(2-\frac{b}{2B}\right)\frac{b}{B} - \frac{3}{2} - \ln\frac{b}{B}\right]} \tag{5.6}$$

where h, B, b, e are sample dimensions as shown in Figure 5.19c, and E is Young's modulus of material.

Three randomly packed samples with average particle diameter $\overline{d} = 1.5mm$, $d_{min} = 1.15mm$ and $d_{max} = 1.85mm$, are generated for simulations. Material Young's modulus is considered as $E = 16254$ MPa (average value of initial modulus in experiments) and the contact stiffness setting are calibrated as $E_{cmod} = 1.30 \times E$ and $k_{ratio} = 1.0$, based on the reaction force and corresponding displacement of supports in bending tests (Equation 5.6).

5.6.1 Simulation results of 2PB tests

Simulation parameters gathered in Table 5.4, and 1350 times scaling is chosen (see Section 5.4.3.1). Comparison between simulation and experimentation is shown in Figures 5.20 and 5.21. More details about fatigue evolution expressed by the reaction force F are shown in Appendix H.

Table 5.4: Parameter setting for 2PB fatigue tests simulations.

ε_{lim}	D_{ini}	p	C (m/cycle/(Pa$\sqrt{\text{m}}$)^m)	m
$70\,\mu\varepsilon$	1×10^{-4}	4.5	3.7×10^{-38}	5.5

Damage distribution and crack trajectories in all three samples are presented in Figure 5.22.

It should be mentioned that in experimentation the same material is used for 4PB and 2PB fatigue tests. As a consequence, one may notice that almost all simulation parameters settings are identical for 4PB and 2PB fatigue tests, except slight differences on parameter C which may relate to the slight difference of material void content, around 4.5% for the 2PB fatigue tests and 2% for the 4PB fatigue tests. And fatigue evolution curves are less dispersed for 4PB than 2PB fatigue tests.

Fatigue lines of experiments and simulations are shown in Figure 5.23. The slopes of fatigue lines in log-log scale coordinates for experimental results is -6.6000 and -4.8279 for simulation, which is close to the value of parameter $m = 5.5$. The linearity of fatigue lines are expressed by the coefficient of determination $R^2 = 0.8688$ for experimental results and $R^2 = 0.9129$ for simulation. The relatively lower value of R^2 for experiments indicates the disparity of fatigue evolution for different specimens at same test strain level, which also can be reflected from the scattered fatigue evolution curves in Figure 5.21. The test strain level ε_6 corresponding to fatigue life equal $N = 1.0 \times 10^6$, for experiments $\varepsilon_6 = 117.49\,\mu\varepsilon$, and $\varepsilon_6 = 120.73\,\mu\varepsilon$ for simulation.

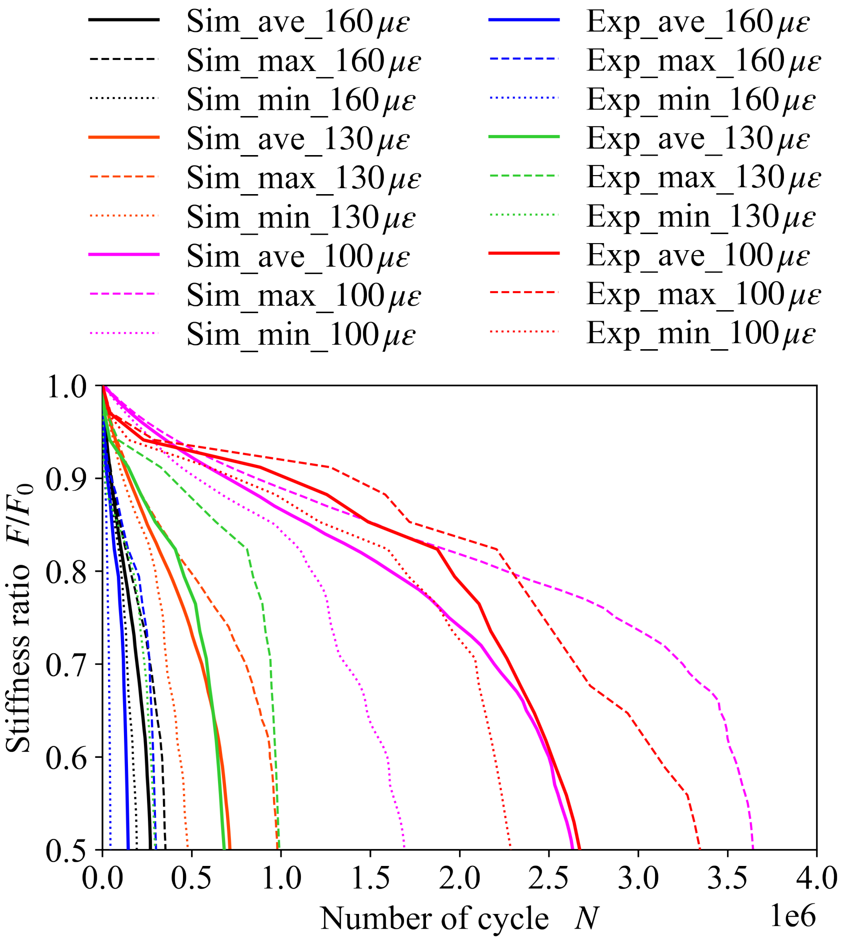

Figure 5.20: Comparison between envelop curves and average curves of 2PB fatigue tests simulation and that of experimentation [150], for different test strain levels. For example, Sim_ave_ 160 $\mu\varepsilon$ is the average curve of simulation of all three samples at test stain level 160 $\mu\varepsilon$, Sim_max_ 160 $\mu\varepsilon$ is the maximum boundary of the envelop of all simulations at test stain level 160 $\mu\varepsilon$, and sign of min for the minimum boundary of the envelop of all simulations. So that for experimental results with sign Exp.

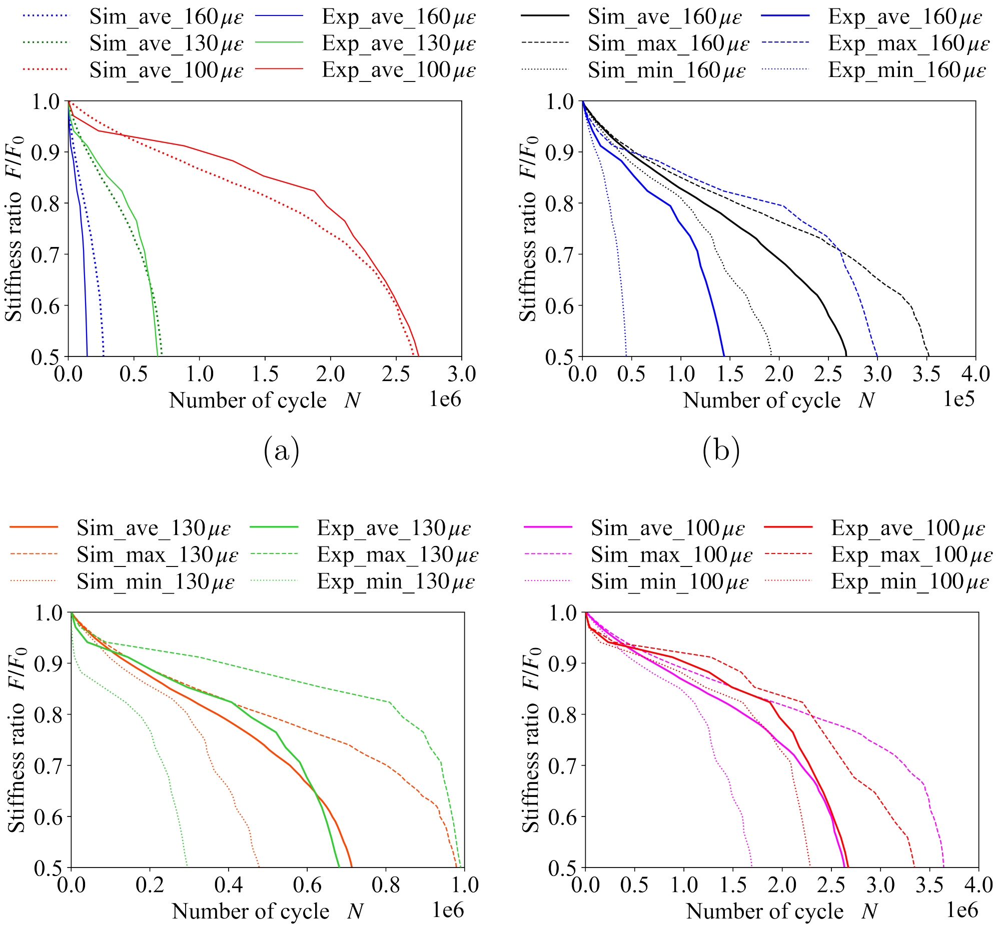

(a) (b)

(c) (d)

Figure 5.21: Comparison between 2PB fatigue tests simulation and experimentation [150], (a) average curves for different test strain levels, (b) average and envelop curves for test strain level 160 $\mu\varepsilon$, (c) 130 $\mu\varepsilon$ and (d) 100 $\mu\varepsilon$. For example, Sim_ave_ 160 $\mu\varepsilon$ is the average curve of simulation of all three samples at test stain level 160 $\mu\varepsilon$, Sim_max_ 160 $\mu\varepsilon$ is the maximum boundary of the envelop of all simulations at test stain level 160 $\mu\varepsilon$, and sign of min for the minimum boundary of the envelop of all simulations. So that for experimental results with sign Exp.

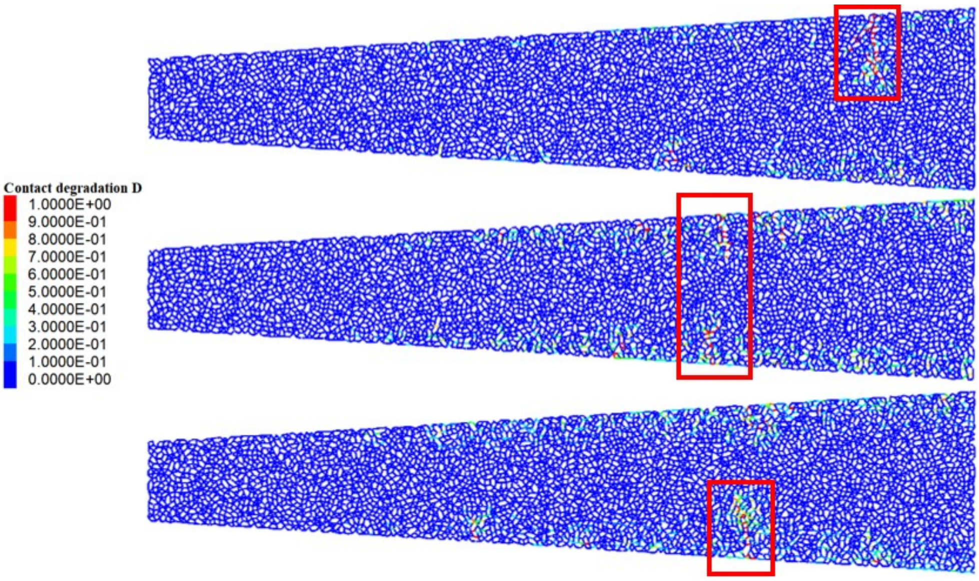

Figure 5.22: Damage distribution maps (where red is totally broken and blue is intact) for all three samples (90° rotated) at stiffness ratio $F/F_0 = 0.5$, for test strain level $160\,\mu\varepsilon$. Main cracks are marked by red rectangular.

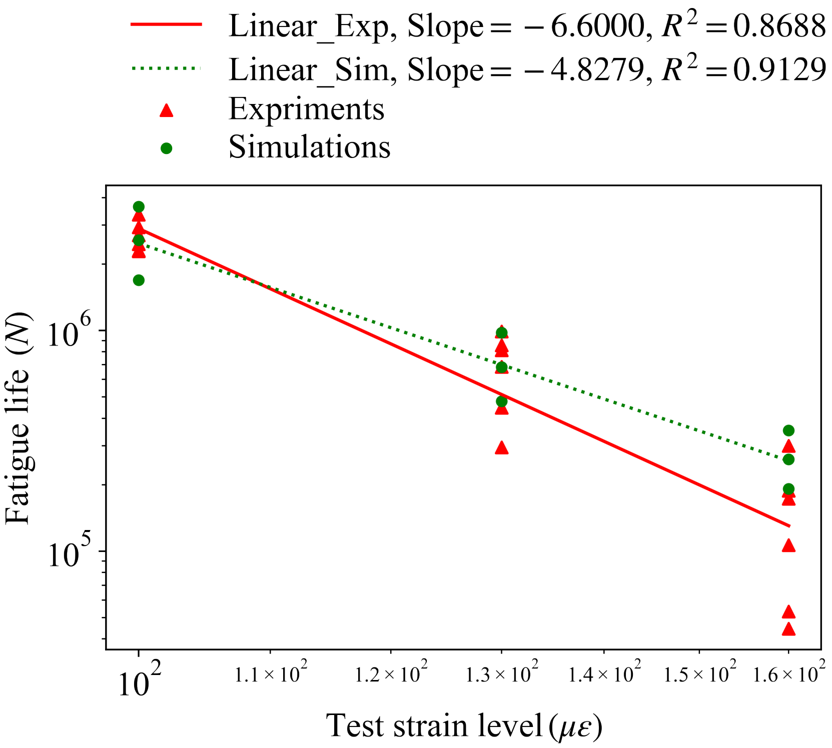

Figure 5.23: Fatigue lines of experiments and simulation for 2PB fatigue tests. The slopes of fatigue lines in log-log scale coordinates and the coefficient of determination R^2 are presented.

5.7 Summary of the chapter

In this chapter, a damage model (*sp*-model) is proposed based on the crack propagation model (*p*-model). It can be employed by all contacts. The collective response of all these contacts (governed by *sp*-model) successfully reflects the fatigue evolution of the whole sample, in both sample stiffness evolution and damage distribution.

A parameter p was introduced in *sp*-model, it directly performs in $da - dD$ transformation (Equations 3.23 and 3.24). For a contact, the amount of the difference between parameter p and its slope ratio k_0/k_p finally has effect on the fatigue rate of this contact. When $p > k_0/k_p$, it leads to a decrease effect on the fatigue rate, and with larger amount of $p - k_0/k_p$, the stronger decrease tendency. On the contrast, when $p < k_0/k_p$, it leads a increase effect on the fatigue rate.

During fatigue test simulation, all contacts behavior are governed by *sp*-model with a constant value of parameter p. Contacts at different positions, near or far from a crack tip, also the surrounding micro structures, have different values of the slope ratio k_0/k_p. Also, with fatigue simulation going, the slope ratio of a contact may change due to degradation of surrounding contacts. That is parameter p keeping constant, while contacts slope ratio changes, which means the amount of the difference between parameter p and contact slope ratio k_0/k_p changes and consequently the fatigue rate of contact changes. The collective fatigue evolution of all contacts finally behaves as the fatigue process of the whole sample.

Good agreements are observed in comparison of simulation and experiment for T-C, 4PB and 2PB fatigue tests. Using the *sp*-model in DEM successfully catches both the fatigue evolution and localized failure in fatigue tests. Also it works well for different test strain levels. Based on the scale effect of parameter C, a scale technique is used in simulations. It can efficiently save computational time.

CHAPTER 6

Conclusions and perspectives

Contents

6.1 Conclusions 123
6.2 Perspectives 124

6.1 Conclusions

In this work, a contact model based on the local release of energy is developed for discrete element simulations of fatigue behavior with applications to asphalt concrete samples.

The discrete element method allows a consistent representation of heterogeneous materials, which leads to more realistic failure processes with localized crack development. As outlined in Chapter 2, two aspects are necessary to properly model fatigue crack propagation: firstly, the capacity of representing small crack increments and, secondly, the evaluation of the energy release rate. For the whole fatigue evolution, the crack initiation must naturally be also considered.

The two main problems for modeling crack propagation, are solved in Chapter 3. The proposed relation between propagation length da and stiffness reduction dD allows the representation of any amount of crack growth, much below the particle scale. This is a fundamental feature for fatigue crack propagation, which is based on tiny increments per loading cycle. This description is supported by the evaluation of the energy release, another key element in the large majority of fracture models. Paris' law is then simply incorporated composing a contact model for fatigue crack growth, called here p-model.

Another important advantage of p-model relay on its local evaluation of the energy release rate, which is a key element in a discrete element contact model. The rupture of the contact at the crack tip is triggered by a small initial stiffness degradation D_{ini} and the subsequent evolution is defined by the direct evaluation of contact forces and displacements. Convergent results were obtained for regular particle packings with progressive reduction of the particle diameter, which confirms the consistency of the formulation in Chapter 4.

In Chapter 5, the effect of the slope rate p is identified on the evaluation of the energy release rate G. Imposed values (instead of the measured values in p-model) leads to the control of the variation of G inside a contact. This micro-structural effect is incorporated in a damage model, called here sp-model. Such model is defined to be applied in all contacts, independently to the existence of initial cracks. This important feature allows a complete description of the rupture process dealing with crack initiation and its subsequent propagation with a single and simple approach. The simulations of experiments of tension-compression, 2-point and 4-point bending tests of asphalt concrete show very good agreements with different strain amplitudes.

6.2 Perspectives

Considering the models proposed in this thesis, several extensions and new applications are worth of more investigation in the future. In particular:

- Phenomena like non-linearity, self-heating and thixotropy, which affects the fatigue response of asphalt materials, can be further discriminated.
- The effect of the granulometry may lead to more complex crack patterns and deserves further analysis.
- The simple extension of the proposed models for three dimensional samples may also cover more complex multi-cracking process.
- The fatigue response of other materials should be analyzed considering the generality of the formulation.

Appendix A

Discrete element method

A.0.1 Algorithm of DEM calculation [101]

Discrete element method (DEM) is a numerical model capable of describing the mechanical behavior of assemblies of discs and spheres. It allows finite displacements and rotations of discrete particles, detects new contacts automatically as the calculation progresses, and solves the time evolution of this discrete system using an explicit dynamic solution to Newton's laws of motion. The fundamental elements for calculation are the dimensions of the particles, their spatial positions and properties.

Being a time-stepping formulation, as the simulation progresses, the model state is advanced in time by a series of calculation cycles. In each single calculation cycle, five operations are executed successively, including the timestep determination, law of motion, advance time, contact detection and force-displacement law, as shown in Figure A.1 [144].

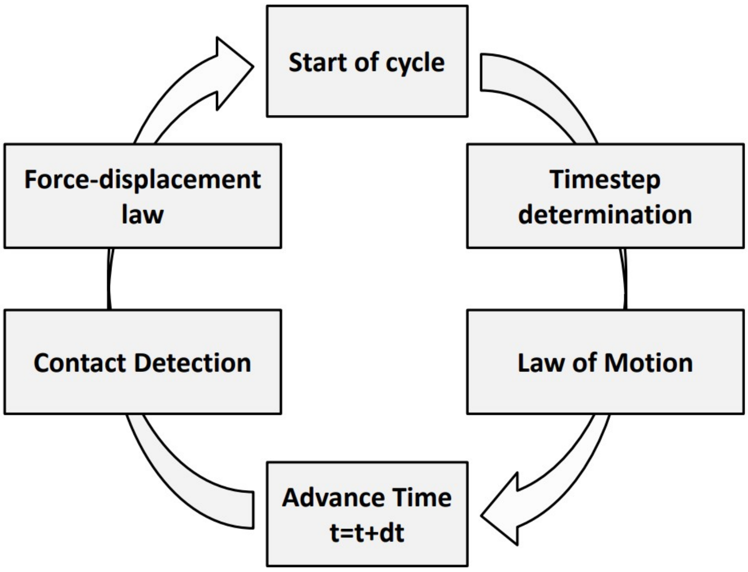
Start of cycle
Timestep determination
Law of Motion
Advance Time t=t+dt
Contact Detection
Force-displacement law

Figure A.1: Operations executed during each calculation cycle.

The detailed information about the operations are well described in the documentation of Particle Flow Code 5.0 and summarized as follows [144]:

1. Timestep determination: The DEM calculation requires a valid, finite timestep to ensure the numerical stability of the model. The critical timestep for one contact is $t_{crit} = \sqrt{m/k^{tran}}$ or $t_{crit} = \sqrt{I/k^{rot}}$, where m is the mass, I is the moment of inertia of the particle, k^{tran} and k^{rot} are the translational and rotational stiffnesses. The critical timestep for the whole structure is decided by the smallest t_{crit} among all the contacts.

2. Law of motion: The position and velocity of each body is updated according to Newton's laws of motion using the current timestep and the forces calculated during the previous cycle.

3. Advance time: The model time is advanced by adding the current timestep to the previous model time.

4. Contact detection: Contacts are dynamically created/deleted based on the current particle positions.

5. Force-displacement law: The forces developing at each contact are updated by the appropriate contact model using the current state of the particles.

A.0.2 Stabilisation [4]

For a simulation under (quasi-)static condition, the model requires the stable state of force distribution or particle equilibrium, which means that enough time or time-steps are required in order to reach such a balance state or equilibrium. For a quasi-static load, the method of stabilization is low loading rate or small time-step. It should be noted the critical time-step is in fact the maximum timestep to keep a stable state of model, but may not small enough for the quasi-static load. In the simulation with requirement of extreme equilibrium, the stabilization within a certain tolerance should be worked out with all boundary condition fixed unmovable.

A.0.3 Viscous damping

The critical damping constant c_i is given by:

$$c_i = 2\sqrt{k_i m_c} \tag{A.1}$$

where $m_c = \dfrac{m_1 m_2}{m_1 + m_2}$, m_1 and m_2 are the mass of two connecting particles.

In this work, $c_n = c_s = 0.7c_i$.

A.0.4 Other

In this work, ball density is set as $2600Kg/m^3$, and time step is set automatically by software PFC. These two settings do not effect the results presented in this work, just for information.

Appendix B

Samples generation [4]

There are many methods to generate the randomly packed assemble in DEM, which can be categorized into dynamic methods (e.g. boundary compaction method, particle drop method and particle size scaling method) and constructive method [153, 154]. In this research work, the randomly packed sample generation procedure is based on the procedure adopted by Potyondy [145], which is mainly the size scaling method. The assembly is generated with three procedures, namely particle generation, internal stress control and floater elimination. During all the model generation, the particles are frictionless ($F_s = 0$, see Equation 3.1), which avoid any internal shear contact force.

B.1 Particle generation and internal stress control

In the first phase, a highly compacted assembly is generated within the domain of rectangular walls with relatively big overlaps between the particles [145]. Normally, when the contact model is applied, the tremendous lock-in force exists among the assembly. Addressing to this issue, a stress control procedure is imposed to reduce the stress of the initial assembly by shrinking all the particle sizes with the same factor step by step. In Potyondy's study [145], a specified isotropic stress is set as the target stress, whose value is 1% of the initial stress. The target stress is naturally dependent on the initial particle distribution and should be adapted to the contact stiffness. In order to avoid any misunderstanding, the internal stress level is expressed by the overlap ratio h_r relative to the mean particle radius $\overline{R}$,

$$h_r = \frac{\overline{\delta}_n}{\overline{R}}, \tag{B.1}$$

where $\overline{\delta}_n$ is the average overlap of all contacts of the assembly.

A scale factor for the particle shrinking X_R is then defined based on the existing overlap ratio h_r and its target h_r^T

$$X_R = \eta \times \left(h_r^T - h_r\right) + 1 \tag{B.2}$$

where η is a hysteresis factor working on the numerical stability of the procedure. Its value is set as $\eta = 0.1$ in this work, which promises the gradual decrease of the particle radius. If h_r is bigger than its target value h_r^T all particles may be decreased by the scale factor $X_R < 1$, otherwise, their radius may increase. The tolerance of the stress control procedure is defined as:

$$\frac{\left(h_r - h_r^T\right)}{h_r^T} < 0.2 \tag{B.3}$$

After the rescaling, the system is no longer in balance. A particle natural rearrangement occurs during a stabilization phase (see Appendix A).

B.2 Floater elimination procedure

Floaters are defined as the particles with less than 3 contacts. These particles are not in stable state because only normal forces exist for all contacts, and thus forming unintended voids inside the material. To eliminate these potential voids, the radius of all particles identified as floaters, are firstly enlarged until they are in contact with more than 2 particles around. Then their radius are decreased step by step until the average overlap of each floater reaches the average overlap of the assembly. During this process, the rest of the particles do not move.

B.3 Interactive procedure and adopted parameters

In practice, after the generation of the particles, a loop containing the Equations B.1 and B.2, followed by the rescaling of radius by the X_R factor is calculated until the relative error between the overlap and the target overlap becomes smaller than 20% as expressed in Equation B.3.

In the following, all numerical samples are generated with a uniform distribution of radius between the minimum to maximum particle radius (respectively R_{min} and R_{max}). If R_{max}/R_{min} is close to 1.0, the assembly will be seriously crystalline arrangement [145], while if R_{max}/R_{min} is too big, the demanded number of particles forming the assembly is too large to have acceptable computational time. The size ratio is set as $R_{max}/R_{min} = 1.6$, which is in the range of the size ratio adopted by other researchers [145,154,155], and is available to produce isotropic macro properties.

An example of generation of a square sample with dimension $L = 40mm$ is presented in Figure B.1. The difference after model generation is presented in Figure B.1b, where a significant reduction of the contact overlap ratio has been obtained, and there is no floater in the assembly. The system presents 429 particles with an average radius $\overline{R} = 1\,mm$ and $L = 40\overline{R}$. A target overlap ratio $h_r^T = 10^{-9}$ is adopted. One may observe the relatively homogeneous overlap distribution at the end of the process, associated to a neglectful internal stress state obtained with the generation procedure.

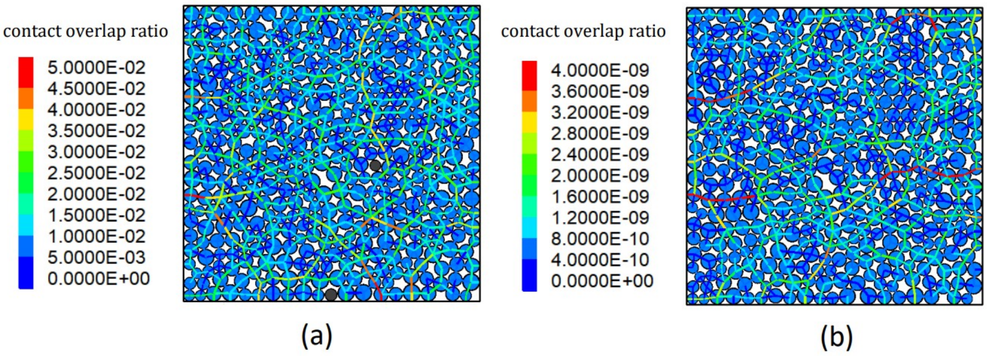

Figure B.1: Square sample generation. (a) Initial particle distribution ($h_r \approx 1.37 \times 10^{-2}$. and 2 floater particles are indicated in black. (b) At the end of the generation process ($h_r \approx 1.04 \times 10^{-9}$, no floater is observed), (Modified from [4]).

B.4 Generator random seed

To generate randomly packed samples, a number is needed as the random seed. By default of the software (PFC), the random seed is 10000. In this work, random seeds for three samples of Tension-Compression and 2PB fatigue tests are 10001, 10002 and 10003, for 4PB fatigue tests are 10021, 10022 and 10023.

Appendix C

Theoretical calculation of cracked plate

C.1 The stiffness of cracked finite plate

Considering a thought experiment, an elastic plate with height H, width $2b$, thickness t, material Young's modulus E, subjected uniformly distributed stress σ, see in Figure C.1a. For the plate without crack, its stiffness k_0^P can described as

$$k_0^P = \frac{F}{\bar{\delta}_0} \tag{C.1}$$

where the net force F and the average relative displacement $\bar{\delta}_0$ can be obtained by

$$F = \sigma \cdot 2bt \tag{C.2}$$

$$\bar{\delta}_0 = \frac{\sigma H}{E} \tag{C.3}$$

In the thought experiment, an edge crack appear at the middle and grows to a length a (see in Figure C.1b). The stiffness of plate after cracking k_a^P may be globally calculated by

$$k_a^P = \frac{F}{\bar{\delta}_a} \tag{C.4}$$

By associating to Equation C.1 and C.4, one may get the ratio of k_a^P to k_0^P,

$$\frac{k_a^P}{k_0^P} = \frac{\bar{\delta}_0}{\bar{\delta}_a} = \frac{\bar{\delta}_0}{\bar{\delta}_0 + \Delta\bar{\delta}} \tag{C.5}$$

In global view, taking the whole plate as an object, the released energy during cracking process U_a can be calculated by the difference between the work done by external force and the elastic potential energy change (see section **??**), and U_a can be geometrically described as the area of the triangle

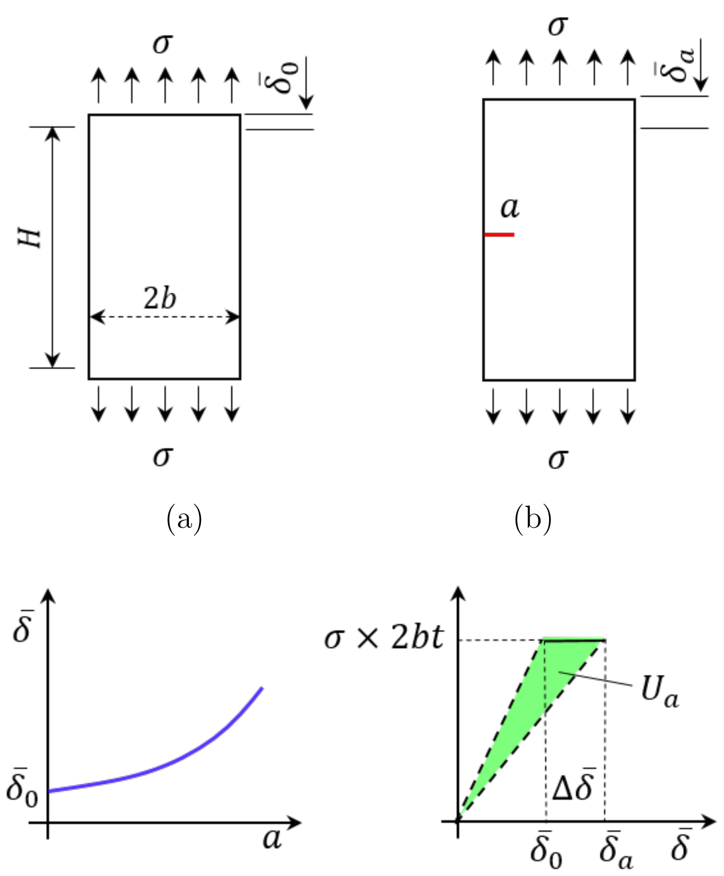
σ
$\bar{\delta}_0$
H
$2b$
σ
σ
$\bar{\delta}_a$
a
σ
$\bar{\delta}$
$\bar{\delta}_0$
a
$\sigma \times 2bt$
U_a
$\Delta\bar{\delta}$
$\bar{\delta}_0$
$\bar{\delta}_a$
$\bar{\delta}$

(a) (b)

(c) (d)

Figure C.1: (a) Plate deformation without crack, (b) plate deformation with crack, (c) the average relative displacement at plate ends versus crack length in the plate, (d) the external force versus the average relative displacement, describing the released energy during plate cracking.

shown in Figure C.1d, therefore,

$$\begin{aligned} U_a &= \frac{1}{2}F(\bar{\delta}_a - \bar{\delta}_0) \\ &= \frac{1}{2}F\Delta\bar{\delta} \end{aligned} \tag{C.6}$$

associated with Equation C.2, we can rewrite Equation C.6 as

$$U_a = \frac{1}{2}\sigma \cdot 2bt\Delta\bar{\delta} \tag{C.7}$$

transform Equation C.7, one may get

$$\Delta\bar{\delta} = \frac{U_a}{\sigma b t} \tag{C.8}$$

combine Equation C.3 and C.8, Equation C.5 can be rewritten as

$$\frac{k_a^P}{k_0^P} = \frac{\bar{\delta}_0}{\bar{\delta}_a} = \frac{\dfrac{\sigma H}{E}}{\dfrac{\sigma H}{E} + \dfrac{U_a}{\sigma b t}} \tag{C.9}$$

Till here, once we get the expression of U_a and submit it into Equation C.9, we can solve Equation C.3.

$$G = \frac{K^2}{E} \tag{C.10}$$

In local view, the energy release only occurs at the crack tip, when crack propagates and new crack surface is generated, since at anywhere else of the plate, material keeps continuous and elastic. Based on Equation **??** and **??** the released energy U_a can be calculated as

$$U_a = \int dU = t \int_0^a G\, da \tag{C.11}$$

and the energy release rate G may be obtained by its relation with the stress intensity factor (SIF) K,for plane stress condition, Equation 2.20.

Thus, the Equation C.11 can be rewritten as

$$U_a = \frac{t}{E} \int_0^a K^2\, da \tag{C.12}$$

For finite width plate with edge crack (see Figure C.1), the stress intensity factor K is described as [108]

$$K = \sigma\sqrt{\pi a}\left(1.122 - 0.231\xi + 10.550\xi^2 - 21.710\xi^3 + 30.382\xi^4\right) \tag{C.13}$$

where $\xi = a/2b$.

Submit Equation C.13 into Equation C.12 and solve U_a, then submit U_a into Equation C.9, one may obtain

$$\frac{k_a^P}{k_0^P} = \frac{\bar{\delta}_0}{\bar{\delta}_a} = \frac{1}{1 + \pi P\left(\dfrac{2b}{H}\right)} \tag{C.14}$$

where,

$$\begin{aligned} P =& 1.261\xi^2 - 0.338\xi^3 + 11.871\xi^4 - 21.404\xi^5 + 63.110\xi^6 \\ & - 134.803\xi^7 + 278.099\xi^8 - 293.149\xi^9 + 184.608\xi^{10} \end{aligned}$$

and $\xi = a/2b$.

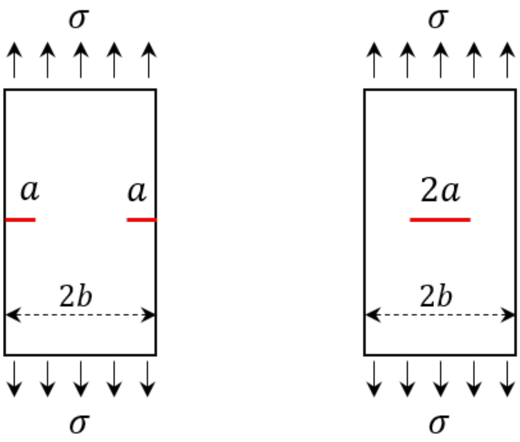

(a) (b)

Figure C.2: (a) Finite plate with symmetric edge cracks, (b) finite plate with center crack.

By the approach above, one can also get the expression of plate stiffness with two symmetric edge cracks or center crack (see Figure C.2).

For the plate with two symmetric edge cracks, stress intensity factor K is described as [108]

$$K = \sigma\sqrt{\pi a} \cdot \frac{1.122 - 0.561\xi - 0.205\xi^2 + 0.471\xi^3 - 0.190\xi^4}{\sqrt{1-\xi}} \tag{C.15}$$

where $\xi = a/b$.

The resultant expression of plate stiffness is

$$\frac{k_a^P}{k_0^P} = \frac{\bar{\delta}_0}{\bar{\delta}_a} = \frac{1}{1 + \pi P\left(\dfrac{2b}{H}\right)} \tag{C.16}$$

where,

$$\begin{aligned} P =& - 0.406 \ln|\xi - 1| - 0.406\xi + 0.427\xi^2 - 0.135\xi^3 - 0.138\xi^4 \\ & + 0.147\xi^5 - 0.029\xi^6 - 0.022\xi^7 + 0.018\xi^8 - 0.004\xi^9 \end{aligned}$$

and $\xi = a/b$.

For the plate with center crack, stress intensity factor K is described as [108]

$$K = \sigma\sqrt{\pi a} \cdot \frac{1 - 0.5\xi + 0.370\xi^2 - 0.044\xi^3}{\sqrt{1-\xi}} \tag{C.17}$$

where $\xi = a/b$.

The resultant expression of plate stiffness is

$$\frac{k_a^P}{k_0^P} = \frac{\bar{\delta}_0}{\bar{\delta}_a} = \frac{1}{1 + \pi P\left(\dfrac{2b}{H}\right)} \tag{C.18}$$

where,

$$\begin{aligned} P = & -0.682\ln|\xi - 1| - 0.682\xi + 0.159\xi^2 - 0.227\xi^3 + 0.077\xi^4 \\ & - 0.030\xi^5 + 0.005\xi^6 - 0.0003\xi^7 \end{aligned}$$

and $\xi = a/b$.

C.2 Verification of formulas describing the stiffness of cracked finite plate

To compare with Equation C.14, C.16 and C.18, three groups simulation for tension test of cracked plates, respectively with edge crack, symmetric edge cracks and center crack. The target plates with height $H = 160\ mm$, width $2b = 100\ mm$ and thickness $t = 1\ m$, material Young's modulus $E = 10$ GPa, subjected uniformly distributed stress $\sigma = 0.625$ MPa, see in Figure C.1a. The regular square-packed samples with particle diameter $d = 2\ mm$, and contact normal stiffness and shear stiffness are set based on material Young's modulus E.

$$k_n = k_s = \frac{EA_c}{l} \tag{C.19}$$

where $A_c = td$ is the area of contact intersection, and $l = d$ is contact length, therefore,

$$k_n = k_s = Et \tag{C.20}$$

in this case, $k_n = k_s = 1 \times 10^{10}\ N/m$.

A series of crack whose length a is integer multiple of particle diameter d, for example, for particle diameter $d = 2mm$, crack length could be set as

$a = 2mm, 4mm, 6mm \cdots$, for $d = 1mm$, $a = 1mm, 2mm, 3mm \cdots$, and cracks were set by accordingly cutting off certain contacts in DEM samples. Subjected the same uniformly distributed stress $\sigma = 0.625$ MPa, the average relative displacement $\bar{\delta}$ result from simulations and that result from the analytic expression are compared in Figure C.3

Good agreements are shown in Figure C.3, which strongly support the validity of the formulas describing the stiffness of cracked finite plate, respectively with respectively with edge crack, symmetric edge cracks and center crack.

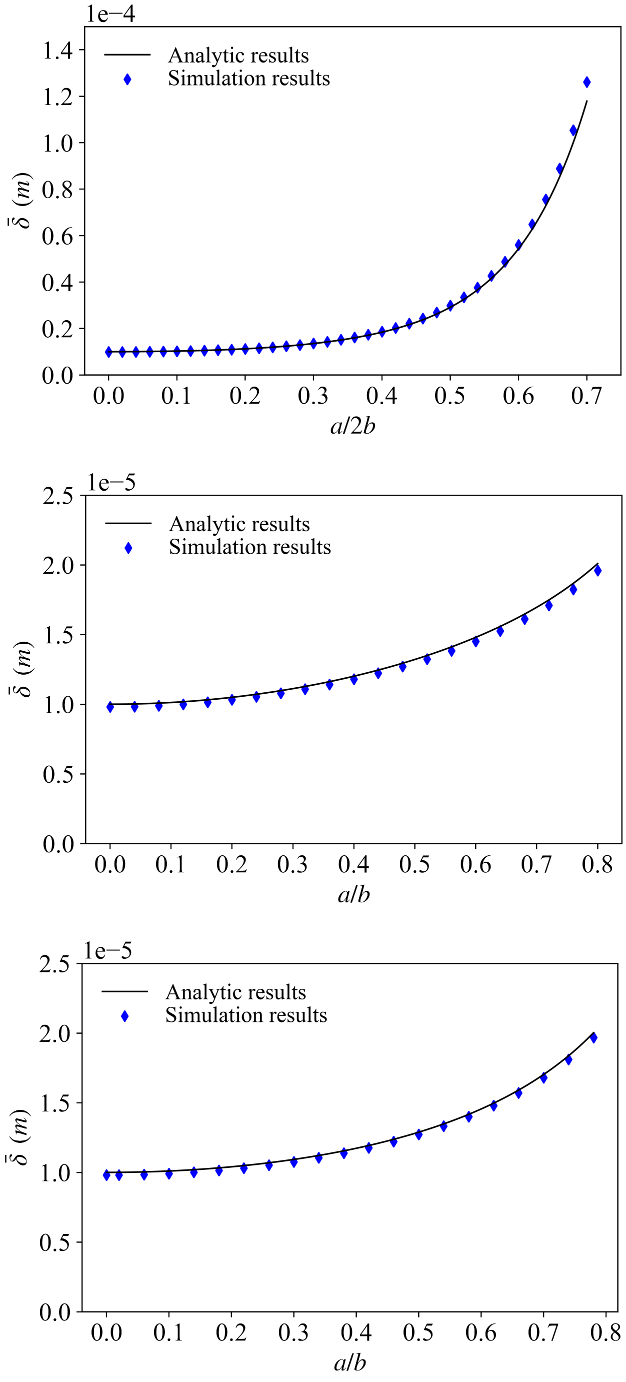

(a)

(b)

(c)

Figure C.3: Comparison of the average relative displacement $\bar{\delta}$ between analytic results and simulation results, for (a) plate with edge crack, (b) plate with symmetric edge cracks, (c) plate with center crack.

Appendix D

Theoretical calculation of fatigue evolution

D.1 Calculation of theoretical results

For several classical scenario of plate with crack, like center crack, edge crack and symmetric edge cracks, there are formulas that can describe the extent of stress concentration at crack tips by the stress intensity factor K (Section C.1, in Appendix C), and combining the formulas that can describe the stiffness of cracked plates in Section 3.7.2, Chapter 3, the theoretical fatigue evolution for these classical scenario can be calculated by the quasi-static method.

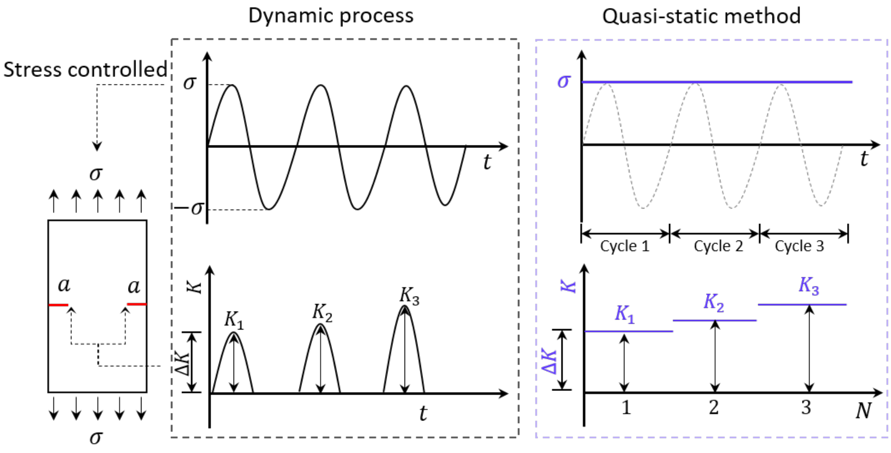
Dynamic process
Quasi-static method
Stress controlled
σ
σ
a
a
σ
−σ
t
K
ΔK
K₁
K₂
K₃
t
σ
t
Cycle 1
Cycle 2
Cycle 3
K
ΔK
K₁
K₂
K₃
1
2
3
N

Figure D.1: Quasi-static process for stress controlled fatigue test.

For stress controlled fatigue test, taking the symmetric edge cracks scenario (see in Figure D.1) as an example, its fatigue evolution both in aspect of crack propagation and plate stiffness change can be obtained by the following steps:

1) Given plate dimension (height H, width $2b$ and thickness t), material property E, the maximum stress during a ‘loading cycle’ σ_{max}, and the initial crack length a_0,

2) With the crack length a_0 and plate dimension, the plate stiffness ratio can be obtained by Equation C.16,

3) With the crack length a_0, plate dimension and the load stress σ_{max}, the corresponding K_{max} can be calculated by Equation C.15,

4) With the K_{max}, by using Paris' law result the crack increment da,

5) Update crack length a and back to step 2 for next 'cycle' till stiffness ratio reach 0.5.

By this approach, the curve of stiffness ratio versus number of cycles and the curve of crack length versus number of cycles can be obtained as the theoretical results of a fatigue test. Mentioned that this approach can also be used for scenario of center crack and edge crack in the same procedures.

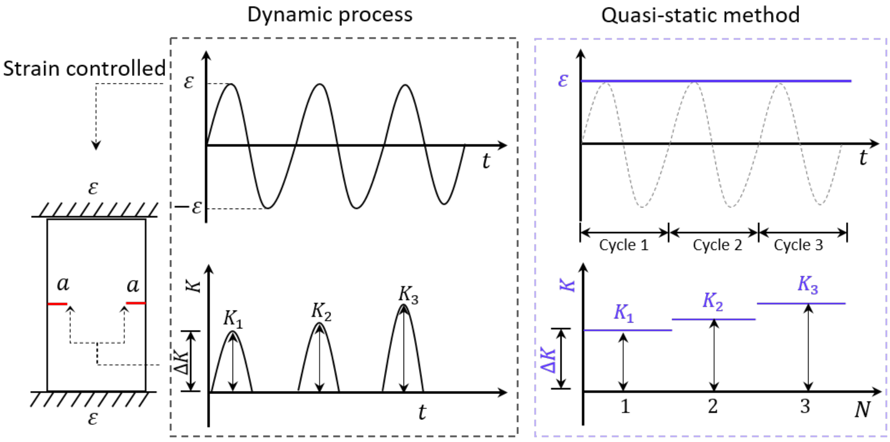

Figure D.2: Quasi-static process for strain controlled fatigue test.

Compared with the stress controlled fatigue test, for the strain controlled fatigue test the main procedures to calculate theoretical results is exact same, only a slight difference in the calculation of the K_{max}. It is that in stress controlled fatigue test the load stress is constant $\sigma = \sigma_{max}$ and can be directly submit into Equation C.16 while for strain controlled fatigue test with the crack growth the holding force F at the ends of plate changes thus the corresponding load stress σ changes accordingly. First the holding force for an intact plate $F_0 = \varepsilon E \cdot 2bt$, the equivalent initial load stress $\sigma_0 = F_0/2bt = \varepsilon E$, then after crack occurrence the equivalent load stress $\sigma = \sigma_0(k^P/k_0^P)$, and σ can be used to calculate the K_{max}.

Also taking the symmetric edge cracks scenario (see in Figure D.2) as an example, its fatigue evolution both in aspect of crack propagation and plate stiffness change can be obtained by the following steps:

1) Given plate dimension (height H, width $2b$ and thickness t), material property E, the maximum strain during a 'loading cycle' ε_{max}, and the initial crack length a_0,

2) With the crack length a_0 and plate dimension, the plate stiffness ratio can be obtained by Equation C.16, and meanwhile the load stress σ,

3) With the crack length a_0, plate dimension and load stress σ, the corresponding K_{max} can be calculated by Equation C.15,

4) With the K_{max}, by using Paris' law result the crack increment da,

5) Update crack length a and back to step 2 for next 'cycle' till stiffness ratio reach 0.5.

Appendix E

Stability and robustness analysis

E.1 Effect of parameter D_{ini}

To investigate the effect of the parameter D_{ini} in the proposed model, three stress controlled fatigue test simulations are compared. The test configuration is same as the test in Section 4.3.3. In three simulations, particle size $d = 2\ mm$, and parameters are set as Table E.1.

Table E.1: Parameters set for simulations to research the effect of parameter D_{ini}.

D_{ini}	C	m
1.0×10^{-2}	1.0×10^{-12}	1.25
1.0×10^{-3}	1.0×10^{-12}	1.25
1.0×10^{-4}	1.0×10^{-12}	1.25
1.0×10^{-5}	1.0×10^{-12}	1.25

Two points may be concluded. First, within a relatively wide range $D_{ini} = 1.0 \times 10^{-2}$ to $D_{ini} = 1.0 \times 10^{-5}$, the parameter D_{ini} does not obviously influence the fatigue evolution (Figure E.1), that is because the parameter D_{ini} only as a trigger to start the contact degradation by calculating the energy release rate G for the first cycle, and not involved in after cycles (Section 3.7.3). This feature allow the proposed model potential user to choose the value of parameter D_{ini} in a relative wide range.

Second, a larger value of parameter D_{ini} leads to a relative stabler calculation of the contact separation ratio p and G at the first several cycles for a contact (see in Figure E.2 to E.9), such a tendency may due to the computation precision of DEM software, since p is calculated by the scope of two sequential points coordinated by the contact forces and contact displacements. If the parameter D_{ini} as an initial degradation of contact is too small, the two points would be very close, which may increase the error for the calculation of p,

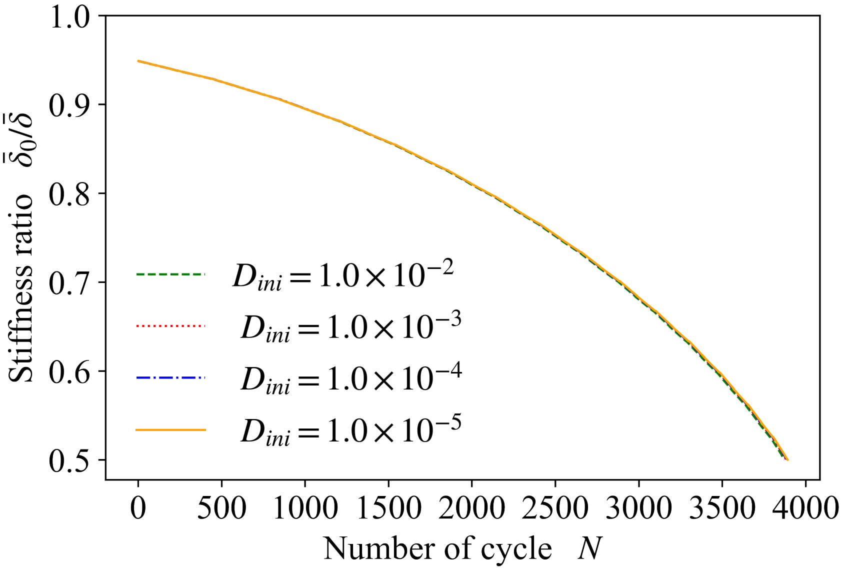

Figure E.1: Fatigue evolution from simulation results with different parameter D_{ini}.

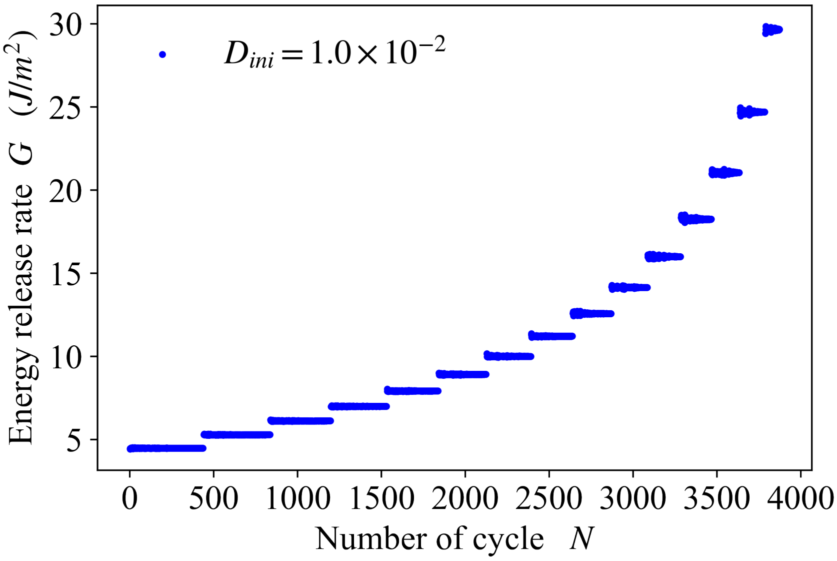

Figure E.2: Energy release rate from simulation results with parameter $D_{ini} = 1.0 \times 10^{-2}$.

otherwise a higher precision of computation of DEM software is required, see in next section.

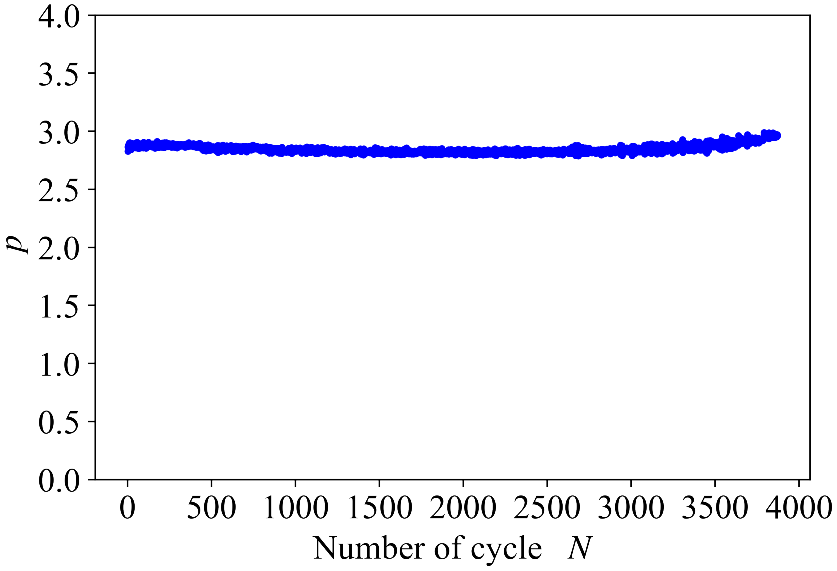

Figure E.3: The contact separation ratio p evolution from simulation results with parameter $D_{ini} = 1.0 \times 10^{-2}$.

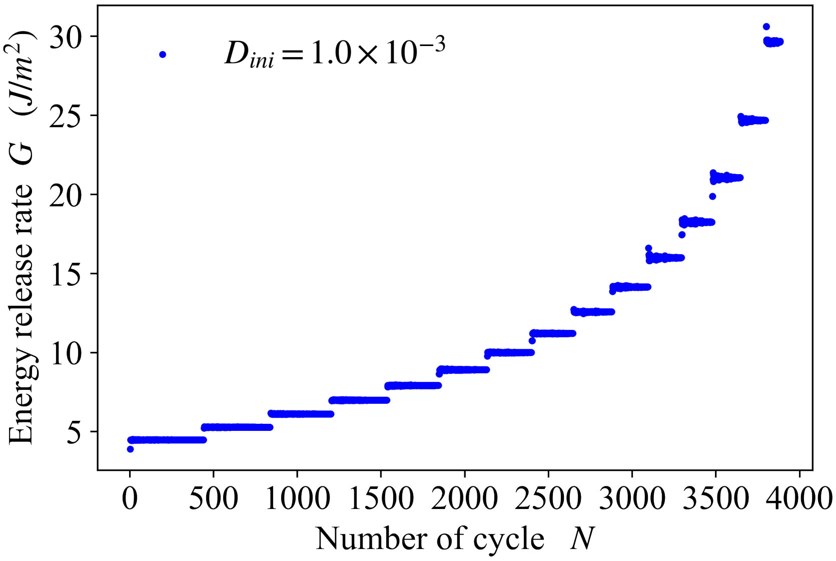

Figure E.4: Energy release rate from simulation results with parameter $D_{ini} = 1.0 \times 10^{-3}$.

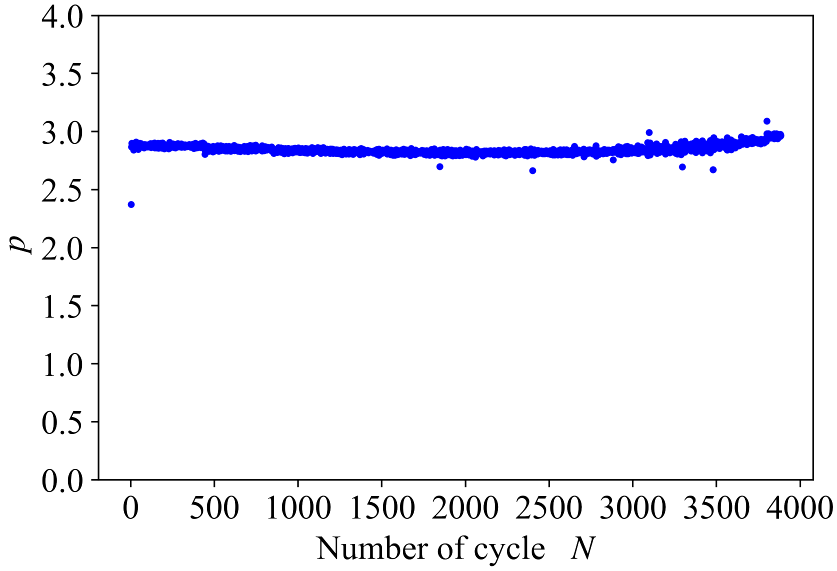

Figure E.5: The contact separation ratio p evolution from simulation results with parameter $D_{ini} = 1.0 \times 10^{-3}$.

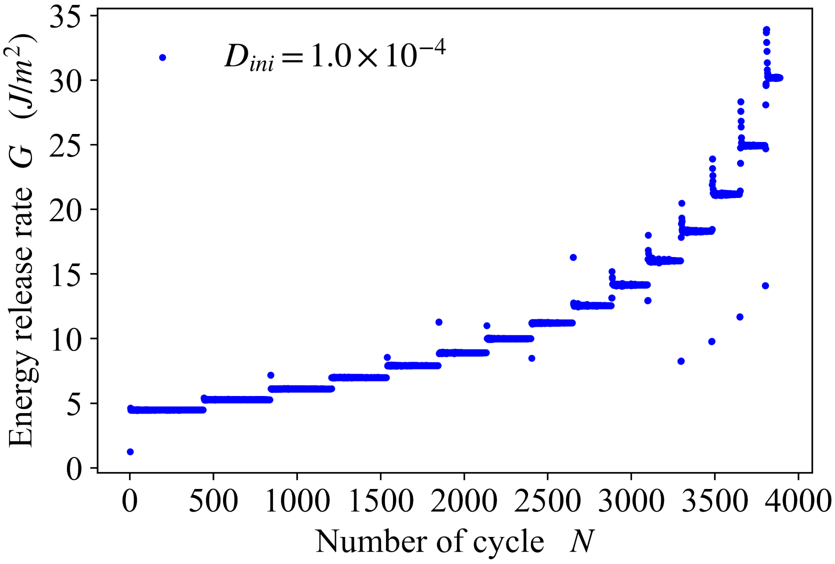

Figure E.6: Energy release rate from simulation results with parameter $D_{ini} = 1.0 \times 10^{-4}$.

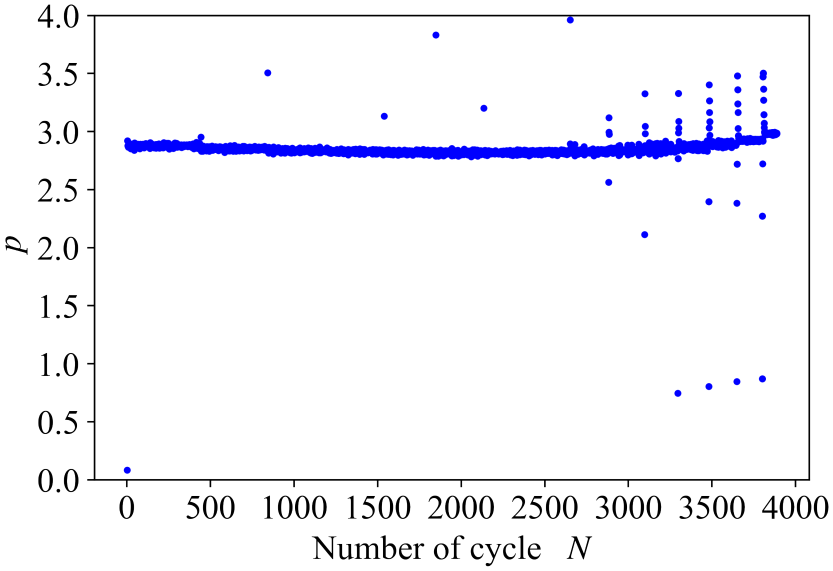

Figure E.7: The contact separation ratio p evolution from simulation results with parameter $D_{ini} = 1.0 \times 10^{-4}$.

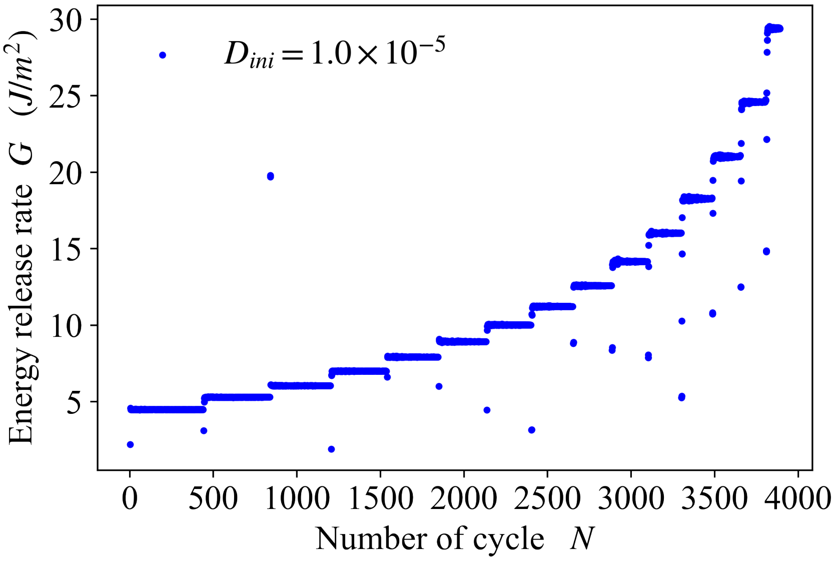

Figure E.8: Energy release rate from simulation results with parameter $D_{ini} = 1.0 \times 10^{-5}$.

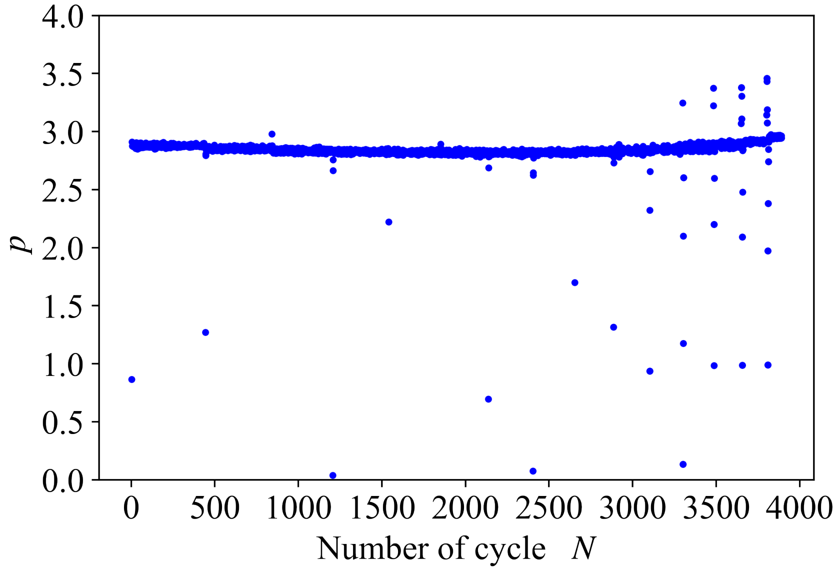

Figure E.9: The contact separation ratio p evolution from simulation results with parameter $D_{ini} = 1.0 \times 10^{-5}$.

E.2 Robustness analysis

As mentioned before, the deviated values of G and p are almost located at the beginning several cycles of a contact, in fact it is the deviated values of parameter p lead to the unrealistic transformation from initial degradation D_{ini} to crack increment da, consequently unrealistic value of da final result a deviated energy release rate G.

While the contact separation ratio p is defined as the absolute value of the ratio of the initial stiffness of contact k_0 (constant)to the slope of contact traction separation k_p, thus obviously the deviated value of p may caused by the error in the calculation of the slope of contact traction separation.

As shown in Figure E.10, two factors may influence the slope calculation. First, the DEM software computation precision determine the precision of contact displacement and contact forces which can be vividly illustrated as the point position (see Figure E.10). Second, the bigger difference of contact force and displacement between current state and the previous cycle, displayed as a larger distance of two points on the contact traction separation path, can be helpful to reduce the error of slope calculation caused by the computation error. That can explain why larger value of initial degradation D_{ini} result stabler p values. And also that is why under same conditions simulation with larger particle size result stabler p values.

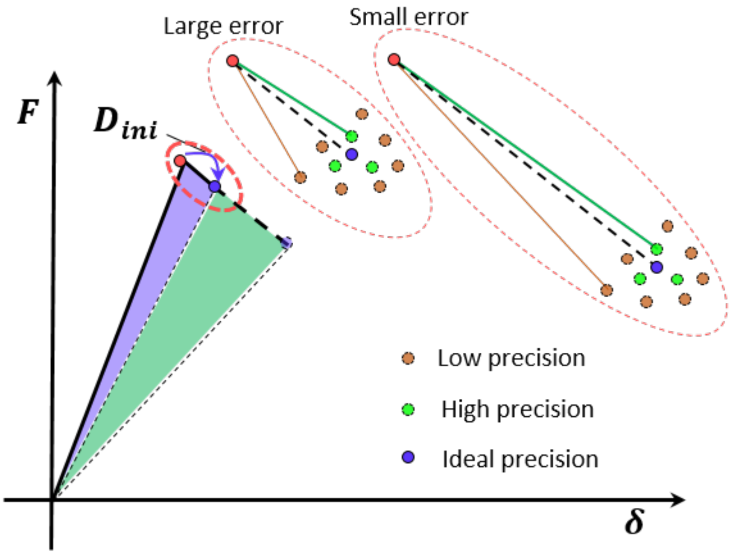

Figure E.10: Schematic description of the error for contact traction separation slope calculation.

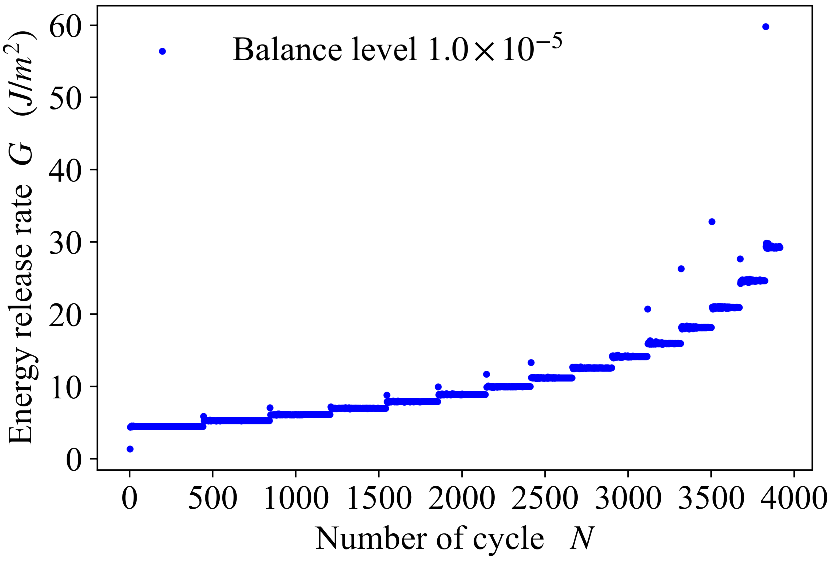

Figure E.11: Energy release rate from simulation results with balance level 1.0×10^{-5}.

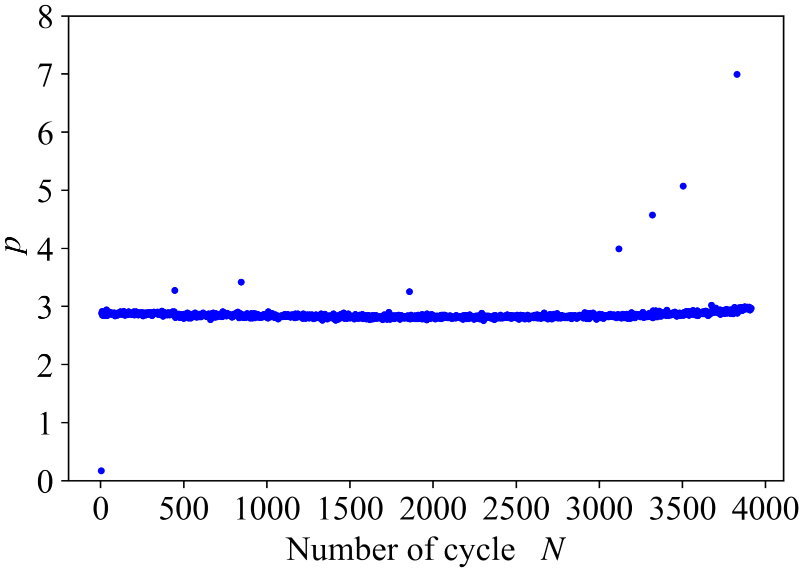

Figure E.12: The contact separation ratio p evolution from simulation results with balance level 1.0×10^{-5}.

In DEM simulations, for every time strain field and stress field redistribution caused by particle displacement change or particle subjected force change,

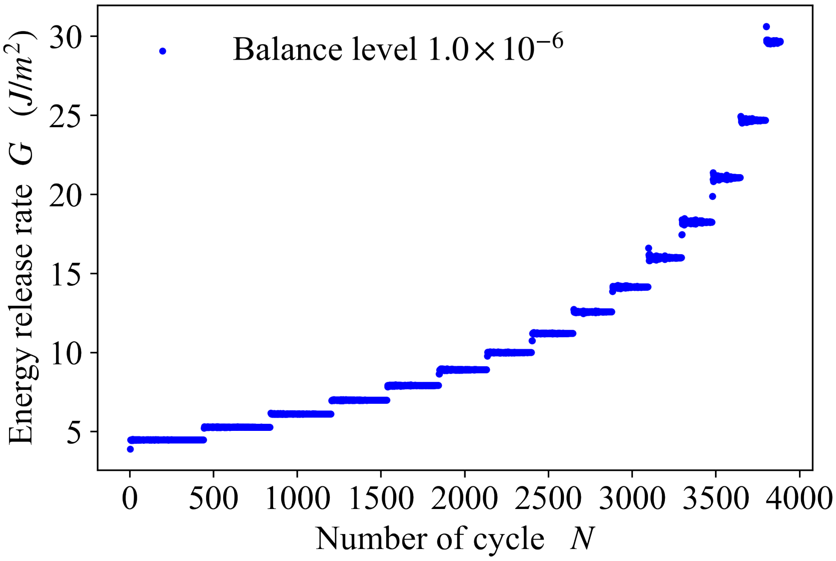

Figure E.13: Energy release rate from simulation results with balance level 1.0×10^{-6}.

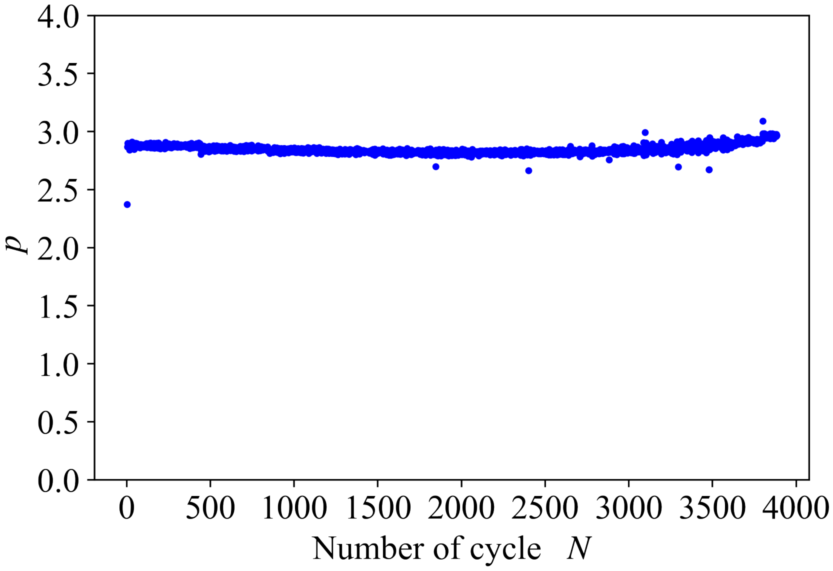

Figure E.14: The contact separation ratio p evolution from simulation results with balance level 1.0×10^{-6}.

the system needs to once again get equilibrium, the balance level of system equilibrium [144] can be defined as the ratio of the magnitude of unbalance

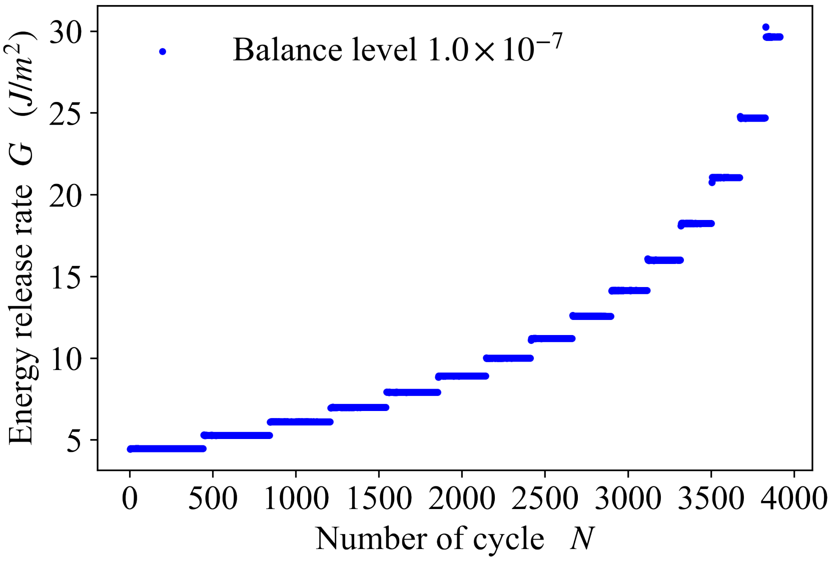

Figure E.15: Energy release rate from simulation results with balance level 1.0×10^{-7}.

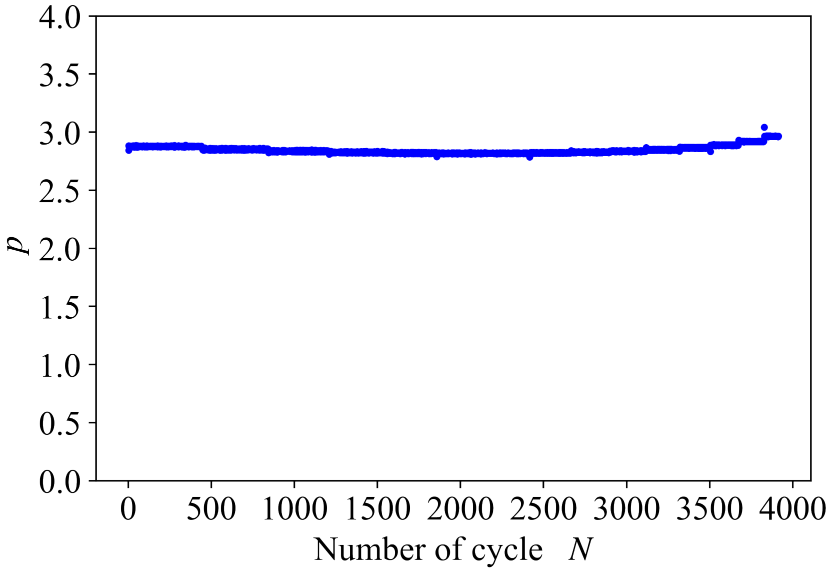

Figure E.16: The contact separation ratio p evolution from simulation results with balance level 1.0×10^{-7}.

force to the magnitude of the resultant force on the particle, like 1.0×10^{-5}. A lower balance level may leads to a higher precision of particle position and contact forces.

To investigate the effect of balance level, three stress controlled fatigue test simulations are compared. The test configuration is same as the test in Section 4.3.3. In three simulations, particle size $d = 2\ mm$, and parameters are set as $D_{ini} = 1.0\times10^{-3}$, $C = 1.0\times10^{-12}$ and $m = 1.25$, while balance level for three simulations are set respectively as 1.0×10^{-5}, 1.0×10^{-6} 1.0×10^{-7}. From Figure E.11 to E.16, it is obvious that with the computation precision increase both the values of p and values of G become stabler.

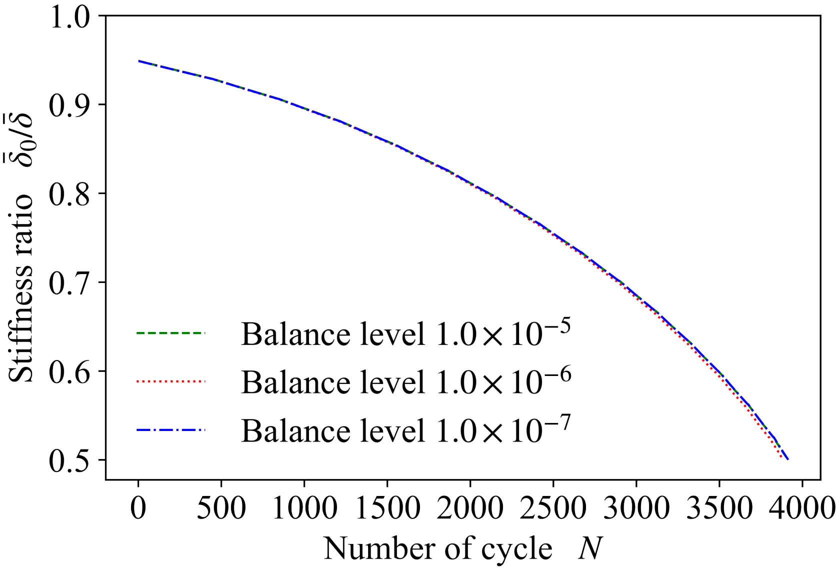

Figure E.17: Fatigue evolution from simulation results with different balance level.

Interestingly, the fatigue evolution seems not influenced by different balance level in computation (see in Figure E.17). And combined with the effect of the initial degradation D_{ini}, the total results prove a strong robustness of the proposed model. The further reason to explain such a robustness is that after the contact degradation is triggered by the given initial degradation D_{ini}, all after calculations are only determined by contact forces and displacements, even though at the beginning several cycles the slope of contact traction separation may be calculated not so precisely, it naturally become stable and precise very soon.

Appendix F

Morphology method

F.1 Using p-model in randomly packed samples

Morphological features of randomly packed samples, can be roughly classified into two types: triangle and polygon contact structures, as shown in Figure F.1. The triangle contact structures can be approximated as hexagonal packed samples, thus, the effective width of contact domain can be considered as $d_c = \frac{1}{2}d_{min}$, d_{min} is the minimum diameter of two particles consisting the contact. Otherwise, the polygon contact structures can be approximated as square-packed samples, $d_c = d_{min}$. By this way, the p-model can be successfully adopted in randomly packed samples.

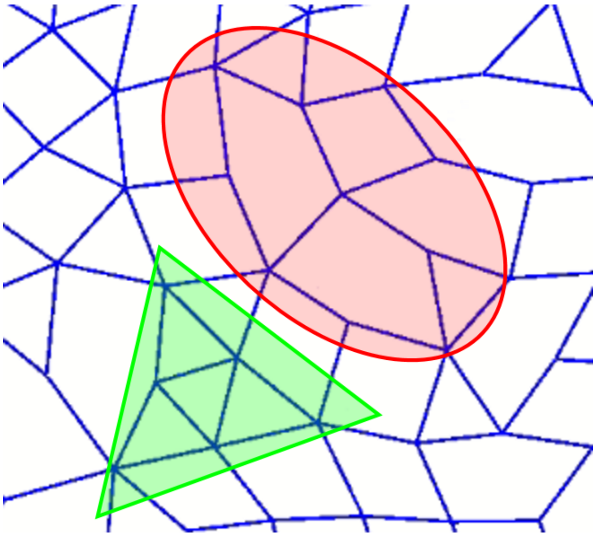

Figure F.1: Examples for triangle and polygon contact structure in randomly packed sample.

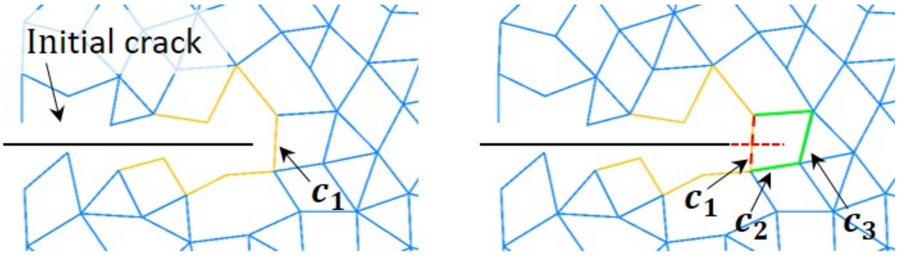

(a) (b)

Figure F.2: (a) Initial crack tip identification, yellow contacts shows crack surface near crack tip, and (b) schematic for the effective width of contact domain d_c detection.

F.1.1 Simulation procedures

Unlike square-packed and hexagonal packed samples have the constant effective width of contact domain d_c, in randomly packed samples, every contacts are identified as the nearest one to crack tip has to detect its surrounding contact structure by which to determine its d_c.

As an example shown in Figure F.2a, the contact nearest initial crack tip is identified as the contact whose strain level is the highest among contacts forming initial crack surface near crack tip (from crack tip till a distance equal to half initial crack length). Let us assume the contact c_1 is identified as the contact nearest initial crack tip, obviously it belongs to a polygon contact structure, therefore for contact c_1, its $d_c = d_{min}$. Continually, with crack propagation, after crack thoroughly permeates contact c_1, the contact nearest new crack tip will be identified based on strain level among contacts forming newly grown crack surface. As shown in Figure F.2b, if contact c_2 is identified as the contact nearest new crack tip, and it belongs to a polygon contact structure, thus its $d_c = d_{min}$. Otherwise, if contact c_3 is identified as the contact nearest new crack tip, and it belongs to a triangles contact structure (already broken contacts do not count as any contact structure), thus its $d_c = \frac{1}{2}d_{min}$. By the method, crack continually propagates. Figure F.3 shows one example of crack path and their d_c in simulation.

F.1.2 Sample preparation

Randomly packed samples generation procedures are detailed in Appendix B. 6 samples with average particle diameter $\overline{d} = 2mm$, and another 6 samples with average particle diameter $\overline{d} = 1mm$ are used in simulations.

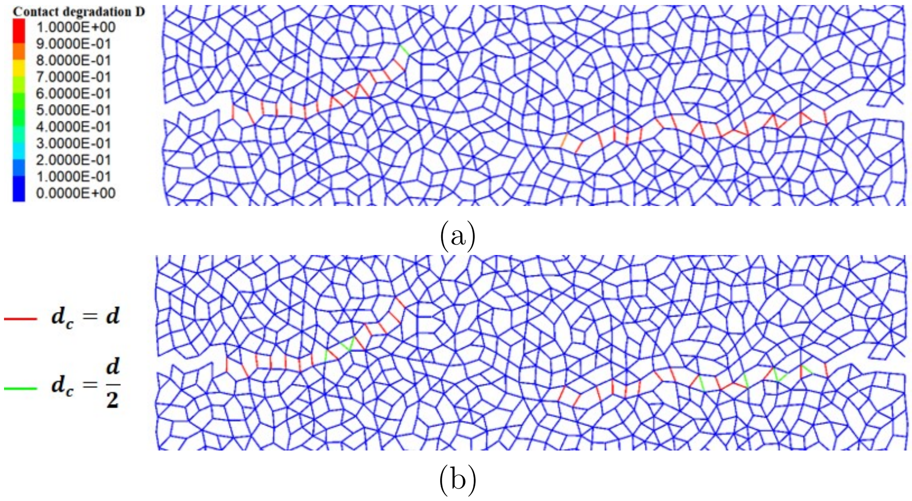

Figure F.3: (a) Crack path in contact degradation map, red to green corresponds to $D = 1$ to $D = 0$, and (b) d_c of contacts on crack path, red contact means its $d_c = d_{min}$ and green means $d_c = \frac{1}{2} d_{min}$.

Based on tension test simulation, the contact stiffness setting are calibrated as $E_{cmod} = 1.21 \times E$ and $k_{ratio} = 1.0$, where E is material Young's modulus. Then every specific contact stiffness are automatically set based on the contact elastic modulus E_{cmod} and $k_{ratio} = 1.0$ following Equation 3.8.

F.1.3 Simulation results in randomly packed samples

The modeled fatigue test is exactly same with Section 4.3.3, the plate dimension are height $H = 160\ mm$, width $2b = 100\ mm$ and thickness $t = 1\ m$, with symmetric edge cracks, initial crack length $a_0 = 10\ mm$, subjected sinusoidal strain $\varepsilon_{max} = 100\ \mu\varepsilon$, material Young's modulus $E = 10$ GPa.

For theoretical results calculation, the parameters relate to material properties are set as $C = 1.0 \times 10^{-12}$ and $m = 1.25$.

For simulation, parameters used in p-model are set as $D_{ini} = 1.0 \times 10^{-3}$, $C = 1.0 \times 10^{-12}$ and $m = 1.25$.

The average results of fatigue evolution from 6 samples with average particle diameter $\overline{d} = 2mm$ shows excellent agreement with theoretical result, as shown in Figure F.4. Compared with the fatigue evolution results from samples with average particle diameter $\overline{d} = 1mm$, in Figure F.6, bigger average particle size leads to more dispersed fatigue curves, caused by more tortuous crack paths (Figure F.5) than that for smaller average particle size

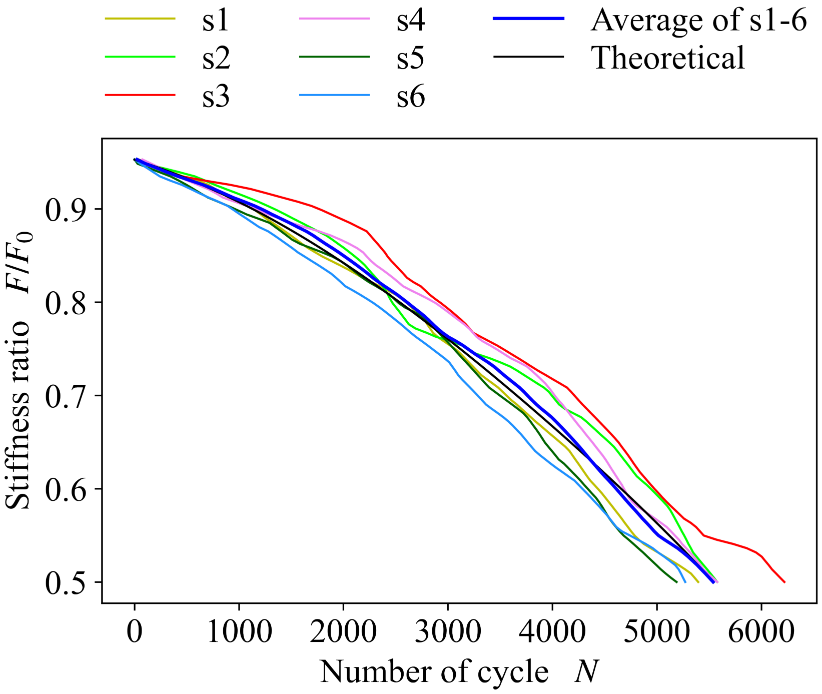

Figure F.4: Comparison of simulations results with theoretical results, in samples with average particle diameter $\overline{d} = 2mm$.

(Figure F.7).

These good agreements between simulations and theoretical results support the usage of p-model in randomly packed samples, and the crack paths indicate the ability of modeling crack propagation for p-model.

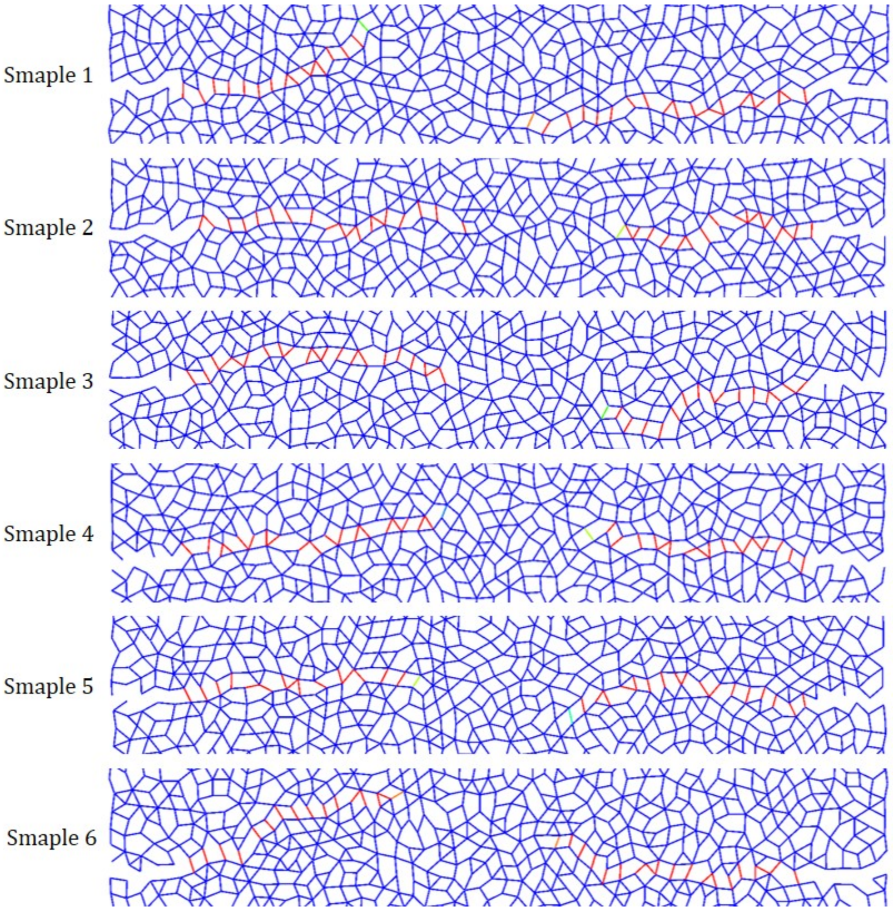
Smaple 1
Smaple 2
Smaple 3
Smaple 4
Smaple 5
Smaple 6

Figure F.5: Crack paths in contact degradation map, red to green corresponds to $D = 1$ to $D = 0$, in samples with average particle diameter $\overline{d} = 2mm$, s1-s6 represent sample 1-sample 6.

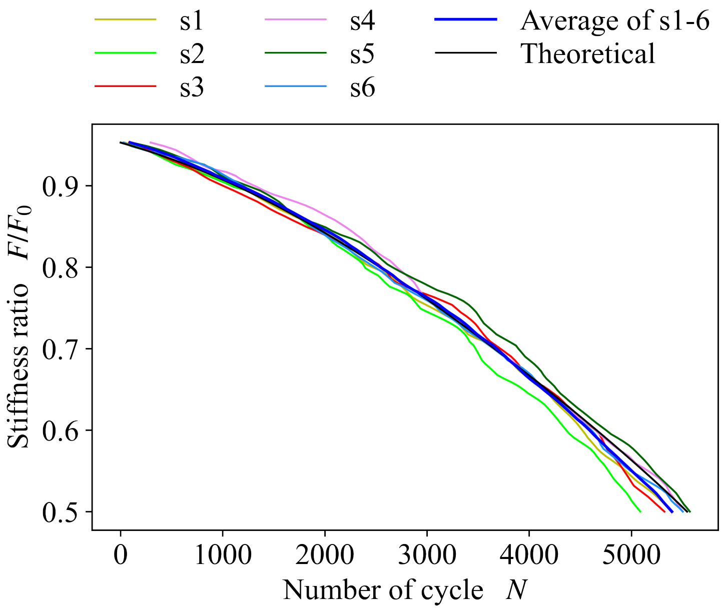

Figure F.6: Comparison of simulations results with theoretical results, in samples with average particle diameter $\overline{d} = 1mm$.

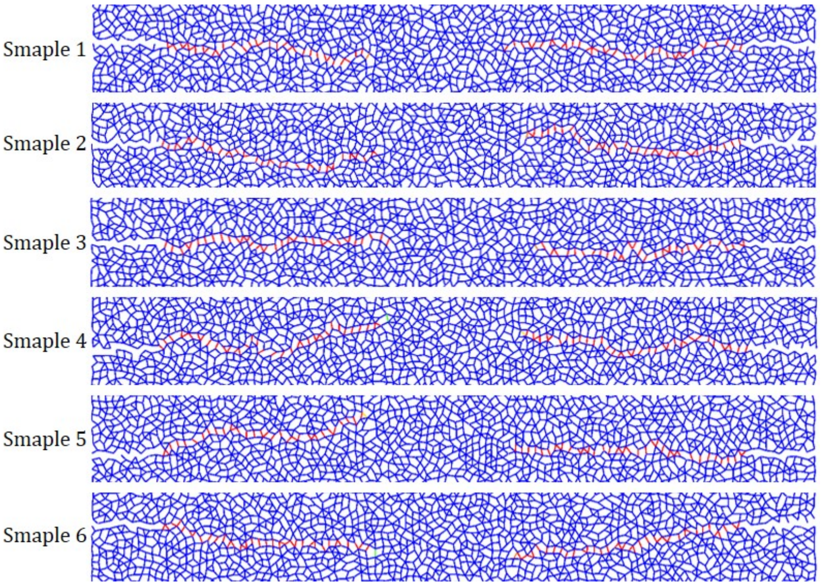
Smaple 1
Smaple 2
Smaple 3
Smaple 4
Smaple 5
Smaple 6

Figure F.7: Crack paths in contact degradation map, red to green corresponds to $D = 1$ to $D = 0$, in samples with average particle diameter $\overline{d} = 1mm$, s1-s6 represent sample 1-sample 6.

APPENDIX G

Technique to save simulation time

From Equation 3.25 and discuss in Section 4.5.1, we know that parameter C has an effect of scaling the fatigue evolution. For example, two simulations have same parameter sets except the parameter C, with respectively C and C' and $C' = \beta C$, based on Equation 3.25 of the Paris' law, one can get the relation of resultant fatigue lives

$$\frac{da}{dN'} = \beta C \left(GE\right)^{m/2}, \tag{G.1}$$

then

$$dN' = \frac{dN}{\beta}. \tag{G.2}$$

In simulation computation, using $C' = \beta C$ will scale the fatigue evolution β times and save β times computation.

Figure G.1 displays the crack growth with different scale times for parameter C. The nature of this scaling technique is using current crack growth rate da/dN to predict crack growth in following a number of cycles. While crack growth rate may change with crack length increase, thus, smaller scale times leads to more accurate result.

To investigate the error caused by this scaling technique, four simulations are compared (Figure G.2), the parameter for simulation without scale is shown in Table 5.2. For other three simulations, except for parameter C, other parameter are set as the same with simulation without scale. For simulation scale 10 times, $C' = 10C$, correspondingly, the resultant number of cycle dN' is multiplied by 10.

From Figure G.2, one may notice that even scale 1000 times, the resultant fatigue evolution curve is still not deviated too much, and a greatly time saving is realized.

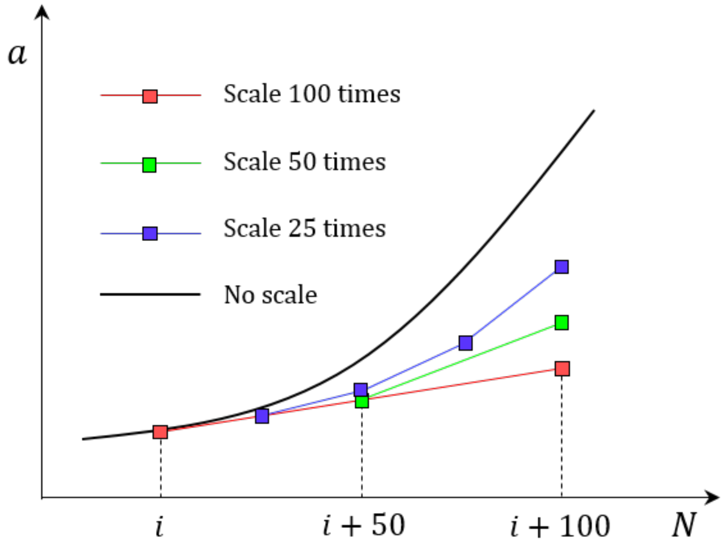
a
Scale 100 times
Scale 50 times
Scale 25 times
No scale
i
i + 50
i + 100
N

Figure G.1: Illustration of scales in simulation.

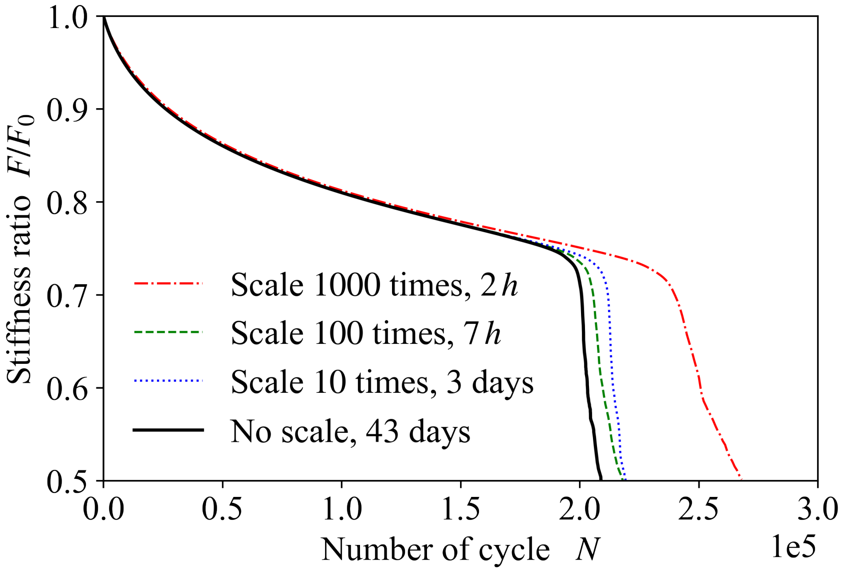

Figure G.2: Examples for different scale times and corresponding consumed time.

Appendix H

Reaction force evolution

Figures H.1, H.2 and H.3 show comparisons of reaction force evolution between simulations and that of experimentation of T-C, 4PB and 2PB fatigue tests.

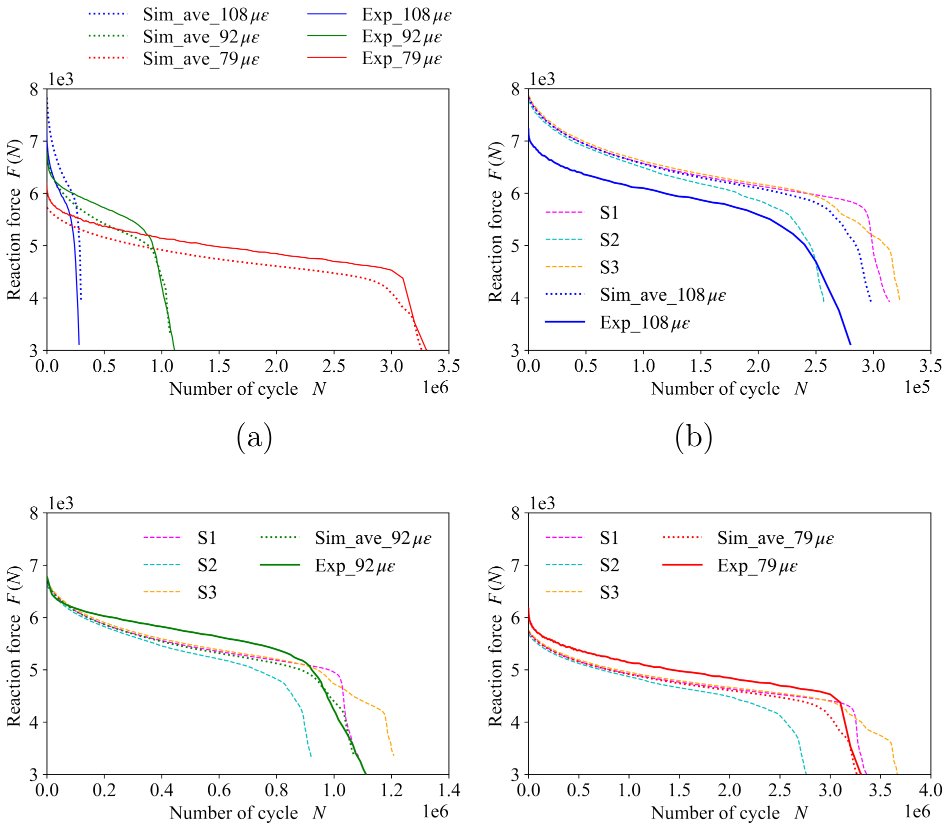

(a) (b)

(c) (d)

Figure H.1: T-C fatigue tests simulation results, (a) comparison of average simulation results and experimentation [1] with different test strain levels, and reaction force evolution of all three samples with strain levels respectively (b) 108 $\mu\varepsilon$, (c) 92 $\mu\varepsilon$ and (d) 79 $\mu\varepsilon$.

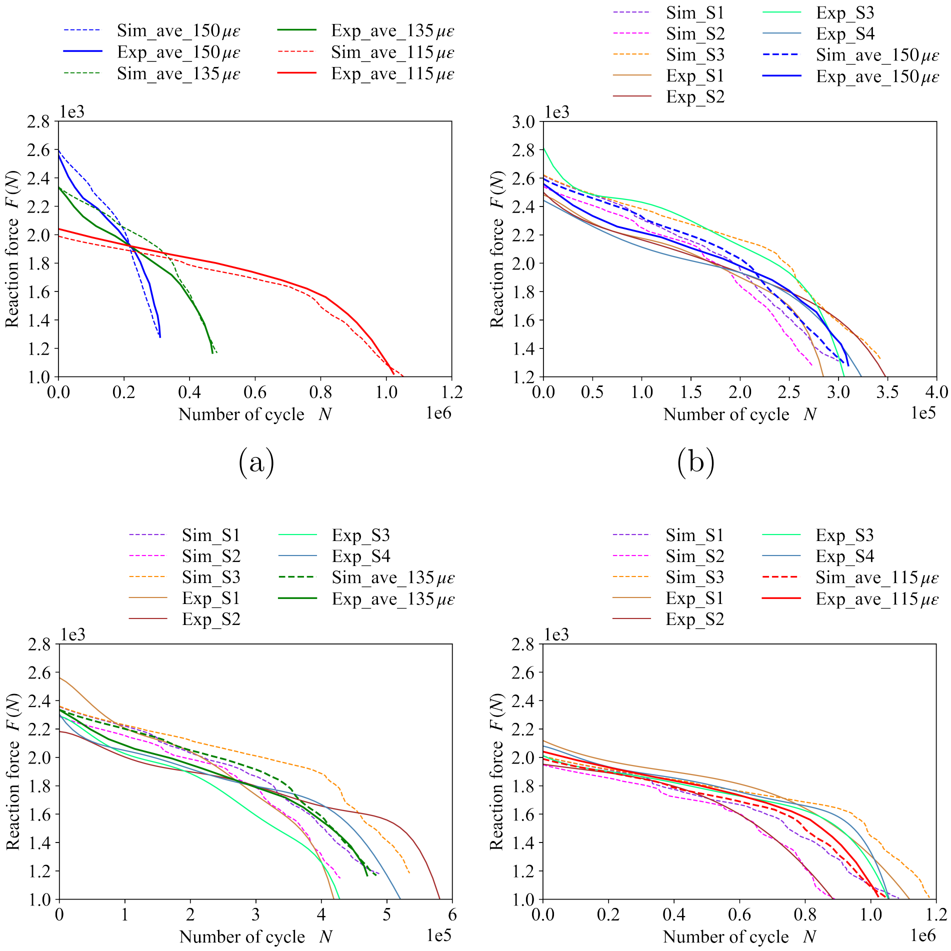

(a) (b)

(c) (d)

Figure H.2: Comparison of reaction force evolution between 4PB fatigue tests simulation and that of experimentation [150], (a) average curves for different test strain levels, (b) average and all curves for test strain level 150 $\mu\varepsilon$, (c) 135 $\mu\varepsilon$ and (d) 115 $\mu\varepsilon$.

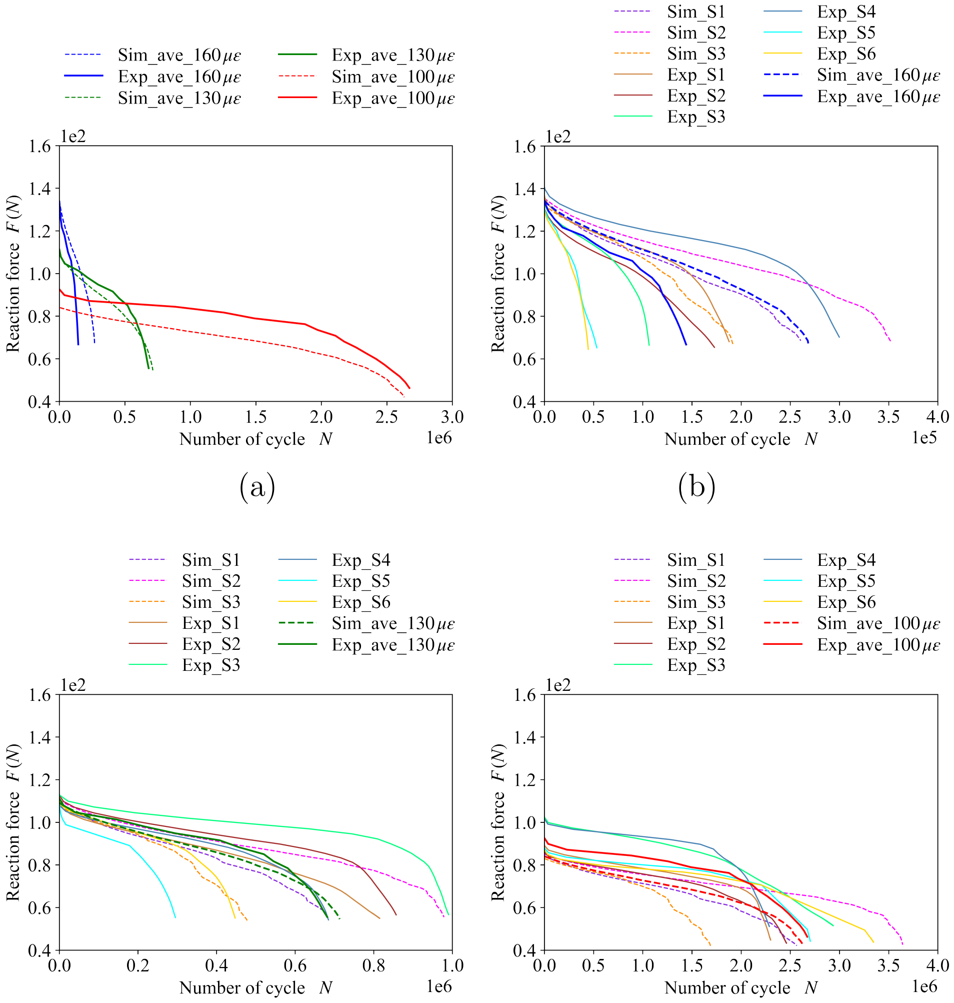

(a) (b) (c) (d)

Figure H.3: Comparison of reaction force evolution between 2PB fatigue tests simulation and experimentation [150], (a) average curves for different test strain levels, (b) average and all curves for test strain level 160 $\mu\varepsilon$, (c) 130 $\mu\varepsilon$ and (d) 100 $\mu\varepsilon$.

Bibliography

[1] R.A. Freire. *Use of fiberglass geogrids to the reinforcement of bituminous mixtures layers*. PhD thesis, Université de Lyon, 2020. (Cited on pages xx, xxxii, xxxiii, xl, xliii, 6, 8, 102, 106, 107 and 165.)

[2] H. Di Benedetto, C. De La Roche, H. Baaj, A. Pronk, and R. Lundström. Fatigue of bituminous mixtures. *Materials and structures*, 37(3):202–216, 2004. (Cited on pages xxxiii, 6, 9, 10 and 40.)

[3] I.M. Arsenie. *Etude et modélisation des renforcements de chaussées à l'aide de grilles en fibre de verre sous sollicitations de fatigue*. PhD thesis, Université de Strasbourg, 2013. (Cited on pages xxxiii, xxxiv, 6, 11, 16, 17, 18, 19, 20 and 21.)

[4] G. Liu. *Discrete element modelling of asphalt concrete reinforced with fiber glass grids*. PhD thesis, Université de Strasbourg, 2019. (Cited on pages xxix, xxxiii, xxxiv, xxxv, xli, 6, 10, 16, 17, 18, 19, 20, 37, 44, 45, 81, 101, 126, 129, 130, 131 and 132.)

[5] E. Yang, Y. Tang, L. Li, W. Yan, B. Huang, and Y. Qiu. Research on the recurrent neural network-based fatigue damage model of asphalt binder and the finite element analysis development. *Construction and Building Materials*, 267:121761, 2021. (Cited on pages 6 and 19.)

[6] L. Ruan, R. Luo, B. Wang, and X. Yu. Morphological characteristics of crack branching in asphalt mixtures under compression. *Engineering Fracture Mechanics*, 253:107884, 2021. (Cited on pages 6 and 33.)

[7] H. Di Benedetto and J.F. Corté. Matériaux routiers bitumineux 2. *Hermès Lavoisier editions*, 2005. (Cited on pages xxxiii, 6 and 12.)

[8] S. Mangiafico. *Linear viscoelastic properties and fatigue of bituminous mixtures produced with Reclaimed Asphalt Pavement and corresponding binder blends*. PhD thesis, Université de Lyon/ENTPE, 2014. (Cited on pages xxxiii, xxxix, xli, 6, 7, 15, 102 and 116.)

[9] W.B. Fuller and S.E. Thompson. The laws of proportioning concrete. *Transactions of the American Society of Civil Engineers*, 59(2):67–143, 1907. (Cited on page 7.)

[10] L.W. Nijboer. *Plasticity as a factor in the design of dense bituminous road carpets*. Elsevier Publishing Company, 1948. (Cited on page 7.)

[11] W.R. Vavrik, W.J. Pine, G. Huber, S.H. Carpenter, and R. Bailey. The bailey method of gradation evaluation: the influence of aggregate gradation and packing characteristics on voids in the mineral aggregate (with discussion). *Journal of the Association of Asphalt Paving Technologists*, 70, 2001. (Cited on page 7.)

[12] F. Olard. GB5 mix design: high-performance and cost-effective asphalt concretes by use of gap-graded curves and SBS modified bitumens. *Road Materials and Pavement Design*, 13(sup1):234–259, 2012. (Cited on page 7.)

[13] R. Roque, B. Birgisson, S. Kim, and A. Guarin. Development of mix design guidelines for improved performance of asphalt mixtures. Final Report UF Project no. 49104554032-12, Florida Department of Transportation, 2006. (Cited on page 7.)

[14] J.C. Santamarina, K.A. Klein, and M.A. Fam. *Soils and waves.* J. Wiley & Sons New York, 2001. (Cited on page 7.)

[15] C. Miller, K.L. Vasconcelos, D.N. Little, and A. Bhasin. Investigating aspects of aggregate properties that influence asphalt mixtures performance. Technical Report Research Rep DTFH61-06-C-00021, Texas A and M University at College Station and The University of Texas at Austin, 2011. (Cited on page 7.)

[16] J. Read and D. Whiteoak. *The shell bitumen handbook.* Thomas Telford, 2003. (Cited on page 7.)

[17] J. C. Petersen, R. E. Robertson, J. F. Branthaver, P. M. Harnsberger, J.J. Duvall, S.S. Kim, and H.U. Bahia. Binder characterization and evaluation: Volume 1. Strategic Highway Research Program Rep. No. SHRP-A-367, National Research Council, Washington, DC, 1994. (Cited on page 7.)

[18] A. Eurobitume. The bitumen industry—a global perspective: Production, chemistry, use, specification and occupational exposure. *Asphalt Institute*, 2011. (Cited on page 7.)

[19] P. Bazin and J. Saunier. Deformability, fatigue and healing properties of asphalt mixes. In *Intl Conf Struct Design Asphalt Pvmts*, 1967. (Cited on page 7.)

[20] H. Di Benedetto and C. De La Roche. State of the art on stiffness modulus and fatigue of bituminous mixtures. *Rilem Report*, pages 137–180, 1998. (Cited on page 7.)

[21] J.S. Miller, W.Y. Bellinger, et al. Distress identification manual for the long-term pavement performance program. Technical report, United States. Federal Highway Administration, 2003. (Cited on pages xxxiii and 9.)

[22] T. Nishizawa, S. Shimeno, and M. Sekiguchi. Fatigue analysis of asphalt pavements with thick asphalt mixture layer. In *Eighth International Conference on Asphalt PavementsFederal Highway Administration*, number Volume II, 1997. (Cited on page 9.)

[23] M. Nunn. Long-life flexible roads. In *Eighth International Conference on Asphalt PavementsFederal Highway Administration*, number Volume I, 1997. (Cited on page 9.)

[24] G. Al-Khateeb and A. Shenoy. A distinctive fatigue failure criterion. *Journal of the association of asphalt paving technologists*, 73:585–622, 2004. (Cited on page 9.)

[25] P.S. Pell and K.E. Cooper. The effect of testing and mix variables on the fatigue performance of bituminous materials. *Journal of the Association of Asphalt Paving Technologists*, 44:1–37, 1975. (Cited on page 9.)

[26] A.A. Tayebali, G.M. Rowe, and J.B. Sousa. Fatigue response of asphalt-aggregate mixtures (with discussion). *Journal of the Association of Asphalt Paving Technologists*, 61, 1992. (Cited on page 9.)

[27] Y.R. Kim, H.J. Lee, and D.N. Little. Fatigue characterization of asphalt concrete using viscoelasticity and continuum damage theory (with discussion). *Journal of the Association of Asphalt Paving Technologists*, 66, 1997. (Cited on page 9.)

[28] A.A. Tayebali, J.A. Deacon, J.S. Coplantz, and C.L. Monismith. Modeling fatigue response of asphalt-aggregate mixtures. *Asphalt Paving Technology*, 62:385–385, 1993. (Cited on page 9.)

[29] G.M. Rowe and M.G. Bouldin. Improved techniques to evaluate the fatigue resistance of asphaltic mixtures. In *2nd Eurasphalt & Eurobitume Congress Barcelona*, volume 2000, 2000. (Cited on page 9.)

[30] R. Reese. Properties of aged asphalt binder related to asphalt concrete fatigue life. *Journal of the Association of Asphalt Paving Technologists*, 66, 1997. (Cited on page 9.)

[31] K.D. Raithby and A.B. Sterling. Some effects of loading history on the fatigue performance of rolled asphalt. Technical Report Report No. LR

496, Transport and Road Research Laboratory (TRRL), Crowthorne, U.K., 1972. (Cited on page 9.)

[32] S.F. Said. *Fatigue characteristics of asphalt concrete mixtures*. Statens Väg-och Trafik-Institutet: Suède, 1988. (Cited on page 9.)

[33] Y. Xiong. *Formulaire de résistance des matériaux*. Eyrolles, 2002. (Cited on page 10.)

[34] H. Baaj, H. Di Benedetto, and P. Chaverot. Fatigue of mixes: an intrinsic damage approach. In *6th RILEM Symposium PTEBM, Zurich*, pages 394–400, 2003. (Cited on page 12.)

[35] H. Di Benedetto, A. Ashayer Soltani, and P. Chaverot. Fatigue damage for bituminous mixtures: a pertinent approach. *Journal of the Association of Asphalt Paving Technologists*, 65, 1996. (Cited on page 12.)

[36] C. De La Roche, J.F. Corté, J.C. Gramsammer, H. Odéon, and L. Tiret. Etude de la fatigue des enrobés bitumineux à l'aide du manège de fatigue du LCPC-Nantes. *Revue générale des routes et des aérodromes*, (716):62–74, 1994. (Cited on page 12.)

[37] R. Lakes and R.S. Lakes. *Viscoelastic materials*. Cambridge university press, 2009. (Cited on page 13.)

[38] R. Delgadillo, D.W. Cho, and H. Bahia. Nonlinearity of repeated creep and recovery binder test and relationship with mixture permanent deformation. *Transportation Research Record*, 1962(1):2–11, 2006. (Cited on page 13.)

[39] S. Kose, M. Guler, H.U. Bahia, and E. Masad. Distribution of strains within hot-mix asphalt binders: applying imaging and finite-element techniques. *Transportation Research Record*, 1728(1):21–27, 2000. (Cited on page 13.)

[40] P.P. Oldyrev. Self-heating and failure of plastics under cyclic loading. *Polymer Mechanics*, 3(3):322–328, 1967. (Cited on page 13.)

[41] E. Riahi, F. Allou, R. Botella, F. Fakhari Tehrani, F. Dubois, J. Absi, C. Petit, and F.E. Pérez-Jiménez. Modelling self-heating and thixotropy phenomena under the cyclic loading of asphalt. *Road Materials and Pavement Design*, 18(sup2):155–163, 2017. (Cited on page 13.)

[42] M.A. Ashayer Soltani. *Comportement en fatigue des enrobés bitumineux*. PhD thesis, ENTPE - INSA Lyon, 1998. (Cited on page 13.)

[43] D. Bodin, H. Soenen, and C. de La Roche. Temperature effects in binder fatigue and healing tests. In *3rd Euraspahlt & Eurobitume Congress*, pages 1996–2004, 2004. (Cited on page 13.)

[44] Q.T. Nguyen, H. Di Benedetto, and C. Sauzéat. Determination of thermal properties of asphalt mixtures as another output from cyclic tension-compression test. *Road Materials and Pavement Design*, 13(1):85–103, 2012. (Cited on page 13.)

[45] J. Mewis and N.J. Wagner. Thixotropy. *Advances in colloid and interface science*, 147:214–227, 2009. (Cited on page 13.)

[46] G. Gauthier, D. Bodin, E. Chailleux, and T. Gallet. Non linearity in bituminous materials during cyclic tests. *Road materials and pavement design*, 11(sup1):379–410, 2010. (Cited on page 13.)

[47] V. Mouillet, C. De la Roche, E. Chailleux, and P. Coussot. Thixotropic behavior of paving-grade bitumens under dynamic shear. *Journal of materials in civil engineering*, 24(1):23–31, 2012. (Cited on page 13.)

[48] L. Shan, Y. Tan, S. Underwood, and Y.R. Kim. Application of thixotropy to analyze fatigue and healing characteristics of asphalt binder. *Transportation research record*, 2179(1):85–92, 2010. (Cited on page 13.)

[49] F.E. Pérez-Jiménez, R. Botella, and R. Miró. Differentiating between damage and thixotropy in asphalt binder's fatigue tests. *Construction and Building Materials*, 31:212–219, 2012. (Cited on page 13.)

[50] E. Santagata, O. Baglieri, L. Tsantilis, and D. Dalmazzo. Evaluation of self healing properties of bituminous binders taking into account steric hardening effects. *Construction and Building Materials*, 41:60–67, 2013. (Cited on page 13.)

[51] B. Delaporte, J. Van Rompu, H. Di Benedetto, P. Chaverot, and G. Gauthier. New procedure to evaluate fatigue of bituminous mastics using an annular shear rheometer prototype. *Pavement cracking: mechanisms, modeling, detection, testing and case histories*, pages 457–467, 2008. (Cited on page 13.)

[52] F. Moreno-Navarro and M.C. Rubio-Gámez. A review of fatigue damage in bituminous mixtures: Understanding the phenomenon from a new perspective. *Construction and Building Materials*, 113:927–938, 2016. (Cited on pages xxxiii, 13, 14 and 16.)

[53] M.K. Darabi, R.K. Abu Al-Rub, E.A. Masad, and D.N. Little. Cyclic hardening-relaxation viscoplasticity model for asphalt concrete materials. *Journal of Engineering Mechanics*, 139(7):832–847, 2013. (Cited on page 13.)

[54] T. Chang and W. Guo. Effects of strain hardening and stress state on fatigue crack closure. *International journal of fatigue*, 21(9):881–888, 1999. (Cited on page 13.)

[55] H.D. Benedetto, T. Gabet, J. Grenfell, D. Perraton, C. Sauzéat, and D. Bodin. Mechanical testing of bituminous mixtures. In *Advances in Interlaboratory Testing and Evaluation of Bituminous Materials*, pages 143–256. Springer, 2013. (Cited on pages xxxiii, 14 and 15.)

[56] W. Schütz. A history of fatigue. *Engineering Fracture Mechanics*, 54:263–300, 1996. (Cited on page 14.)

[57] J. Schijve. Fatigue of structures and materials in the 20th century and the state of the art. *International Journal of fatigue*, 25(8):679–702, 2003. (Cited on page 14.)

[58] F.P. Beer, E.R. Johnston Jr, J.T. Dewolf, and D.F. Mazurek. *Mechanics of materials*. New York7 McGraw-Hill, 1992. (Cited on page 14.)

[59] Y.H. Huang. *Pavement analysis and design*. Prentice-Hall, Englewood Cliffs, NJ, 1993. (Cited on page 14.)

[60] F.N. Hveem. Pavement deflections and fatigue failures. Highway Research Board Bulletin No. 114, National Research Council, Washington, DC, 1955. (Cited on page 15.)

[61] S.H. Carpenter, K.A. Ghuzlan, and S. Shen. Fatigue endurance limit for highway and airport pavements. *Transportation research record*, 1832(1):131–138, 2003. (Cited on page 15.)

[62] A. Soltani, M. Solaimanian, and D.A. Anderson. An investigation of the endurance limit of hot-mix asphalt concrete: Using a new uniaxial fatigue test protocol. Technical report, United States. Federal Highway Administration, 2006. (Cited on page 15.)

[63] W.A. Zeiada, M.I. Souliman, K.E. Kaloush, and M. Mamlouk. Endurance limit for HMA based on healing concept using uniaxial tension-compression fatigue test. *Journal of materials in civil engineering*, 26(8):04014036, 2014. (Cited on page 15.)

[64] M. Buncher, D. Newcomb, and J. Huddleston. Perpetual pavements. *Asphalt Magazine*, 15(3):20–22, 2000. (Cited on page 15.)

[65] A. Norouzi, M. Sabouri, and Y. Richard Kim. Fatigue life and endurance limit prediction of asphalt mixtures using energy-based failure criterion. *International journal of pavement engineering*, 18(11):990–1003, 2017. (Cited on page 15.)

[66] C.L. Monismith, K. Inkabi, D.B. McLean, and C.R. Freeme. Design considerations for asphalt pavements, report no. te 77-1. *University of California, Berkeley*, 1977. (Cited on page 15.)

[67] Z. Wu, Z. Q. Siddique, M. Hossain, and A.J. Gisi. Kansas turnpike: an example of long lasting asphalt pavement. In *International Symposium on Design and Construction of Long Lasting Asphalt Pavements, 2004, Auburn, Alabama, USA*, 2004. (Cited on page 15.)

[68] S. Bhattacharjee, A.K. Swamy, and J.S. Daniel. Application of elastic–viscoelastic correspondence principle to determine fatigue endurance limit of hot-mix asphalt. *Transportation research record*, 2126(1):12–18, 2009. (Cited on page 15.)

[69] M.R. Thompson and S.H. Carpenter. Considering hot-mix-asphalt fatigue endurance limit in full-depth mechanistic-empirical pavement design. In *Proc., International Conference on Perpetual Pavement*. Citeseer, 2006. (Cited on page 15.)

[70] B.D. Prowell, E.R. Brown, R.M. Anderson, S. Shen, and S.H. Carpenter. Endurance limit of hot mix asphalt mixtures to prevent bottom-up fatigue cracking. In *Asphalt Paving Technology: Association of Asphalt Paving Technologists-Proceedings of the Technical Sessions*, volume 79, pages 519–559. Association of Asphalt Paving Technologist, 2010. (Cited on page 15.)

[71] E. Papa and A. Taliercio. Anisotropic damage model for the multiaxial static and fatigue behaviour of plain concrete. *Engineering Fracture Mechanics*, 55(2):163–179, 1996. (Cited on page 16.)

[72] A. Alliche. Damage model for fatigue loading of concrete. *International Journal of Fatigue*, 26(9):915–921, 2004. (Cited on page 16.)

[73] D. Bodin. *Modèle d'endommagement par fatigue: application aux enrobés bitumineux*. PhD thesis, Université de Nantes, 2002. (Cited on pages 16, 19 and 20.)

[74] M. Jirásek and B. Patzák. Consistent tangent stiffness for nonlocal damage models. *Computers & structures*, 80(14-15):1279–1293, 2002. (Cited on page 16.)

[75] M. Klesnil and P. Lukáš. Influence of strength and stress history on growth and stabilisation of fatigue cracks. *Engineering Fracture Mechanics*, 4(1):77–92, 1972. (Cited on page 16.)

[76] S. Ray and J.M.C. Kishen. Fatigue crack propagation model for plain concrete–an analogy with population growth. *Engineering fracture mechanics*, 77(17):3418–3433, 2010. (Cited on page 16.)

[77] V. Slowik, G.A. Plizzari, and V.E. Saouma. Fracture of concrete under variable amplitude fatigue loading. *Materials Journal*, 93(3):272–283, 1996. (Cited on page 16.)

[78] N.H.T. Nguyen, H.H. Bui, J. Kodikara, S. Arooran, and F. Darve. A discrete element modelling approach for fatigue damage growth in cemented materials. *International Journal of Plasticity*, 112:68–88, 2019. (Cited on pages xxxiv, xxxv, 16, 20, 35, 36 and 39.)

[79] N. Moës, C. Stolz, and N. Chevaugeon. Coupling local and non-local damage evolutions with the thick level set model. *Advanced Modeling and Simulation in Engineering Sciences*, 1(1):1–21, 2014. (Cited on pages 17 and 40.)

[80] M. Jirásek. Nonlocal damage mechanics. *Revue européenne de génie civil*, 11(7-8):993–1021, 2007. (Cited on page 17.)

[81] G. Pijaudier-Cabot and D. Grégoire. A review of non local continuum damage: Modelling of failure? *Networks & Heterogeneous Media*, 9(4):575, 2014. (Cited on page 17.)

[82] M.K. Samal, M. Seidenfuss, and E. Roos. A comparative assessment of local and nonlocal damage models for prediction of fracture behavior during mixed-mode loading. *Procedia Engineering*, 55:493–498, 2013. (Cited on page 17.)

[83] F.A. Tavarez. *Discrete element method for modelling solid and particulate materials*. PhD thesis, University of Wisconsin–Madison, 2005. (Cited on pages xxxiv and 19.)

[84] G. Gibert, B. Prabel, A. Gravouil, and C. Jacquemoud. A 3d automatic mesh refinement X-FEM approach for fatigue crack propagation. *Finite Elements in Analysis and Design*, 157:21–37, 2019. (Cited on pages xxxiv and 20.)

[85] A. Hrennikoff. Solution of problems of elasticity by the framework method. *ASME J. Appl. Mech.*, 8:A619–A715, 1941. (Cited on page 17.)

[86] T. Belytschko, Y. Krongauz, D. Organ, M. Fleming, and P. Krysl. Meshless methods: an overview and recent developments. *Computer methods in applied mechanics and engineering*, 139(1-4):3–47, 1996. (Cited on page 17.)

[87] P.A. Cundall and O.D.L. Strack. A discrete numerical model for granular assemblies. *geotechnique*, 29(1):47–65, 1979. (Cited on page 17.)

[88] M. Sharafisafa and M. Nazem. Application of the distinct element method and the extended finite element method in modelling cracks and coalescence in brittle materials. *Computational Materials Science*, 91:102–121, 2014. (Cited on page 17.)

[89] R.A. Schapery. A theory of mechanical behavior of elastic media with growing damage and other changes in structure. *Journal of the Mechanics and Physics of Solids*, 38(2):215–253, 1990. (Cited on page 18.)

[90] R.A. Schapery. Correspondence principles and a generalizedj integral for large deformation and fracture analysis of viscoelastic media. *International journal of fracture*, 25(3):195–223, 1984. (Cited on page 18.)

[91] M.E. Kutay and M. Lanotte. Viscoelastic continuum damage (VECD) models for cracking problems in asphalt mixtures. *International journal of pavement engineering*, 19(3):231–242, 2018. (Cited on page 18.)

[92] W. Cao, L. Mohammad, and P. Barghabany. Use of indirect tension test and viscoelastic continuum damage theory for fatigue characterization of asphalt mixtures. *Construction and Building Materials*, 187:38–49, 2018. (Cited on page 18.)

[93] W. Cao and C. Wang. Fatigue performance characterization and prediction of asphalt binders using the linear amplitude sweep based viscoelastic continuum damage approach. *International Journal of Fatigue*, 119:112–125, 2019. (Cited on page 18.)

[94] A. Al Assi, H. Sadek, C. Massarra, M. Sadeq, and C.J. Friedland. Development of an analysis tool for deterministic and probabilistic viscoelastic continuum damage approach. *Construction and Building Materials*, 306:124853, 2021. (Cited on page 18.)

[95] N. Hernandez-Fernandez, B.S. Underwood, and A. Ossa-Lopez. Simulation of the asphalt concrete stiffness degradation using simplified

viscoelastic continuum damage model. *International Journal of Fatigue*, 140:105850, 2020. (Cited on page 18.)

[96] C.S. Desai. *Mechanics of materials and interfaces: The disturbed state concept*. CRC press, 2000. (Cited on page 18.)

[97] C.S. Desai. Unified DSC constitutive model for pavement materials with numerical implementation. *International Journal of Geomechanics*, 7(2):83–101, 2007. (Cited on page 19.)

[98] C.S. Desai. Constitutive modeling of materials and contacts using the disturbed state concept: Part 1–background and analysis. *Computers & Structures*, 146:214–233, 2015. (Cited on page 19.)

[99] C. Szydłowski, Ł. Smakosz, M. Stienss, and J. Górski. The use of a two-phase monte carlo material model to reflect the dispersion of asphalt concrete fracture parameters. *Theoretical and Applied Fracture Mechanics*, 119:103326, 2022. (Cited on pages xxxiv, 19 and 20.)

[100] P. Cao, G. Li, J. Yu, M. Zhang, F. Jin, and Z. Zhao. Research and application of random aggregate model in determining the fracture behavior of four-point bending beam with notch. *Construction and Building Materials*, 202:276–289, 2019. (Cited on page 19.)

[101] X. Gao. *Modelling of nominal strength prediction for quasi-brittle materials: application to discrete element modelling of damage and fracture of asphalt concrete under fatigue loading*. PhD thesis, Université de Strasbourg, 2017. (Cited on pages xxix, xxxiii, xxxiv, xxxv, 18, 19, 20, 21, 23, 30, 35, 38 and 125.)

[102] I.M. Arsenie, C. Chazallon, J.L. Duchez, and S. Mouhoubi. Modelling of the fatigue damage of a geogrid-reinforced asphalt concrete. *Road Materials and Pavement Design*, 18(1):250–262, 2017. (Cited on pages xxxiv and 21.)

[103] I.M. Arsenie, C. Chazallon, J.L. Duchez, and P. Hornych. Laboratory characterisation of the fatigue behaviour of a glass fibre grid-reinforced asphalt concrete using 4PB tests. *Road Materials and Pavement Design*, 18(1):168–180, 2017. (Cited on pages xxxiv and 21.)

[104] C.T. Sun and Z. Jin. *Fracture mechanics*. Academic Press, 2011. (Cited on pages xxxiv, 22 and 25.)

[105] G.R. Irwin. *Analysis of stresses and strains near the end of a crack traversing a plate*. American Society of Mechanical Engineers, 1957. (Cited on pages xxxiv, 22, 23 and 25.)

[106] H.M. Westergaard. Bearing pressures and cracks. *SPIE MILESTONE SERIES MS*, 137:18–22, 1997. (Cited on page 22.)

[107] B.R. Lawn. *Fracture of brittle solids*. Cambridge solid state science series. Cambridge University Press, Cambridge ; New York, 2nd ed edition, 1993. (Cited on page 24.)

[108] H. Tada, P.C. Paris, and G.R. Irwin. *The stress analysis of cracks handbook*. ASME Press,New York, 2000. (Cited on pages 24, 35, 135, 136 and 137.)

[109] A.A. Griffith. The phenomenon of rupture and flow in solids. *Phil. Trans. Royal Soc. London, A*, 221:163–198, 1920. (Cited on page 24.)

[110] P.C. Paris and F. Erdogan. A critical analysis of crack propagation laws. *Journal of Basic Engineering*, 85:528–534, 1963. (Cited on page 31.)

[111] R.J. Donahue, H. Clark, P. Atanmo, R. Kumble, and A.J. McEvily. Crack opening displacement and the rate of fatigue crack growth. *International Journal of Fracture Mechanics*, 8(2):209–219, 1972. (Cited on page 31.)

[112] M.H. El Haddad, T.H. Topper, and K.N. Smith. Prediction of non propagating cracks. *Engineering fracture mechanics*, 11(3):573–584, 1979. (Cited on page 31.)

[113] M. Ciavarella, M. Paggi, and A. Carpinteri. One, no one, and one hundred thousand crack propagation laws: a generalized barenblatt and botvina dimensional analysis approach to fatigue crack growth. *Journal of the Mechanics and Physics of Solids*, 56(12):3416–3432, 2008. (Cited on page 31.)

[114] N. Pugno, M. Ciavarella, P. Cornetti, and A. Carpinteri. A generalized paris' law for fatigue crack growth. *Journal of the Mechanics and Physics of Solids*, 54(7):1333–1349, 2006. (Cited on pages xxxiv, xxxix, 31, 32, 91, 92 and 96.)

[115] J. Glucklich. Fracture of plain concrete. *Journal of the Engineering Mechanics Division*, 89(6):127–138, 1963. (Cited on page 32.)

[116] S. Kumar and S.V. Barai. Fracture mechanics of concrete–state-of-the-art review. *Concrete Fracture Models and Applications*, pages 9–63, 2011. (Cited on page 32.)

[117] J. Bhargava and Å. Rehnström. High-speed photography for fracture studies of concrete. *Cement and Concrete Research*, 5(3):239–247, 1975. (Cited on page 32.)

[118] Y. Sakata and M. Ohtsu. Crack evaluation in concrete members based on ultrasonic spectroscopy. *Materials Journal*, 92(6):686–698, 1995. (Cited on page 32.)

[119] K.N. Derucher. Application of the scanning electron microscope to fracture studies of concrete. *Building and Environment*, 13(2):135–141, 1978. (Cited on page 32.)

[120] F. Ansari. Mechanism of microcrack formation in concrete. *Materials Journal*, 86(5):459–464, 1989. (Cited on page 32.)

[121] S. Mindess and S. Diamond. A preliminary SEM study of crack propagation in mortar. *Cement and Concrete Research*, 10(4):509–519, 1980. (Cited on page 32.)

[122] S. Mindess and S. Diamond. A device for direct observation of cracking of cement paste or mortar under compressive loading within a scanning electron microscope. *Cement and Concrete Research*, 12(5):569–576, 1982. (Cited on page 32.)

[123] X. Hu and F.H. Wittmann. Experimental method to determine extension of fracture-process zone. *Journal of Materials in Civil Engineering*, 2(1):15–23, 1990. (Cited on page 32.)

[124] A. Maji and S.P. Shah. Process zone and acoustic-emission measurements in concrete. *Experimental mechanics*, 28(1):27–33, 1988. (Cited on page 32.)

[125] K. Otsuka and H. Date. Fracture process zone in concrete tension specimen. *Engineering fracture mechanics*, 65(2-3):111–131, 2000. (Cited on pages xxxiv, 32 and 33.)

[126] F. Zhou, X. Hu, S. Hu, L.F. Walubita, and T. Scullion. Incorporation of crack propagation in the ME fatigue cracking prediction. *Road Materials and Pavement Design*, 9(sup1):433–465, 2008. (Cited on page 33.)

[127] J. Kollmann, P. Liu, G. Lu, D. Wang, M. Oeser, and S. Leischner. Investigation of the microstructural fracture behaviour of asphalt mixtures using the finite element method. *Construction and Building Materials*, 227:117078, 2019. (Cited on page 33.)

[128] L. Chang and N. Kaijian. Simulation of asphalt concrete cracking using cohesive zone model. *Construction and Building Materials*, 38:1097–1106, 2013. (Cited on page 33.)

[129] X. Teng and T. Wierzbicki. Evaluation of six fracture models in high velocity perforation. *Engineering Fracture Mechanics*, 73(12):1653–1678, 2006. (Cited on page 33.)

[130] Y. Wang, X. Zhou, and M. Kou. Peridynamic investigation on thermal fracturing behavior of ceramic nuclear fuel pellets under power cycles. *Ceramics International*, 44(10):11512–11542, 2018. (Cited on page 33.)

[131] G. Teng, C. Zheng, X. Chen, X. Lan, Y. Zhu, and C. Shan. Numerical fracture investigation of single-edge notched asphalt concrete beam based on random heterogeneous FEM model. *Construction and Building Materials*, 304:124581, 2021. (Cited on pages xxxv, 33 and 34.)

[132] P. Thamburaja, K. Sarah, A. Srinivasa, and J.N. Reddy. Fracture of viscoelastic materials: FEM implementation of a non-local & rate form-based finite-deformation constitutive theory. *Computer Methods in Applied Mechanics and Engineering*, 354:871–903, 2019. (Cited on page 33.)

[133] E. Mahmoud, S. Saadeh, H. Hakimelahi, and J. Harvey. Extended finite-element modelling of asphalt mixtures fracture properties using the semi-circular bending test. *Road Materials and Pavement Design*, 15(1):153–166, 2014. (Cited on page 33.)

[134] H. Wang, J. Wang, and J. Chen. Fracture simulation of asphalt concrete with randomly generated aggregate microstructure. *Road Materials and Pavement Design*, 19(7):1674–1691, 2018. (Cited on page 33.)

[135] J.M. Melenk and I. Babuška. The partition of unity finite element method: basic theory and applications. *Computer methods in applied mechanics and engineering*, 139(1-4):289–314, 1996. (Cited on page 33.)

[136] I.M. Lancaster, H.A. Khalid, and I.A. Kougioumtzoglou. Extended FEM modelling of crack propagation using the semi-circular bending test. *Construction and Building Materials*, 48:270–277, 2013. (Cited on pages xxxv, 34 and 35.)

[137] G.I. Barenblatt. The formation of equilibrium cracks during brittle fracture. general ideas and hypotheses. axially-symmetric cracks. *Jour-*

nal of applied mathematics and mechanics, 23(3):622–636, 1959. (Cited on page 36.)

[138] K. Park and G.H. Paulino. Cohesive zone models: a critical review of traction-separation relationships across fracture surfaces. *Applied Mechanics Reviews*, 64(6), 2011. (Cited on page 36.)

[139] H. Kim, M.P. Wagoner, and W.G. Buttlar. Numerical fracture analysis on the specimen size dependency of asphalt concrete using a cohesive softening model. *Construction and Building Materials*, 23(5):2112–2120, 2009. (Cited on page 36.)

[140] H. Kim and W.G. Buttlar. Discrete fracture modeling of asphalt concrete. *International Journal of Solids and Structures*, 46(13):2593–2604, 2009. (Cited on pages xxxv, 36, 37 and 38.)

[141] H. Kim, M.P. Wagoner, and W.G. Buttlar. Micromechanical fracture modeling of asphalt concrete using a single-edge notched beam test. *Materials and Structures*, 42(5):677–689, 2009. (Cited on page 36.)

[142] H. Baaj, H. Di Benedetto, and P. Chaverot. Effect of binder characteristics on fatigue of asphalt pavement using an intrinsic damage approach. *Road Materials and Pavement Design*, 6(2):147–174, 2005. (Cited on page 40.)

[143] N. Moës, C. Stolz, P.E. Bernard, and N. Chevaugeon. A level set based model for damage growth: the thick level set approach. *International Journal for Numerical Methods in Engineering*, 86(3):358–380, 2011. (Cited on pages xxxv and 40.)

[144] Itasca Consulting Group Inc. *Particle Flow Code 5.0 documentation*, 2018. (Cited on pages 46, 125, 126 and 153.)

[145] D.O. Potyondy and P.A. Cundall. A bonded-particle model for rock. *International journal of rock mechanics and mining sciences*, 41(8):1329–1364, 2004. (Cited on pages 46, 129, 130 and 131.)

[146] F.A. Tavarez and M.E. Plesha. Discrete element method for modelling solid and particulate materials. *International journal for numerical methods in engineering*, 70(4):379–404, 2007. (Cited on page 47.)

[147] B.D. Le. *Modélisation discrète en mécanique de la rupture des matériaux fragiles*. PhD thesis, Université de Strasbourg, 2013. (Cited on page 47.)

[148] Z.P. Bažant and K. Xu. Size effect in fatigue fracture of concrete. *ACI Mater. J*, 88(4):390–399, 1991. (Cited on page 86.)

[149] S. Ma, X.B. Zhang, N. Recho, and J. Li. The mixed-mode investigation of the fatigue crack in CTS metallic specimen. *International Journal of Fatigue*, 28(12):1780–1790, 2006. (Cited on page 86.)

[150] M.L. Nguyen, P. Hornych, X.Q. Le, M. Dauvergne, L. Lumière, C. Chazallon, M. Sahli, S. Mouhoubi, D. Doligez, and E. Godard. Development of a rational design procedure based on fatigue characterisation and environmental evaluations of asphalt pavement reinforced with glass fibre grid. *Road Materials and Pavement Design*, 22(sup1):S672–S689, 2021. (Cited on pages xxi, xxiii, xxxii, xxxiii, xl, xli, xliv, 110, 111, 112, 116, 118, 119, 166 and 167.)

[151] EN 12697-24 (F). Bituminous mixtures - test methods - part 24: Resistance to fatigue. Standard, November 2018. (Cited on pages xli and 116.)

[152] EN 12697-26 (F). Bituminous mixtures. test methods stiffness. Standard, July 2018. (Cited on page 116.)

[153] K. Bagi. An algorithm to generate random dense arrangements for discrete element simulations of granular assemblies. *Granular Matter*, 7(1):31–43, 2005. (Cited on page 129.)

[154] B. Yang, Y. Jiao, and S. Lei. A study on the effects of microparameters on macroproperties for specimens created by bonded particles. *Engineering Computations*, 2006. (Cited on pages 129 and 131.)

[155] J. Yoon. Application of experimental design and optimization to PFC model calibration in uniaxial compression simulation. *International Journal of Rock Mechanics and Mining Sciences*, 44(6):871–889, 2007. (Cited on page 131.)

Lei MA

Discrete element modeling of asphalt concrete fatigue behavior by an energetic method.

Résumé

Deux modèles discrets, le modèle de propagation des fissures et le modèle d'endommagement sont proposés dans ce travail. Tout d'abord, pour représenter l'incrémentation des fissures dans la méthode des éléments discrets, la relation entre la croissance des fissures et l'endommagement du contact est formulée, sur la base de l'équivalence énergétique entre l'énergie dissipée en raison de la dégradation de la rigidité du contact et l'énergie libérée pendant la propagation des fissures. Ensuite, selon la relation entre le facteur d'intensité de contrainte et le taux de libération d'énergie, la loi de Paris est incorporée dans le modèle de propagation des fissures pour régir la croissance des fissures de fatigue. Les comparaisons du modèle de propagation des fissures proposé avec les résultats théoriques et expérimentaux présentent de bons accords et une grande précision. Le modèle d'endommagement proposé considère que le développement de l'endommagement du matériau est causé par le développement d'un réseau de microfissures qui peut être représenté comme une seule croissance de fissure courte régie par une variante de la loi de Paris. Un paramètre supplémentaire est introduit pour exercer un effet sur le calcul du taux de libération d'énergie, ce qui entraîne un effet de variante sur la loi de fatigue, ce qui permet au modèle d'endommagement de capturer l'ensemble du processus d'évolution de la fatigue pendant les essais de fatigue. Enfin, les simulations sont comparées aux expérimentations des essais de tension-compression, de flexion à deux points et de flexion à quatre points. Les bons accords de ces comparaisons soutiennent la capacité du modèle proposé à modéliser l'ensemble du processus d'évolution de la fatigue de différents matériaux à différents niveaux de chargement.

Mots-clés: béton bitumineux ; fatigue ; endommagement ; fissuration ; méthode des éléments discrets

Abstract

Two discrete models, crack propagation model and damage model are proposed in this work. Firstly, to represent crack increment in discrete element method, the relation between crack growth and contact damage is formulated, based on the energy equivalence between the energy dissipated due to contact stiffness degradation and the energy released during crack propagation. Then, according to the relation between stress intensity factor and energy release rate, Paris' law is incorporated in the crack propagation model to govern fatigue crack growth. Comparisons of the proposed crack propagation model with theoretical and experimental results present good agreements and high precision. The proposed damage model considers that the damage development of material is caused by micro-cracks network development which can be represented as a single short crack growth governed by a variant Paris' law. An additional parameter is introduced to exert effect on the calculation of energy release rate, hence results a variant effect on fatigue law, which allows the damage model to capture the whole process of fatigue evolution during fatigue tests. Finally, simulations are compared to experimentations of Tension-Compression, Two-Point Bending and Four-Point Bending tests. Good agreements of these comparisons support the capacity of the proposed model for modeling the whole process of fatigue evolution of different materials under different loading levels.

Keywords: asphalt concrete; fatigue; damage; crack propagation; discrete element method